AD NUMBER

ADB008070

LIMITATION CHANGES

TO:

Approved for public release; distribution is unlimited.

FROM:

Distribution authorized to U.S. Gov't. agencies only; Test and Evaluation; MAY 1975. Other requests shall be referred to Air Force Avionics Lab., Wright-Patterson AFB, OH 45433.

AUTHORITY

AFWAL ltr 9 May 1980

AFAL-TR-75-45

OPTOELECTRONIC ASPECTS OF AVIONIC SYSTEMS II

SPECTRONICS, INC.
830 EAST ARAPAHO ROAD
RICHARDSON, TEXAS 75080

MAY 1975

TECHNICAL REPORT AFAL-TR-75-45

AIR FORCE AVIONICS LABORATORY
AF WRIGHT AERONAUTICAL LABORATORIES (AFSC)
Wright-Patterson Air Force Base, Ohio 45433

NOTICE

When Government drawings, specifications, or other data are used for any purpose other than in connection with a definitely related Government procurement operation, the United States Government thereby incurs no responsibility nor any obligation whatsoever; and the fact that the government may have formulated, furnished, or in any way supplied the said drawings, specifications, or other data, is not to be regarded by implication or otherwise as in any manner licensing the holder or any other person or corporation, or conveying any rights or permission to manufacture, use, or sell any patented invention that may in any way be related thereto.

This report has been reviewed and is approved.

K.C. TRUMBLE, Project Engineer
Information Transfer Group
Information Management Branch

FOR THE COMMANDER

ROBERT N. SPANBAUER, LT COL, USAF
Chief, System Avionics Division
Air Force Avionics Laboratory

Copies of this report should not be returned unless return is required by security considerations, contractual obligations, or notice on a specific document.

UNCLASSIFIED

SECURITY CLASSIFICATION OF THIS PAGE (When Data Entered)

REPORT DOCUMENTATION PAGE

READ INSTRUCTIONS BEFORE COMPLETING FORM

1. REPORT NUMBER: AFAL-TR-75-45	2. GOVT ACCESSION NO.
3. RECIPIENT'S CATALOG NUMBER	
4. TITLE (and Subtitle): OPTOELECTRONIC ASPECTS OF AVIONIC SYSTEMS II.	5. TYPE OF REPORT & PERIOD COVERED: Final Report for Period Apr 1973 — Dec 1974
6. PERFORMING ORG. REPORT NUMBER	
7. AUTHOR(s): J. R. Biard	8. CONTRACT OR GRANT NUMBER(s): F33615-73-C-1272
9. PERFORMING ORGANIZATION NAME AND ADDRESS: SPECTRONICS, INC. 830 E. Arapaho Road Richardson, Texas 75080	10. PROGRAM ELEMENT, PROJECT, TASK AREA & WORK UNIT NUMBERS: Project 2003 Task AF-2003
11. CONTROLLING OFFICE NAME AND ADDRESS: Air Force Avionics Laboratory AFAL/AAM Air Force Systems Command Wright-Patterson AFB, Ohio 45433	12. REPORT DATE: May 1975 13. NUMBER OF PAGES: 348
14. MONITORING AGENCY NAME & ADDRESS (if different from Controlling Office)	15. SECURITY CLASS. (of this report): UNCLASSIFIED
	15a. DECLASSIFICATION/DOWNGRADING SCHEDULE

373p.

16. DISTRIBUTION STATEMENT (of this Report)

Distribution limited to US Government Agencies only; Test and Evaluation; May 1975. Other requests for this document must be referred to AFAL/AAM, Wright-Patterson AFB, Ohio 45433.

17. DISTRIBUTION STATEMENT (of the abstract entered in Block 20, if different from Report)

18. SUPPLEMENTARY NOTES

19. KEY WORDS (Continue on reverse side if necessary and identify by block number) (continued on reverse side)

Optoelectronic	suboptimum detection	light emitting diode
electro-optic	matched filter	LED
data bus	fiber optic bundle	photodetector
multiplex	optical interconnect	photodiode
data transmission	packing fraction	preamplifier

20. ABSTRACT (Continue on reverse side if necessary and identify by block number) (continued on reverse side)

This document is the final report of a second year study of the optoelectronic aspects of avionic systems. Avionics systems are moving toward the use of a combination of multiplex data buses for the transmission of the growing number of digital signals found in modern aircraft and high performance dedicated cables for the transmission of wide-band analog signals. Optoelectronic technology based on the use of light emitting diodes (LEDs), multimode flexible fiber optic bundles, and photodiodes offers a data transmission capability that is consistent with military requirements and potentially superior to wire.

DD FORM 1 JAN 73 1473 EDITION OF 1 NOV 65 IS OBSOLETE

AIR FORCE - 22-9-75 - 400

UNCLASSIFIED

SECURITY CLASSIFICATION OF THIS PAGE (When Data Entered)

389 381

19. Key Words (continued from front)

numerical aperture	radial coupler	EMP	transient
simplex	T coupler	X-ray	decay
uniform duplex	data rate	gamma ray	absorption
tapered duplex	error rate	neutron	
radial duplex	nuclear	radiation hardening	
star coupler	radiation effects	luminescence	

20. Abstract (continued from front)

techniques. The optoelectronic interface is suitable for use in high data rate digital data buses and wide-band analog channels. The primary objective of this program is to study non-coherent optical components, devices and techniques in order to discover the unique constraints imposed on opto-electronic data transmission systems. This second year study starts with the results of the initial study performed on contract number F33615-72-C-1565 and goes further into the study of signaling and detection, data bus structure and optoelectronic components. A study of radiation effects on active and passive optical components is also presented. Presently available components are capable of data rates in excess of 200M bit/s. However, LED and fiber optic development is required to improve the efficiency and reduce the complexity of high performance systems.

FOREWORD

This report describes a study of optoelectronic data buses conducted by Spectronics, Incorporated; Richardson, Texas. The work was performed for the System Avionics Division, Air Force Avionics Laboratory, Wright-Patterson AFB, Ohio. The work was done on contract number F33615-73-C-1272, Project 2003, Task 2003 07. The United States Air Force project engineer was Mr. K.C. Trumble of the Information Management Branch (AFAL/AAM). Dr. J.R. Biard was the principal investigator of the program. He was assisted in the preparation of this report by Dr. J.P. Mize. Research on this contract was conducted from April 1973 to December 1974. The draft report was submitted for approval in February 1975.

The author wishes to acknowledge the contributions to this program made by K.C. Trumble and D.A. Zann of the Air Force Avionics Laboratory, Dr. J.P. Mize, J.E. Shaunfield and J.F. Leezer of Spectronics, Inc., and Dr. K.W. Heizer of Southern Methodist University.

TABLE OF CONTENTS

TABLE OF CONTENTS (continued)

LIST OF ILLUSTRATIONS

LIST OF ILLUSTRATIONS (continued)

LIST OF ILLUSTRATIONS (continued)

LIST OF ILLUSTRATIONS (continued)

LIST OF ILLUSTRATIONS (continued)

LIST OF ILLUSTRATIONS (continued)

LIST OF TABLES

LIST OF TABLES (continued)

LIST OF SYMBOLS

SYMBOL	DEFINITION	UNIT
a	Current, constant for curve fit	A
ac	Alternating current	-
a_n	Maximum fiber optic attenuation	-
a_o	Average fiber optic attenuation per station	-
a_T	Total optical attenuation	-
a_1	Distance in depletion layer	μm
b	Time, constant for curve fit	s
C_N	Coupling factor for station N in a tapered in-line data bus	-
C_T	Total capacitance at preamp input	PF
C_T	Coupling factor of T coupler	-
C_d	Photodiode capacitance	pF
C_a	Capacitor in overdrive network	F
C_f	Preamp feedback capacitor	pF
C_k	Coupling factor for station k in a tapered duplex data bus	-
C_{opt}	Optimum value of C_T	-
C_*	Coupling factor of Radial Coupler	-
c	Velocity of light in vacuum	m/s
D_{R*}	Dynamic range of a radial data bus	-
D_{RT}	Dynamic range of an in-line duplex bus	-
D_s	Scrambler rod diameter	m
*D	Symbol denoting a radial duplex data bus	-

LIST OF SYMBOLS (continued)

SYMBOL	DEFINITION	UNIT
dc	Direct current	-
E	Electric field	V/cm
E_c	Electric field, constant for curve fit	V/cm
E_ϕ	Photon energy	eV
e_o	Output voltage	V
e_{on}	Preamp output noise voltage	V
$F(\omega)$	Fourier transform of f(t)	-
f	Frequency	Hz
"f^2"	Component of $\frac{i_n^2}{\Delta f}$ that has f^2 dependence	=
f_a	Low corner frequency (zero) of LED overdrive network	Hz
f_b	Overdrive network $\sqrt{2}$ frequency	Hz
f_d	LED corner frequency	Hz
f_e	Amplifier 3dB frequency	Hz
f_{e1}	Preamp noise transition frequency	Hz
f_n	Noise corner frequency	Hz
f_T	Transistor gain-bandwidth product	Hz
f(t)	Impulse response, general	-
f_o	Preamp corner frequency	Hz
f_2	Postamp corner frequency	Hz
f_{3dB}	Photodiode 3dB frequency	Hz

LIST OF SYMBOLS (continued)

SYMBOL	DEFINITION	UNIT
f_ϕ	LED 0.707 frequency	Hz
Δf_a	Total equivalent noise bandwidth	Hz
Δf_{f^2}	"f^2" noise bandwidth	Hz
Δf_W	"White" noise bandwidth	Hz
G	Geometric area coverage of fibers in a termination	-
$H(\omega)$	Transfer function of matched filter	-
$H_n(\omega)$	Transfer function of noise whitening filter	-
$H_n^*(\omega)$	Complex conjugate of $H_n(\omega)$	-
h_{FE}	Common emitter dc current gain	-
$h(\tau)$	Impulse response of matched filter	-
$h_n(\tau)$	Impulse response of noise whitening filter	-
$h(t-\tau)$	$h(\tau)$ reversed in time and delayed through all values of t	-
$h_n(t-\tau)$	$h_n(\tau)$ reversed in time and delayed through all values of t	-
$h(t_o-\tau)$	$h(t-\tau_o)$ at optimum sample time	-
I_B	DC base current of preamp input transistor T1	A
I_{DC}	DC drive current	A
I_E	DC emitter current of T1	A
$I_E\|_{opt}$	Optimum value of I_E	A

LIST OF SYMBOLS (continued)

SYMBOL	DEFINITION	UNIT
Im	Imaginary part	-
I_n	Electron current	A
I_o	Steady state current	A
I_P	Hole current	A
I_R	Diode reverse current	A
I_s	Steady state photodiode signal current	A
$I(\omega)$	Photocurrent frequency response	A
$I_2^*(\omega)$	Complex conjugate of $I_2(\omega)$	A
$I_{\ell}(\omega)$	AC steady state output of noise whitening filter	A
$i(t)$	Transient current response	A
i_a	Input current to overdrive network	A
i_d	Ac component of LED current	A
$i_m(t)$	Output signal of matched filter	A
$I_m(t_o)$	Max value of $i_m(t)$	A
$\frac{i_n^2}{\Delta f}$	Mean square noise current spectral density	A^2/Hz
i_{nT}^2	Total mean square noise current	A^2
i_{n1}^2	First term of i_{nT}^2	A^2
$i_{n2,3}^2$	Second and third terms of i_{nT}^2	A^2
i_{n4}^2	Fourth term of i_{nT}^2	A^2
i_n	RMS value of equivalent input noise current	A

LIST OF SYMBOLS (continued)

SYMBOL	DEFINITION	UNIT
i_{pk}	Peak value of ac drive current	A
i_s	Photodiode signal current	A
i_{sat}	Saturated value of pulse photo current	A
$i_1(\tau)$	Input signal to noise whitening filter	A
$i_2(t)$	Output signal of noise whitening filter	A
K	"White" mean square noise spectral density	A^2/Hz
K_1	Constant, in-line data bus	-
k	Boltzmann's constant	J/°K
LED	Light Emitting Diode	-
L	Length of data bus	m,ft
L_s	Scrambler rod length	m
M	Avalanche multiplication gain	-
m	Overall quality factor of T coupler	-
m_a	Overdrive factor	-
m_c	Coupling quality factor of T coupler	-
m_T	Transmission quality factor of T coupler	-
m_*	Quality factor of radial coupler	-

LIST OF SYMBOLS (continued)

SYMBOL	DEFINITION	UNIT
m_{opt}	Optimum value of avalanche gain	-
N	Integer, number of stations	-
N_o	Number of photons	-
NA	Numerical aperture of the acceptance cone	-
NA_ϕ	Numerical aperture of exit cone	-
NEP	Noise equivalent power	$W/Hz^{\frac{1}{2}}$
NRZ	Non-return to zero	-
n	Index of refraction	-
n_1	Index of refraction of the external medium	-
n_2	Index of the core glass	
n_3	Index of the cladding	
P_{ik}	Input power at the LED port of station k	W
P_{ON}	Output power at the detector port of station N	W
P_s	Steady state optical power on detector	W
p_n	Optical signal power to give $i_s = i_{nT}$	-
P_1, P_2	Optical signal power designation	W
Q_e	Photodiode/r_b' quality factor at fe	-
Q_o	Photodiode/r_b' quality factor at f_o	-
Q-1, Q-2, Q-3	Transistors in LED driver network	-

LIST OF SYMBOLS (continued)

SYMBOL	DEFINITION	UNIT
q	Electronic charge	C
R_A, R_B	Resistors in overdrive network	Ω
$\mathcal{R}_d$	Front surface reflectivity of core glass	-
$\mathcal{R}_d$	Photodiode responsivity	A/W
R_E	Emitter follower load resistor	Ω
Re	Real Part	-
R_{PT}	Worst case fractional power ratio in an in-line data bus	-
$R_{PT}\|_{max}$	Maximum value of R_{PT}	-
R_{p^*}	Worst case fractional power ratio of a radial data bus	-
$\mathcal{R}_V$	Voltage responsivity	V/W
RZ	Return to zero	-
R_a	Core/fiber area ratio in a termination	-
R_f	Preamp feedback resistor	Ω
$R_{1,2}$	Preamp resistors	Ω
rms	Root mean square	-
r_b'	Base resistance of T1	Ω
r_s	Photodiode series resistance	Ω
T	Bit time	s
T/2	Half bit time	s
TD	Symbol denoting a tapered duplex data bus	-

LIST OF SYMBOLS (continued)

SYMBOL	DEFINITION	UNIT
T_j	Junction temperature	°C
T_T	Transmission factor of T coupler	-
T_a	Absolute temperature of amplifier	°K
T_c	Transmission of conventional fiber optic termination	-
T_f	Transmission of a fiber/fiber interface	-
T_{tp}	Transmission factor = $a_o m_T T_c T_c$	-
T_*	Transmission factor of radial coupler	-
T1-T3	Preamp transistors	-
T4	Emitter follower transistor for drift cancellation	-
t	Time, general	s
t_a	Amplifier rise time (10-90%)	s
t_d	Rise time of the detector (10-90%)	s
t_f	Fall time, 10-90%	s
t_m	Rise time of measurement setup (10-90%)	s
t_r	Rise time (10-90%)	s
t_t	Transit time	s
t_o	Sample time that gives maximum value of im(t)	s
t_d	LED rise time (10-90%)	s
Δt	Pulse distortion	-
UD	Symbol denoting a uniform duplex data bus	-

LIST OF SYMBOLS (continued)

SYMBOL	DEFINITION	UNIT
V	Voltage, general	V
V_{BE}	DC emitter-base voltage	V
V_{CE}	DC collector-emitter voltage	V
V_R	Diode reverse bias voltage	V
v	Electron and hole drift velocities	m/s
W	Depletion layer width	m
x	Distance, general	m

LIST OF GREEK SYMBOLS

α	Attenuation coefficient	m^{-1}
$1-\zeta(T/2)$	Fractional response of amplifier at T/2	-
η_q	Quantum efficiency	-
θ	Angle from axis	--°
θ_1	Angle between incident ray and normal to surface	--°
θ_2	Angle between refracted ray and normal to surface	--°
λ	Wavelength	nm
μ	Carrier mobility	$cm^2/V\text{-}s$
μ_o	Carrier mobility, low field value	$cm^2/V\text{-}s$
μ_n	Electron mobility	$cm^2/V\text{-}s$
ρ_n	Resistivity, n-type	ohm-cm

LIST OF SYMBOLS (continued)

SYMBOL	DEFINITION	UNIT
τ_d	Effective time constant of photodiode	s
ϕ	AC component of optical power	W
ϕ_o	Incident optical power	W
X	$2\pi fb = \omega b$	-
ω	Angular frequency	rad/s
ω_n	Noise corner angular frequency	rad/s

SECTION I

INTRODUCTION

This two volume document constitutes the final report of a 12 month study of optoelectronic data transmission that was begun on contract number F33615-72-C-1565. The purpose of this continuing study has been to evaluate and characterize non-coherent optical components, devices and techniques in order to discover and define the factors that limit the performance of optoelectronic data transmission systems. Particular emphasis has been given to those phenomena and effects which impose design and performance constraints that are different from the familiar constraints found in wire systems. Recommendations are made for profitable areas of continued study.

This report makes full use of data and information presented in Final Technical Report AFAL-TR-73-164[1], Interim Technical Report AFAL-TR-74-314[2], and Final Technical Report AFAL-TR-73-271[3].

Optoelectronic data transmission is based on the use of light emitting diodes (LEDs), multimode flexible fiber optic bundles and silicon photodiodes. This optoelectronic technology offers an information transmission capability that is consistent with military requirements and potentially superior to wire techniques. The optoelectronic interface is suitable for use in both high data rate digital data buses and wide band analog channels. Thus, this emerging technology offers a viable means of responding to the increasing bandwidth requirements of new avionics systems. At the same time the optoelectronic interface offers the unique features of

- isolation from ground plane signals from dc to RF,
- light weight
- dramatically improved EMI/EMP characteristics, and
- elimination of cross talk.

The performance of present optoelectronic components makes it possible to operate digital optoelectronic systems at data rates in

excess of 200M bit/s (Manchester).

The following paragraphs summarize the study items covered in Volume I of the report.

- The characteristics of optoelectronic signaling and detection are discussed in detail. This discussion includes the unique features of unipolar Manchester signals, a study of clock recovery and synchronization in a data bus, an analysis of a photodiode preamp interface, a detailed presentation of the Spectronics, Inc. suboptimum detection scheme an analysis of a matched filter detector for an optical receiver, and an analysis of a speed-up technique to increase the signal bandwidth of an LED.

- The analysis of data bus structures is expanded to include the radial data bus. The characteristics of other structures are reviewed and the terminology is revised to allow a more accurate comparison of uniform duplex, tapered duplex, and radial duplex structures. An approximate technique for designing scrambler rods is also presented.

- The measurement techniques and performance data for available optoelectronic components are presented. This characterization effort includes evaluation of three preamps, several test adapters, an LED driver stage, two LED types, four photodiodes, two avalanche photodetectors and Galileo fiber optic bundles.

Appendix V of the report is devoted entirely to a study of radiation effects on active and passive optical components. This part of the report begins with general background information and terminology of the interaction of radiation with matter. It also covers radiation damage effects in the specific materials of optoelectronic data transmission systems. The presentation then turns to radiation effects on the specific components of the optical system and concludes with a summary of radiation damage threshold values and failure modes for optical system peripheral circuitry such as digital and linear integrated circuits.

SECTION II

OPTOELECTRONIC SIGNALING AND DETECTION

Fiber optic data transmission systems using noncoherent LEDs and p-i-n photodiodes have used various signaling schemes (RZ, NRZ, Manchester), with some form of suboptimum detection scheme in the receiver to sense the transmitted bit sequence. Spectronics, Inc. has featured and employed Manchester coded data in the transmitter with a particular suboptimum detection scheme that has utility in a wide range of applications. This section reviews the characteristics of the Spectronics, Inc. suboptimum detection scheme and compares its Signal-to-Noise (S/N) ratio performance to that of a matched filter. Problems associated with sync detection and signaling on a multiterminal data bus are also discussed. The preamp S/N analysis introduced in Ref 1. is extended and an analysis of an LED speed-up network is presented.

A. MANCHESTER CODED DATA

Manchester coded data finds great utility in the optoelectronic transmission of digital data because it has a constant duty cycle of 0.5 regardless of the transmitted bit sequence. Since there is no information contained in the average value of the Manchester waveform, the receiver may be ac coupled without losing any of the data content of the signal. The use of ac coupling in the receiver eliminates drift in the preamp and photodiode dark current as error souces so that the S/N ratio is determined by the thermal and shot noise generated in the preamp and photodiode.

In Manchester code, a "one" is represented by a clock cycle and a "zero" is represented by the logical inverse of a clock cycle. Thus, a signal is transmitted for both a "one" and a "zero". In particular, if the input of a Manchester transmitter is a string of "ones" or a string of "zeroes" the output is a square wave at clock frequency. Manchester data has a signal transition at least

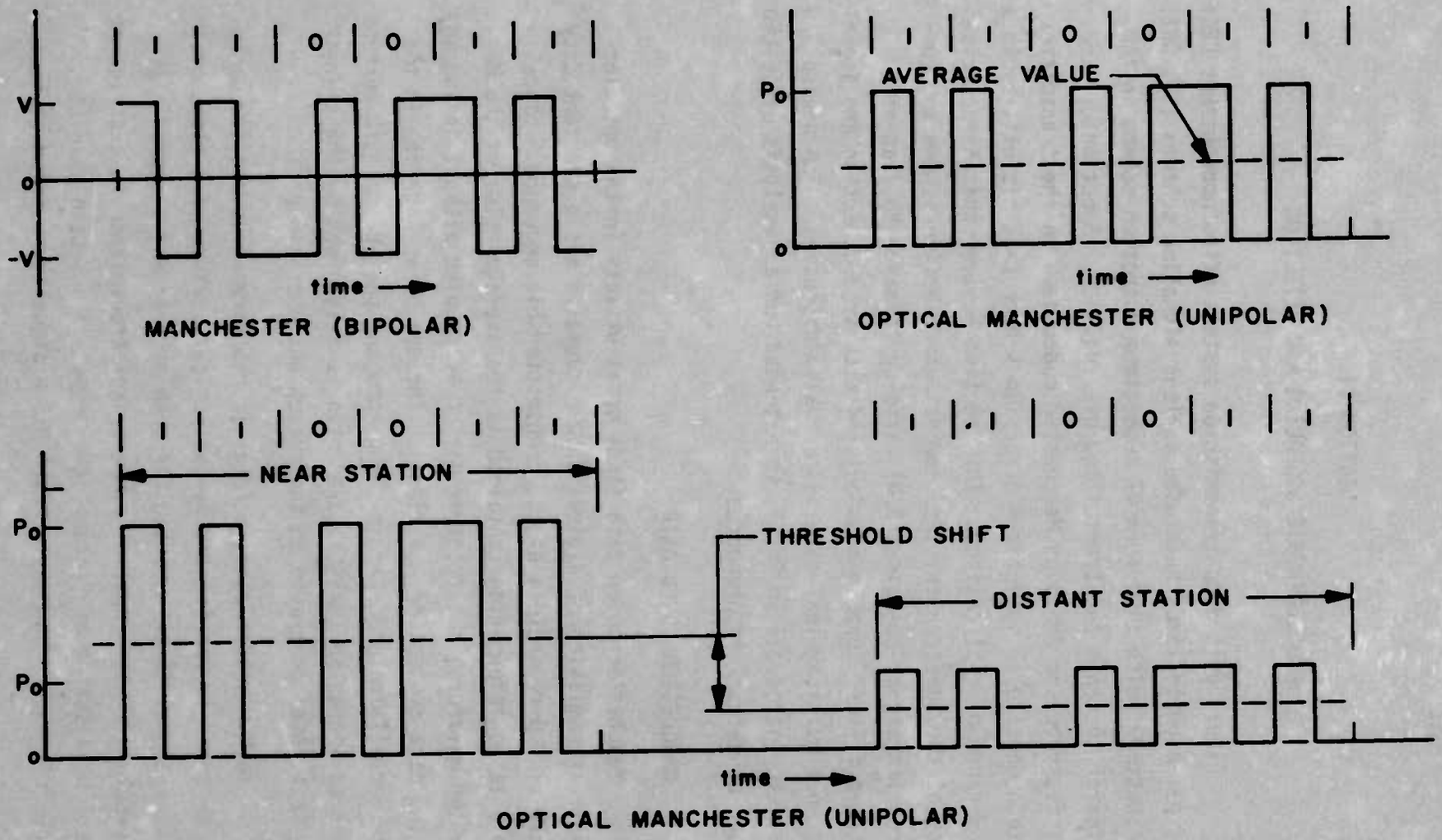

Figure 1. Bipolar and Unipolar Manchester

once in each bit time. This makes it possible to recover the clock from the data sequence using relatively simple circuits.

Light emitted from an LED is not coherent and must therefore be treated as a photon flux or power. Thus, a modulated LED emits a time varying power that has no negative values. Because the light output of an LED can be only zero or positive, an optical Manchester signal is unipolar. The conventional Manchester signal used in wire data buses is bipolar with equal positive and negative excursions and an average value of zero. Figure 1 shows a comparison of bipolar and unipolar Manchester signals. For the conventional bipolar signal the threshold level of an ac coupled receiver is independent of both data sequence and signal amplitude. The unipolar Manchester signal used with ac coupling also eliminates data sensitivity of the threshold level. It does not, however, eliminate threshold shift due to signal amplitude as shown in Figure 1. This inherent characteristic of noncoherent optical signals is the basis of most of the significant differences between the signaling and detection schemes used in optoelectronic and wire data buses.

The dependence of threshold on signal amplitude makes it highly desirable to use an optoelectronic data bus structure that provides a small dynamic range of optical signals; that is, a constant signal level at each receiver on the data bus regardless of which station is transmitting.

If the physical arrangement used is a uniform duplex data bus[1] then the different values of attenuation between stations will produce a large dynamic range in the amplitude of the received signals. The resulting transient shifts in threshold level will make it necessary to use extra dead time between words to allow the receiver coupling capacitors time to discharge. This extra dead time will lower the efficiency of the data bus. The efficiency reduction due

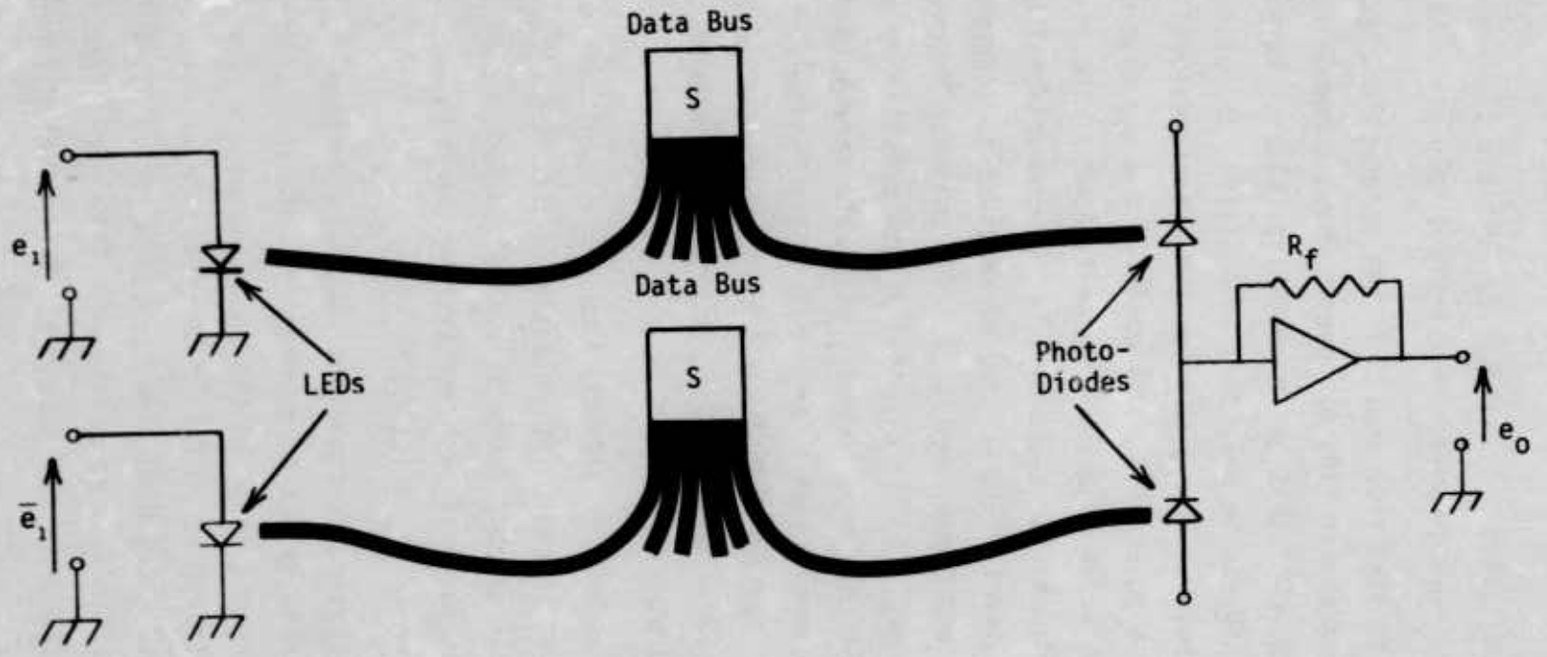

Figure 2. Balanced Optoelectronic Circuit

to this effect will be less at high data rates because the dead time required for the propagation delay of the bus can serve as all or part of the dead time required for discharge of the coupling capacitors.

If the physical configuration used is a radial data bus, then the dynamic range of received signals can be reduced to the range of 3-4dB[2] and the dead time required to discharge the coupling capacitors can be minimized. The tapered duplex data bus[4] should also provide a low dynamic range for the received signals. However, the radial construction is less complex and provides a larger received signal than either the uniform or tapered in-line configurations.

It is also possible to construct an optoelectronic data bus which eliminates the dependence of threshold on signal amplitude. This can be accomplished by using two sets of LEDs, fiber optic bundles and photodetectors to form a composite bipolar system from two unipolar systems. In this configuration, the LEDs are driven with oppositely phased signals so that one LED is "on" when the Manchester signal is "high" and the other LED is "on" when the Manchester signal is "low". If the signal transmission of the two systems are matched, a bipolar electrical signal can be formed at the input of the receiver preamp by connecting the photodetectors in opposition as shown in Figure 2. This technique has been used successfully in optoelectronic data telemetry systems used in EMI tests on large electronic systems[4]. Application of this technique to wideband optoelectronic data buses could result in simplification of the electronic circuitry required in the receivers.

In a duplex data bus, each station transmits to all other stations and receives signals from all other stations. With noncoherent optical signals and passive optical couplers, it does not

appear to be possible to transmit and receive simultaneously nor to have more than one station transmitting at a time. Thus, optoelectronic data buses must operate in a half duplex mode with one station at a time transmitting and all other stations receiving. With Manchester coding, half duplex operation cannot be achieved by feeding data to the input of one transmitter at a time with "zero" input to all other transmitters. Each station with "zero" input will be transmitting a clock frequency square wave that will be delayed in time by the path length through the fiber bundle and summed with all of the other "zero" signals and the data at each receiver on the bus. Under these conditions the received signal would bear little resemblance to the transmitted data.

What is required for multiterminal data buses is a three state Manchester code consisting of signals for "one", "zero" and "off". The "one" and "zero" signals are standard; the "off" signal is characterized by no output from the transmitter. This signaling scheme can be implemented by gating off all transmitters except the one sending out data. Thus, only data signals will be received at all stations. This requirement is not peculiar to optoelectronic data buses; it is also valid for shielded twisted pair data buses.

Some other signaling schemes like Unipolar RZ and Unipolar NRZ do not require this three level modification for use in data buses. These two signaling schemes transmit signal only for a "one" input. Therefore, the output remains in the "off" condition for a "zero" input and only the station transmitting data is received at the other stations. Signals of this type do not have a constant average value and are, therefore, not suitable for use with ac coupled receivers.

Low-noise preamps using either discrete components or hybrid construction can be expected to have an output voltage drift of 20 to 40μV/°C. Thus, for a useful military temperature range of -50°C to +100°C the total output drift is 3 to 6mV. The rms value

of the output noise voltage of a low-noise preamp is about 374μV. For the type of preamp described later in this report, the output noise voltage is roughly independent of temperature and bandwidth. A typical bit error rate of 10^{-8} is associated with the noise peaks that are greater than 5.62 times the rms value of the noise; this gives an effective peak noise voltage of 2.1mV. Comparing this peak output noise voltage (2.1mV) with the output voltage drift (3 to 6mV) shows that for a direct coupled preamp the drift is 1.4 to 2.8 times higher than the noise. This ratio is valid for any preamp bandwidth; it represents the state-of-the-art for low-noise photodiode preamps. For less than optimum preamp designs, the drift and/or noise may be different from the values indicated above. For example, an amplifier with higher noise could make the drift term look negligible; however, the overall performance would be degraded because of the higher absolute value of the noise.

The use of ac coupling in the receiver gives an optical S/N improvement of 2.4 to 3.8 times (3.8 to 5.8dB). For many practical systems this extra S/N performance is not required and sufficient signal is available at the detector to allow the receiver to be direct coupled. In particular, this is true for laboratory or commercial grade equipment which will have low drift because it is operated in a narrow temperature range. For the full military temperature range of -50°C to +100°C the use of an ac coupled receiver will increase the maximum data rate by 2.4 to 3.8 times or will allow 3.8 to 5.8dB more optical attenuation for a fixed data rate.

Problems concerning data bus architecture can often be solved by either a unique physical structure (radial bus, differential bipolar bus) or by a different logical organization (extra dead time, direct coupled NRZ, ac coupled Manchester). If the design decisions are made to maximize performance, then the unique physical

structures offer the greatest advantage. However, if considerations of complexity, flexibility and uniformity govern the design, then the best approach is not clear but will probably involve combinations of unique structure and logical organization that will have to be selected to satisfy the requirements of each application.

B. CLOCK RECOVERY AND SYNCHRONIZATION

Continued study of multiterminal data buses has shown that a dedicated clock line with a continuous clock signal is not workable in a wideband data bus. In particular, with stations transmitting one at a time in random sequence, the presence of propagation delay dictates that there is no single clock signal that is acceptable for the entire data bus. This effect is more noticeable in high-speed data buses for which the propagation delay of the bus approaches a half bit time. For example, a 32ft long data bus made from glass fiber optic bundles having n=1.6 has a propagation delay of ∿50ns which is also one half of the bit time for a 10M bit/s signal. This performance is well within the present capability of opto-electronic data buses; therefore, the use of a dedicated clock line is not indicated for present or future optoelectronic data buses.

The use of a dedicated clock line in the Optoelectronic Data Bus Demonstrator[3] made it possible to achieve an error-free clock by using a phase-locked loop in the clock channel of the receiver. In principal, a phase-locked loop will also work without a dedicated clock line. However, this approach is generally unacceptable in multiterminal data buses because of the long synchronization time of the phase-locked loop and the resulting loss in data handling efficiency. As a result, multiterminal data buses must rely on other techniques for clock recovery which are less accurate but more efficient than the phase-locked loop. The most commonly used system in 1.0M bit/s twisted pair data buses recovers the clock signal from the Manchester coded data. Manchester code is ideal for clock

recovery because there is always at least one signal transition in each bit time.

Clock recovery from Manchester coded data is normally accomplished by some form of time domain filtering. The Air Force Multiplex Standard[5] describes a technique of this type which employs a non-standard Manchester bit for the synchronizing preamble. The use of a non-standard sync bit with time domain filtering avoids the potential problem of a standard bit sync pattern which might be identical to some random sequence of bits occurring in the middle of a data word.

Time domain filtering and sync bit recognition may be performed by either analog or digital means. In low-speed data buses, the signal slicing (digital) approach probably gives the best results. In this system, the data signal waveform is sampled 8-10 times in each bit with an "on-off" decision being made each time the data is sampled. The decision as to whether or not a given bit sequence is a sync preamble is made by processing the digital signal formed by the "on-off" decisions at the sample points. In high-speed data buses this approach presents a practical problem because of the difficulty of implementing the high sampling rate. For example, in a 10M bit/s data bus, a 10/1 sampling ratio will require a 100MHz oscillator; for a 100M bit/s data rate the same sampling scheme would require a 1GHz oscillator. The sampling oscillator is normally not synchronized with the received data. Thus, fewer than 8 samples/bit is unsatisfactory because of the timing errors that would result.

Analog detection of the sync bit is similar to the vertical sync system used in home TV receivers. A representative analog detection scheme could be implemented by passing the data signal (as received) through a threshold circuit and then integrating the resulting constant amplitude waveform. The detection of a sync preamble would be accomplished by analog processing of the signal on the output of the integrator.

After a sync preamble is detected, the receiver must shift into a "data receive" mode. For Manchester coded signals with a suboptimum detection technique, the data is normally strobed only one time per bit at the center of the bit (T/2). Strobing the data at this point minimizes the adverse effects of intersymbol interference[1] and, therefore, gives the best S/N for any sequence of bits. It is also customary to strobe the data at the end of the bit (T) so that the data can be continuously checked for invalid Manchester bits. This test for invalid bits requires a larger bandwidth in the preamp to overcome the intersymbol interference at the end of the bit. For the Spectronics' suboptimum detection scheme, a bandwidth increase of 2.5 times is sufficient and the optical S/N is reduced by 3.95dB. With time domain filtering, other more elaborate bit detection techniques can be envisioned. At a minimum, time domain filtering implies that the timing of the data strobe signal is not completely predetermined by the sync preamble but that it can be corrected during the time a word is being received. This sort of time domain filtering is sometimes implemented by strobing the data at a fixed time after a zero crossing of the data. The detection of the zero crossing can also be time domain filtered by accepting only zero crossings which occur in a narrow time interval that is delayed by a fixed time after a data strobe. The necessary delay times can be generated by either counting a high-frequency local oscillator (digital) or by integrating a switched dc signal (analog). For the digital technique it is necessary to use a local oscillator frequency that is 8 to 10 times the bit rate frequency in order to achieve the required timing accuracy. For 100Mbit/s a local oscillator frequency of 0.8 to 1.0GHz is required. The local oscillator is not synchronized to the incoming data; thus, timing errors of 10-12.5% of a bit time can result. The timing signals for bit detection can also be generated using an analog integrator or "one shot" circuit which generates a strobe signal that is delayed by a fixed amount from an input

trigger. When the analog timing circuit is used, the bit rate is the highest frequency required in the receiver. This is a significant advantage for the analog timing circuit in a high data rate system. Again the digital techniques are probably best for low-speed data buses but lead to practical draw-backs in high-speed systems. The analog techniques for sync detection and data detection should be thoroughly investigated for possible use in high-speed (10-100M bit/s) optoelectronic data buses.

Whatever sync detection and data detection systems are used in a multiterminal data bus, the result will be an increase in error rate as compared to a phase-locked loop system. This increase in error rate with the time domain filtering is the result of the finite probability of clock errors in addition to the data errors observed in the phase-locked loop system. It should be possible to hold the increase in error rate to a factor of 2 or less. For an error rate of 2×10^{-8} the signal only needs to be increased by a few percent ($\sim$2%) to achieve an error rate of 10^{-8}.

C. PHOTODIODE/PREAMP S/N ANALYSIS

Most of the effort reported in this document has been concerned with the implementation of multiterminal optoelectronic data buses to be used for the transmission of digital signals. However, the preamp used in the data bus receivers is a broad band linear amplifier that is also capable of handling low-distortion analog signals.

In many practical applications, dedicated optoelectronic data channels will be used for transmission of base-band analog signals. Typical signals that could be transmitted in analog form are

- Low Light Level TV (LLLTV),
- Forward Looking Infra Red (FLIR), and
- Radar

These signals require large bandwidth and usually have limited distribution in the aircraft. Their inclusion in the data bus would cause an unnecessary increase in cost and complexity of the system.

The preamp design and S/N analysis introduced in Ref 1 has been modified so that it covers both analog and digital receivers. The steady state ac frequency response of the basic optoelectronic data transmission channel is presented in Section III B. The noise analysis is based on the use of a transresistance amplifier with a silicon p-i-n photodiode; however, many features of the analysis are also useful in designing transresistance amplifiers for use with avalanche photodiodes.

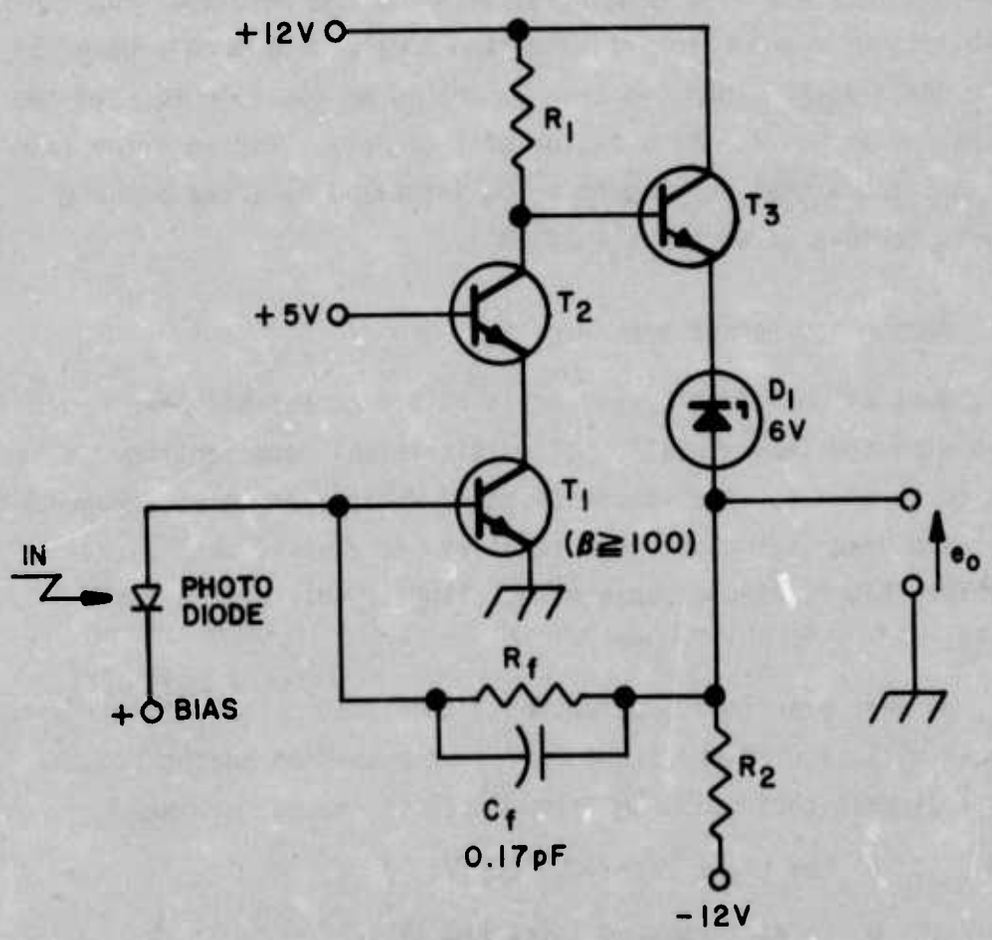

Figure 3. Transresistance Preamp for Analog and Digital Signals

The basic nature of the photodiode/preamp interface insures that all high-performance optical receivers will have a significant component of mean square equivalent input noise current that is proportional to f^2; frequency independent or "white" noise is also present at the input. For a suboptimum detection scheme, the presence of the "f^2" noise dictates that the amplifier chain must have at least two poles in the high-frequency cutoff characteristic so that the total noise will be bounded. The basic photodiode/preamp schematic is shown in Figure 3.

The low-frequency pole at f_o is determined by the feedback network of the preamp. Limiting the bandwidth of the preamp gives a lower noise level than could be achieved with the same input transistor in a wideband preamp followed by a filter. The required second pole is set at $f_2 = 1.85\ f_o$; this pole is located in the postamp. For a Manchester coded digital signal, the bit time, T, is related to f_o by

$$f_o = \frac{1}{2\pi R_f C_f} = \frac{1}{\sqrt{2}\ T} \tag{1}$$

From Eq (1) the second pole located in the postamp is

$$f_2 = 1.85 f_o = \frac{1.85}{\sqrt{2}\ T} \tag{2}$$

For a 15M bit/s system f_o = 10.6MHz and f_2 = 19.6MHz. For analog signals, the amplifier response should be stated in terms of the 3dB frequency, f_e, or 10-90% rise time, t_a. From Ref 1 and Eq(1), the 3dB frequency is

$$f_e = .81 f_o = \frac{.81}{2\pi R_f C_f} \tag{3}$$

and f_e and t_a are related by[6]

$$t_a = \frac{.350}{f_e} = \frac{.432}{f_o} \tag{4}$$

Combining Eqs (1) and (3) gives the 3dB bandwidth required for a specified bit time

$$f_e = \frac{.573}{T} \tag{5}$$

Since the photodiode produces a signal current at the input of the preamp, the noise of the circuit will be expressed in terms of the rms value of the equivalent input noise current.

The "white" noise sources at the preamp input are shot noise on the dc base current of the input transistor, I_B, and thermal noise on the preamp feedback resistor, R_f. The mean square noise current spectral density due to these "white" noise sources is

$$\frac{i_n^2}{\Delta f} = 2qI_B + 4kT_a/R_f \tag{6}$$

where T_a is the absolute temperature of the amplifier, and
k is Botlzmann's constant

The "f^2" noise results from the various noise voltages in the preamp input circuit interacting with the capacitance of the photodiode and input transistor. The mean square noise current spectral density for the "f^2" noise is

$$\frac{i_n^2}{\Delta f} = 2kT_a\left(\frac{kT_a}{qI_E}\right)(2\pi fC_T)^2 + 4kT_a(r_s+r_b')(2\pi fC_d)^2 \tag{7}$$

where I_E is the dc emitter current of the input transistor,

C_d is the photodiode capacitance,

C_T is the total capacitance at the preamp input,

r_s is the series resistance of the photodiode, and

r_b' is the base resistance of the input transistor T1.

The noise terms presented in Eqs (6) and (7) are shown schematically in Figure 4. The frequency, f_n, at which the "white" noise is equal to the "f^2" noise is called the noise corner frequency.

For the preamp and postamp cutoff frequencies defined by Eqs (1) and (2), it has been shown[1] that the "white" noise bandwidth is

$$\Delta f_W = f_o \tag{8}$$

and the "f^2" noise bandwidth used with the spectral density evaluated at f_o is

$$\Delta f_{f^2} = 1.825\ f_o \approx f_z \tag{9}$$

Using Eqs (8) and (9) with Eq (7) the total mean square noise current at the preamp input is

$$i_{nT}^2 = \frac{4kT_a f_o}{R_F} + \frac{2qI_E f_o}{1+h_{FE}} + 2kT_a \left(\frac{kT_a}{qI_E}\right)\left(2\pi f_o C_T\right)^2 (1.825\ f_o) + 4kT_a(r_s+r_b')(2\pi f_o C_d)^2(1.825 f_o) \tag{10}$$

where h_{FE} is the dc common emitter current gain of the input transistor.

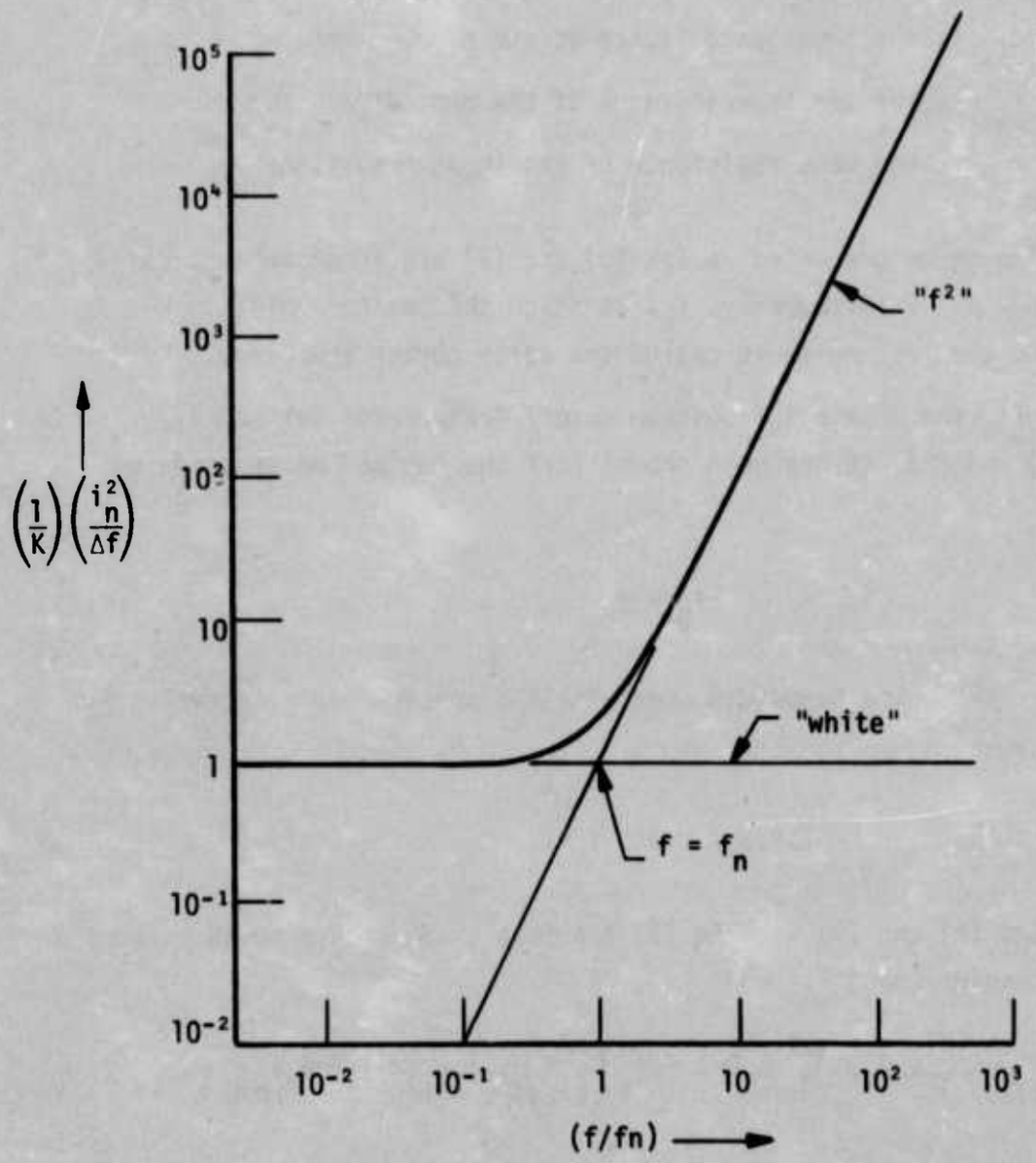

Figure 4. Equivalent Mean Square Noise Spectral Density

Using Eq (1) the first term in Eq (10) may be written

$$i_{n_1}^2 = 4kT_a(2\pi f_o^2 C_f) \tag{11}$$

The second and third terms of Eq (10) are both functions of I_E. The sum of these two terms will be minimum for the optimum value of I_E. This optimum occurs when the second and third terms are equal

$$I_E\Big|_{opt} = \frac{kT_a}{q}(2\pi f_o C_T)\sqrt{1.825(1+h_{FE})} \tag{12}$$

At the optimum bias point given by Eq (12) the sum of the second and third noise terms is

$$i_{n_{2,3}}^2 = 4kT_a(2\pi f_o^2 C_T)\left(\frac{1.825}{1+h_{FE}}\right)^{1/2} \tag{13}$$

The fourth noise term may be written

$$i_{n_4}^2 = 4kT_a(2\pi f_o^2 C_d)\left(\frac{1.825}{Q_o}\right) \tag{14}$$

where Q_o is the photodiode/r_b' quality factor at f_o given by

$$Q_o = \frac{1}{(r_s+r_b')2\pi f_o C_d} \tag{15}$$

Combining Eqs (11), (13) and (14) gives the expression for the total equivalent input noise current at optimum bias

$$i_{nT}^2 = 4kT_a\left[C_f + \frac{1.825C_d}{Q_o} + \frac{1.35C_T}{1+h_{FE}}\right]2\pi f_o^2 \tag{16}$$

The following parameter values are appropriate for use in Eq (16) based on the use of presently available components.

$$\begin{aligned} C_f &= 0.17\text{pF} \\ C_d &= 2.7\text{pF} \quad (\text{SPX } 1615) \\ C_T &= 6.0\text{pF} \quad (\text{MMT } 807) \\ r_s &= 15\Omega \quad (\text{SPX } 1615) \\ r_b' &= 100\Omega \quad (\text{MMT } 807) \\ 1+h_{FE} &= 100 \quad (\text{MMT } 807) \end{aligned} \tag{17}$$

Using these values Eq (16) becomes

$$i_{nT}^2 = 10.2 \times 10^{-32} f_o^2 + 10.0 \times 10^{-40} f_o^3 \tag{18}$$

The term involving f_o^3 comes about as a result of the frequency dependence of of Q_o shown in Eq (15).

For analog signals, the amplifier response should be stated in terms of the 3dB frequency or the 10-90% rise time. Using Eq (3) to express Eq (18) in terms of the 3dB frequency gives

$$i_{nT}^2 = 15.5 \times 10^{-32} f_e^2 + 18.8 \times 10^{-40} f_e^3 \tag{19}$$

From Eq (19) the expression for the rms value of the input noise current is

$$i_{nT} = 4 \times 10^{-16} f_e (1 + 1.2 \times 10^{-8} f_e)^{1/2} \tag{20}$$

For amplifiers with 3dB frequency up to

$$f_{e_1} = \frac{1}{1.2 \times 10^{-8}} = 83\text{MHz} \tag{21}$$

the input noise current is proportional to f_e; for higher values of f_e the input noise current is dominated by thermal noise on r_s and r_b' and increases as f_e. The expression for the noise transition frequency is

$$f_{e_1} = \frac{.071\left[C_f + \frac{1.35C_T}{\sqrt{1+h_{FE}}}\right]}{(r_s+r_b')(C_d^2)} \tag{22}$$

The noise transition frequency can be increased by reducing the photodiode capacitance and series resistance and the r_b' of the input transistor. For the parameter values shown in Eq (17) the limiting items are C_d and r_b'.

Equation (20) depends on the emitter current being optimum at each bandwidth. From Eqs (3) and (12) the expression for the optimum emitter bias current is

$$I_E\Big|_{opt} = 1.63 \times 10^{-11} f_e \tag{23}$$

Typical photodiode responsivities at a wavelength of 907nm range between 0.4-0.65A/W with a typical value of

$$R_d = 0.5A/W \tag{24}$$

The optical signal power, p_n, required to give a detector signal current, i_s, equal to the rms noise current, i_{nT}, is given by

$$p_n = \frac{i_{nT}}{R_d} \tag{25}$$

Combining Eqs (19) and (25) gives the required signal power for S/N = 1 vs. the cutoff frequency of the amplifier (which is also the signal bandwidth of the system). Thus

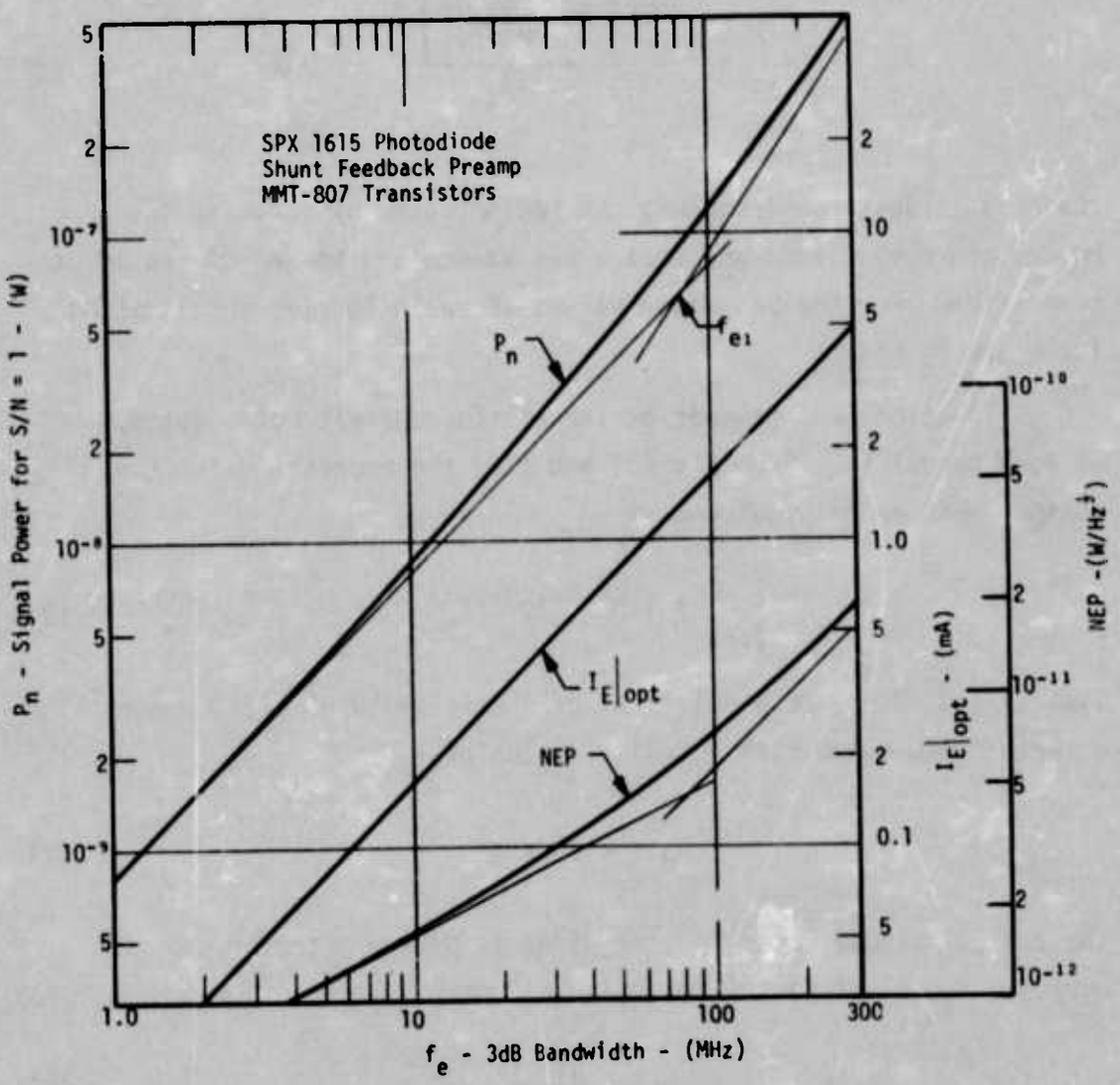

Figure 5. Photodiode/Preamp Noise Characteristic

$$p_n = 8 \times 10^{-16} f_e (1 + 1.2 \times 10^{-8} f_e)^{1/2} \quad (26)$$

Equations (23) and (26) are plotted vs. f_e in Figure 5.

Referring again to Figure 3 the value of f_n at the optimum emitter current can be obtained by substituting Eq (12) into the various "white" and "f^2" noise terms in Eqs (6) and (7)

$$f_n = \left[\frac{1 + \frac{2\sqrt{1+h_{FE}}}{1.35} \frac{C_f}{C_T}}{1 + \frac{2.2\sqrt{1+h_{FE}}}{Q_e} \frac{C_d}{C_T}} \right]^{1/2} (1.67 f_e) \quad (27)$$

wehre Q_e is the photodiode/r_b' quality factor at f_e given by

$$Q_e = \frac{1}{(r_s + r_b')(2\pi f_e C_d)} \quad (28)$$

The total equivalent noise bandwidth, Δf_a, of the amplifier is given by

$$\Delta f_a = 2 f_o = 2.48 f_e \quad (29)$$

A common figure of merit for optical receivers is noise equivalent power (NEP). NEP is defined as

$$NEP = \frac{P_n}{\sqrt{\Delta f_a}} \quad (30)$$

Combining Eqs (26), (29) and (30) gives

$$NEP = 5.1 \times 10^{-16} f_e^{1/2} (1 + 1.2 \times 10^{-8} f_e)^{1/2} \quad (31)$$

This expression is also plotted in Figure 5.

For a signal bandwidth of 40MHz this photodiode/preamp interface has an NEP of about 3.9×10^{-12} W/Hz$^{1/2}$. By comparison, the Texas Instruments, Inc. avalanche diode module (60mil diameter detector) at the same signal bandwidth has a quoted room temperature NEP of 5×10^{-13} W/Hz$^{1/2}$. Thus, at 25°C the avalanche detector module requires 7.8 times (8.92dB) less signal power than the photodiode/preamp interface. As the temperature is increased to 100°C the noise of the avalanche module will increase by about 2.5 times due to the change in bulk dark current. However, the noise of the photodiode/preamp interface is essentially independent of temperature. Thus, at 100°C the NEP of the avalanche module will only be about 3 times better than the photodiode/preamp interface.

The preamp is a shunt feedback amplifier which provides an output voltage in response to an input current. The transimpedance of this amplifier is within a few percent of the feedback impedance. Thus, for frequencies less than f_o the transresistance of the amplifier is equal to R_f. For each different bandwidth the value of R_f is specified by Eq (3)

$$R_f = \frac{.81}{2\pi C_f f_e} \tag{32}$$

The rms value of the output noise voltage of the preamp is given by multiplying R_f from Eq (32) by the equivalent input noise current from Eq (20)

$$e_{on} = i_{nT} R_f = 3.74 \times 10^{-4}(1 + 1.2 \times 10^{-8} f_e)^{1/2} \tag{33}$$

For frequencies less than f_{e_1} = 83MHz the rms output noise voltage is constant at 374μV regardless of the bandwidth of the amplifier. This result is used in Section II.A. in the discussion of the relative magnitude of noise and drift at the output of the preamp.

In order to obtain an acceptable output drift, additional drift cancellation elements must be employed in the circuit of Figure 3. The two major sources of drift in the preamp are the V_{BE} and I_B drift of the transistor T1. These two drift sources can be effectively cancelled by following the preamp with the emitter follower stage shown in Figure 6. The emitter follower transistor T4 should be matched to T1 in Figure 3 and the emitter follower bias current must be set at $I_E\big|_{opt}$,

$$R_E = \frac{12V}{I_E\big|_{opt}} \tag{34}$$

The physical component layout should be designed to keep T1 and T4 at the same temperature. With adequate matching and layout, the combined circuits of Figures 3 and 6 will provide an output voltage drift of 20 to 40μV/°C.

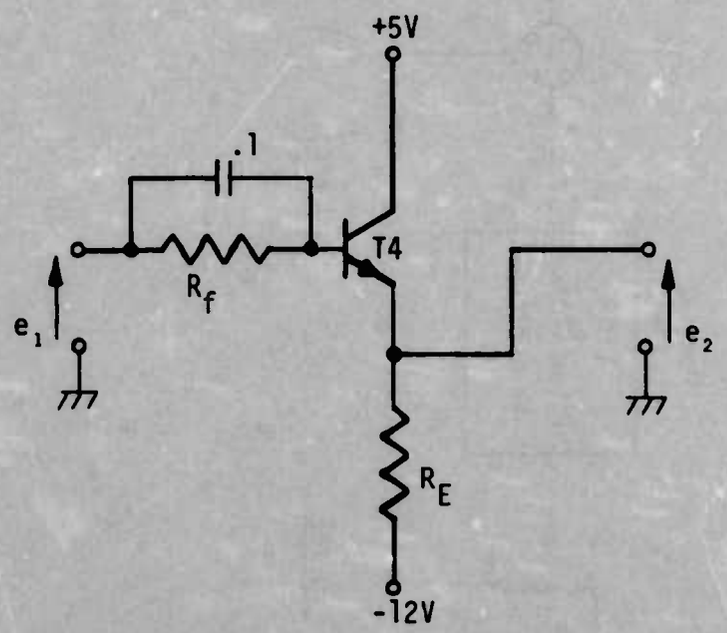

Figure 6. Emitter Follower for Drift Cancellation

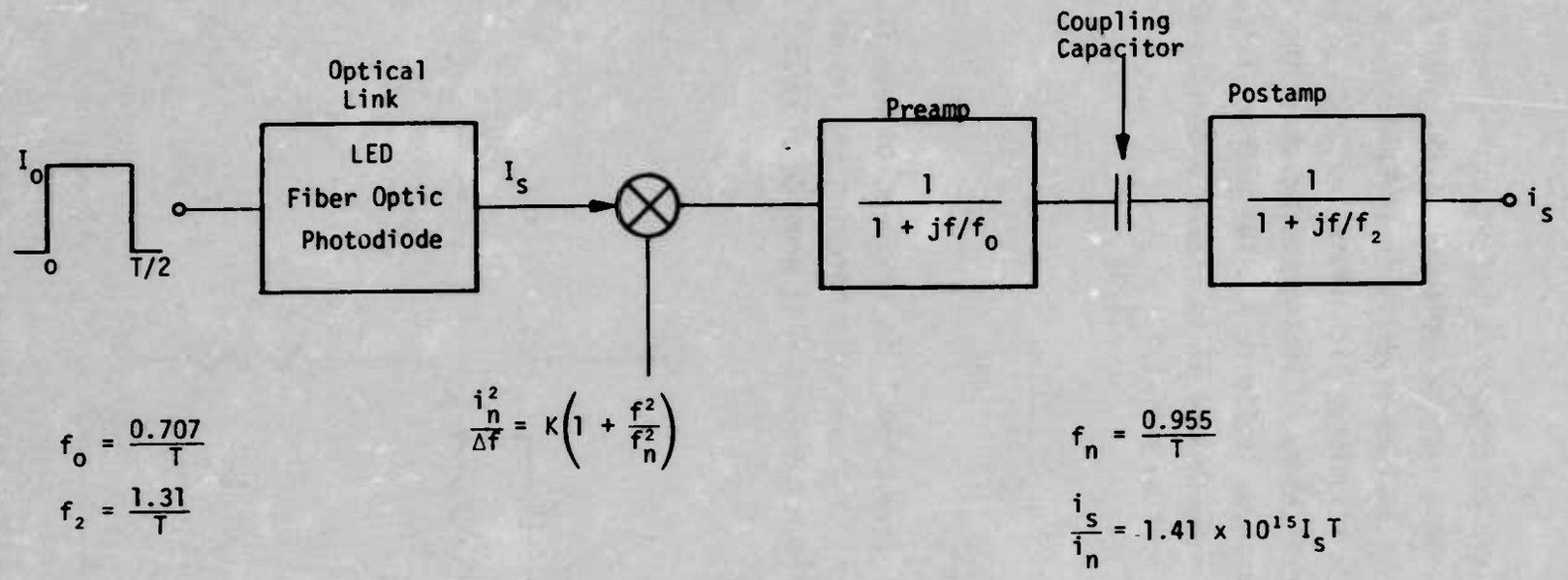

Figure 7. Suboptimum Detector

D. SUBOPTIMUM DETECTION SCHEME

The Spectronics, Inc. suboptimum detection scheme for Manchester data is based on the photodiode/preamp interface described in Section II.C. The receiver is shown in block diagram form in Figure 7. The photodiode is direct coupled to the shunt feedback preamp which is ac coupled to the postamp. The average value of the Manchester signal will appear across the coupling capacitor in the receiver. As a result, the signal past the coupling capacitor will have the form of a bipolar signal with positive and negative peak values that are one half of the peak value of the signal voltage ahead of the coupling capacitor. Figure 8 shows a typical unipolar Manchester signal and the signal voltages on each side of the coupling capacitor.

The Manchester signal can be decoded by sampling at either T/2 or T. However, sampling at T/2 is used in the Spectronics, Inc. suboptimum detection scheme because it gives the best S/N for all bit sequences with the worst case being a string of "ones" or a string of "zeros". The value of signal current, i_s, at sample time (T/2) is

$$i_s(T/2) = \frac{I_s}{2}\left[\frac{1 - \zeta(T/2)}{1 + \zeta(T/2)}\right] \tag{35}$$

where I_s is the steady state signal current, and

$1-\zeta(T/2)$ is the fractional response of the two pole amplifier chain.

The factor 1/2 is the result of the coupling capacitor charging up to the average value of the signal. In order to keep the S/N comparison of the matched filter and suboptimum detection scheme manageable, the only bandwidth limitations that will be considered are those in the receiver. This means that LED cutoff, pulse distortion in the fiber optic bundle and transit time cutoff in the photodiode will be neglected. Also, the noise terms involving Q_o

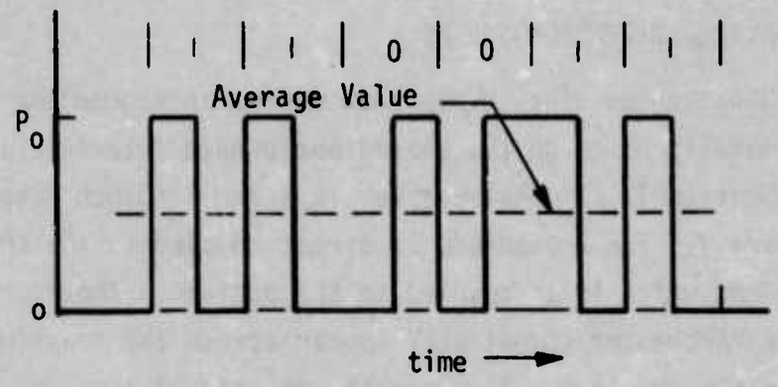

Optical Manchester (Unipolar)

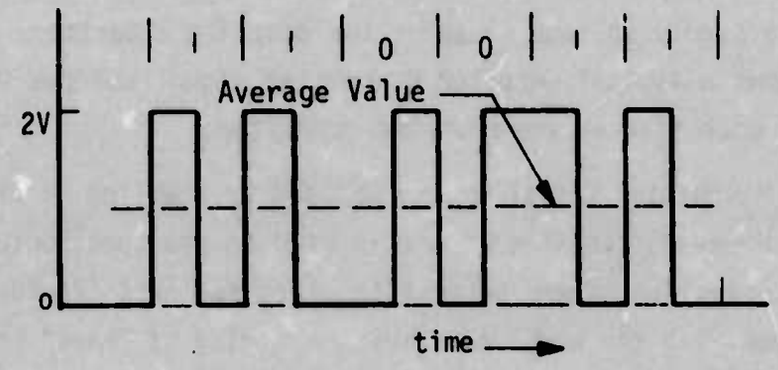

Signal Ahead of Coupling Capacitor

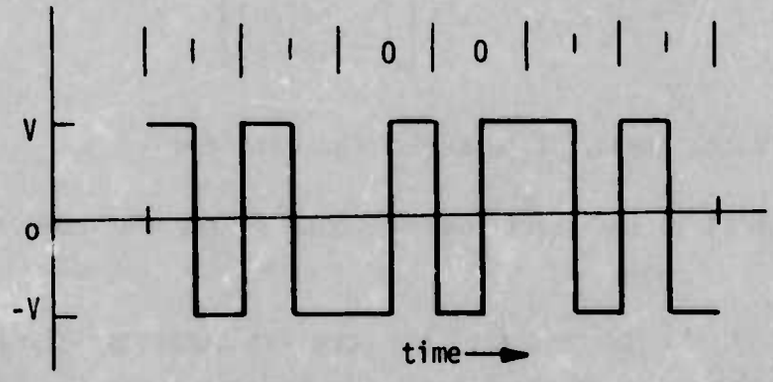

Signal Past Coupling Capacitor

Figure 8. Manchester Code Waveforms

will be neglected. These four effects are important only at high data rates. Section II.G. shows that LED bandwidth can be extended by about a factor of 10 using speed-up techniques. In Section IV.D., the measured rise time with speed-up for an edge emitter LED (SPX 1527-DB) is 1.1ns. From Eq (4), this corresponds to a 3dB frequency of 318MHz. Thus, neglecting LED cutoff will not introduce serious errors for data rates up to 300Mbit/s. From the discussion in Section IV.F., the pulse distortion of a fiber optic bundle is dependent on the length of the bundle and the NA of the light coupled into the bundle. For 150ft of Galileo fiber optic bundle and NA = 0.24, the expected pulse distortion is Δt = 2.66ns; this corresponds to a 3dB frequency of about 164MHz. Thus, neglecting pulse distortion in the fiber optic bundle will not introduce serious errors for data rates up to 150Mbit/s. An analysis of the SPX 1615 p-i-n silicon photodiode presented in Appendix I shows that the transit time cut off frequency is 330MHz. Thus, neglecting the photodiode transit time cutoff will not introduce serious errors for data rates up to 300Mbit/s. Section II.C. shows that the effect of Q_o is to introduce excess noise above a noise transition frequency f_{e_1}. From Eq (21) f_{e_1} = 83MHz; this value is consistent with measured amplifier characteristics presented in Section IV.A. Thus, neglecting excess noise due to Q_o will not introduce serious errors for data rates up to about 75Mbit/s. This latter condition is the most severe limitation on the analysis.

For the two-pole low-pass characteristic defined by Eqs (1) and (2), the fractional response at T/2 is[1]

$$1 - \zeta(T/2) = 0.784 \tag{36}$$

and the signal current at (T/2) from Eq (3) is

$$i_s(T/2) = \frac{I_s}{2}\left[\frac{.784}{2 - .784}\right] \tag{37}$$

$$i_s(T/2) = 0.322\ I_s$$

Since the photodiode produces a signal current at the input of the preamp, the noise of the circuit will be expressed in terms of the rms value of the equivalent input noise current. The ratio of signal current, $i_s(T/2)$, to the rms noise current, i_n, gives the S/N ratio that is needed to calculate the error rate. Both analysis and experiment have shown that the receiver is preamp noise limited. Since the shot noise on the photodiode signal current is negligible compared to the preamp noise, the equivalent input noise current is the same value for both "on" and "off" conditions of the LED. In this case, a S/N ratio of

$$\frac{i_s}{i_n} = 5.62 \tag{38}$$

is required to achieve a bit error rate of 10^{-8} (Ref 1).

Combining Eqs (1), (3) and (16) with $Q_0 >> 1$ gives the expression for the minimum noise of the suboptimum detection scheme in terms of the bit time

$$i_n^2 = 4kT_a\left(\frac{\pi}{T^2}\right)\left[C_f + \frac{1.35\ C_T}{(1+h_{FE})^{1/2}}\right] \tag{39}$$

For the minimum noise condition and the parameter values of Eq (17) the noise corner frequency from Eq (27) is

$$f_n = 1.61 f_o = \frac{1.14}{T} \tag{40}$$

Combining Eqs (37) and (39) gives

$$\left(\frac{i_s}{i_n}\right)^2 = \frac{(.104)(TI_s)^2}{4\pi kT_a\left[C_f + \frac{1.35\ C_T}{(1+h_{FE})^{1/2}}\right]} \tag{41}$$

For the typical parameter values shown in Eq (17) the S/N current ratio for the suboptimum detection scheme is

$$\frac{i_s}{i_n} = \sqrt{2} \times 10^{15}\ I_s T \tag{42}$$

Equations (39), (40), (41) and (42) are valid for present components at data rates up to 75Mbit/s which corresponds to $T \geq 13.3$ns.

E. MATCHED FILTER DETECTOR

Much of the effort on practical matched filter detection techniques has been concerned with systems limited by "white" noise. The integrate and dump system[7] is one common matched filter detector used with square pulses in "white" noise. The general theory of matched filter detectors requires that the frequency dependence of the noise be included as a part of the matched filter characteristic. A fiber optic data transmission system has two unique design constraints, both of which are related to the noise. First, the dominant source of noise is the first stage of the receiver; this places the noise characteristics somewhat under the control of the designer. Second, the basic nature of the photodiode/preamp interface insures that there will be a significant "f^2" noise term present. Thus, even though the equivalent input noise characteristic of the preamp can be optimized by the designer it will always be "non-white" with the general characteristic shown in Figure 4.

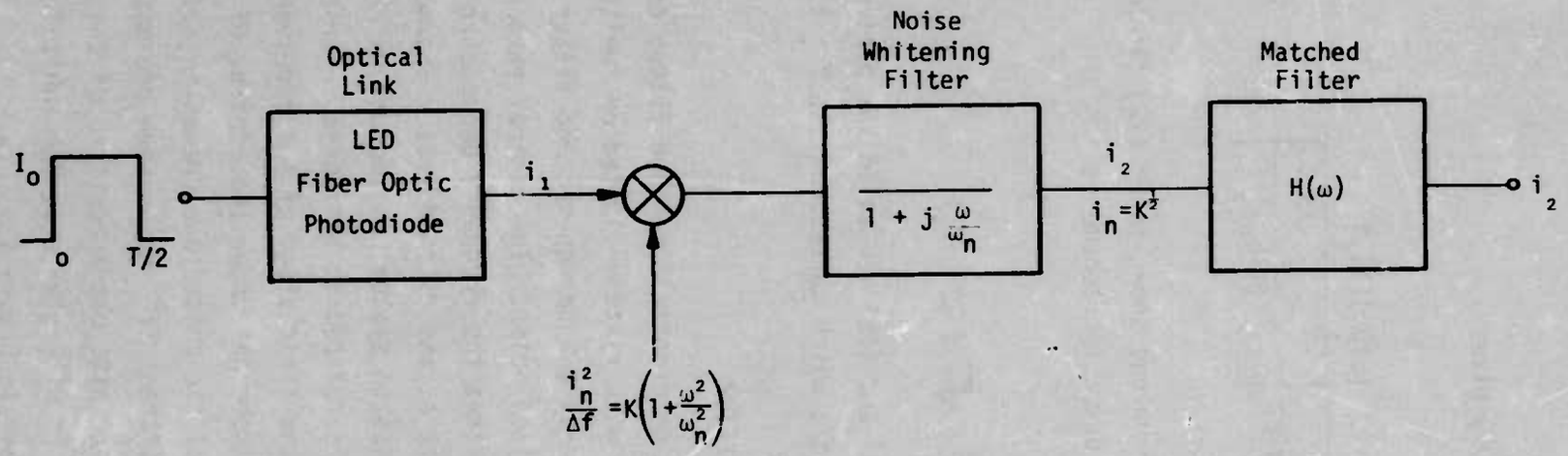

$\omega_{nT} = 0$

$\frac{i_s}{i_n} = 4.36 \times 10^{15} I_s T$

$\omega nT = 6.0$

$\frac{i_s}{i_n} = 2.94 \times 10^{15} I_s T$

Figure 9. Matched Filter Detector

The filter characteristic (frequency response) of a receiver system is called a matched filter when the ratio of peak signal to rms noise at sample time at the output of the filter is the maximum value of S/N that can be achieved. Since the matched filter gives the best possible value of S/N, no other filter can give a higher S/N. The value of S/N for a matched filter is

$$S/N = \left(\frac{\text{energy of the pulse}}{K}\right)^{1/2} \tag{43}$$

where K is the "white" mean square noise spectral density.

When working with a system with "non-white" noise, the matched filter formalism requires that a noise whitening filter be provided ahead of the matched filter. Referring to the typical input noise characteristic of Figure 4, the noise whitening filter will have a pole at f_n. The transfer function of the noise whitening filter is

$$H_n(\omega) = \frac{1}{1 + j\frac{\omega}{\omega_n}} \tag{44}$$

where $\omega_n = 2\pi f_n$. A block diagram of a fiber optic data link using a matched filter detector is shown in Figure 9. Since the matched filter is unique and provides the best possible S/N, the addition of the noise whitening filter has not really changed the system. If the noise whitening filter is not needed to maximize S/N, then it will be cancelled out by the matched filter derived for the system. This determination will be made automatically by the mathmatics.

To better understand the matched filter concept, consider the system of Figure 9 in which a signal $i_1(t)$ is passed through a noise whitening filter with a transfer function $H_n(\omega)$ and an impulse response $h_n(t)$ and a matched filter with a transfer function $H(\omega)$

and an impulse response h(t). The entire system is linear between the point at which the noise is introduced and the point at which the S/N is measured.

The convolution integral[8] can be used to determine the signal output of the noise whitening filter, $i_2(t)$,

$$i_2(t) = \int_{-\infty}^{\infty} i_1(\tau)\, h_n(t - \tau)\, d\tau \tag{45}$$

where τ is the variable of integration and $h_n(t - \tau)$ is the impulse response $h_n(\tau)$ reversed in time and delayed through all successive values of t. At the output of the noise whitening filter, the signal is $i_2(t)$ and the noise is "white" with a mean square noise spectral density, $K = \frac{i_n^2}{\Delta f}$, equal to the low-frequency value of the equivalent input noise of the preamp.

The convolution integral can be used again to determine the output signal of the matched filter, $i_n(t)$,

$$i_n(t) = \int_{-\infty}^{\infty} i_2(\tau)\, h(t - \tau)\, d\tau \tag{46}$$

where $h(\tau)$ is the impulse response of the matched filter. From Eq (43) the peak S/N at the output of the matched filter is

$$S/N = \left(\frac{\text{energy of } i_2(t)}{K}\right)^{1/2} \tag{47}$$

this maximum S/N will occur at the sample time, t_o. At $t = t_o$, the output signal current from Eq (46) has a value of

$$i_m(t_o) = \int_{-\infty}^{\infty} i_2(\tau)\, h(t_o - \tau)\, d\tau \tag{48}$$

Notice in Eq (48) that if

$$i_2(\tau) = h(t_o - \tau) \tag{49}$$

then the integral reduces to

$$i_m(t_o) = \int_{-\infty}^{\infty} i_2^2(\tau) d\tau \tag{50}$$

which is the energy in the pulse i_2. Thus, the signal current $i_s(t_o)$ is proportional to the energy in the pulse at i_2. From Eq (49) the matched filter impulse response is given by

$$h(t) = i_2(t_o - t) \tag{51}$$

This equation states that the impulse response of the matched filter must be tailored to the specific shape of the current pulse at its input. Specifically, the shape of the matched filter impulse response is the shape of the pulse reversed in time and delayed by t_o.

The mean square noise current at the output of the matched filter is

$$i_n^2 = K \int_{-\infty}^{\infty} h^2(\tau)\, d\tau \tag{52}$$

However, since the noise is Gaussian and white, it is unaffected by time reversal or delay so that

$$i_n^2 = K \int_{-\infty}^{\infty} h^2(t_o - \tau)\, d\tau = K \int_{-\infty}^{\infty} i_2^2(\tau)\, d\tau \tag{53}$$

Combining Eqs (50) and (53) gives an expression for $(S/N)^2$

$$\frac{i_m^2(t_o)}{i_n^2} = \frac{\left[\int_{-\infty}^{\infty} i_2^2(\tau)\, d\tau\right]^2}{K\int_{-\infty}^{\infty} i_2^2(\tau)\, d\tau} \tag{54}$$

$$= \frac{\int_{-\infty}^{\infty} i_2^2(\tau)\, d\tau}{K}$$

From Eq (54) the S/N ratio at the output of the matched filter is

$$\frac{i_m}{i_n} = \left[\frac{1}{K}\int_{-\infty}^{\infty} i_2^2(\tau)\, d\tau\right]^{1/2} \tag{55}$$

which is in agreement with Eqs (43) and (47).

If Eq (27) which defines the impulse response of the matched filter is transformed into the frequency domain, the transfer function of the matched filter is[9]

$$H(\omega) = I_2^*(\omega)\, e^{-j\omega t_o} \tag{56}$$

where $I_2^*(\omega)$ is the complex conjugate of $I_2(\omega)$. The phase term $e^{-j\omega t_o}$ represents the delay time which determines when the output data should be sampled to achieve the peak S/N.

The block diagram of Figure 9 is consistent with the assumptions used for the suboptimum detection scheme. That is, bandwidth limitations resulting from the LED cutoff, pulse distortion in the

fiber optic bundle, transit time cutoff in the photodiode and Q_o limitations are neglected. For present components this limits the analysis to data rates of 75Mbit/s or less. The only bandwidth limiting terms considered are in the receiver and in this case are represented by the noise whitening filter and the matched filter. Since the noise whitening filter is the only frequency dependent term in $I_2(\omega)$, it follows that

$$I_2(\omega) = H_n(\omega) \tag{57}$$

and Eq (56) becomes

$$H(\omega) = H_n^*(\omega)\ e^{-j\omega t_o} \tag{58}$$

Thus, the required matched filter transfer function is

$$H(\omega) = \frac{e^{-j\omega t_o}}{1-j\ \frac{\omega}{\omega_n}} \tag{59}$$

which is physically unrealizable because the negative sign in the denominator indicates a pole in the right half plane. The combined transfer function of the noise whitening filter and the matched filter is

$$H_n(\omega)\ H(\omega) = \frac{e^{-j\omega t_o}}{\left[1+\frac{\omega^2}{\omega_n^2}\right]} \tag{60}$$

which has the same amplitude response as a double pole at ω_n but with a linear phase shift with frequency. Notice that the matched filter cancels only the phase of $H_n(\omega)$ but not the amplitude response. Thus, the noise whitening filter was not an unnecessary addition to the receiver.

The fact that $H(\omega)$ in the matched filter is not physically realizable is to be expected; unfortunately, this is true for many cases of practical interest. Even though the ideal matched filter cannot be constructed, Eq (55) can still be used to determine the best possible S/N and this value can be used as the basis of evaluating the performance of practical approximations.

The lowest equivalent input noise in the matched filter receiver will be achieved if the noise whitening pole at ω_n is built into the preamp feedback network. Thus,

$$f_n = \frac{1}{2\pi R_f C_f} \tag{61}$$

The "white" noise at the preamp input is

$$\frac{i_n^2}{\Delta f} = \frac{2qI_E}{1+h_{FE}} + 4kT_a(2\pi f_n C_f) \tag{62}$$

and the "f^2" noise is given by Eq (63) for $Q_o >> 1$

$$\frac{i_n^2}{\Delta f} = 2KT_a \left(\frac{KT_a}{qI_E}\right)(2\pi f C_T)^2 \tag{63}$$

The noise corner frequency can be evaluated by equating Eq (62) and Eq (63) for $f = f_n$

$$f_n = \frac{qI_E}{2\pi kT_a C_T}\left[\frac{C_f}{C_T} + \left(\frac{C_f^2}{C_T^2} + \frac{1}{1+h_{FE}}\right)^{1/2}\right] \tag{64}$$

For the typical parameter values shown in Eq (17), the expression for $\omega_n = 2\pi f_n$ reduces to

$$\omega_n = 8.5 \times 10^{11} I_E \tag{65}$$

Substituting Eq (65) and the typical parameter values into Eq (62) gives the expression for K

$$K = \frac{i_n^2}{\Delta f} = 5.6 \times 10^{-21} I_E \tag{66}$$

Both ω_n and K are directly proportional to I_E.

By direct integration[10] of Eq (55) the S/N ratio at the output of the matched filter is

$$\frac{i_s}{i_n} = \frac{I_s}{\sqrt{K\omega_n}} \left[\omega_n t_o - \left(1 - e^{-\omega_n t_o} \right) \right]^{1/2} \tag{67}$$

where t_o is the sample time for maximum S/N. For Manchester data of period T, the sample time is

$$t_o = T/2 \tag{68}$$

Analysis of Eq (67) using the numerical values for ω_n and K from Eqs (65) and (66) shows that the optimum value of I_E which maximizes S/N is

$$\left[I_E \right]_{opt} = 0 \tag{69}$$

and at this optimum point

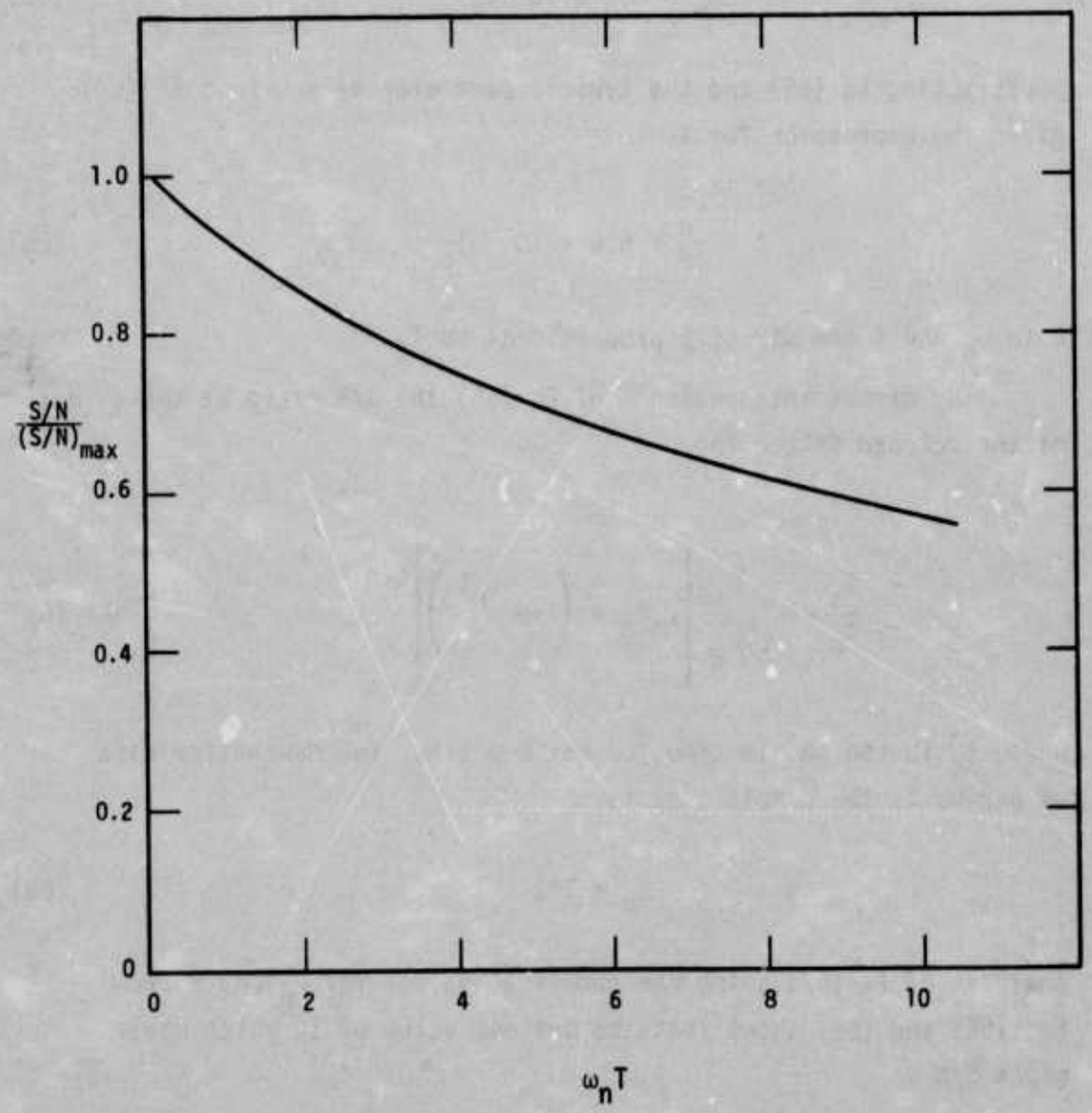

Figure 10. Relative S/N Vs $\omega_n T$

$$\frac{i_s}{i_n} = \left(\frac{\omega_n}{4K}\right)^{1/2} I_s T = 4.36 \times 10^{15} I_s T \qquad (70)$$

The S/N ratio is plotted as a function of $\omega_n T$ in Figure 10. From Eq (40) the suboptimum detector was biased for

$$\omega_n = \frac{7.16}{T} \qquad (71)$$

which in Eq (64) using the typical parameter values in Eq (17) gives

$$I_E = 8.4 \times 10^{-12} \frac{1}{T} \qquad (72)$$

From this bias condition the S/N ratio of the matched filter is 65% of the optimized value. Simplifying assumptions made at the beginning of this analysis limit the results to data rates of 75Mbit/s or less; this corresponds to $T \leq 13.3$ns.

F. DETECTION SCHEME COMPARISON

Comparing the S/N expressions in Eqs (42) and (70) shows that the maximum S/N of the matched filter is 3.08 times higher than the S/N of the suboptimum detector. When both preamps are operated at the same bias point, the matched filter S/N is 2.00 times higher than the suboptimum detector. Taking into account the factor of 2 signal loss due to the coupling capacitor in the suboptimum detector, the matched filter and suboptimum detection schemes give the same S/N.

Selection of the emitter bias current must consider other factors than S/N. If the bias current is too low, the f_T of the input transistor will be inadequate to provide the required frequency response. In general the emitter bias current should be increased proportional to the bit rate. The emitter bias current specified by Eq (72) is a good compromise between speed and S/N for most applications.

The Spectronics, Inc. suboptimum detection scheme would have a S/N ratio equal to that of a matched filter detector if a way could be found to recover the factor of two in signal amplitude that is lost at the coupling capacitor. The conclusion is that the suboptimum detector that has been used is a good practical approximation to a matched filter and no more than a factor of 2 (3dB) improvement in the S/N can be expected.

G. LED SPEED-UP TECHNIQUE

The measured frequency response of GaAs diffused junction LEDs is presented in Section IV.A. These data show that the high-frequency cut off of the modulated light output can not be properly represented by a single pole transfer function. However, the observed frequency response is the expected characteristic for a p-n junction diode dominated by minority carrier diffusion effects. The measured modulation transfer function of a diffused junction GaAs LED is

$$\frac{\phi}{i_d} = \frac{\eta_q E_\phi}{(1+jf/f_d)^{1/2}} \tag{73}$$

where ϕ is the ac component of optical power,

i_d is the ac component of LED current,

η_q is the quantum efficiency,

E_ϕ is the emitted photon energy, and

f_d is the LED corner frequency.

The term corner frequency is used to denote the intersection of the extended high-frequency and low-frequency asymptotes. For the characteristic of Eq (73) the corner frequency is not the 0.707 frequency; the expression for the 0.707 frequency in this case is

$$f_\phi = \sqrt{3}\, f_d \tag{74}$$

The 0.707 frequency, f_ϕ, is the easiest value to measure for the LED. It can be measured directly with ac(sine wave) modulation or it can be determined from t_ϕ, the 10-90% rise time of the LED driven with a constant current pulse.

$$f_\phi = \frac{.35}{t_\phi} \tag{75}$$

From the transfer function of Eq (73) the shape of the LED pulse response follows an error function rather than an exponential. However, Eq (75) is a valid relationship for 0.707 frequency and 10-90% rise time for both the exponential and the error function responses.

The LED transfer function of Eq (73) is plotted in Figure 11. The high-frequency asymptote has an $f^{-\frac{1}{2}}$ frequency dependence. The frequency response of tne LED can be extended by using a driving network which provides an LED drive current that increases with frequency. A specific example of an RC network which has this desired property is shown in Figure 12. The SE3450 GaAs LED is used as a reference diode to provide a prebias to the output LED. The current i_a is presumed to be supplied from a high impedance source such as the collector of a transistor; the bias current for the reference diode should be larger than the peak value of i_a. The transfer function of the overdrive circuit is

$$\frac{i_d}{i_a} = \frac{1}{m_a}\left[\frac{1+jf/f_a}{1+jf/m_a f_a}\right] \tag{76}$$

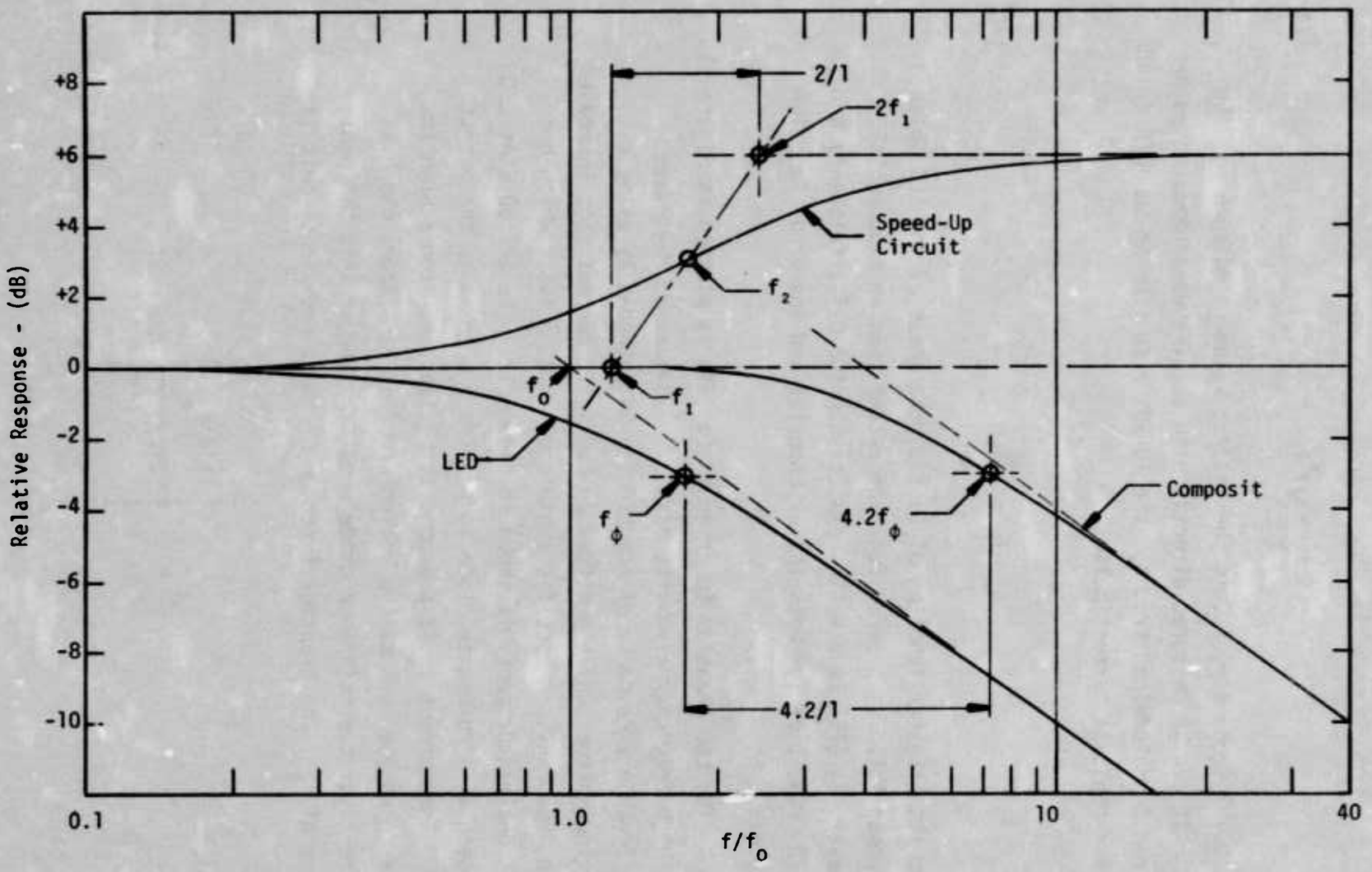

Figure 11. LED High-Frequency Compensation

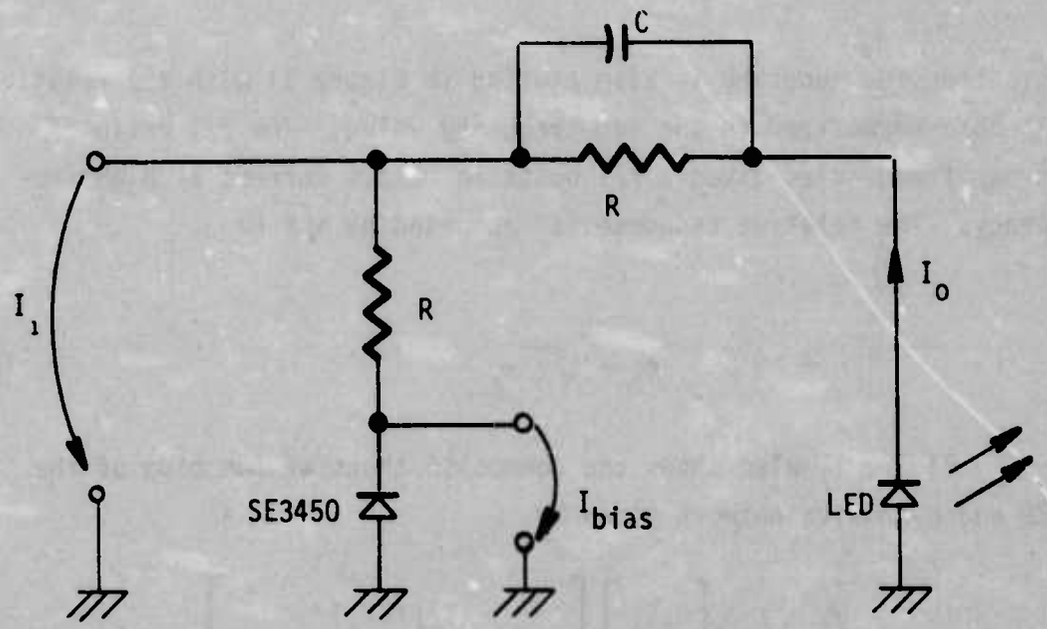

Figure 12. Overdrive Circuit with LED and Bias Diode

where

$$f_a = \frac{1}{2\pi R_a C_a} \tag{77}$$

and

$$m_a = \frac{R_a+R_b}{R_b} \tag{78}$$

The special case of $R_a = R_b$ will be used as an example to illustrate a method of selecting the proper value of C_a to use with a particular LED. In this special case, $m_a = 2$ and Eq (76) becomes

$$\frac{i_d}{i_a} = \frac{1}{2}\left[\frac{1+jf/f_a}{1+jf/2f_a}\right] \tag{79}$$

This transfer function is also plotted in Figure 11 with the relative response normalized to the low-frequency value. The 2/1 ratio of corner frequencies gives a 2/1 boost in output current at high frequency. The relative response is increased by $\sqrt{2}$ at

$$f_b = \sqrt{2}\, f_a \tag{80}$$

Figure 11 also shows the composite transfer function of the LED and overdrive network given by

$$\frac{\phi}{i_a} = \left(\frac{i_d}{i_a}\right)\left(\frac{\phi}{i_d}\right)\left[\frac{\eta_q E_\phi}{2}\right]\left[\frac{(1+jf/f_a)}{(1+jf/2f_a)(1+jf/f_d)^{1/2}}\right] \tag{81}$$

the relative response is normalized to the low-frequency value. The particular composite response shown in Figure 11 was achieved by selecting f_b (the $\sqrt{2}$ frequency of the network) to be equal to f_ϕ (the .707 frequency of the LED).

$$f_b = f_\phi \tag{82}$$

Combining Eqs (80) and (82) gives

$$\sqrt{2}\, f_a = \frac{.35}{t_\phi} \tag{83}$$

and from Eq (77) the selection rule for the value of C_a to be used with a particular LED is

$$C_a = \frac{\sqrt{2}}{2.2}\,\frac{t_\phi}{R_a} \tag{84}$$

From Figure 11 the effective bandwidth of the LED is increased by 4.2 times by the 2/1 overdrive network. The selection rule shown in Eq (84) is good only for $m_a = 2$; however, a similar selection rule can be found for each value of m_a. In general, the increase in bandwidth provided by an overdrive network is about m_a^2. However, values of m_a larger than $\sqrt{10}$ do not give a flat composite transfer function and the resulting peaks and valleys in the transfer function give rise to ringing and other undesirable features in the pulse response. Thus, the overdrive circuit of Figure 12 is in practice limited to a factor of 10 increase in bandwidth; the use of more complex overdrive networks can provide larger increases in bandwidth.

The increased bandwidth achieved with an overdrive network is obtained at the expense of the efficiency of the drive circuit. With a 2/1 overdrive, the drive circuit must supply a peak current that is 2 times larger than the low-frequency value of the LED peak current. The extra power required from the drive circuit is dissipated in R_a and R_b.

The type of overdrive network shown in Figure 12 connects directly to the LED terminals. This type of circuit is useful with both analog and pulsed signals. With pulse or digital signals the overdrive network provides speed up of the optical rise time, fall time and repetition rate.

SECTION III

DATA BUS STRUCTURE

Construction of a data bus requires the use of signal coupling devices which make it possible for each station to receive signals from the bus and transmit signals onto the bus. The vital nature of the signal transactions on an avionic data bus dictates that a strong emphasis on system reliability be used in the coupler design. In general, repeater systems are not employed in data buses because damage to one repeater would interrupt signal flow on the entire data bus.

In an optoelectronic data bus, the various stations are interconnected with flexible fiber optic bundles. The desired signal coupling device should provide the following functions:

- A portion of the optical signal should be removed from the bus for detection.
- The undetected remainder of the optical signal should be passed on for distribution to the other terminals on the bus.
- Optical signals generated in that terminal should be coupled onto the bus and distributed to the other terminals.

Meeting these requirements provides fault isolation on the optoelectronic data bus so that failure of one of the stations on the bus will affect only that station and will leave the remainder of the bus unimpaired. Two basic schemes have been reported[11,12] for providing these functions in an optoelectronic data bus; both schemes have been investigated on this program. One approach uses an in-line configuration in which individual stations are sequentially interconnected by flexible fiber optic bundles. The other approach uses a radial configuration in which all stations are connected by flexible fiber optic bundles to a centrally located mixing point.

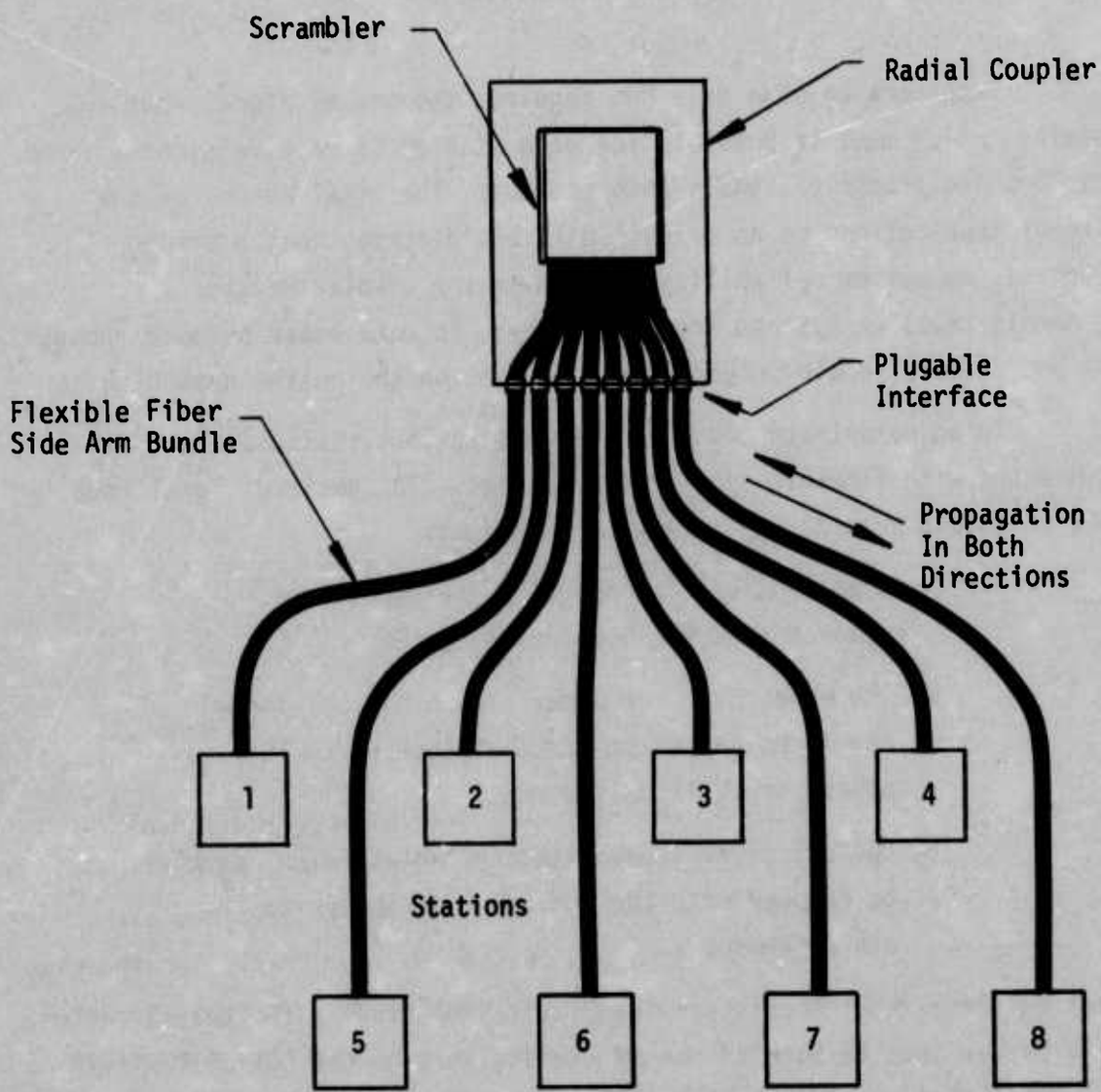

Figure 13. Radial Duplex Data Bus

Reference 1 presented an analysis and comparison of three in-line data bus structures,

- Simplex Loop,
- Uniform Duplex Loop, and
- Tapered Duplex.

All three of these in-line structures are based on the use of passive T couplers with plugable optical interfaces.

This section presents an analysis of a fourth physical data bus structure which employs a radial geometry. The radial data bus offers several advantages over the in-line structures. Among these advantages are:

- Fewer plugable interfaces,
- Ease of construction,
- Less optical attenuation, and
- Minimum dynamic range.

With the in-line data bus configurations the individual stations on the data bus are sequentially interconnected by flexible fiber optic bundles. With the radial geometry all stations are connected by flexible fiber optic bundles to a centrally located mixing point as shown in Figure 13. The radial configuration as represented in this figure gives the impression of requiring more fiber bundle than the in-line structures presented in Ref 1. However, closer analysis shows that just the opposite is actually true. The fiber bundles in the radial data bus each connect to one LED and one photodiode and are, therefore, smaller in diameter than the fiber bundles required for an in-line system with the same number of stations. Also, in the radial system, the fiber bundles go directly from the radial coupler to the various stations so that the length

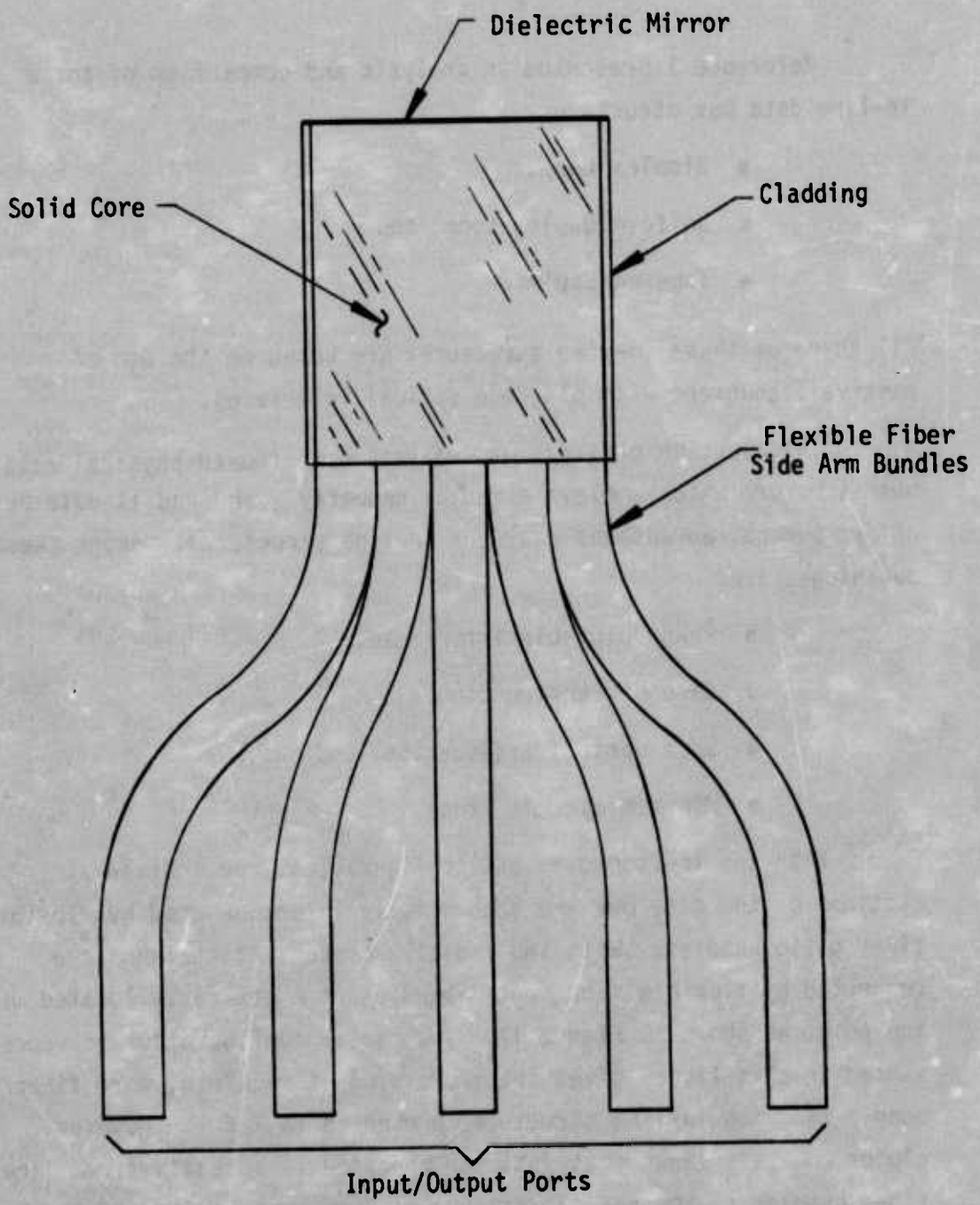

Figure 14. Duplex Radial Coupler

of the individual fiber bundles is minimized. In an aircraft installation, the various fiber bundles can be cabled together in a harness for convenient installation or purposely separated to provide greater damage immunity. The duplex data bus depends entirely on the proper functioning of one passive coupler. If that coupler is damaged, the entire system fails. However, damage to a radial arm or a station does not affect the performance of the remainder of the system. The in-line data bus structures are also protected against failure of a station. However, damage to the connecting fiber optic bundle or any one of the T couplers separates the data bus into two isolated parts. From an operational standpoint, the radial coupler should be located half way between the two most distant stations. This optimum location can be closely approximated in practice because the radial coupler is a completely passive component that does not have to be located near any of the data bus stations. However, in military aircraft, reliability considerations may dictate that the radial coupler be located near the cockpit or near a central computer so that the zone of vulnerability can be minimized. In any case, the radial coupler is much smaller than the sum of all of the T couplers and connecting fiber optic bundles in an equivalent in-line data bus. Because of this size advantage the radial data bus structure offers the highest probability of surviving in a battle damage situation.

A. DEFINITIONS

Figure 14 shows a schematic representation of a radial coupler. In this case the scrambler has a diameter equal to the diameter of all of the radial arms bundled together. The mirror reflects all rays back into the scrambler so that every radial arm can couple to every other radial arm. A T coupler schematic is shown in Figure 15. The scramblers shown in Figures 14 and 15 are short lengths of solid clad glass rod with the same diameter as the body of the coupler. The

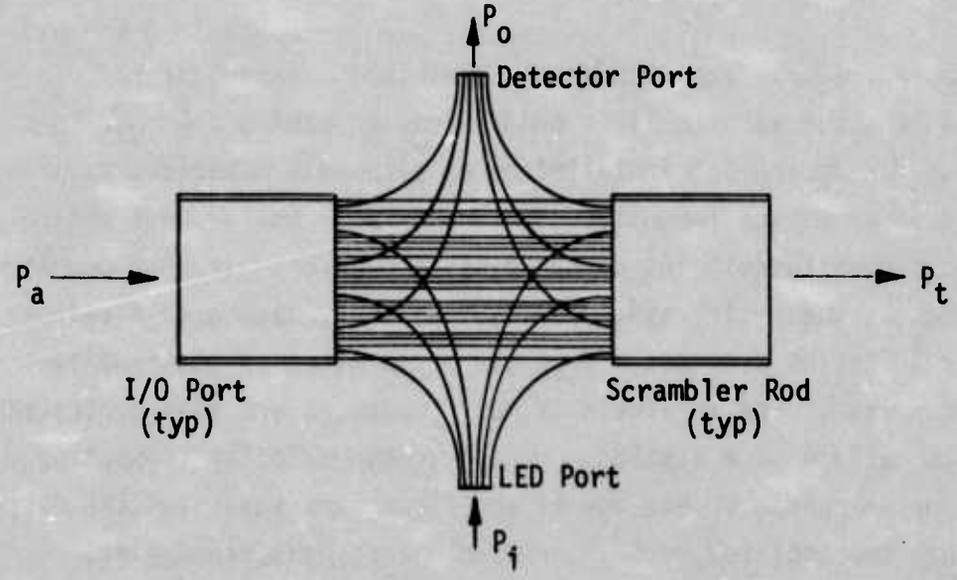

Figure 15. Uniform Duplex T Coupler

purpose of the scrambler is to uniformly distribute the optical energy entering the LED port over the area of the exit port so that it will be coupled into all of the individual fibers in the fiber optic cable leading to the next station. This insures a reproducible sample of the total signal on the bus at each station.

The performance of a passive optical coupler can be described in terms of a transmission factor, one or more quality factors and a coupling factor. In this report, T_T and C_T are used to designate the transmission factor and coupling factor for a T coupler; for a radial coupler the symbols $T_\star$ and $C_\star$ are used. The transmission factor describes the fraction of input optical power (at an input port) that is coupled to the output port. The definition of transmission factor is

$$T_T \text{ or } T_\star = \frac{\text{(power at output port)}}{\text{(power at input port)}} \qquad (85)$$

The transmission factor is always less than one because of the intentional removal of optical power at other ports and because of optical losses in the coupler. The coupling factor is basically an area ratio

which describes the fraction of total power removed from the bus. The definition of coupling factor is

$$C_T \text{ or } C_* = \frac{\text{(scrambler area attributed to a detector port)}}{\text{(total area of the scrambler)}} \quad (86)$$

This definition of the coupling factor is very basic and general. It was chosen because it accurately represents the performance of both T and radial couplers and allows the use of common terminology in describing both types of data bus systems. The fraction of input power coupled to the detector port will always be less than predicted by Eq (86) because of reflection, packing fraction, and attenuation losses in the detector side arm. The coupling factor defined by Eq (86) cannot be measured optically on a finished coupler. However, this coupling factor has great practical value as a design parameter because it specifies the area that should be attributed to the detector port independent of the losses in the detector side arm. For the radial coupler of Figure 15 the term detector port should be interpreted to mean input/output port.

1. T Coupler

Two quality factors are required to accurately represent the performance of a T coupler. A general T coupler schematic is shown in Figure 15. The transmission quality factor, m_T provides a measure of the losses in the transmission path. Using Eqs (85) and(86) and assuming equal scrambler areas attributed to LED and detector ports, the transmission quality factor is defined as

$$m_T = \frac{T_T}{1-2C_T} \quad (87)$$

which may be rearranged as

$$T_T = m_T(1-2C_T) \quad (88)$$

From Eq (87), m_T is the ratio of the power at the output port to the power into the area attributed to the output port. The coupling quality factor, m_C, provides a measure of the losses in the detector side arm; it is defined by

$$m_C = \frac{\text{(power at detector port)}}{\text{(power into scrambler area attributed to detector port)}} \quad (89)$$

The detector port output power P_o can now be expressed as a function of coupler output power P_a:

$$P_o = C_T m_C P_a \quad (90)$$

Due to the physical symmetry of the T coupler, it will be assumed that the coupling quality factor is the same for the LED side arm and the detector side arm. In an actual coupler, the values could be different because of broken fibers and/or differences in packing fraction. In addition, the amount of power coupled into the LED port is strongly dependent on the radiation pattern of the LED. Losses at the LED port over and above those included in m_C should be charged against the LED and not the coupler. An LED quality factor, m_L, should be used to represent the LED-dependent losses. The definition of m_L is

$$m_L = \frac{\text{(power into area and NA of LED port)}}{\text{(total output power of LED)}} \quad (91)$$

Thus the product $m_C m_L$ represents the efficiency with which the total LED output power P_i is coupled to the bus.

$$P_t = \frac{m_C m_L}{2} P_i \quad (92)$$

The factor 2 in the denominator of Eq (92) describes the equal division of the LED power between the two directions of propagation.

The values of m_T and m_C can be combined to give an overall quality factor, m, for the T coupler. This overall quality factor is defined by

$$m = \frac{\text{(power sum at output, detector \& LED ports)}}{\text{(power at input port)}} \tag{93}$$

This factor does not appear in the system design equations; however, it is useful as a parameter to assess the quality and perfection of the technology used to construct a coupler. The value of m can be obtained from Eq (93) using Eqs (85) and (86).

$$m = T_T + 2m_C C_T \tag{94}$$

Combining Eq (43) with Eq (38) to eliminate T_T gives

$$m = m_T \left[1-2C_T\left(1 - \frac{m_C}{m_T}\right)\right] \tag{95}$$

If the coupling factor, C_T, is small, Eq (95) shows that the overall quality factor is about equal to m_T. In fact, if $m_C = m_T$, the overall quality factor is equal to m_T for all values of C_T. In general, quality factor is a transmission parameter which designates the complement of the attenuation or loss; when losses are zero, quality factor has its maximum value of one.

A serious effort has been made to define parameters that describe the performance of T couplers without resorting to any particular technology or construction technique. Because of this, Eqs (85) through (95) have relied heavily on general word definitions rather than schematics or pictures of a specific type of T coupler. This general T coupler model is used in Appendix II in the analysis of an in-line uniform duplex data bus and in Appendix III in the analysis of an in-line tapered duplex data bus.

2. Radial Coupler

Due to the symmetry of the radial coupler, only one quality factor, m_*, is required to describe its performance. A radial coupler is shown in schematic form in Figure 14. The quality factor, m_*, is defined by

$$m_* = \frac{\text{(sum of output power at all ports)}}{\text{(power in at input port)}} \tag{96}$$

This is similar to the overall quality factor of the T coupler given in Eq (93). For the radial coupler there is no possibility of optimizing the coupling factor because the area ratio is uniquely determined by the geometry. For an N-station radial duplex bus there are N input/output ports all of the same area. Therefore, the total area of the composite fiber optic bundle at the scrambler rod must be N times the area of each input/output port. From Eq (86) the coupling factor for the radial coupler is

$$C_* = \frac{1}{N} \tag{97}$$

Equations (86) and (97) combine to specify the fraction of the area of the scrambler that should be used for the detector (input/output) port.

$$\frac{\text{(Area attributed to one input/output port)}}{\text{(Area of scrambler)}} = \frac{1}{N} \tag{98}$$

When power is coupled into any one LED port of a radial data bus, all N detector ports receive power. In the ideal case of uniform power distribution in the scrambler the transmission factor of the radial coupler is the same for all stations and is given by

$$T_* = m_* C_* \tag{99}$$

Combining Eqs (51) and (53) gives

$$T_* = \frac{m_*}{N} \tag{100}$$

B. RADIAL DATA BUS ANALYSIS

In a radial data bus, flexible fiber optic bundles are used for the connections between the stations and the radial coupler as shown in Figure 16. The length of a radial data bus (for signal attenuation) is not the total length of the fiber optic bundles used in the system. For the radial geometry, the length of the bus, L, will be taken as the greatest length of fiber optic bundle between any two stations on the bus. For the analysis, the radial coupler is assumed to be centrally located so that all other transmission paths between stations have lengths equal to or less than L. In this case the maximum fiber optic attenuation, a_m, is given by

$$a_m = \exp[-\alpha L] \tag{101}$$

where α is the attenuation coefficient of the fiber optic bundle.

Comparison to Eq (202) in the T coupler analysis given in Appendix II shows that

$$a_m = a_o^{N-1} \tag{102}$$

where a_o is the average fiber optic attenuation between adjacent stations, and

N is the number of stations.

In order to facilitate the comparison between the radial and in-line data bus systems, the concept of average fiber optic attenuation per station will be retained in the radial data bus analysis with a_o defined by Eq (202).

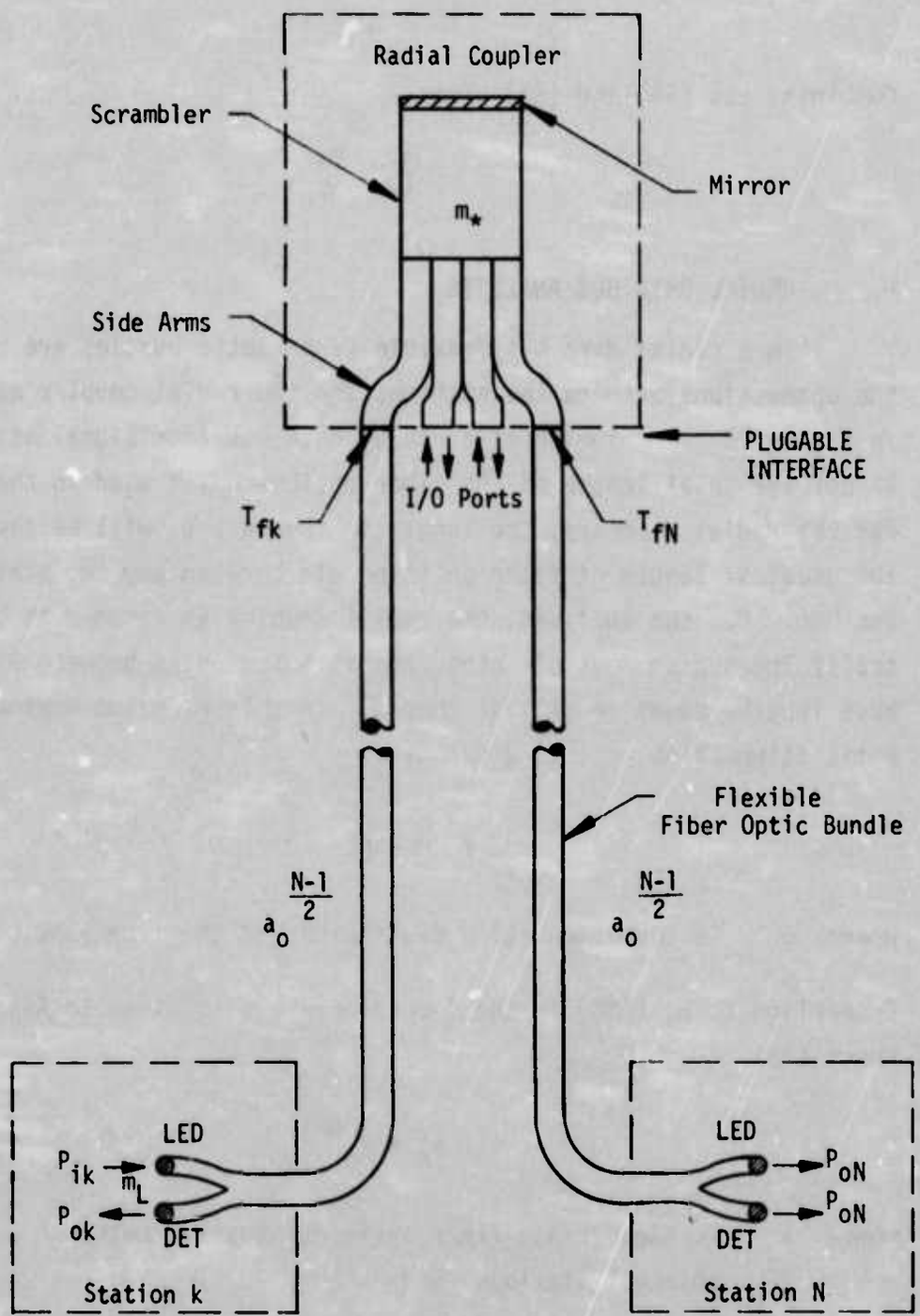

Figure 16. Signal Power Relationships in a Radial Data Bus

For purposes of analysis the longest transmission path is assumed to be between stations k and N. When station k is transmitting, the signal power relationships can be determined from Figure 16. When an optical power, P_{ik}, is emitted by the LED of station k, the power at the LED port is $m_L P_{ik}$, where m_L is the LED quality factor defined by Eq (91). The power at the input port of the radial coupler, P_{if}, is given by

$$P_{if} = m_L T_c T_{fk} a_o^{\frac{1}{2}(N-1)} P_{ik} \tag{103}$$

where T_c is the transmission of the fiber optic termination at the LED interface given by

$$T_c = (1-R_c)GR_a \tag{104}$$

where R_c is the front surface reflectivity of the core glass,

G is the geometrical area coverage of the fibers in the termination, and

R_a is the core/fiber area ratio.

The symbol T_{fk} represents the portion of the interface transmission at the radial coupler input port that can be attributed to the exit end of the fiber optic bundle between station k and the radial coupler.

When power is coupled into any port of a radial coupler, all N ports receive output power. In the ideal case of uniform power distribution in the radial coupler, the output power at the detector port of station N as a function of the station k LED power is

$$R_{p*} = \frac{P_{oN}}{P_{ik}} = \frac{m_L m_* T_c T_{fk} T_{fN} a_o^{N-1}}{2N} \tag{105}$$

The symbol T_{fN} represents the portion of the interface transmission at the radial coupler output port that can be attributed to the entrance end of the fiber optic bundle between the radial coupler and station N. If the side arms of the radial coupler are made from fiber optic bundles, then these two interfaces are fiber bundle/fiber bundle interfaces and $T_{fK} = T_{fN}$. When solid side arms are used in the radial coupler the plugable interfaces are similar to fiber/scrambler interfaces used in the T coupler. In this case, T_{fk} is the transmission of the core/air interface which is denoted by the symbol T_c where

$$T_c = (1-R_c) \tag{106}$$

and

$$R_c = \left(\frac{n_2 - n_1}{n_2 + n_1}\right)^2 \tag{107}$$

where n_2 is the index of refraction of the core glass, and

n_1 is the index of refraction of the coupling medium ($n_1 = 1$ for air),

and $T_{fN} = T_c$ given by Eq (104). The values of T_{fk} and T_{fN} must be determined for each different radial coupler design; no part of T_{fk} or T_{fN} is included in m_*. The factor 2 in the denominator of Eq (105) results from the power split between the LED and detector ports at station N. Equation (105) is the worst case power ratio, R_{p*}, for the radial data bus.

All of the signals on a radial data bus pass through the same centrally located radial coupler. If the radial coupler gives a uniform power distribution to all input/output ports, then the dynamic range of the radial data bus is due entirely to the difference in attenuation of the various fiber optic bundles.

If the stations of a radial data bus are uniformly spaced, the greatest distance between a station and the radial coupler is $0.5L$ and the shortest distance between a station and the coupler is $\frac{0.5L}{(N-1)}$. In this case, the fiber optic attenuation for the most distant station is $a_o^{\frac{1}{2}(N-1)}$ and for the closest station is $a_o^{\frac{1}{2}}$. Assuming the radial coupler gives the uniform power division shown in Eq (97) the worst case dynamic range results at a station close to the radial coupler. The largest detector signal occurs when another close station transmits and the attenuation is a_o. The smallest detector signal occurs when a distant station transmits and the attenuation is $a_o^{\frac{1}{2}N}$. In this case the worst case dynamic range, D_{R*}, is given by Eq (108)

$$D_{R*} = \left[\frac{1}{a_o}\right]^{\frac{N-2}{2}} \tag{108}$$

For any given station the dynamic range can be significantly reduced by lowering the LED drive current in the stations that have short fiber optic bundles. If the drive currents are adjusted such that the optical power reaching the coupler is the same for all LEDs, then the dynamic range at any particular detector is 1.0. Each detector, on an individual basis receives the same power from all LEDs. However, this constant signal level is different for different detectors because of the variation in the fiber optic attenuation between the radial coupler and the various detectors. In this case, the ratio of power levels over all detectors is the ratio of the attenuation of the shortest $\left(a_o^{\frac{1}{2}}\right)$ and longest $\left(a_o^{\frac{1}{2}N-\frac{1}{2}}\right)$ fiber optic bundles which is $a_o^{\frac{1}{2}(2-N)}$.

The dynamic range of the radial data bus can in theory be reduced to the ideal value of 1.0 (zero dB) by including equal attenuation in all of the fiber optic bundles. In this case, each detector receives the same signal regardless of which LED is transmitting

and all detectors receive the same signal when any LED transmits. One way to make a uniform attenuation radial system is to make all of the fiber optic bundles the same length. A more practical way to achieve uniform attenuation is to include a neutral density filter element in the shorter fiber optic bundles to bring all fiber optic bundles to the same attenuation regardless of their length.

In military aircraft, reliability considerations may dictate that the radial coupler be located near the cockpit or near a central computer so that the zone of vulnerability can be minimized. These requirements may preclude locating the radial coupler half way between the two most distant stations. For example, one remote station may be near the tail of the aircraft with all other stations about equidistant from the radial coupler located at the central computer. For a fighter aircraft, typical fiber optic cable lengths might be 50ft between the radial coupler and the remote station in the tail and 10ft between the radial coupler and the next most distant station in the nose. For fiber optic bundle with attenuation of 0.2dB/ft the cable attenuation to the remote tail station is 10dB and to the nose station is 2dB. The actual total cable attenuation in this case is 12dB. However, if neutral density filters are used to minimize dynamic range, the result is that all cables are brought to an attenuation of 10dB and the effective total cable attenuation is 20dB. This is 8dB more cable attenuation than would be achieved if the radial coupler were located half way between the nose and the tail stations (two 30ft, 6dB fiber optic cables). When the radial coupler is not centrally located, the maximum fiber optic attenuation given by Eq (101) should be calculated using a value of L which is two times the length of the longest cable. This has the effect of decreasing (degrading) the worst case power ratio, R_{p*}, given by Eq (105) as compared to the optimum value for central location of the radial coupler. The dynamic range of the radial data bus need

not be affected by the placement of the coupler if current adjustment or neutral density filters are used.

The effectiveness of the scrambler in the radial coupler must be determined experimentally. Measurements on the radial couplers reported in Ref 2 show both nonuniform scrambling and nonreciprocal coupling between the various ports; that is, port 1 does not couple an equal fraction of power to the other ports and port 1 does not couple the same fraction of power to port 5 that port 5 couples to port 1. The best radial coupler reported in Ref 2 shows a power output ratio of 2.9/1; this gives a dynamic range of

$$D_{R*} = 2.9 \qquad (4.62\text{dB}) \tag{109}$$

The measured nonreciprocal coupling is less than 2/1. Proposed improvements in fabrication techniques are expected to reduce the dynamic range to less than 2/1 (3.0dB) and essentially eliminate nonreciprocal coupling. Use of neutral density filters in the radial arms to achieve the uniform attenuation condition will also make it possible to compensate for nonuniform signal distribution between the radial arms. Using the pair of ports with the highest coupling factor for the two longest radial arms will result in an improvement in system performance over that calculated above.

The possibility of achieving a zero dB dynamic range in the radial data bus is a very significant advantage in overall system performance. The nonuniform and nonreciprocal coupling reported in Ref 2 results from the mixing properties of the cylindrical scrambler rods used in the construction of the couplers. These effects are described in Section III.E. A rectangular scrambler rod is proposed to provide more uniform power distribution. In a practical radial data bus, the dynamic range will be determined by the uniformity of the power division provided by the radial coupler. The rectangular

scrambler approach is expected to give a dynamic range of less than 2/1 ($\leq$3.0dB).

The discussion in Section II of this report shows that the unipolar nature of the optical signal causes the average value (threshold level) of the received signal to shift with changes in signal level for transactions between different stations (dynamic range). Accommodation of a large dynamic range results in added complexity in the receiver electronics and the necessity of long dead times between transactions and long sync preambles which reduce the efficiency of the data bus. The practical attainment of a small dynamic range in the radial data bus simplifies the receiver electronics and removes the restrictions on the efficiency of the bus.

The value of R_{p*} can be calculated for a state-of-the-art radial duplex bus from Eq (105). For L = 100ft and using 0.45dB/m fiber optic bundle, Eq (101) gives

$$a_m = a_o^{N-1} = 4.27 \times 10^{-2} \qquad (-13.70\text{dB}) \qquad (110)$$

The best radial coupler reported in Ref 2 has

$$m_* T_c T_{fk} T_{fN} = 0.102 \qquad (-9.91\text{dB}) \qquad (111)$$

Using Eqs (110) and (111) the value of R_{p*}/m_L for an 8 station radial data bus is

$$\frac{R_{p*}}{m_L} = 2.72 \times 10^{-4} \qquad (-35.75\text{dB}) \qquad (112)$$

For 10Mbit/s Manchester data, the preamp 3dB frequency, f_e, from Eq (5) is 8.1MHz. Allowing 2.5 times more bandwidth for synchronization and clock recovery, the required 3dB bandwidth is 20MHz. From Figure 5 or Eq (26) the receiver requires p_n = 17.9nW for S/N = 1. For a bit error rate of 10^{-8} including clock errors and

data errors the required S/N is about 5.75. For 2.5 times excess bandwidth, the fractional response is 1.0; thus, from Eq (35) the required steady state detector power, P_s, is

$$P_s = (2)(5.75)\, P_n$$
$$= 206\text{nW} \tag{113}$$

Using Eq (113) with the value of R_{p*}/m_L from Eq (112) the required useful LED power, $m_L P_i$, is given by

$$m_L P_i = \frac{206\text{nW}}{2.72 \times 10^{-4}} = 0.76\text{mW} \tag{114}$$

In this context, the term useful LED power refers to the optical power coupled into the aperture of the fiber optic termination within an acceptable launch cone. For Galileo 45mil diameter fiber optic bundles the SPX 1527 and SPX 1775 LEDs offer values of useful LED power in the range of 1.0 to 2.0mW. Thus, the required power of 0.76mW in Eq (114) is well within the capability of available components.

The conclusion is that presently available optoelectronic components and technologies are adequate for the construction of an 8-station, 100ft, 10Mbit/s radial duplex data bus with an error rate of less than 10^{-8}.

C. IN-LINE DATA BUS SUMMARY

Three in-line data bus structures were presented in Ref 1. One of these structures the simplex loop, was used mainly as an analysis vehicle and does not represent a practical data bus construction technique. The uniform duplex and tapered duplex systems are viable approaches and their key performance equations are

presented here to facilitate comparison to the radial data bus. The in-line uniform duplex data bus analysis is presented in Appendix II; the analysis of the in-line tapered duplex data bus is presented in Appendix III.

The symbols at the left margin in some of the following equations are used to avoid complicated subscripts and ambiguity in the comparison. These symbols and their meanings are

*D Radial Duplex
UD Uniform Duplex
TD Tapered Duplex

For the uniform duplex data bus, the worst case signal transfer occurs when the station at one end of the bus is communicating with the station at the other end of the bus. From Appendix II the worst case fractional power ratio, R_{PT}, for an N station data bus is

$$\text{UD} \quad R_{PT} = \frac{P_{oN}}{P_{i_1}} = \left[\frac{a_o T_c T_c m_L m_C^2 C_T}{2}\right]\left[a_o T_c T_c m_T (1-2C_T)\right]^{N-2} \qquad (115)$$

where P_{oN} is the output power at the detector port of station N, and

P_{i_1} is the input power at the LED port of station 1.

The term a_o represents the average attenuation between adjacent stations and is defined in Eq (202) of Appendix II. The term T_c is the transmission of the termination on the fiber optic bundles used to interconnect the stations; T_c is defined in Eq (104). The term T_c is the transmission of the core/air interface given by Eq (106).

Equation (115) shows the relative importance of the parameters of the T coupler in determining overall system performance. The transmission quality factor, m_T, appears with the exponent N-2; whereas, the

coupling quality factor, m_C, appears with the exponent 2 independent of the number of stations on the bus. Thus, m_T has much greater significance than m_C in determining system performance and the greatest emphasis should be placed on increasing the value of m_T. The worst case power ratio can be maximized by setting the derivative of Eq (115) with respect to C_T equal to zero, and solving for the optimum value of C_T. This operation gives (see Appendix II for derivation)

UD
$$C_{opt} = \frac{1}{2(N-1)} \tag{116}$$

From Eq (116), the optimum value of C_T is dependent only on the number of stations on the bus. Specifically, this means that C_{opt} is independent of quality factor and fiber optic attenuation; this is a very general result with no limiting assumptions or approximations.

The maximum value of the worst case power ratio for the duplex bus is calculated by substituting Eq (116) into Eq (115). This operation gives

UD
$$R_{PT}\Big|_{max} = \left[\frac{a_o T_c T_c m_L m_C^2}{4(N-1)}\right]\left[\frac{a_o T_c T_c m_T (N-2)}{(N-1)}\right]^{N-2} \tag{117}$$

Referring again to the in-line uniform data bus analysis presented in Appendix II, the worst case dynamic range when the coupling factor is equal to C_{opt} is given by

UD
$$D_{RT}\Big|_{opt} = \left[\frac{1}{a_o T_c T_c m_T}\ \frac{N-1}{N-2}\right]^{N-2} \tag{118}$$

The tapered duplex data bus features a different coupling factor for each station to provide a uniform response at all detectors when either one of the end stations is transmitting. To accomplish

this, the coupling factors must depend on the fiber optic attenuation, quality factor, and termination transmission. From the analysis presented in Appendix III the coupling factor for station k in an N-station bus is

$$\text{TD} \qquad C_k = \frac{0.5(a_o m_T T_c T_c)^{k-1}(1-a_o m_T T_c T_c)}{1 - (a_o m_T T_c T_c)^k} \tag{119}$$

The worst case fractional power ratio for the tapered duplex bus is

$$\text{TD} \qquad R_{PT} = \frac{a_o m_L m_C^2 T_c T_c}{2} \; \frac{(a_o m_T T_c T_c)^{N-2}\,(1-a_o m_T T_c T_c)}{1 - (a_o m_T T_c T_c)^{N-1}} \tag{120}$$

Again the factor $m_T T_c$ appears with the exponent N-2 and is therefore much more significant than the term m_C^2.

The worst case dynamic range of the tapered duplex bus is

$$\text{TD} \qquad D_{RT} = 1 + a_o m_T T_c T_c \tag{121}$$

This expression assumes that the stations are uniformly spaced along the bus and that the various LED drive currents are optimally reduced toward the center of the bus. Deviations from these assumptions and practical imperfections in the couplers will increase the dynamic range.

D. RADIAL/IN-LINE COMPARISON

The worst case fractional power ratios for the in-line uniform and radial data bus systems are given in Eqs (117) and (105)

respectively. Comparison of these expressions shows that fiber optic attenuation (a_o^{N-1}) is the same for both systems. However, for everything except fiber optic attenuation, the radial coupler gives superior performance. The ratio of worst case detector power for the two systems can be obtained by dividing Eq (105) by Eq (117). This operation gives the improvement factor

$$\frac{*D}{UD} \qquad \frac{R_{P*}}{R_{PT}} = \frac{2m_* T_c T_{fk} T_{fN}}{m_C^2 T_c T_c (m_T T_c T_c)^{N-2}} \left(\frac{N-1}{N}\right)\left(\frac{N-1}{N-2}\right)^{N-2} \tag{122}$$

This expression can be further simplified by comparing specific systems. The T_c in the numerator of Eq (122) arises at the LED/fiber optic interface in the radial data bus and is therefore about equal to m_C in the denominator which arises at the LED/fiber optic interface in the in-line data bus. For a solid side arm radial coupler and a split-rod T coupler $T_{fN} \simeq T_c$ and $T_{fk} \simeq T_c$. With index matching materials used at the internal interfaces in the two couplers, typical values of the quality factors are $m_* = .848$ and $m_C = .558$. Using these approximations, the improvement factor, Eq (122), reduces to

$$\frac{*D}{UD} \qquad \frac{R_{P*}}{R_{PT}} = \frac{3.04}{(m_T T_c T_c)^{N-2}} \left(\frac{N-1}{N}\right)\left(\frac{N-1}{N-2}\right)^{N-2} \tag{123}$$

With no index matching at the plugable interface, m_T is about equal to T_c^2. For lead glass fiber $T_c \simeq .94$ and from Ref 2 a typical value of T_c is .656. Using these values gives $m_T T_c T_c = 0.545$; the best T coupler reported in Ref 2 has a measured value of $m_T T_c T_c = 0.452$. If index matching is used at the plugable interfaces then ideally $m_T = 1$, $T_c = 1$, and $T_c = GR_a = 0.696$ for Galileo fibers; these values give $m_T T_c T_c = 0.696$. If the cladding material is removed from the

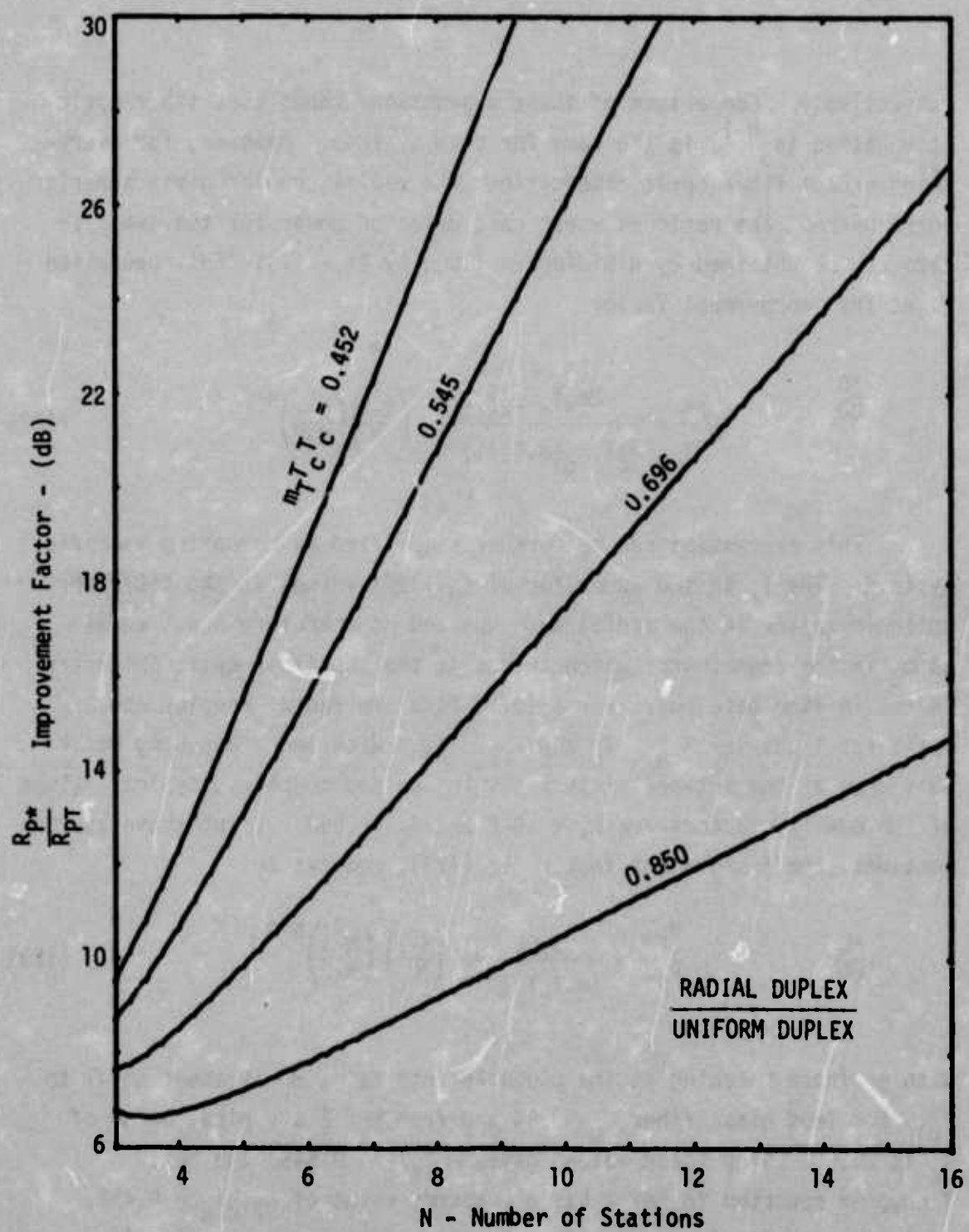

Figure 17. Worst Case Power Improvement Factor
Radial Duplex/Uniform Duplex

fibers in the termination region then $R_a = 1$, $G = .85$; this gives $m_T T_c T_c = 0.85$. The values of the quantity $m_T T_c T_c$ are recorded in Table I.

Table I. Typical Values of $m_T T_c T_c$

$m_T T_c T_c$	Remarks
0.452	Best measurement, Ref. 2
0.545	Theory, index matching in coupler no index matching at plugable interface
0.696	Theory, full index matching
0.850	Theory, full index matching and cladding removed at termination

Figure 17 is a plot of the worst case power improvement ratio of Eq (123) for the four values of $m_T T_c T_c$ shown in Table I. Since Eq (123) and Figure 17 are independent of fiber optic attenuation, the improvement ratio is independent of the type of fiber optic bundle used and the length of the bus as long as these parameters are the same for both systems.

From Figure 17 the improvement factor for an 8 station bus when $m_T T_c T_c = 0.452$ is about 26dB. This means that for the best measured T coupler performance[2], the worst case power ratio in the radial bus is 400 times (26dB) higher than the worst case power ratio in the in-line data bus.

The improvement in dynamic range of the radial system over the uniform duplex can be obtained by dividing Eq (118) by the value of D_{R*}; this will give the improvement as a number greater than 1. If neutral density filters are used to give equal attenuation in the side arms then D_{R*} will have a value of about 2.0 and the dynamic range improvement is

$$\frac{UD}{*D} \qquad \frac{D_{RT}}{D_{R*}} = \frac{1}{2}\left[\frac{1}{a_o m_T T_c T_c}\left(\frac{N-1}{N-2}\right)\right]^{N-2} \tag{124}$$

The average spacing between stations in avionics data buses is about 3m. Table II shows different types fiber optic bundles and the value of a_o corresponding to a length of 3m. Using $a_o = 0.748$ and $m_T T_c T_c = 0.452$ in Eq (124), the dynamic range improvement for an 8 station bus is 844 or 29.26dB. Thus, comparing the uniform duplex bus and the radial duplex bus, the latter gives a significant improvement in both worst case fractional power ratio and dynamic range. Also, the radial bus only requires one passive coupler for the entire system whereas the uniform duplex bus requires a coupler of comparable complexity for each station.

As previously discussed, reliability considerations may dictate that the radial coupler not be located half way between the two most distant stations in the aircraft. In this case, the maximum transmission path in the duplex bus will be somewhat longer than in the uniform in-line bus. If neutral density filters are used to equalize the attenuation of the transmission paths in the radial data bus, then the dynamic range ratio of Eq (124) will be unaffected by the placement of the radial coupler. However, the worst case power improvement ratio in Eq (122) is sensitive to the radial coupler placement. For the 60ft bus discussed in Section III.B., the radial system would have 8dB more attenuation than if the radial coupler were centrally located.

Thus, the worst case power improvement ratio, Eq (123), for an 8 station bus would be 18dB rather than the 26dB value shown by Figure 17. This result assumes that there are no problems in routing the fiber optic cables in the in-line system. In general, the worst case power improvement ratio in Eq (123) should be multiplied by the maximum attenuation ratio for the two systems when those attenuation values are different for any reason; the dynamic range improvement ratio is not affected by differences in maximum attenuation.

A comparison of the worst case fractional power ratio of the radial duplex bus and the tapered duplex bus is obtained by dividing Eq (105) by Eq (120)

$$\frac{*D}{TD} \qquad \frac{R_{P*}}{R_{PT}} = \frac{m_* T_c T_{fk} T_{fN}}{N m_C^2 (m_T T_c T_c)^{N-2}} \frac{1-(a_o m_T T_c)^{N-1}}{1-(a_o m_T T_c)} \qquad (125)$$

The term T_c in the numerator arises in the radial bus at the LED/fiber optic station interface and is therefore about equal to m_C in the denominator which arises at the LED/fiber optic interface in the T coupler.

Table II. Fiber Optic Bundle Average Attenuation Vs Type

Fiber Optic Bundle Type	Loss Factor dB/m	dB	a_o -
Galileo	0.60	1.8	0.660
Rank	0.42	1.26	0.748
Pilkington	0.10	.30	0.935
Corning	0.03	.09	0.979

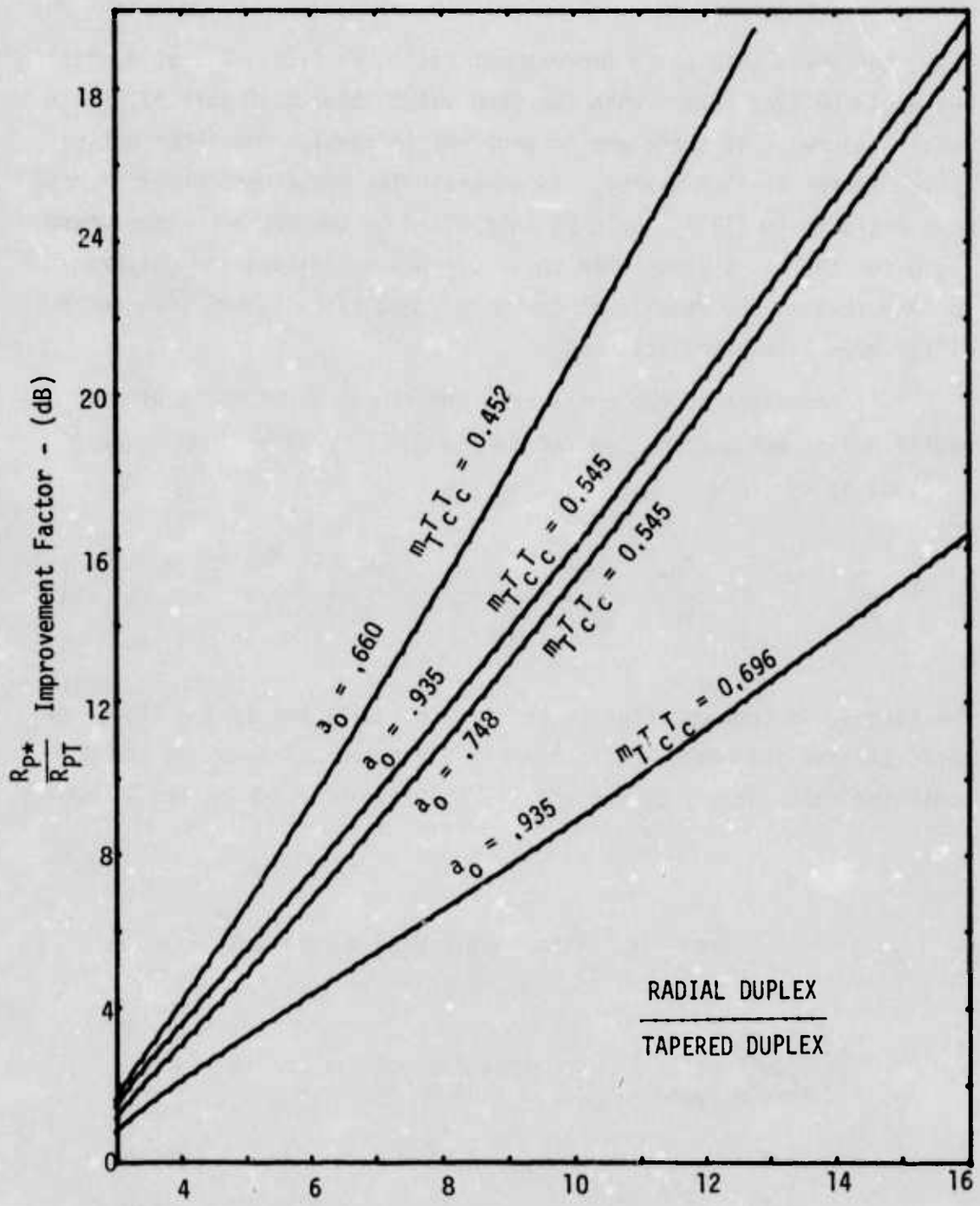

Figure 18. Worst Case Power Improvement Factor
Radial Duplex/Tapered Duplex

For a solid side arm radial coupler and a split-rod T coupler $T_{tk} \simeq T_c$ and $T_{fN} \simeq T_c$. With index matching materials used at the internal interfaces in the two couplers, typical values of the quality factors are $m_* = .848$ and $m_c = .558$. Using these approximations, the improvement factor, Eq (125), reduces to

$$\frac{*D}{TD} \qquad \frac{R_{p*}}{R_{PT}} = \frac{1.52}{N}\left[\frac{1-(a_o m_T T_c T_c)^{N-1}}{1-(a_o m_T T_c T_c)}\right]\left[\frac{1}{m_T T_c T_c}\right]^{N-2} \tag{126}$$

Figure 18 is a plot of the worst case power improvement ratio of Eq (126) for the indicated parameter values taken from Tables I and II.

From Figure 18 the improvement factor for an 8 station bus when $m_c T_c T_c = 0.452$ and $a_o = 0.660$ is about 15dB. Thus, the worst case power ratio in the radial bus is 32 times (15dB) higher than the worst case power ratio in the tapered in-line data bus. The tapered duplex and radial duplex structures provide comparable and desirably low values of dynamic range.

Comparing a tapered duplex bus to a radial duplex bus, the dynamic range and total amount of fiber bundle are comparable. The principle advantages of the radial systems are the worst case fractional power ratio and ease of fabrication. The fabrication advantage is considerable because the single radial coupler is much easier to build than the N couplers of N/2 different designs required in the tapered duplex bus. Also, the fiber optic bundles in the radial system are all the same diameter whereas the tapered duplex bus requires N/2 different fiber bundle diameters.

If reliability considerations dictate that the radial coupler be located other than centrally, then the worst case power improvement ratio given by Eq (125) must be modified by the ratio of maximum attenuation of the two data bus systems. For the 60 foot example discussed in Section III.B., the maximum attenuation ratio is 8dB. In this case,

the improvement ratio is 7dB rather than the 15dB value given by Figure 18. This result assumes that there are no problems with routing the fiber optic cables in the in-line tapered bus that would add to its total attenuation.

For every performance factor considered in this comparison

- worst case detector power ratio,
- dynamic range,
- quantity of fiber optic bundle,
- ease of fabrication, and
- battle damage immunity,

the radial data bus is equal or superior to the in-line data bus. The only apparent disadvantage to the radial system is the difficulty of adding stations after the system is built. In this regard, the radial system is inferior to the uniform duplex configuration but superior to a tapered duplex design. Stations can always be added to the short arms on the radial system by replacing all or part of the neutral density filter attenuation with a power divider (modified T coupler) to split the available power between two or more lines. In general, however, the addition of widely separated or remote stations to a radial system will require a new radial coupler.

E. SCRAMBLER DESIGN

Passive couplers for both in-line and radial data buses require the use of scramblers. Figure 15 shows a T coupler for use in a uniform duplex bus (in-line) which requires two scramblers. Figure 14 shows a radial coupler for use in a radial bus which requires one scrambler. The purpose of a scrambler in a passive

coupler is to accept light from a small number of fibers and spread that light as uniformly as possible over the area of the scrambler without altering the axial angular distribution of the light. This function can be performed by an optically smooth glass rod that is mirrored on the external surface but not on the ends as shown in Figure 19. The optical function of a scrambler is much the same as that of each fiber in a fiber optic bundle.

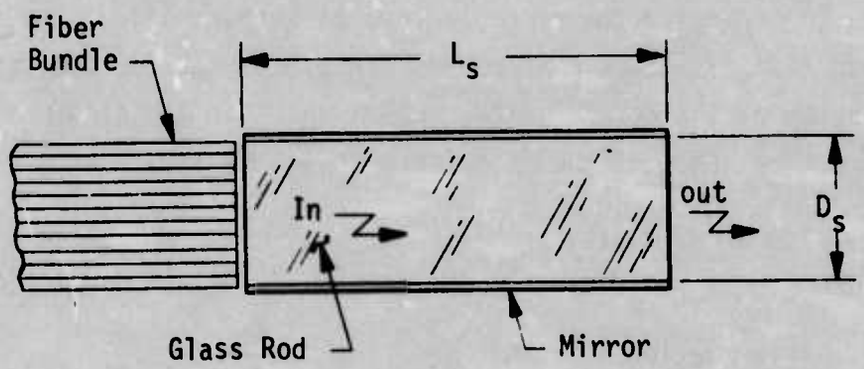

Figure 19. Scrambler Rod

As in the case of the glass fiber, the mirror on the external surface should be provided by total internal reflection. The total internal reflection phenomenon produces a 100% reflective mirror while a metal mirror reflects only 97-98% of the incident light. This 100% reflective mirror can be achieved by using a high-index glass rod similar to the core glass of the fibers and cladding it with a lower index material. An all-glass rod with a high-index core and low-index cladding can be used for the scrambler. However, it is difficult to obtain a clad glass rod with adequate precision of the core diameter. It is usually more expedient to use a low-index silicone or epoxy resin for the cladding layer. This makes it possible to grind and polish the

glass rod to close mechanical tolerances and provide a good optical quality finish on the external surface of the rod. The plastic cladding layer can also serve as the mounting medium which properly positions the scrambler rod and anchors it to the coupler housing. Many useful plastic materials have greater optical attenuation than glass. However, the length of a scrambler is not more than a few inches and the resulting loss due to absorption in the cladding layer is negligible.

In order for the scrambler rod to support all of the rays coupled into it, there must be an adequate change in index of refraction at the core/cladding interface. The limiting numerical aperture, NA_s, of the acceptance cone of a scrambler is

$$NA_s = (n_2^2 - n_3^2)^{\frac{1}{2}} \tag{127}$$

where n_2 is the index of the core, and

n_3 is the index of the cladding.

Numerical aperture is defined by

$$NA = n_1 \sin\theta_1 \tag{128}$$

where θ_1 is the half angle of any ray measured in the outside medium having an index of n_1. When the external medium is air, then $n_1 = 1$ and NA_s specifies the maximum half angle of the launch cone. Due to the form of Eq (128) and Snells law,[1] the value of NA is the same inside and outside the scrambler

$$NA = n_1 \sin\theta_1 = n_2 \sin\theta_2 \tag{129}$$

In some data bus systems, the NA_ϕ of the light input to the scrambler will be known and Eq (127) can be used to determine the minimum index difference in the scrambler. In many cases it will be adequate to make the NA_S of the scrambler equal to the NA of the fiber bundle being used. This will insure that the scrambler will support any ray that will propagate on the fiber optic bundle.

The length and diameter of the scrambler rod are also important parameters in the design and construction of passive couplers. This is true for both radial and T couplers. The scrambler should be long enough that light exiting any individual fiber in the input bundle spreads out to fill the entire bundle at the exit surface. Ideally, the scrambler should be short enough that no ray reflects from the clad surface more than one time. Figure 20 shows a scrambler for a radial coupler. In this case, the length, L_s, is 2 times the physical length of the rod due to the mirror at the open end of the scrambler. The dashed lines indicate the mirror image of the radial coupler in the end mirror. For a T coupler, the physical length of the scrambler rod is the full length, L_s. The diameter of a scrambler must be equal to the diameter of the composite fiber optic bundle used in the data bus. The mirror over the flat end of the scrambler should ideally be a multilayer dielectric coating similar to that used on laser mirrors. Again, the dielectric mirror will produce a higher reflectivity ($\sim$ 100%) than can be achieved with a metal mirror. Figure 19 shows optical output from two typical fibers -- one at the center and one at the edge of the composite bundle. The optimum length is seen to be dependent on the $NA\phi$ of the light from the optical fibers. From Figure 19 the best scrambler length is about

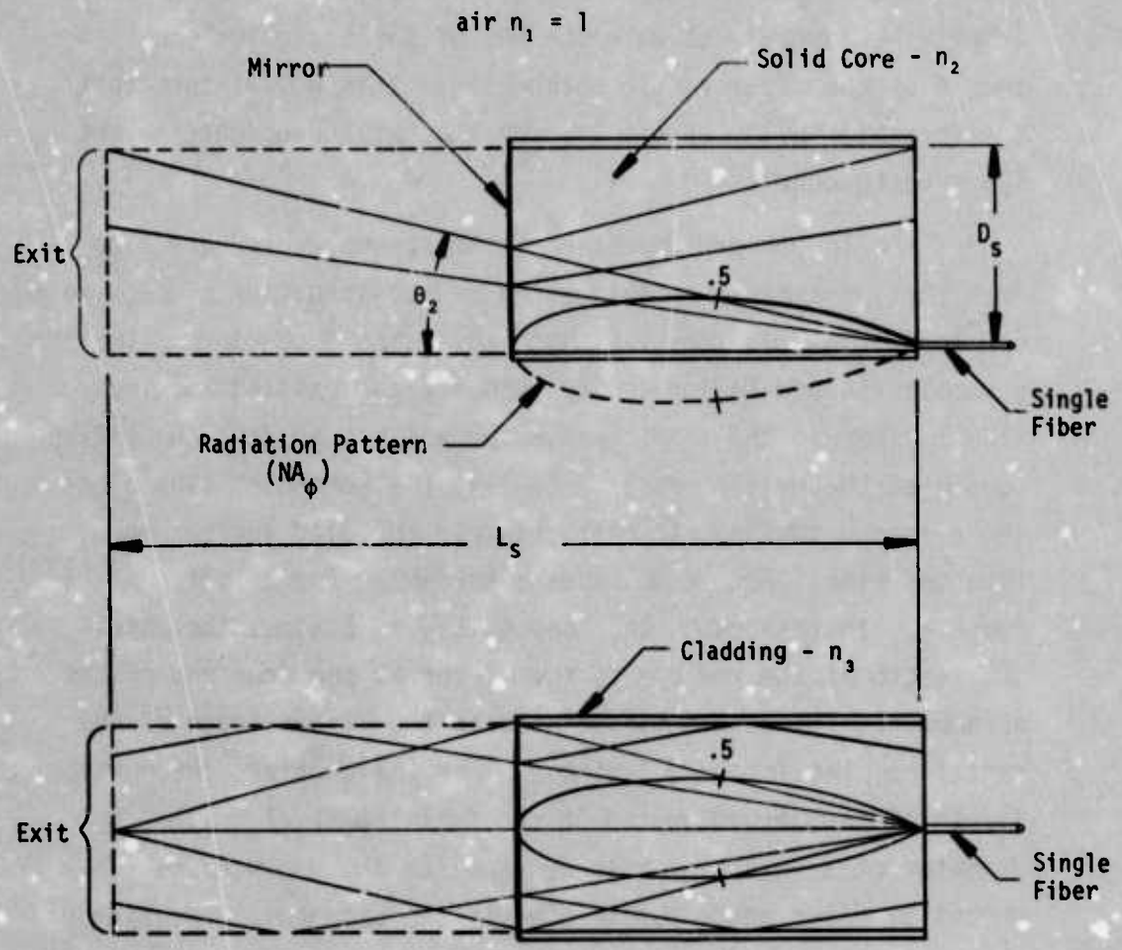

Figure 20. Scrambler Rod Operation

$$L_s = \frac{D_s}{\tan\theta_2} \tag{130}$$

The angle θ_2 should be selected such that

$$NA_\phi = n_2 \sin\theta_2 \tag{131}$$

then

$$\cos\theta_2 = (1-\sin^2\theta_2)^{\frac{1}{2}}$$

$$\cos\theta_2 = \frac{1}{n_2}(n_2^2 - NA_\phi^2)^{\frac{1}{2}} \tag{132}$$

and

$$\tan\theta_2 = \frac{\sin\theta_2}{\cos\theta_2} = \frac{NA_\phi}{(n_2^2 - NA_\phi^2)^{\frac{1}{2}}} \tag{133}$$

Substituting Eq (133) into Eq (130) gives the desired relationship between L_s and D_s in terms of the angular distribution of the light entering the scrambler.

$$L_s = \frac{(n_2^2 - NA_\phi^2)^{\frac{1}{2}}}{NA_\phi} D_s \tag{134}$$

For the equilibrium angular distribution of long Galileo fiber bundles (See Section IV B)

$$NA_\phi = .24 \tag{135}$$

For

$$n_2 = 1.625 \tag{136}$$

Eq (134) becomes

$$L_s = 6.70\ D_s \quad \text{(Galileo)} \tag{137}$$

If Corning low loss fibers are used the typical parameters are

$$NA_\phi = 0.14$$
$$n_2 = 1.5 \tag{138}$$

and Eq (134) becomes

$$L_s = 10.7\ D_s \quad \text{(Corning)} \tag{139}$$

A comparison of Eqs (137) and (139) shows the effects of NA_ϕ on scrambler length. If $D_s = 0.187$ in the T coupler scrambler for the Galileo fiber has a length of 1.25in whereas L_s for the Corning fiber is 2.0in. For radial couplers these lengths should be halved.

Equation (134) results from a very simple model of the scrambler and for that reason should be considered only as an approximate expression. In order for Eq (134) to give a useful result, it is necessary to properly interpret the value of NA_ϕ. Figure 20 implies that the half angle of the launch cone is associated with the half power point of the radiation pattern. This is not a valid assumption for all radiation patterns. A more detailed analysis that includes the shape of the radiant intensity distribution at the exit end of the fiber optic bundle could give the optimum scrambler length for any given application.

Figure 20 and the preceding discussion represent the scrambler as having a circular cross section. A circular scrambler has many advantages such as ease of fabrication, good mechanical tolerance, and ease of alignment. However, the circular scrambler inherently gives nonuniform power distribution at the exit face because of skew rays that can not be shown in the axial plane representation shown in Figure 20. Both skew rays and meridional rays are shown in Figure 21 along with photographs showing the uniformity of power distribution over the end of a cylindrical scrambler rod. The light from the on-axis fiber shown in the upper part of Figure 21 is uniformly distributed because all rays are meridional. Off-axis light introduced at the edge of the scrambler is not uniformly distributed because many of the rays make a small angle with the clad surface. These small angle rays (skew rays) describe a helical trajectory made up of many reflections that keep the ray always close to the outside surface of the scrambler. Some of the off-axis light is spread over the end of the scrambler; however, most of it stays near the edge. Thus, a scrambler with circular cross section tends to give nonuniform power distribution with the highest power density at the edge of the scrambler and the lowest power density in the center. Even with the noted deficiencies in the model, Eq (134) gives a good approximation for the best scrambler length.

In a radial coupler, uniform power distribution can be achieved by uniformly distributing the fibers from the various radial arms over the entire area of the composite bundle. Another approach uses a hollow glass tube for the scrambler[13] so that all fibers are near the edge of the scrambler. Reference 2 proposes the use of rectangular scramblers as shown in Figure 22. The four orthogonal faces of the rectangular rod act as plane mirrors very much like a child's kaleidoscope. Each point on the exit end of

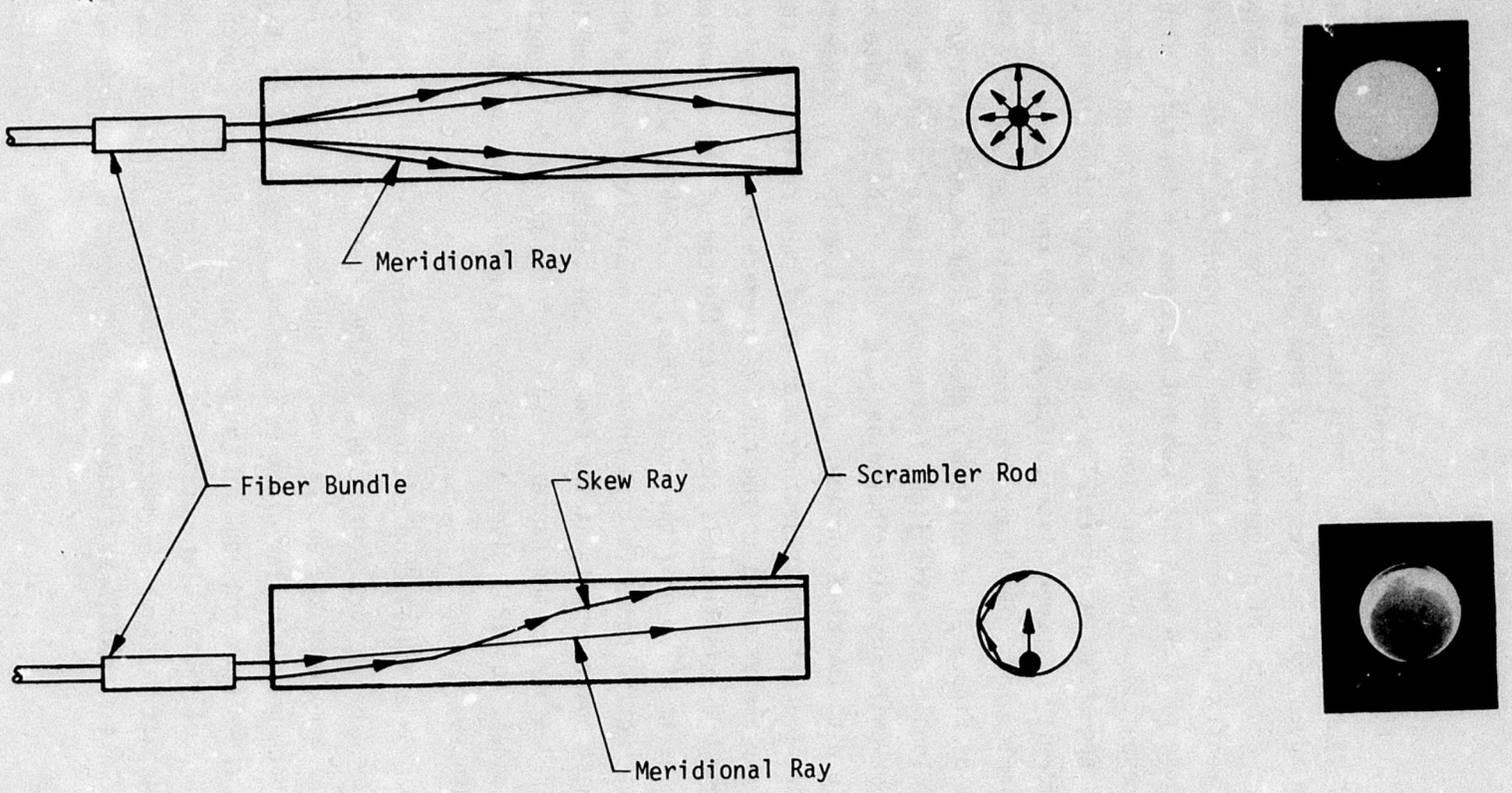

Figure 21. Power Distribution in a Cylindrical Scrambler Rod

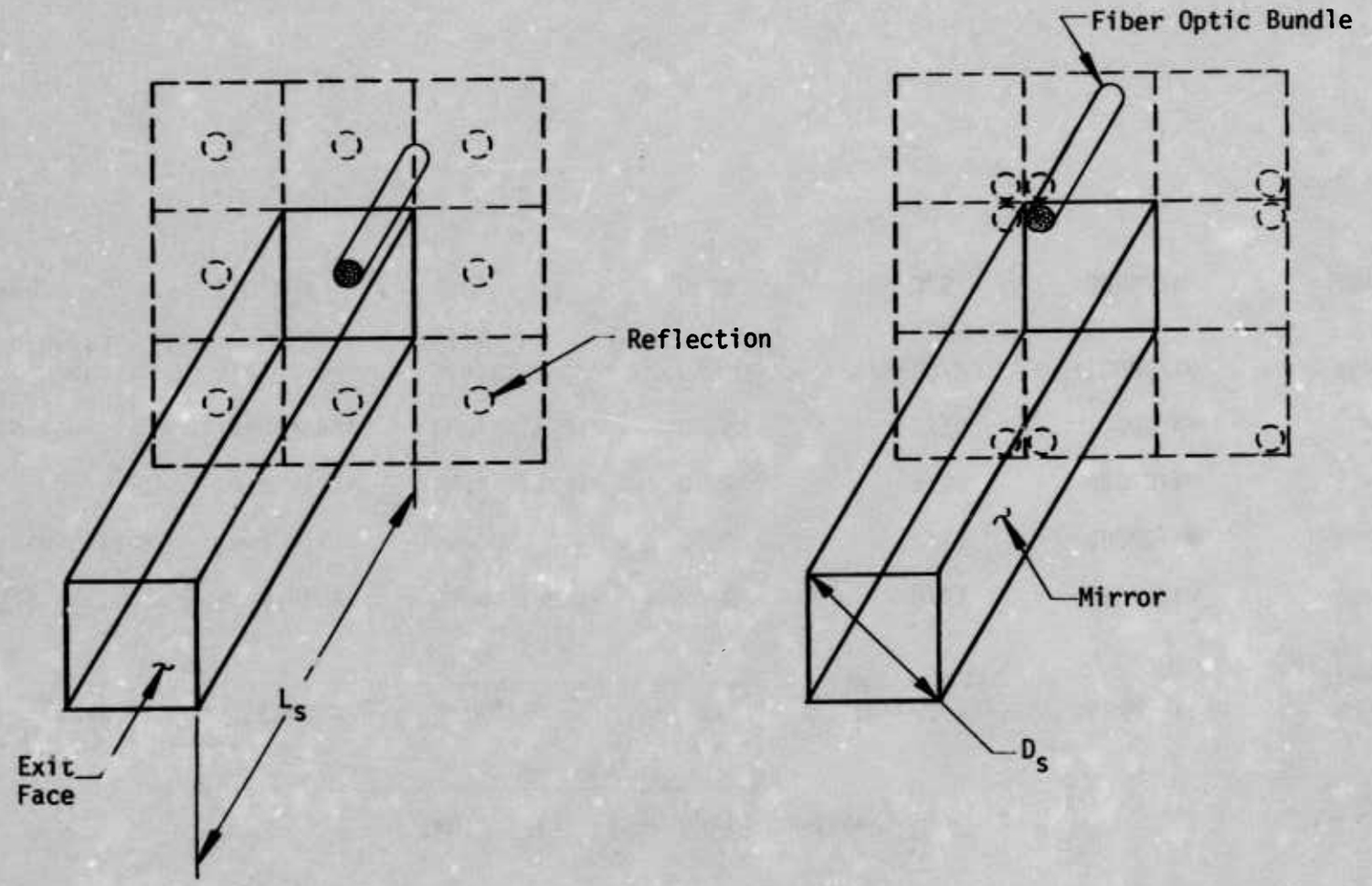

Figure 22. Power Distribution in a Rectangular Scrambler Rod

Table III. Fiber Optic Bundles

Manufacturer	Core	Clad	NA	Core/Fiber Dia. Ratio	Attenuation	Bundle Diameter
Galileo	lead glass	borosilicate	0.66	19/21	<590dB/km	46mil
American Optical	lead glass	borosilicate	0.66	17/19	<400dB/km	46mil
Rank	lead glass	borosilicate	0.58	9/10	<420dB/km	31mil
Pilkington	lead glass	borosilicate	0.50	17/20	<100dB/km	23mil
Valtec, Schott (and others)	SiO_2	plastic (>125°C)	0.3-0.4	4/5-20/23	<100dB/km	25mil
Corning	SiO_2:Ge	SiO_2	0.14	3/5	<30dB/km	25mil

the scrambler sees the input fiber and 8 virtual images (reflections) for all positions of the input fiber. Figure 22 shows a centrally located input fiber and its reflections on the left and an off-center input fiber and its reflections on the right. Light from each input fiber is distributed uniformly over the exit face of the scrambler.

Equation (134) gives a good length for a rectangular scrambler rod if D_s is interpreted as the diagonal of the rectangular cross section; again, NA_ϕ must be properly interpreted to achieve the best result.

The key parameters of the fiber optic bundle which have the greatest impact on the design of passive couplers are the NA_ϕ and bundle diameter. The effect of these two parameters on the required length of the scrambler rod is shown in Eqs (137) and (139). There are various types of fiber optic bundles that are commercially available or will be available before the end of 1975. The characteristics of several of these fiber optic bundles are shown in Table III. In order for a scrambler rod to give the same performance wnether the light reaching it has traversed a long fiber bundle or a snort fiber bundle, the NA_ϕ must be the same in all parts of the data bus. For Galileo fiber optic bundles, Section IV B shows that both the angular transfer characteristic and the exit end radiation pattern (NA_ϕ) change as a function of length. This effect is produced by scattering and mode mixing in the fibers. Due to the large amount of scattering in the Galileo fiber, the equilibrium value of $NA_\phi = 0.24$ is reached in about 150ft. Therefore, the use of Galileo fiber in a 100ft data bus requires that the scrambler rods and LEDs both have radiation patterns characterized by $NA_\phi = 0.24$. This is the NA_ϕ of the SPX 1527 LED coupled to the Galileo fiber optic bundle with a lens as shown in Section IV.F.

The Pilkington fiber and plastic clad-fused silica fiber both have attenuation of less than 100dB/km and most of the attenuation

at 900nm wavelength is due to absorption in the core glass. Thus, these fiber types have very weak scattering; and at a length of 100ft are expected to preserve the NA_ϕ of the LED at the exit end of the fiber. The scrambler rods to be used with these two types of fiber optic bundle should be designed for the NA_ϕ of the LED. The SPX 1775 is an edge emitter LED developed for the Naval Avionics Facility at Indianapolis under contract N00163-73-C-0544. This LED is designed to couple directly to small diameter fiber optic bundles without a lens and has a numeric aperture of $NA_\phi = 0.21$.

The Corning fiber also has very weak scattering; at 100ft length, it is expected to preserve the launch angles at the exit end of the fiber. In this case, the fiber bundle has a lower value of NA than any available LED. Therefore, a data bus built with Corning low-loss fiber optic bundles will require scrambler rods designed for $NA_\phi = 0.14$ regardless of what LED is used.

As shown in Appendix V the plastic clad-fused silica core fibers have the best radiation resistance of any available fiber optic bundles. The maximum operating temperature for the plastic clad-fused silica fibers will be greater than 125°C. The limited data available suggests that these plastic clad-fused silica fiber bundles will be the dominant type of fiber optic bundle used in optoelectronic data transmission and data bus applications for lengths up to 300ft. Bell Northern Research of Ottawa Canada and a number of other companies are developing low-loss, graded index single fibers for long distance optical transmission ($\geq$1.0km); because of the intended application, these graded index fibers are usually not available in bundles. These fibers have NA = 0.25 but the grading of the index in the core provides a self focusing action that dramatically reduces the pulse spreading and increases the bandwidth. It is expected that in the future bundles of 19 or more graded index fibers will find application in high-speed data buses ($\geq$100Mbit/s).

The requirement for constant NA_ϕ in all parts of a system is peculiar to a data bus and is necessary to insure that all scramblers give the same performance. In point-to-point data transmission, the launch cone should have the smallest possible value of NA_ϕ because small angle rays have lower pulse spreading and attenuation than wide angle rays. The transmission characteristic of Galileo fiber optic bundles as a function of launch angle and bundle length is shown in Section IV.F.

SECTION IV

OPTOELECTRONIC COMPONENTS

This section presents the results of evaluation of various optoelectronic components including

- photodiodes
- avalanche photodiodes
- LEDs
- fiber optic bundles

Two discrete component preamps of the type described in Section II.C were constructed for use in testing the above components. Evaluation of these preamps is presented; their performance is compared to a commercially available hybrid preamp. The LED evaluation includes the use of the speed-up techniques described in Section II.G.

A. PREAMP PERFORMANCE

Figure 23 shows the schematic of a high-frequency preamp constructed on this program for use in component testing. The first stage of this amplifier uses the basic design philosophy presented in Section II.C; the second stage is an emitter-coupled driver amplifier to interface the preamp to an oscilloscope. Considerable difficulty was encountered in the design and construction of this circuit. This difficulty was primarily brought about by the high input capacitance of the Tektronic oscilloscope (20-25pF). All attempts at driving the oscilloscope with an emitter follower resulted in oscillations at frequencies between 100MHz and 2GHz. This high-frequency instability problem was finally overcome by use of the non-inverting emitter-coupled driver stage shown in Figure 23. This scope drive has a voltage gain of one and a bandwidth of about 300MHz (t_r = 1.2ns, 10-90%).

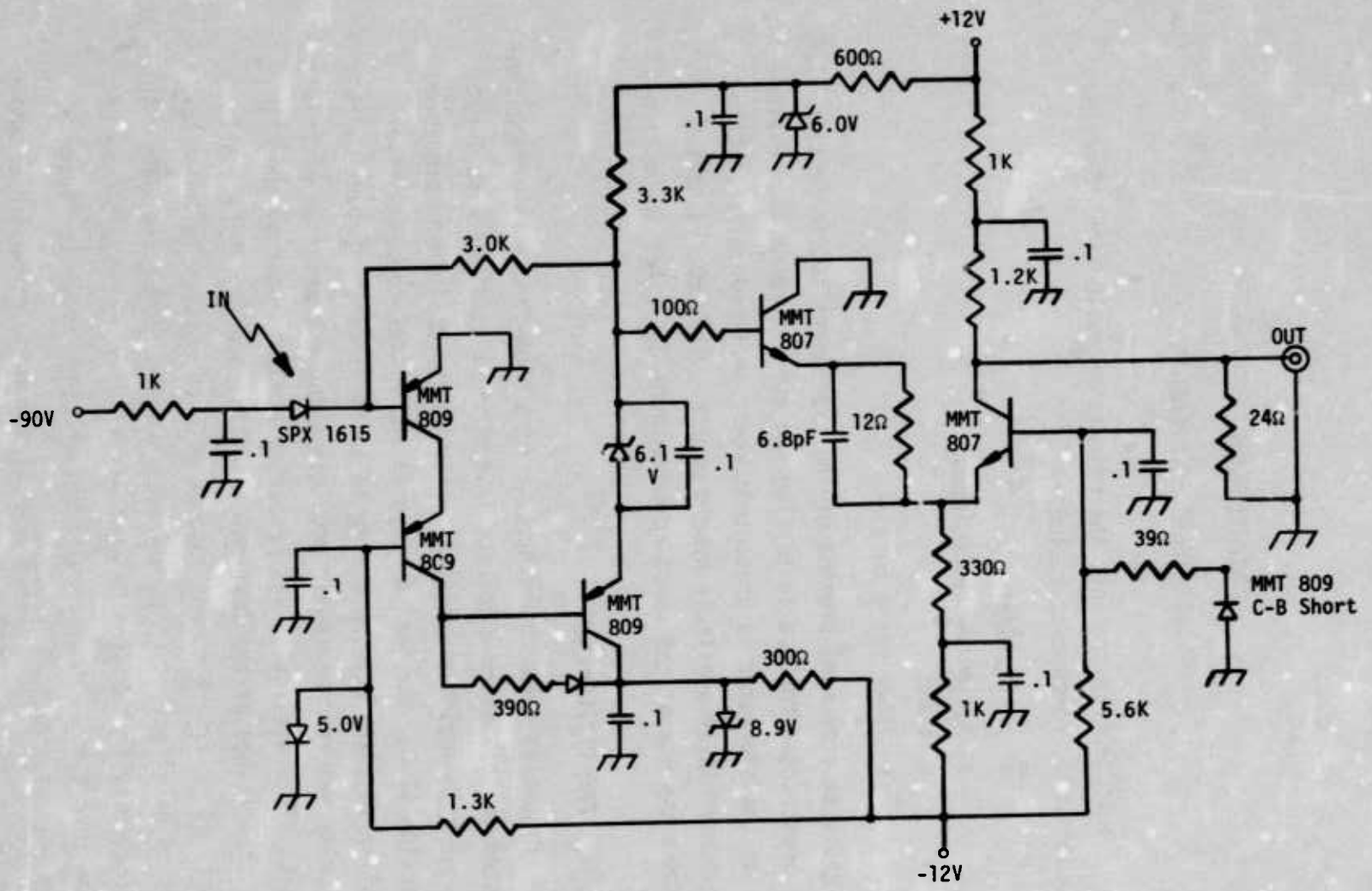

Figure 23. High-Frequency Preamp/Scope Driver

The preamp portion of Figure 23 uses Motorola MMT 809 transistors. These pnp transistors have f_T=2.5GHz at I_E=1.0mA and V_{CE}=1.0V. While it is difficult to tell from the data sheet, the MMT 809, being a pnp device, should have a lower value of r'_b than the MMT 807 transistor (npn) that is used in other versions of the preamp. The preamp alone has a 3dB bandwidth of about 175MHz (t_r = 2ns, 10-90%).

When biased at 90V the SPX 1615 photodiode used with the preamp has a 10-90% rise time of about 1.0ns (see Section IV.E) and the Tektronix 454 oscilloscope used with the amplifier has a specified cutoff frequency of 150MHz or greater ($t_r \leq$ 2.4ns, 10-90%). Measurements made with this photodiode/preamp/postamp/oscilloscope combination give a composite rise time (10-90%) of 3ns which corresponds to a cutoff frequency of about 117MHz. Since this amplifier has been used primarily for speed of response testing, no direct measurement of the equivalent input noise was made. However, the noise level observed on the oscilloscope trace is consistent with the value calculated for this specific circuit; i_{nT} = 0.1μA, e_{on} = 300μV.

If the oscilloscope is removed from the circuit, the resulting combination of photodiode/preamp/postamp should have a rise time of about 2.8ns and a 3dB bandwidth of 125MHz. From Eq (5), the circuit of Figure 23 is an adequate receiver for data rates up to 218M bit/s.

Figure 24 shows another discrete component preamp that was constructed and evaluated to offer a direct comparison to the TIXL151 hybrid preamp. This amplifier uses npn MMT 807 transistors in the preamp and pnp MMT 809 transistors in the postamp. When driving the Tektronix 454 oscilloscope input, the 3dB bandwidth is 61MHz with no peaking observed at any frequency. The measured transimpedance for this circuit is

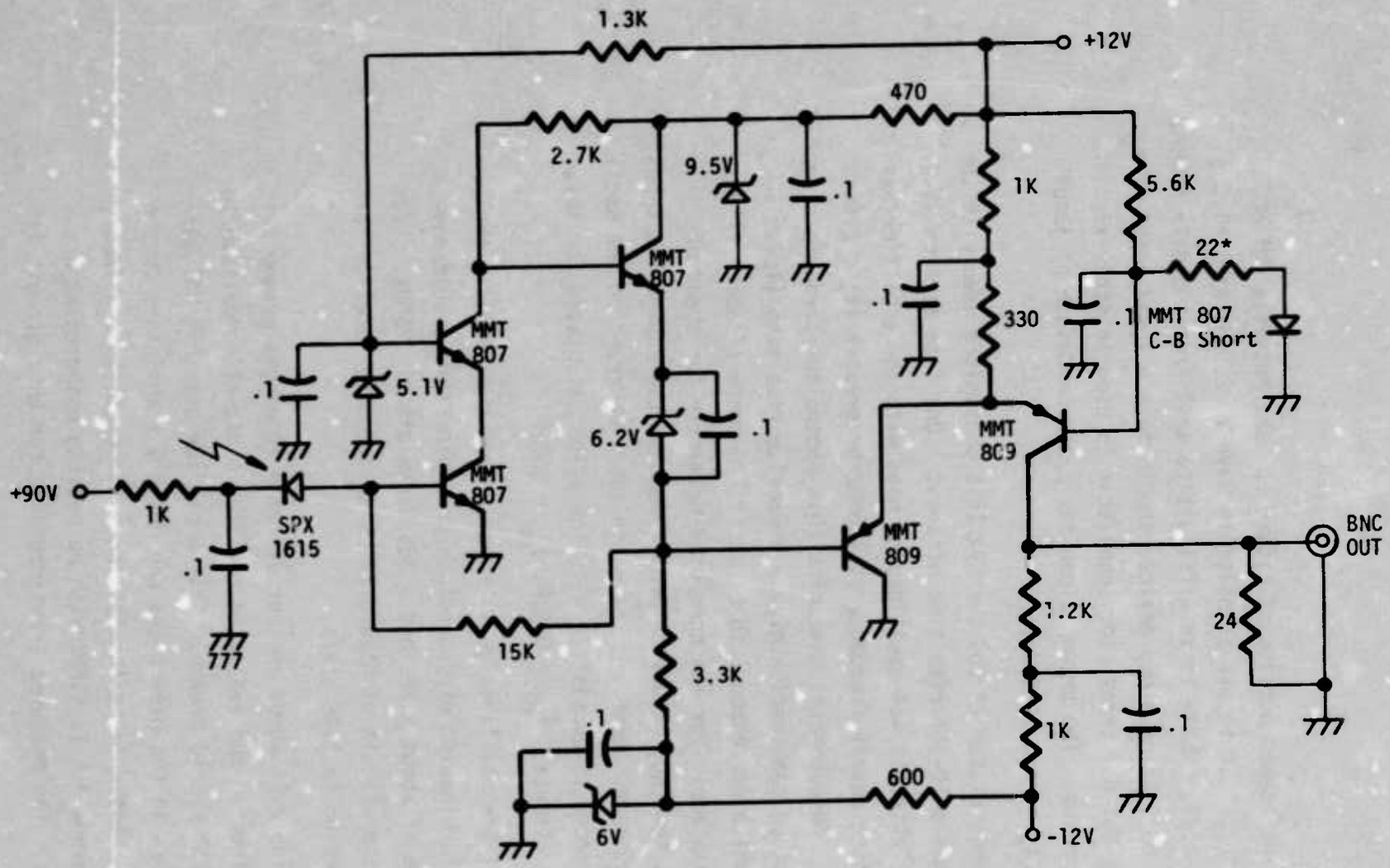

Figure 24. Intermediate Bandwidth Preamp

16.8kΩ at 4MHz for an output voltage swing of 80mV (peak to peak). Noise measurements were made on this amplifier with the oscilloscope using the tangential noise measurement technique[14]. This measurement technique uses an oscilloscope to determine the rms value of the noise by displaying the noise on both dual trace inputs of the oscilloscope. The two noise traces are separated and then brought together until the dark band disappears between the two traces. The separation of the base lines of the two traces under these conditions is equal to two times the rms value of the noise. This tangential noise measurement was implemented by inserting a Hewlett-Packard 11549A power divider and a Hewlett-Packard 461A amplifier between the preamp and the two oscilloscope inputs. This power divider is a broad band resistive device that attenuates the input signal power by 3dB and then splits it equally between the two output ports. The voltage at each output port is therefore one-half of the voltage at the input port. When this power divider is used, the factor of two voltage attenuation compensates for the 2 x rms factor in the tangential noise measurement with the result that the trace separation is equal to the rms value of the noise at the input of the power divider. The tangential noise measurement technique is ideally suited to amplifier and detector comparisons of this type because it allows the bandwidth, rise time, and noise to be measured under the same conditions. Any bandwidth limitations of the oscilloscope are included equally in all measurements.

When the HP 461A amplifier and HP 11549A power divider are inserted in the receiver system the 3dB bandwidth drops from 61MHz to 54MHz. The transient response of the combined system is well behaved. The tangential noise measurement gives an rms output noise voltage of

$$e_{on} = 400\mu V \tag{140}$$

This value is 20% less than the value of 480μV calculated from Eq (33) for f_e = 54MHz. Discrepancy of this magnitude is expected because the complete amplifier chain including the oscilloscope used in this test is not the two pole network assumed in the derivation of Eq (33). The transimpedance of 16.8kΩ used with Eq (140) gives an equivalent input noise current of

$$i_{nT} = 23.8nA \tag{141}$$

This value of equivalent input noise current compares favorably to the value of 27.7nA calculated from Eq (20).

The TIXL151 is a shunt feedback hybrid preamp manufactured by Texas Instruments, Incorporated. The amplifier is packaged in a TO-5 header and operates from a single power supply voltage. For best operation, the photodiode should be biased from a negative supply with the cathode of the photodiode connected to the preamp input. This causes the preamp output voltage to move in a positive sense for increasing light on the photodiode. The TIXL151 driving the Tektronix 454 oscilloscope (50Ω termination) gave a 3dB bandwidth of 61.5MHz. However, when the HP 461A amplifier and HP 11549A power divider are inserted into the system the 3dB bandwidth drops to 49MHz. For pulse operation, this amplifier/oscilloscope combination shows a 10% overshoot at the beginning and end of the pulse. The transimpedance of the TIXL151was measured to be 4.68kΩ at 4.0MHz for an output voltage swing of 80mV; this is 3.6 times less than the 16.8kΩ measured for the circuit of Figure 24. The tangential noise measurement on the TIXL151 gives an output noise voltage of

$$e_{on} = 140\mu V \tag{142}$$

This is considerably below the value predicted by Eq (33) because of the low transimpedance. Using the transimpedance of 4.68kΩ with Eq (142) gives an input noise current of

$$i_{nT} = 30nA \tag{143}$$

This is 26% higher than the 23.8nA measured for the circuit of Figure 24 and 21% higher than the value calculated from Eq (20) for f_e = 49MHz. Referred to the optical side of the photodiode, the TIXL151 gives about a 1.0dB degradation in S/N compared to the discrete component circuit of Figure 24.

Based on the ∿61MHz measured bandwidth, Eq (5) gives a data rate of 106M bit/s for the TIXL151 and the circuit of Figure 24. The TIXL151 is a good product for use in fiber optic data transmission. The major limitations of the TIXL151 preamp are its low transimpedance and limited flexibility. Because it is a hybrid circuit, the design is fixed and, therefore, is optimum for only one bandwidth. The bandwidth can be reduced with external components but the bias current can not be optimized to produce minimum noise.

Figure 25 is a plot of Eq (20) which is the expected rms noise current for shunt feedback preamps as a function of the 3dB bandwidth, f_e. The figure also shows the measured input noise current for the amplifier of Figure 24 and the TIXL151 The point at 8.6MHz is the measured performance of the preamp used in the Ten-Channel Data Bus Demonstrator[3]. The noise in this amplifier is 20% higher than the expected value. This excess noise is the result of the extra components used in the compression circuitry to increase the dynamic range.

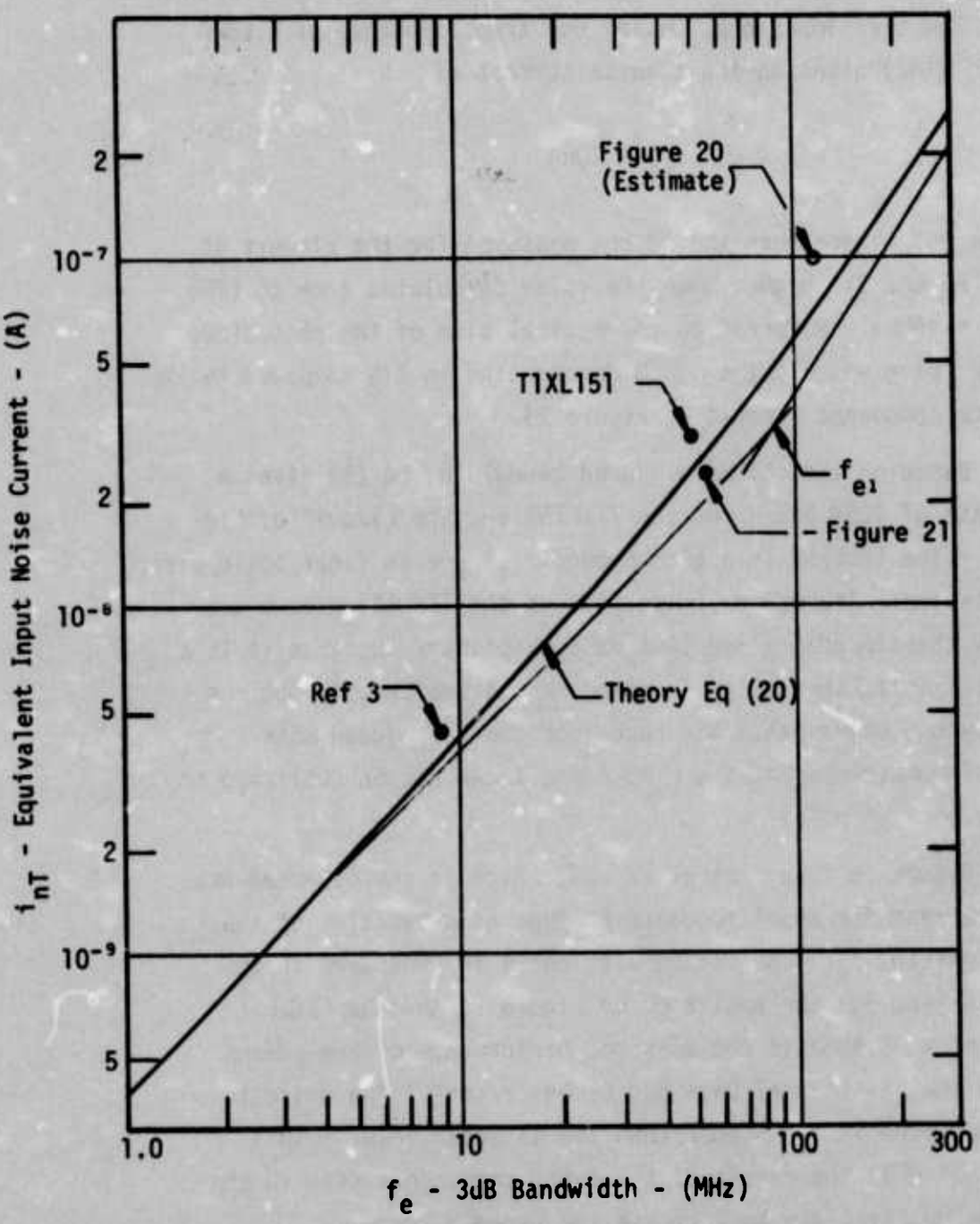

Figure 25. Preamp Noise Summary

B. TEST ADAPTERS

Test adapters have been designed and constructed for use with high-speed photodiodes and edge emitting LEDs. These test adapters are made from standard BNC connectors to ensure compatibility with existing test equipment. Specification drawings for the LED adapter, SPX 1629, and photodiode adapter, SPX 1631 are shown in Appendix IV.

The SPX 1629 LED adapter is designed to accept the stud mounted edge emitting LED (SPX 1527) used in the Ten-Channel Data Bus Demonstrator[3] developed for the Air Force. It provides a good heat sink for the LED while adding only 23pF in parallel with the junction. This unit has a 50Ω resistor in series between the BNC connector and the cathode of the LED. The LED anode is grounded; thus, the BNC center conductor must be driven with a negative voltage to forward bias the LED. The 50Ω resistor serves as a termination for a standard laboratory pulse generator and a current limiting resistor for the LED. A voltage pulse of -12V will result in an LED forward current of about 200mA. The LED adapter is supplied with a removable plastic insert designed to hold a fiber optic bundle terminated with the SPX 1525[3] fiber optic lens.

The SPX 1631 photodiode adapter is designed to accept the SPX 1615 p-i-n photodiode, the SD5425[3] photodiode or any other photodiode in a TO-46 header. This unit has a 1000Ω decoupling resistor and a 0.1μF bypass capacitor on the orange high-voltage lead which projects from the side of the connector. The black and white lead is ground. The orange wire can be biased to ±90V(dc); for use with the SPX 1615 or SD5425 a positive (+) bias should be applied to the orange wire. This unit has a 100Ω load resistor between the BNC center pin and ground. The adapter

with 90V reverse bias on an SPX 1615 or SD5425 contributes a shunt capacitance at the output of 11.6pF. Attached to a Tektronix 454 oscilloscope with an input capacitance of 20pF. the 10-90% rise time of the adapter is about 7.0ns--the 3dB bandwidth is 50MHz. The photodiode adapter is also supplied with a removable plastic insert designed to hold a fiber optic bundle terminated with the SPX 1525[3] fiber optic lens.

Appendix IV also shows the specification drawing for the SPX 1633 fiber optic bundle. This fiber bundle is terminated on each end with the SPX 1523[3] ferrule and the SPX 1525[3] fiber optic lens. The SPX 1633 is compatible with the SPX 1629 LED adapter and the SPX 1631 photodiode adapter. The SPX 1633 uses Galileo 46mil diameter fiber optic bundle and can be made up in any desired length. Most of the component testing performed on this contract used a four foot long SPX 1633. Some of the uses of these units are listed below:

- The LED adapter with the 4 foot fiber optic bundle and a SPX 1527 LED can be driven from a pulse generator to provide a flexible high-speed light source for use in testing detectors and optoelectronic receivers.

- The photodiode adapter with the 4 foot fiber optic bundle and a SPX 1615 photodiode can be connected to the input of an oscilloscope to provide a flexible high-speed photodetector probe for use in evaluating LEDs and opto-electronic transmitters.

- When the two adapters with appropriate LED and detector are coupled to each other through the 4 foot fiber a simple data link is formed that is useful in observing the effect of input current waveform and drive frequency on the received signal current.

- Since the LED and photodiode are easily removed and replaced, both adapters may be used as standard test sockets for evaluating large numbers of LEDs and photodiodes under standard test conditions.

When the SPX 1631 is used with the Tektronix 454 oscilloscope, the low signal level normally makes it necessary to use the 5mV/cm sensitivity range. At this sensitivity the 3dB bandwidth of the oscilloscope is 65MHz. This combines with the 50MHz cutoff of the adapter to give a 36MHz cutoff frequency for the photodiode adapter/oscilloscope combination. The corresponding 10-90% rise time is 9ns.

A fixture was also developed for measuring the modulation transfer of LEDs. A schematic of this circuit is shown in Figure 26. This fixture provides for independent ac and dc bias in the LED so that different modulation depths can be investigated. The test point makes it possible to measure series resistance and series inductance on LEDs. The fixture has a BNC connector to interface with a sine wave signal generator and a plastic insert designed to hold a fiber optic bundle terminated with the SPX 1525 fiber optic lens.

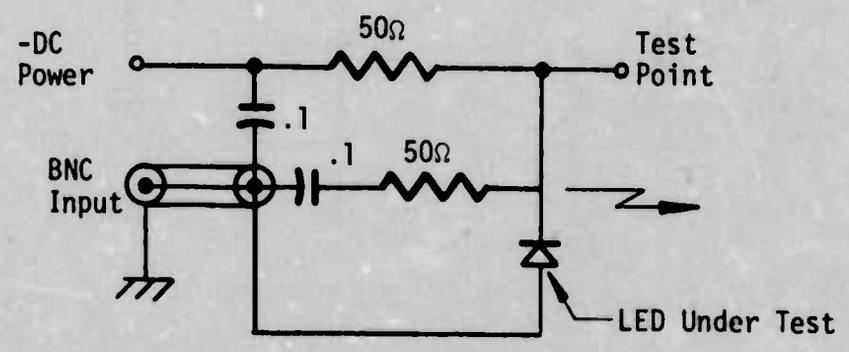

Figure 26. LED Modulation Transfer Fixture

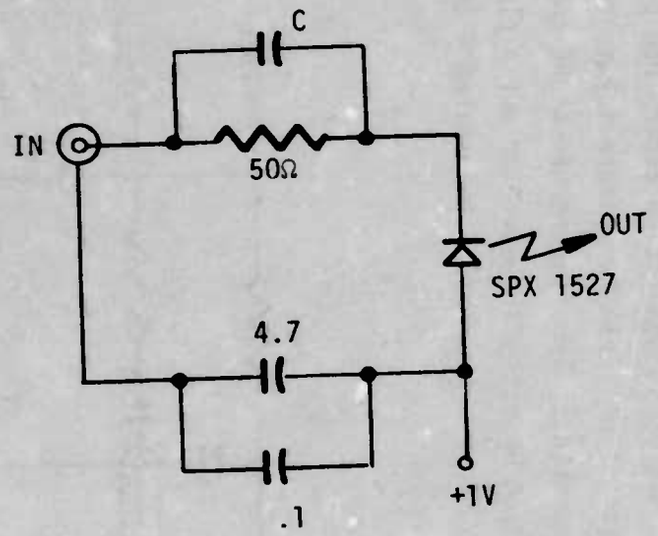

2/1 Overdrive

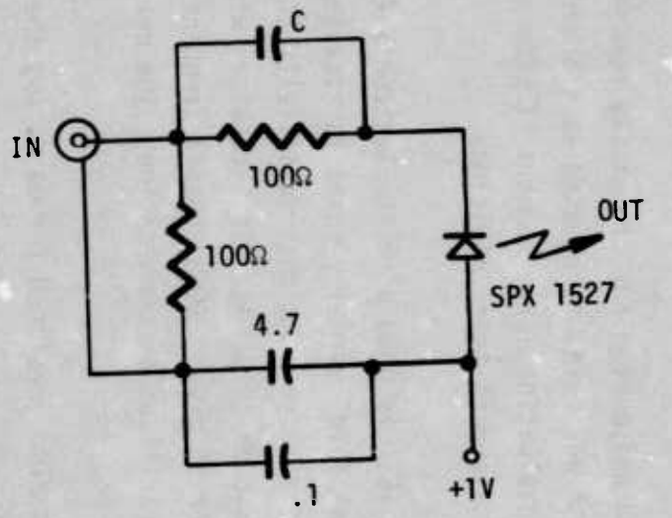

4/1 Overdrive

Figure 27. LED Speed-Up Networks

An LED pulse fixture was constructed to measure the effect of the speed-up technique discussed in Section II.G. This fixture also uses a BNC connector to interface with a pulse generator and a plastic insert to position and hold the fiber optic lens. A terminal is provided to pre-bias the LED to about 1.0V forward bias so that more efficient use can be made of the pulse generator output swing. Figure 27 shows two different versions of the overdrive circuit. Referring to Figure 12, all or part of the resistor R_b is provided by the 50Ω output impedance of the pulse generator. The value of C_a for a particular LED is determined by using the appropriate selection rule; the selection rule for the 2/1 overdrive circuit is given in Eq (84). The 2/1 overdrive circuit should reduce the LED rise time by a factor of about 4; the 4/1 overdrive circuit should reduce the rise time by a factor of 16.

C. LED DRIVER

Figure 28 shows the schematic of a broad-band LED driver circuit developed and evaluated on this program. The circuit was designed to accommodate both analog and pulse modulation. Current feedback is used in the emitters of Q-1 and Q-2 to achieve good linearity. The non-inverting emitter-coupled pair (Q-1 and Q-2) eliminates Miller-effect capacitance at the input and output and gives good response at high frequency. The transistor Q-3 insures a constant current load on the power supply during the complete modulation cycle. The current through Q-3 is selected so that, in normal operation, neither Q-1 or Q-2 will be driven into the saturation region. Under large signal conditions, the driver limits by turning off either Q-1 or Q-2. This is similar to the circuit and operation of ECL integrated circuits. Since saturation is avoided the delay time associated with recovery from saturation is eliminated.

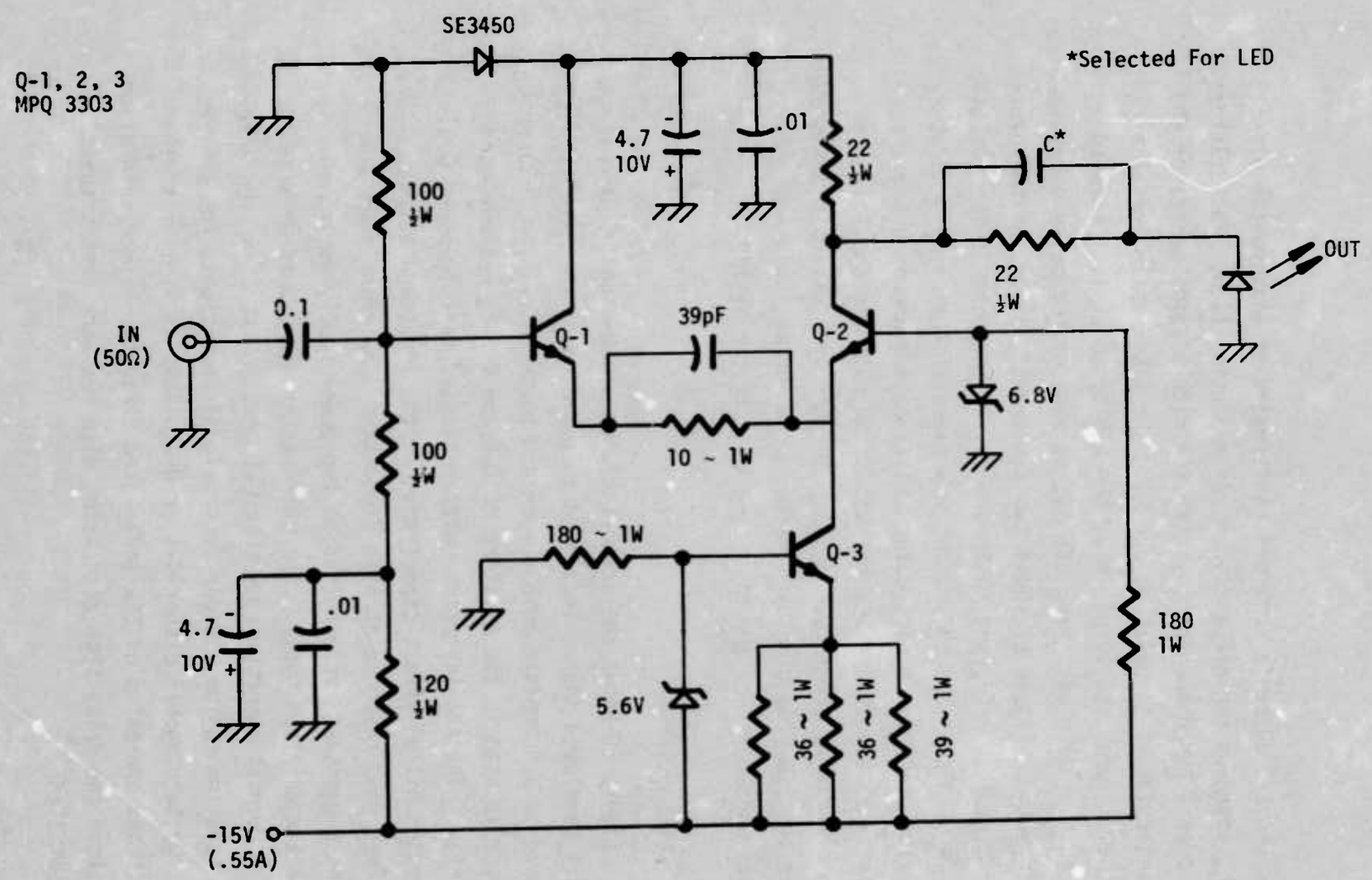

Figure 28. LED Driver Circuit

The LED is driven in the collector of Q-2 with a 2/1 overdrive similar to Figures 12 and 27. The impedance level has been lowered to 22Ω to decrease the total power dissipation of the circuit.

The collector current of Q-1 provides bias for the SE 3450 GaAs diode. The forward voltage of this large area GaAs diode provides the dc reference bias for the LED. This is the basic circuit arrangement shown in Figure 12; in Figure 27 this dc reference bias was provided with an external 1.0V power supply. Providing the reference bias with the SE 3450 eliminates the 1.0V power supply and makes it possible to ground the anode of the LED. In this configuration the cathode lead of the LED can be completely surrounded by a metal ground plane to give optimum EMI shielding.

For the component values shown in Figure 28, the current in Q-3 is 400mA. With no ac input, this current divides equally between Q-1 and Q-2 so that the average collector current of Q-2 is 200mA. The dc collector current of Q-2 divides equally between the two 22Ω resistors to provide a 100mA dc bias to the LED. When a sinusoidal signal is applied to the base of Q-1, the LED current swings symmetrically about the 100mA dc bias level. For 100% modulation at low frequency where the speed-up capacitor has no effect, the LED current swings ±100mA about the dc level and, therefore, covers the peak-to-peak range 0 to 200mA. At high frequency where the speed-up capacitor has full effect, the LED current swings ±200mA about the dc level and, therefore covers the peak-to-peak range -100mA to +300mA. This high-frequency overdrive compensates the LED cut-off and extends the 0.707 frequency of the light output by a factor of about 4.

The speed-up network is also effective for large signal square wave inputs. When Q-2 turns "on" suddenly, the entire 400mA current of Q-3 is momentarily coupled to the LED through the

speed-up capacitor. As time continues, the speed-up capacitor charges up and the LED current decays exponentially to 200mA. When Q-2 turns "off", the charge stored in the speed-up capacitor momentarily reverses the LED current to a value of -200mA. As time continues, this reverse current decays exponentially to zero. The overdrive current of the turn-on transient stores the minority carrier charge needed in the LED to get the light output up to the steady state value more rapidly. The reverse current of the turn-off transient extracts the stored minority carrier charge from the LED and causes the light output to fall to zero more rapidly.

The MPQ 3303 is a dual in-line package containing four core driver transistors. The specified minimum f_T of these transistors is 400MHz. However, the 3dB bandwidth of the circuit in Figure 25 will be limited by the input capacitance of Q-1. The two 100Ω resistors at the base of Q-1 appear in parallel at the input terminal and provide a 50Ω input resistance. When the input is driven from a 50Ω source the total resistance at the input is 25Ω. The expected 42pF of input capacitance at the base of Q-1 will give a 3dB frequency of about 150Milz. Thus, the circuit should be able to provide a current at the collector of Q-2 with a 10-90% rise time of about 2.3ns. Wider bandwidth in this circuit will require a buffer stage with low output impedance to drive the base of Q-1.

Evaluation of the circuit of Figure 28 showed that the bandwidth was less than anticipated due to the presence of a significant series inductance in the emitter leads of the MPQ 3303.

Tests were performed using an LED with an uncompensated 3dB bandwidth of 40MHz. An optical modulation bandwidth of about 110MHz was expected with that LED; however, the best that could be achieved was 65MHz. Thus, the circuit shown in Figure 28 is capable of providing an optical rise time of about 5.4ns.

The emitter lead inductance problem can be solved by using four or more lower power transistors in parallel for Q-1 and Q-2. This will split up the total current load and effectively reduce the emitter series inductance by the number of transistors connected in parallel. It is also possible that some of the microwave transistor strip line packages have sufficiently low inductance to operate satisfactorily without having to parallel transistors.

An optoelectronic data link using the LED driver of Figure 28 and the preamp of Figure 24 would give a 0.707 bandwidth of about 44MHz for analog signals. For Manchester coded digital signals, Eq (5) gives a data rate of 77M bit/s. The other performance factors of such a system can be predicted by assuming a set of typical component parameters and applying the suboptimum detection scheme analysis presented in Section II.D. For an SPX 1527 edge emitting LED with a 4mW output power at 200mA and an SPX 1615 photodiode with a responsivity of 0.5A/W the maximum allowable optical attenuation for a 10^{-8} bit error rate at 77Mbit/s is

$$\alpha_m = 2.08 \times 10^{-4} \qquad (-36.8dB) \qquad (144)$$

Using 500dB/km Galileo fiber optic bundle and assuming a total 9dB interface loss[3] at the LED and detector, this data link will have a maximum length of 55.6m (182ft).

Present diffused junction LEDs can be operated at high data rates using speed-up networks--see Section IV.D for measured data. However, supplying the overdrive current required to achieve this high-speed operation makes the LED driver complex and inefficient. The results obtained working with the circuit of Figure 28 suggest that a successful wide-band LED driver will require a buffer amplifier and four or more parallel transistors for Q-1 and Q-2. This leads to the conclusion that each LED driver will be of comparable complexity to the output stage of a commercial laboratory pulse generator designed to operate at the same frequency.

Further development effort on LEDs to increase the basic speed of response and power output will result in considerable saving of size, weight, complexity and power consumption of the LED driver.

D. LED EVALUATION AND COMPARISON

A comparison of various LED structures and their utility in fiber optic data transmission systems was presented in Ref 1. The conclusion of this comparison was that the shaped LEDs such as the hemispherical dome and cylindrical edge emitter geometries offered the most promise for coupling to fiber optic bundles. It was further concluded that the edge emitter geometry was superior to the dome geometry in terms of manufacturability and mechanical tolerance control. Thus, even though the dome structure has a theoretical performance advantage over the edge emitter, the measured performance of the two structures should be comparable

In order to check these conclusions, comparison tests were made of the SPX 1527 edge emitter LED made by Spectronics, Inc. and the TIL 09 and SL 1314 dome LEDs made by Texas Instruments.

Both LEDs are mounted in reflector packages with 0.080in diameter reflector apertures; both LEDs use 0.018in diameter GaAs wafers with planar diffused p-n junctions. Because of the similarity of the two LEDs, the comparison can be made on a one-to-one basis with very little normalization or extrapolation required.

The three LED types were compared for coupling to fiber optic bundles using the LED/fiber optic interface developed for the Ten-Channel Data Bus Demonstrator[3]. The critical parameter in this case is the power into a 10° cone. The results of this test are shown in Table IV. The two SPX 1527 LEDs are known to come from different lots which used significantly different starting material. No fabrication history is available for the TI devices. Microscopic examination shows that the SL 1314 LEDs have epoxy filled reflectors while the TIL 09 units contain no epoxy and are

Table IV. LED Output at 50mA

Unit	Total Output	Output Into 10° Cone	Percent 10° Cone
SPX 1527-59	.774mW	.311mW	40.2%
-DB	.757mW	.280mW	37.0%
SL 1314-1	.963mW	.138mW	14.3%
-2	2.098mW	.220mW	10.5%
-3	1.428mW	.186mW	13.0%
-4	.998mW	.193mW	19.3%
-5	1.170mW	.172mW	14.7%
-6	2.270mW	.267mW	11.8%
-7	2.012mW	.296mW	14.7%
-8	2.253mW	.289mW	12.8%
-9	1.634mW	.210mW	12.9%
-10	1.152mW	.163mW	14.1%
TIL 09 -11	.602mW	.181mW	30.1%
-12	.602mW	.172mW	28.6%
-13	.671mW	.169mW	25.2%
-14	.688mW	.163mW	23.7%
-15	.722mW	.212mW	29.4%
-16	.722mW	.198mW	27.4%
-17	.688mW	.205mW	29.8%
-18	.636mW	.158mW	24.8%
-19	.654mW	.169mW	25.8%
-20	.929mW	.263mW	28.3%

sealed with a flat glass window. For equal values of internal quantum efficiency the epoxy filled SL 1314 should have 1.3 times more output than the glass window TIL 09 and 2.3 times more output than the SPX 1527. For the data shown in Table IV, the average SL 1314 output is 2.3 times more than the average TIL 09 output and 2.1 times more than the average SPX 1527 output. Thus, it appears that the SPX 1527 LEDs have the highest internal quantum efficiency of the three groups. In order to compare the potential performance of the three types of LEDs the SL 1314 output power values should be multiplied by 1.095 and the TIL 09 output power values should be multiplied by 1.937. These adjusted average output values are shown in Table V. The two SPX 1527 LEDs used in this comparison are typical units that have only about 44% of the output power of the 10 selected SPX 1527 LEDs used in the Ten-Channel Data Bus Demonstrator[3].

Table V. Adjusted Average LED Output at 50mA

Unit	Total Output	Output 10° Cone	Percent 10° Cone
SPX 1527	.766mW	.296mW	38.6%
SL 1314	1.750mW	.233mW	13.3%
TIL 09	1.338mW	.336mW	27.4%

The LED/fiber optic interface developed for the Optoelectronic Data Bus Demonstrator has a launch cone numerical aperture of 0.24. With a fiber optic bundle diameter of 45mils the product of NA and diameter is

$$NA \times \text{diameter} = 10.8\text{mils} \tag{145}$$

Referring to Figure 13 of Report No. AFAL-TR-73-164[1], at 10.8mils the TIL 09 type dome should put 36.4% more light on the fiber optic bundle than the SPX 1527. From the adjusted average

data in Table V. the TIL 09 is only 13.5% better than the SPX 1527 and the epoxy filled SL 1314 is 21.3% worse than the SPX 1527. Thus, even though all three types of LEDs have performance considerably less than theoretical limit, the SPX 1527 comes closer to its idealized performance than the two dome LEDs.

The Spectronics Model 170 Radiation Pattern Plotter was used to plot the angular distribution of the light output from representative LEDs. These far field radiation patterns were measured using the test set up shown in Figure 29. An SPX 1615 photodiode is used in the moving arm on the radiation pattern plotter. This detector has an aperture of 0.140in. When the detector is positioned on the moving arm at 4.0in radius the angular resolution is 2° or a half angle of 1°. The far field radiation patterns of three LEDs are shown in Figures 30, 31 and 32; the angular resolution of the detector is indicated in each of the figures. A far field radiation pattern plot is a graph of radiant intensity, I, (W/str), as a function of angle from the axis of the device under test. The two plots in each figure were taken before and after a 90° rotation of the LED about its axis. As expected, the dome LEDs have wider beam angles than the edge emitter. The gain was adjusted for each plot so that the peak radiant intensity reached full scale on the plot.

The radiation pattern plot only gives information about the angular distribution, NA_{ϕ}, of the light emitted by the LED. It tells nothing about the shape of the light emitting area. Spot scans of edge emitter and dome LEDs at the aperture of the reflector show that both devices have an effective light emitting area shaped like a donut. In the case of the dome LEDs there is also a bright spot in the center of the hole in the donut due to direct illumination from the top of the dome.

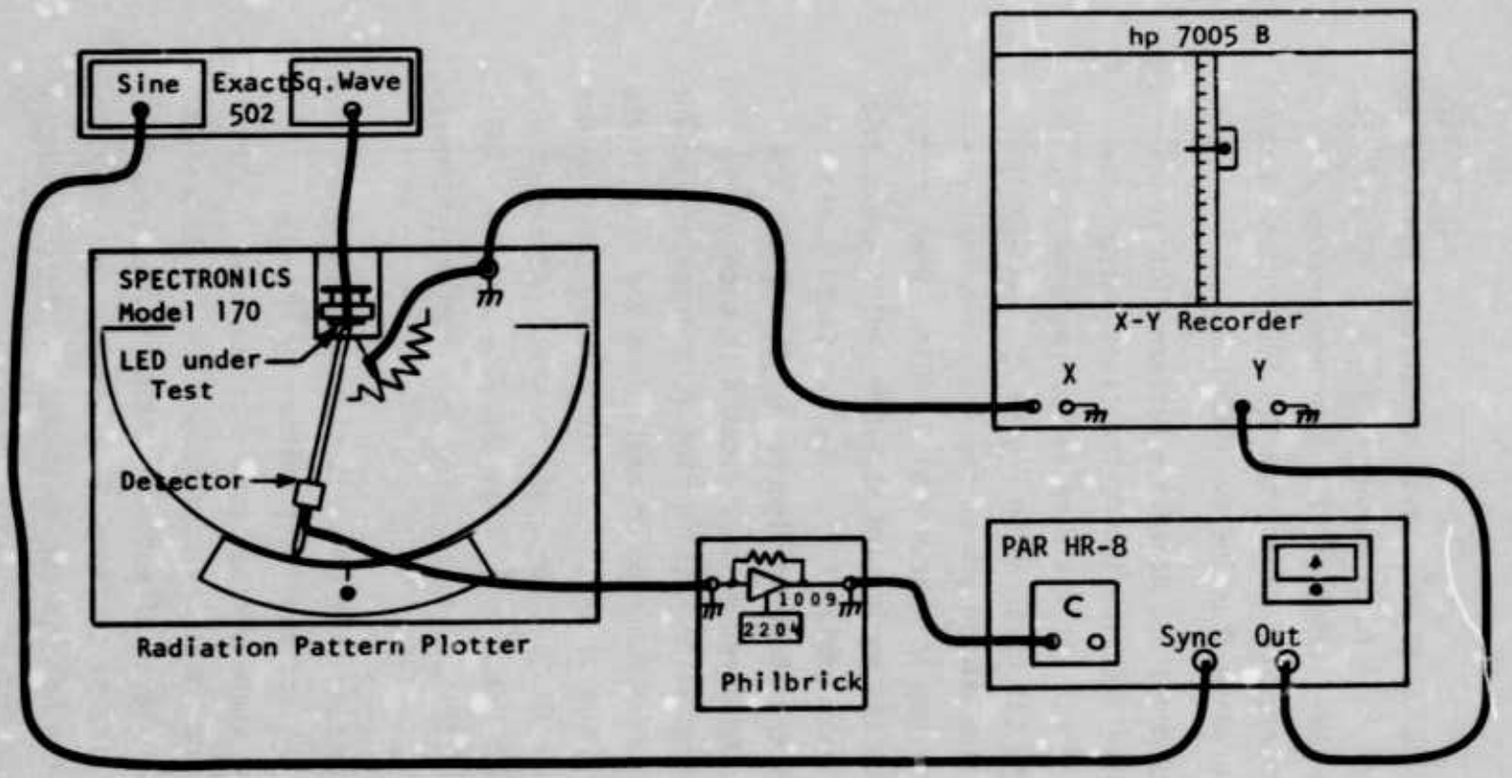

Figure 29. Far Field Radiation Pattern
LED Test Set Up

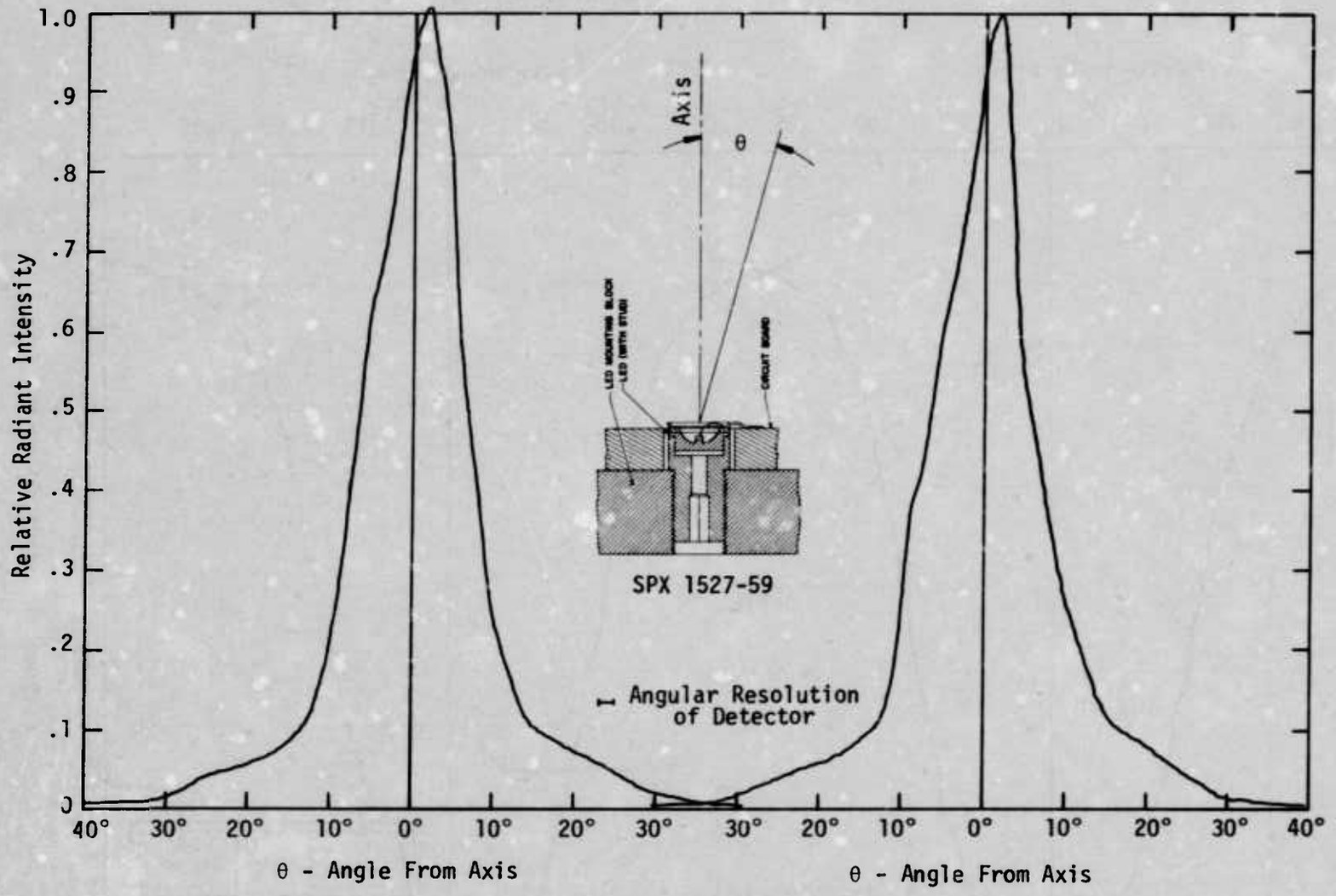

Figure 30. Far Field Radiation Pattern For SPX 1527-59

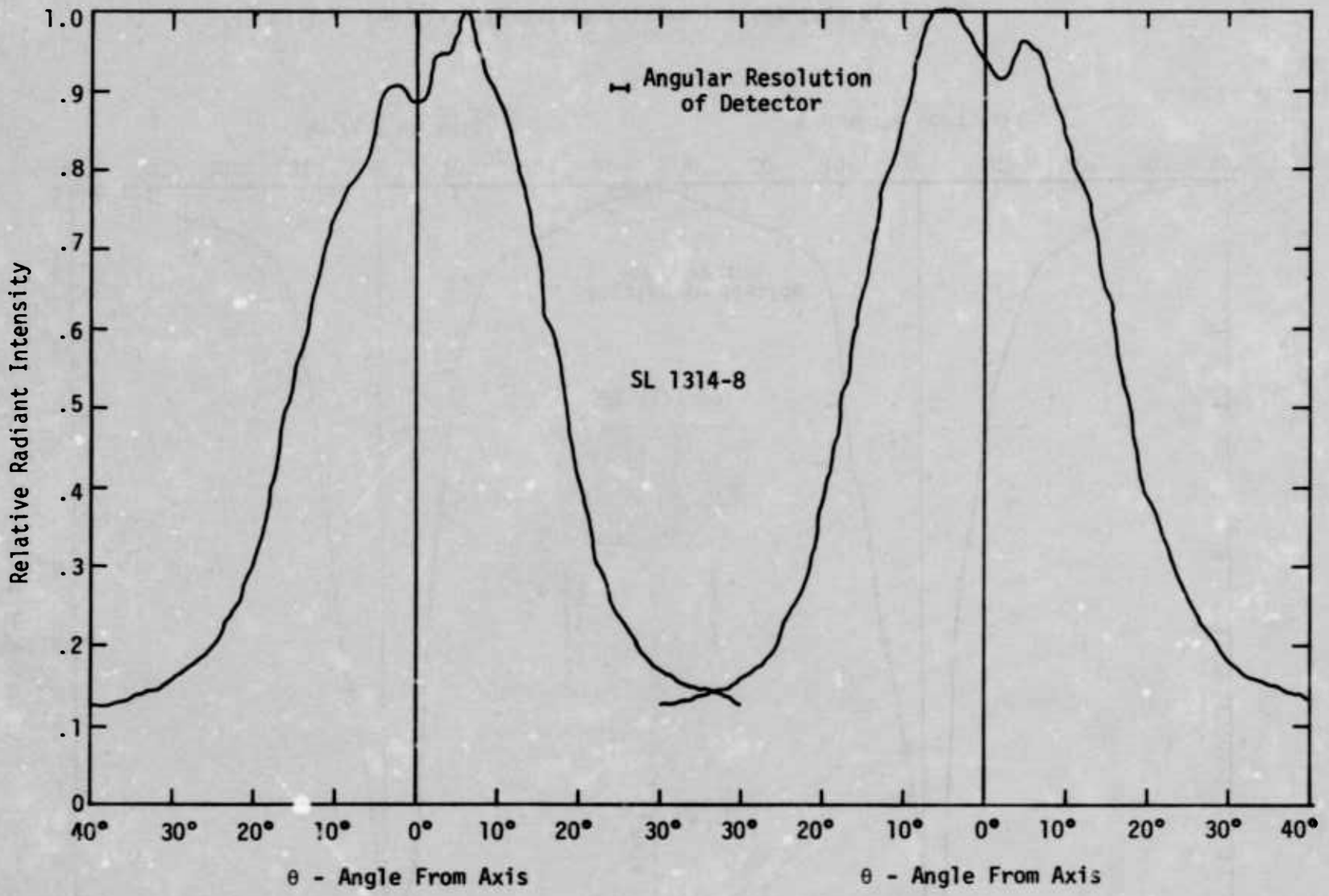

Figure 31. Far Field Radiation Pattern for SL 1314-8

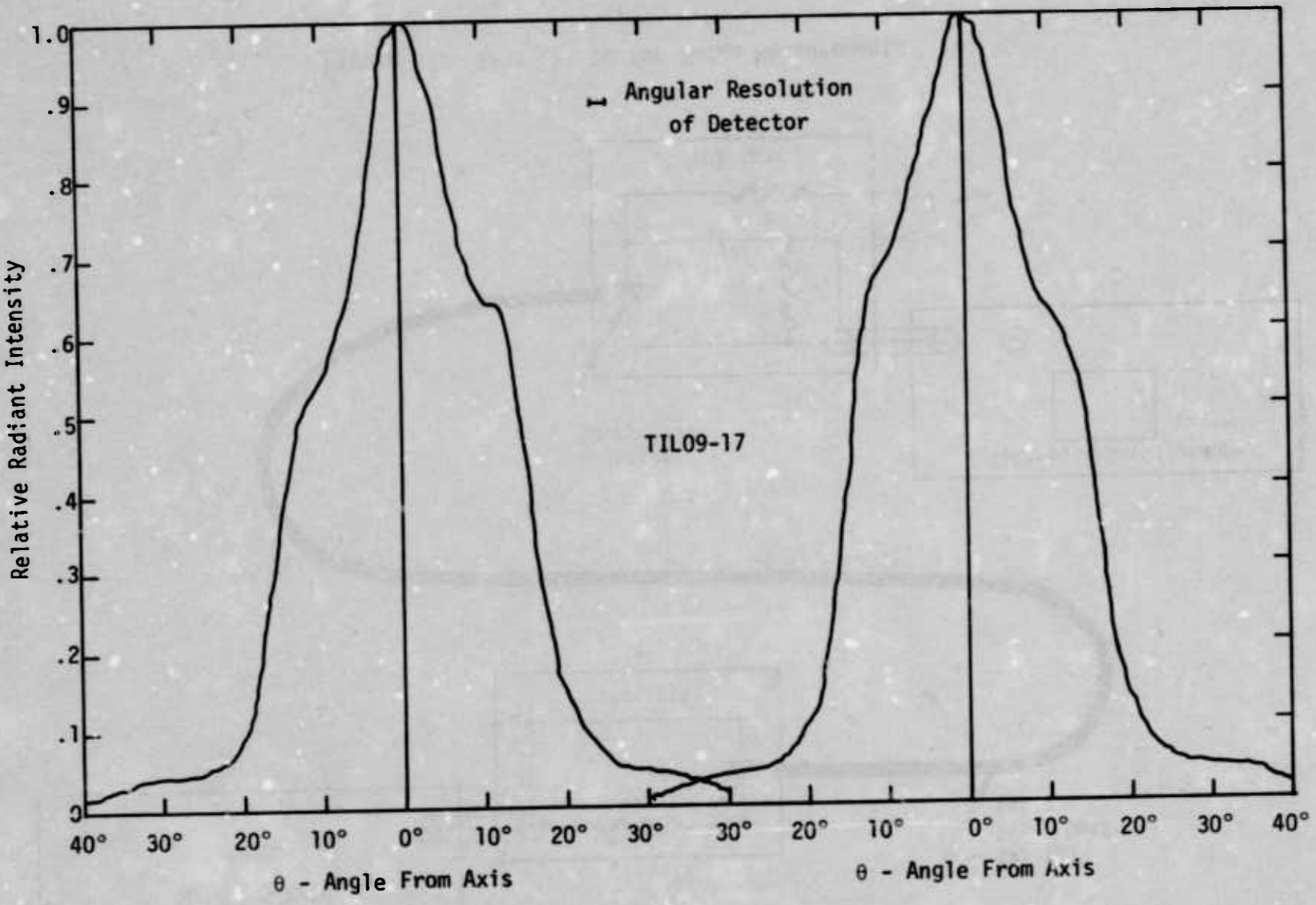

Figure 32. Far Field Radiation Pattern for TIL09-17

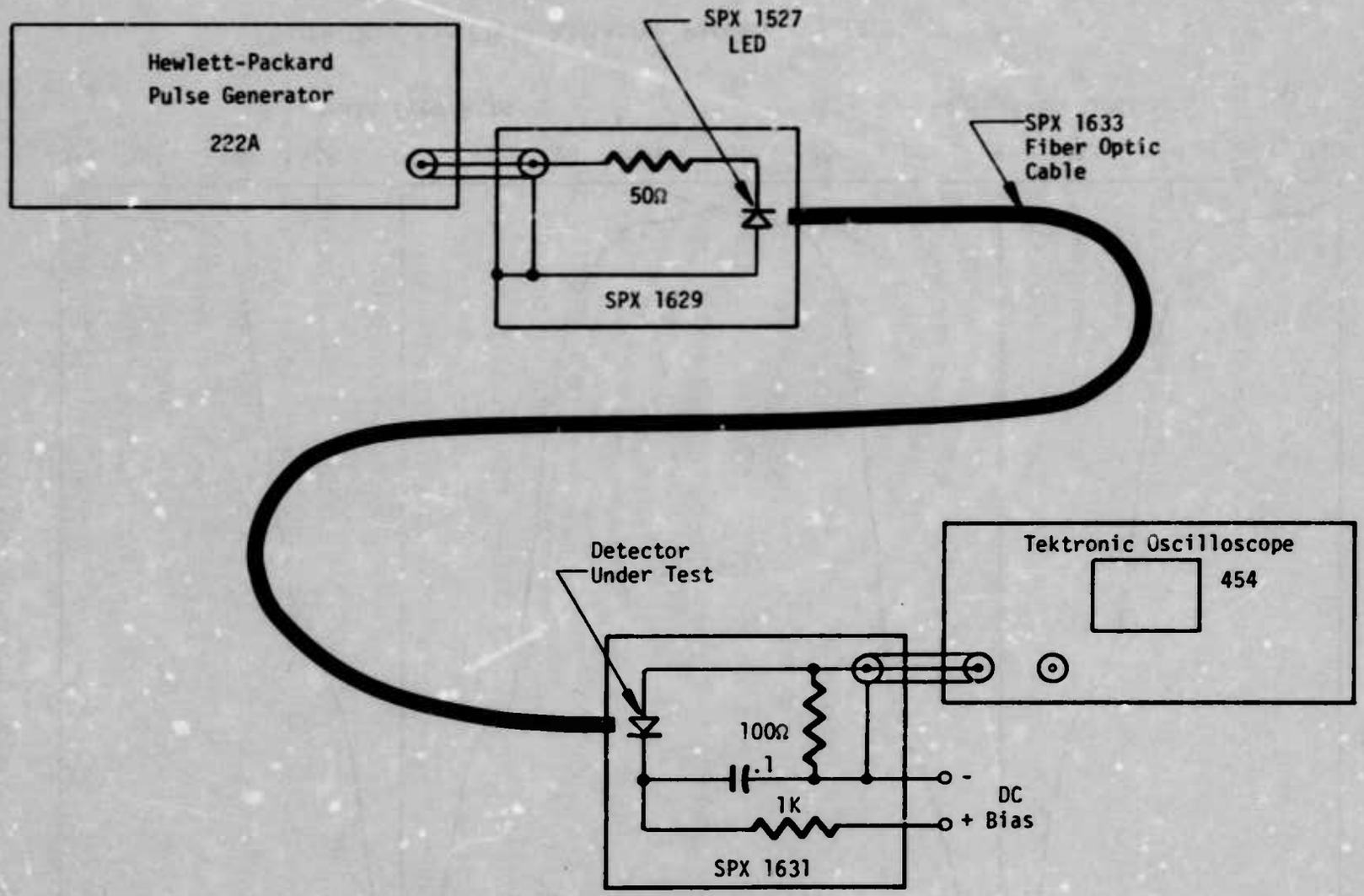

Figure 33. Test Set Up for Pulse Measurements

The test set up shown in Figure 33 was used to measure the rise and fall times of representative LEDs of each type. The results of this test are shown in Table VI. The measurements used a pulse current of about 200mA delivered through the 50Ω resistor in the SPX 1629 LED adapter; both the rise time, $t_{\phi r}$, and the fall time, $t_{\phi f}$, are 10-90% values. The rise times are consistently longer than the fall times because of the presence of differential heating[3] observed in both the dome and edge emitter structures. Also, the absence of pre-bias in the SPX 1629 LED adapter gives a small amount of speed-up of the fall time. The measured fall time more accurately represents the true speed of the LED.

The term differential heating refers to the transient temperature difference between the LED junction and other parts of the GaAs wafer. When forward bias current is applied to an LED constructed like an edge emitter or a dome, most of the applied power is converted to heat in the region of the junction. This causes the junction temperature to rise with respect to the remainder of the GaAs wafer. As the junction temperature rises the internal emission peak shifts to longer wavelength at about 3Å/°C. Since the temperature of the material between the junction and the exit surface does not rise, its absorption edge does not shift with the internal emission peak. The net effect is a transient reduction in absorption which causes the light output to rise slowly during the current pulse.

SPX 1527-59 is from the same lot of devices as the LEDs used in the Ten-Channel Data Bus Demonstrator[3] and has the same rise and fall times as those LEDs. Note that TIL 09-18 has a comparably slow response. SPX 1527-DB is an LED from a lot of devices made using more heavily doped GaAs. The measured response of this device is the same as TIL 09-17 which is the fastest of the TI units. For these fast units the measured rise and fall times are significantly

in error due to the basic 9ns rise time of the measurement equipment described in Section IV.B. The estimated fall times for the LEDs shown in the fourth column of Table VI is obtained from the approximation

$$t_{\phi f}(\text{est.}) = (t_{\phi f}^2 - t_m^2)^{1/2} \tag{146}$$

where t_m is the 10-90% rise time of the measurement set up. Whatever the actual rise times and fall times are, the data in Table VI show that the Spectronics and TI LEDs cover the same range of values.

Table VI. LED Rise Time and Fall Time

Unit No.	$t_{\phi r}$	$t_{\phi f}$	$t_{\phi f}$(est.)	$t_\phi(\omega)$
SPX 1527-59	20.0ns	17.0ns	14.4ns	15.2ns
-DB	11.5ns	10.0ns	4.4ns	4.4ns
SL 1314-2	13.0ns	10.5ns	5.4ns	-
-6	14.5ns	11.5ns	7.2ns	-
-7	13.0ns	11.0ns	6.3ns	-
-8	15.0ns	12.0ns	7.9ns	7.6ns
TIL 09-11	13.0ns	10.0ns	4.4ns	-
-14	12.0ns	10.5ns	7.2ns	-
-17	11.5ns	10.0ns	4.4ns	4.4ns
-18	22.0ns	19.0ns	16.7ns	-

The SPX 1631 photodiode adapter in Figure 33 was replaced with the high-frequency preamp/scope driver shown in Figure 23 and this set up was used to measure the rise and fall times of the two SPX 1527 LEDs. Table VII shows the response times measured with this test set up; these values have been corrected for the 3.0ns rise time of the receiver system. These values are more accurate than those in Table VI because of the smaller correction required for the measuring system.

Table VII. SPX 1527 Response Time (10-90%)

Unit No.	$t_{\phi r}$	$t_{\phi f}$
SPX 1527-59	17.7ns	12.6ns
SPX 1527-DB	5.2ns	5.2ns

The basic test setup of Figure 33 was further modified by replacing the SPX 1629 LED adapter with the speed-up fixture shown in Figure 27. The response times of the two SPX 1527 LEDs were measured using this set up. The 2/1 overdrive network shown in Figure 27 with a 47pF capacitor was used with SPX 1527-DB. The 4/1 overdrive network with a 100pF capacitor was used with SPX 1527-59. Figure 34 shows the measured response of the two LEDs with their respective speed up networks. These curves were traced directly from polaroid photographs of the oscilloscope display. Correcting for the 3.0ns rise time of the receiver, unit-DB has a rise time of 1.1ns and unit-59 has a rise time of 1.6ns. This is in reasonably good agreement with the predicted improvement; Unit-59 improved by only a factor of 11 rather than the predicted factor of 16 and Unit-DB improved by a factor 4.7 rather than the predicted factor of 4.0. When the pulse is lengthened on unit-59 the tilt observed in Figure 34 develops into an undershoot followed by a slow rise back up to the initial peak value. No value of capacitance could be found which did not give a significant overshoot or undershoot in the 4/1 overdrive network. The 2/1 overdrive network on unit-DB is well behaved at all pulse widths.

The studies of LED drive techniques performed on the Ten-Channel Data Bus Demonstrator[3] seemed to indicate the presence of a mechanism in the LED that made it impossible to speed up the optical fall time of the light output. Figure 34 shows that the speed-up networks shown in Figure 27 improve the fall time

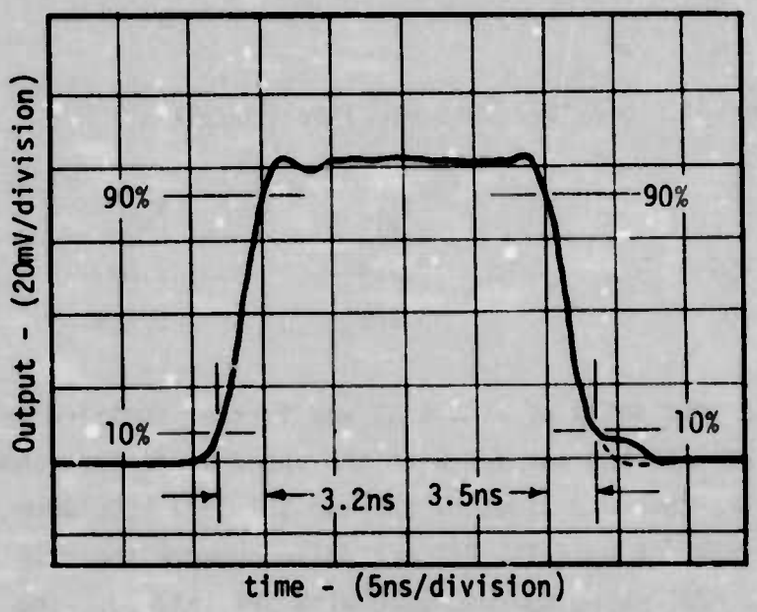

SPX 1527 - Unit DB

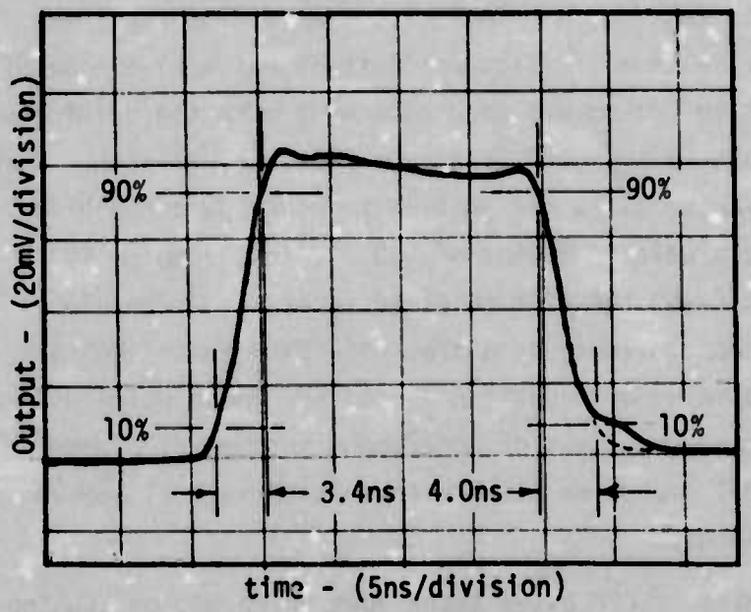

SPX 1527 - Unit 59

Figure 34. LED Response Time with Speed-Up Network

almost as much as the rise time. This result shows that the problem encountered on the previous contract was associated with the drive circuits and not the LEDs. Perhaps the most significant result related to Figure 34 is the clear demonstration of high-speed data transmission using both fast and slow LEDs. Correcting for the response time of the oscilloscope, it is clear that both the LED/speed-up network shown in Figure 27 and the high-frequency photodiode/preamp shown in Figure 23 are adequate for data rates in excess of 200M bit/s.

The steady state frequency response or modulation transfer function was measured for the Spectronics and TI LEDs. The test set up for these measurements is shown in Figure 35; the LED is driven with the test fixture shown in Figure 26.

Figure 36 shows the modulation transfer function of SPX 1527-59; this curve was run at a current modulation depth of 75%. The raw data have been corrected for the measured frequency response of the test equipment. The observed 20% droop in optical modulation depth between 0.1MHz and 5MHz is the result of differential heating in the LED and the slow tail response of the SD5425 detector. The H-P 606A signal generator has a top frequency of 65MHz. However, the corner frequency of unit-59 is such that the slope of the high-frequency asymptote is clearly demonstrated. This basic characteristic which falls off as $f^{-\frac{1}{2}}$ at high-frequency is the expected response from any p-n junction which operates on the diffusion of minority carriers. An expression for this modulation transfer function is given in Eq (73); the 0.707 frequency, f_ϕ, is given by Eq (74) and the 10-90% rise time, t_ϕ, by Eq (75). Using Eq (74) the rise time of unit-DB from Figure 36 is

$$t_\phi(\omega) = 15.2\text{ns} \qquad (147)$$

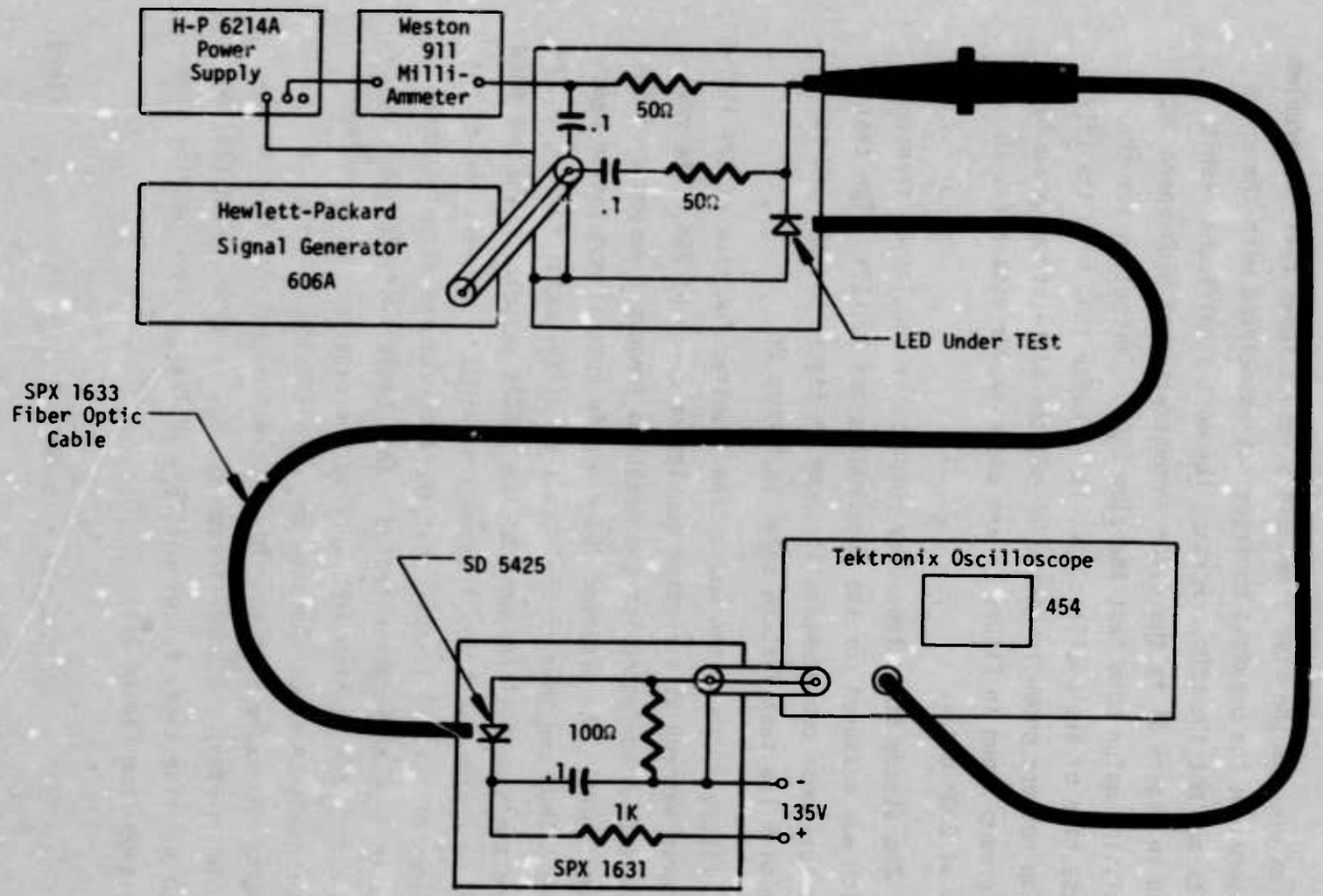

Figure 35. Test Set Up for Modulation Transfer Function

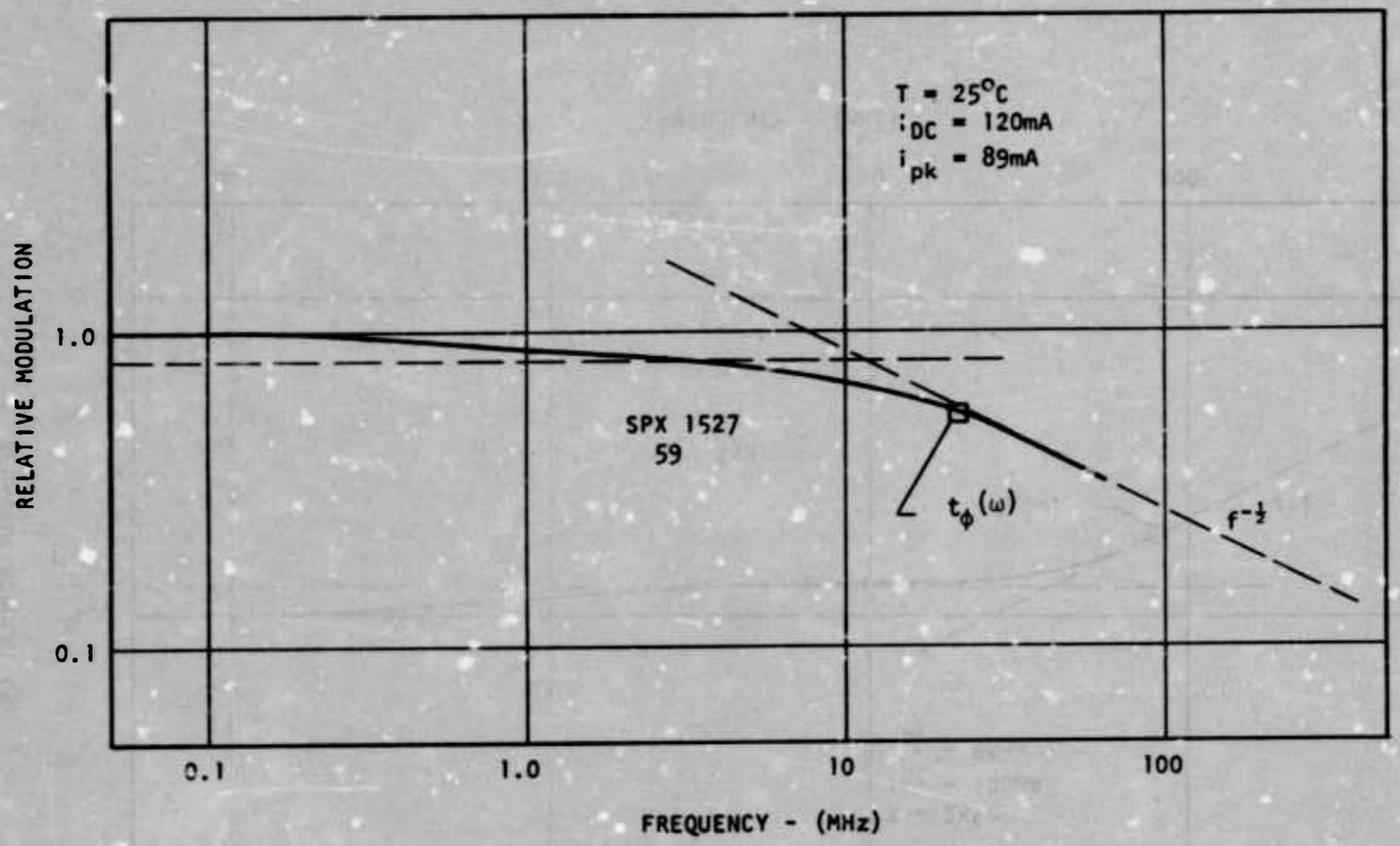

Figure 36. Modulation Transfer Function for SPX 1527-59

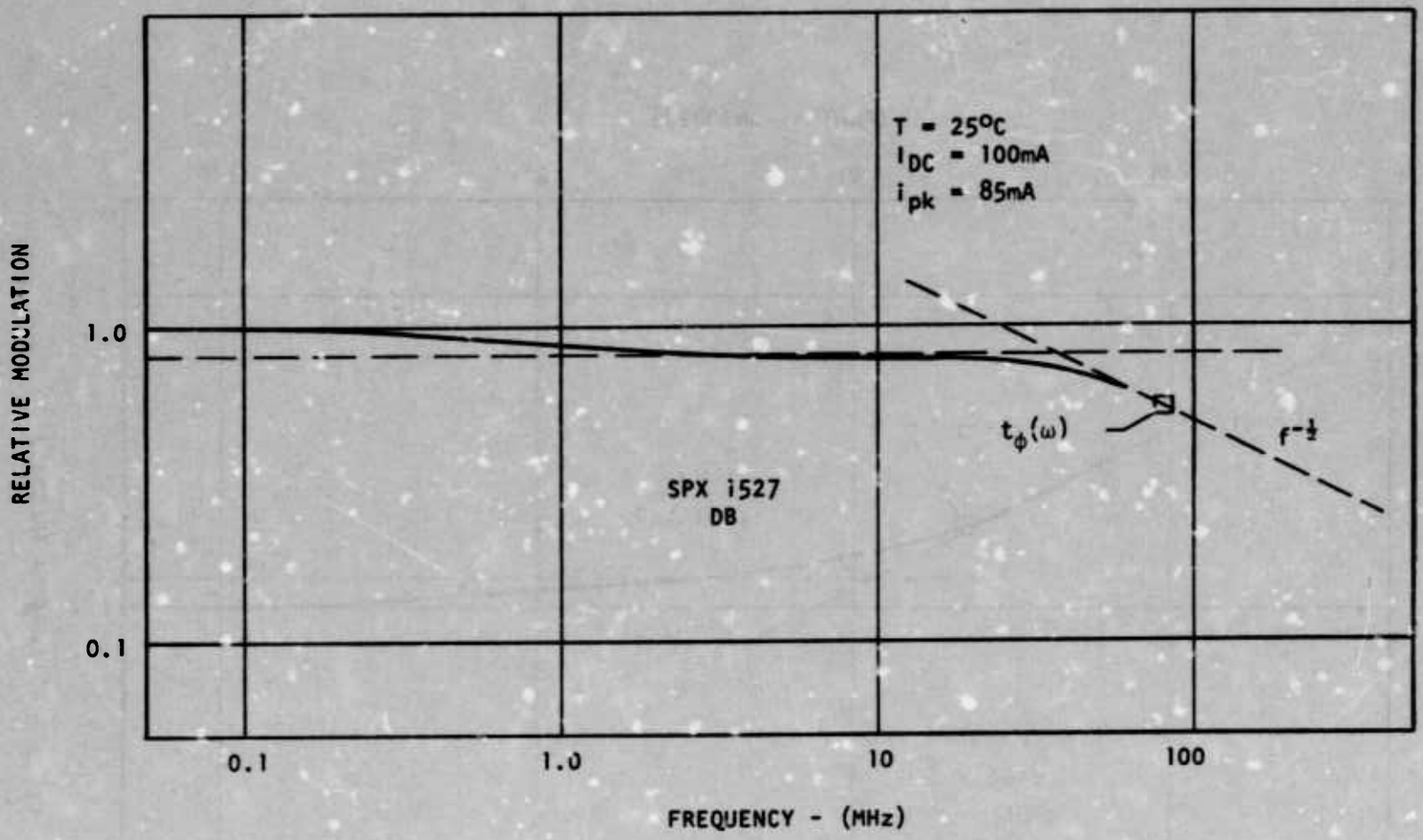

Figure 37. Modulation Transfer Function for SPX 1527-DB

This value is recorded in the last column of Table VI for comparison; the value 15.2ns is between the values of rise time (17.7ns) and fall time (12.6ns) shown for unit-59 in Table VII.

Figures 37, 38 and 39 show the modulation transfer functions for SPX 1527-DB, SL 1314-8, and TIL 09-7 respectively. All of these units show the 20% droop between 0.1MHz and 5MHz. The high-frequency asymptotes have been drawn in with the $f^{-\frac{1}{2}}$ slope observed in Figure 36. The 0.707 frequency is marked with a square in each figure and the corresponding value of $t_\phi(\omega)$ recorded in Table VI for reference. As expected, the modulation transfer functions of the two fast LEDs (SPX 1527-DB and TIL 09-17) are almost identical.

The high-frequency overdrive characteristic of the two edge emitter LEDs was also checked using the test set up shown in Figure 35. The maximum voltage output of the H-P 606A oscillator is 3.16V (rms) or 4.47V (peak). Thus, with a 50Ω drive resistor, the maximum peak modulation current that can be supplied is 89mA. In order to achieve current overdrive on the LED it is, therefore, necessary to reduce the dc bias to a value less than 89mA. SPX 1527 units 59 and DB were both tested to see if overdrive current at high frequency could maintain a constant depth of modulation in the optical signal. Both units were operated at a constant optical modulation depth (∿100%) from 50kHz to 65MHz by adjusting the peak modulation current with frequency. SPX 1527-59 was operated at a dc bias of 30mA with 1.06V rms providing 100% optical modulation at low frequency. As the frequency was increased to 65MHz, the ac voltage had to be increased to about 3.1V rms to maintain the ac optical signal at the low-frequency value. Unit SPX 1527-DB was operated at a dc bias of 50mA with 1.9V rms providing ∿100% modulation at 1.0MHz. When the frequency was increased to 65MHz the ac voltage had to be increased to 2.45V rms to maintain a constant optical signal. For each of the two LEDs, the current overdrive required for constant depth of optical modulation vs frequency is comparable to the fall off in optical modulation with frequency for that LED. Based on

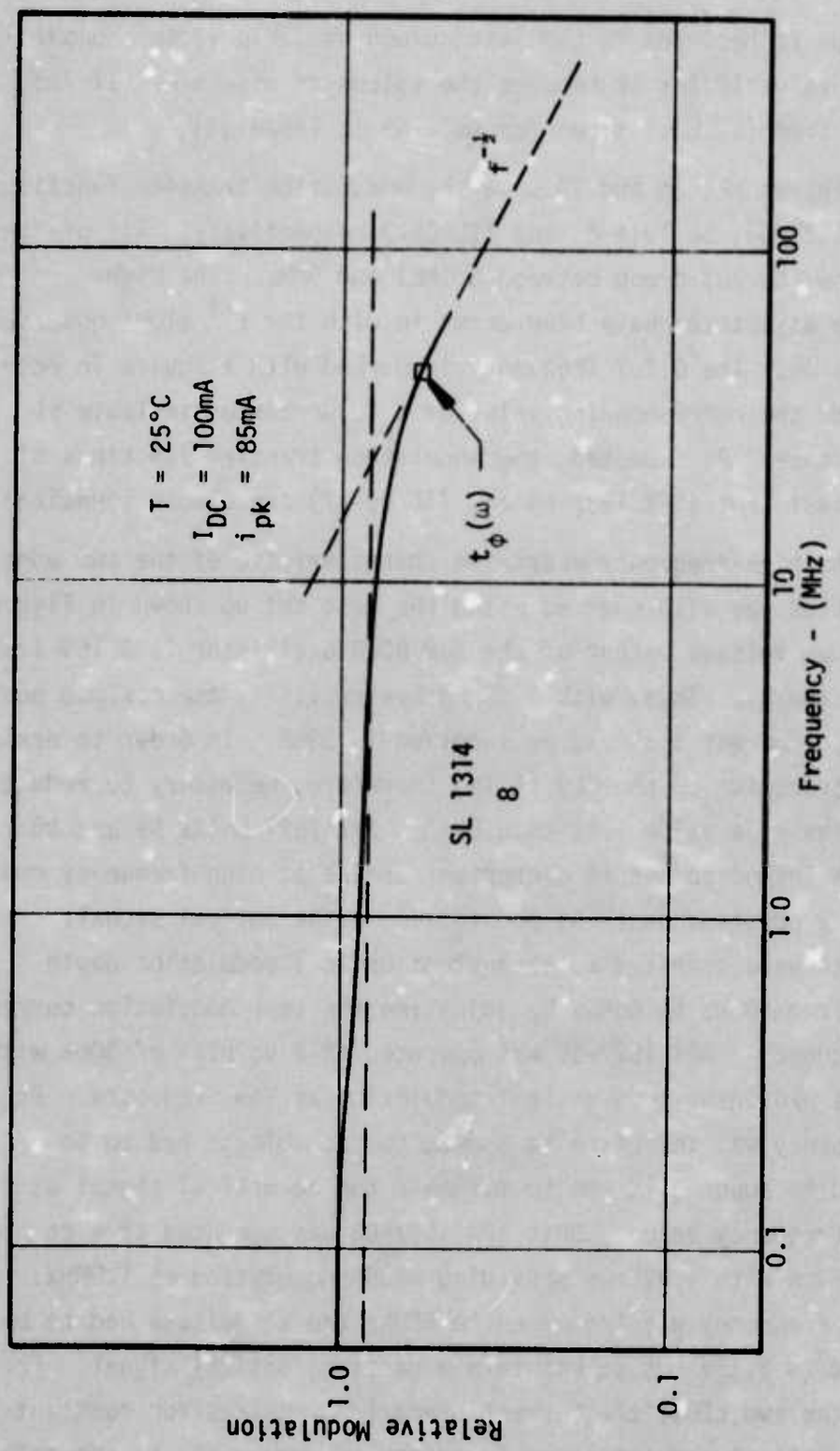

Figure 38. Modulation Transfer Function for SL 1314-8

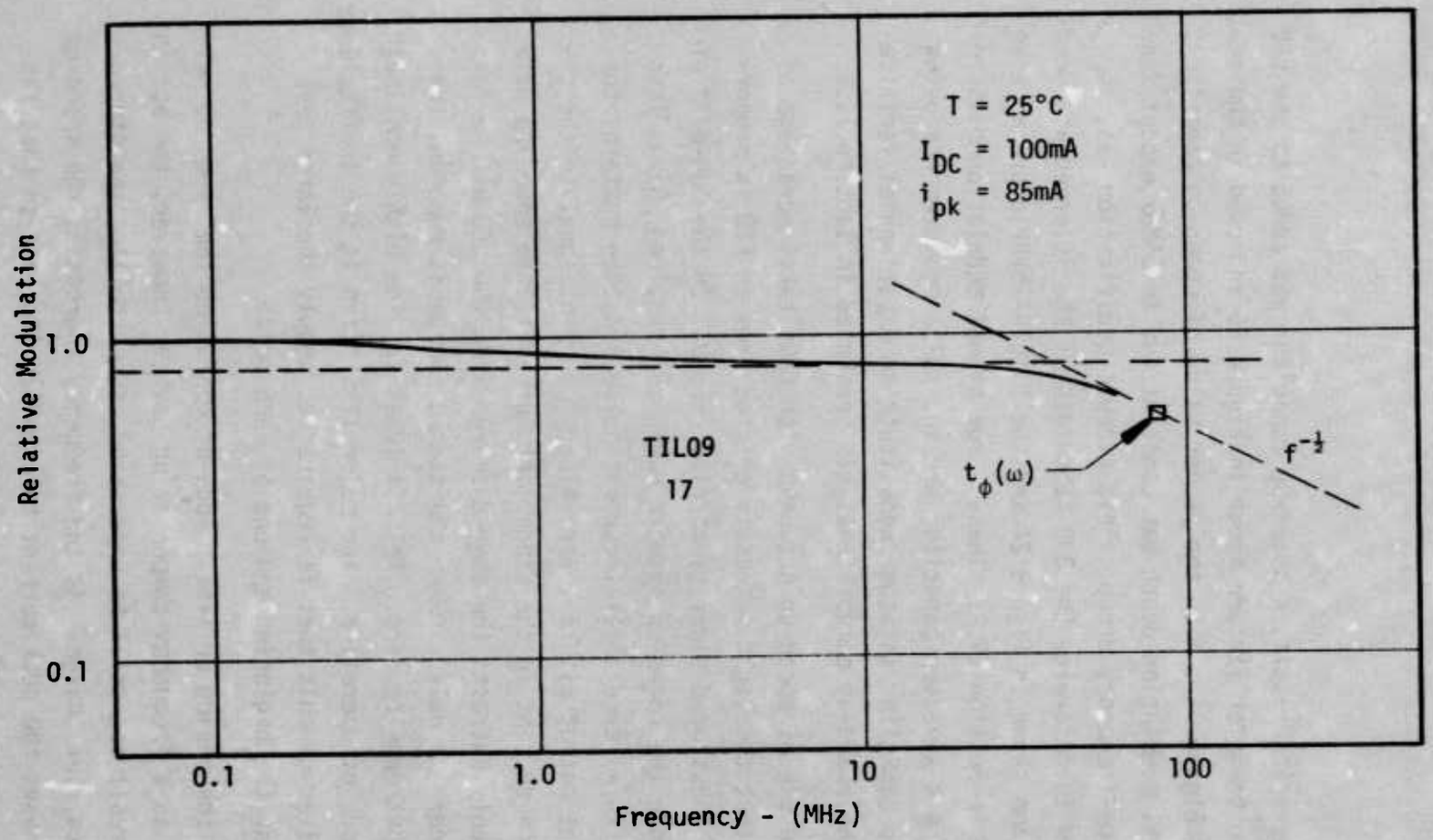

Figure 39. Modulation Transfer Function for TIL 09-17

this encouraging result, a speed-up capacitor was added to the LED modulation transfer fixture shown in Figure 26 and used in the test set up of Figure 35. With the proper value of speed-up capacitor, the optical modulation depth was constant out to 65MHz except for the 20% low-frequency droop. This circuit modification was, in fact, used to determine the 3dB bandwidth of the intermediate bandwidth preamp shown in Figure 24 and the TIXL151 hybrid preamp also described in Section IV.A. These large signal modulation measurements using a speed-up capacitor and the pulse measurements using a speed-up capacitor together constitute an experimental verification of the speed-up network analysis presented in Section II.G.

The use of speed-up networks with LEDs takes advantage of the fact that the light intensity emitted from an LED is proportional to the stored minority carrier charge. In the "on-off" or digital mode the speed-up network dumps the required charge into the LED with a large initial current pulse and then sustains the steady light output with a lower value of current equal to the recombination current in the diode. At turn-off, the speed-up network suddenly extracts the stored charge from the LED with a large negative current pulse. When the stored charge is removed, the light output goes to zero. This is ideal for the highly nonlinear digital mode of operation. The major limitation is the inefficiency of the driver circuit that is required to supply the large peak currents at the beginning and end of each pulse.

In the analog or linear mode of operation the speed up network acts as a frequency compensating device. However, the action of the circuit can still be understood as controlling the stored minority carrier charge. As the frequency increases, the speed-up network causes the peak current to steadily increase so that the stored charge is moved in and out of the LED more rapidly. This

produces a constant amplitude sine wave modulation of the stored charge and, therefore, maintains a constant optical modulation depth at frequencies above the natural 0.707 frequency of the LED. No harmonic distortion measurements were made on this contract. However, no serious harmonic distortion problems associated with the speed-up networks are anticipated. Again, the major limitation of speed-up networks in analog or linear LED drivers is the complexity and inefficiency of the drive circuit.

In conjunction with the modulation tests, measurements were also made of the series resistance and series inductance of several of the LEDs. These measurements were made at a dc bias current of 100mA with a modulation voltage of 1.0V rms; this corresponds to a 28% current modulation. Voltage readings at the LED terminals at 1MHz and 65MHz make it possible to separate the diode impedance into series resistance and inductance. The values measured in this way are shown in Table VIII. The incremental junction resistance of 0.26Ω at 100mA has been subtracted so that the resistance values in Table VI represent the parasitic body resistance only. A comparison of the SPX 1527 data indicates that unit-DB is at least three times more heavily doped than unit 59. This is in good agreement with the fall time data; the more heavily doped unit is 3.45 times faster than the lightly doped unit. Everything else being equal, higher doping levels in the starting n-type wafer should improve the rise and fall time on about a one-to-one basis. A similar comparison can not be made on the TI LEDs because of the unknown value of resistance in the submount. The series inductance has about the same value for all three types of LEDs used in this comparison. This parasitic inductance is probably the limiting factor in determining the optical rise time that can be obtained using a speed-up network.

Table VIII. Series Resistance and Inductance of LEDs

Unit	Resistance	Inductance
SPX 1527-59	1.52Ω	4.6nH
-DB	.50Ω	3.5nH
SL 1314-2	.36Ω	4.5nH
-8	.54Ω	4.0nH
TIL 09 -17	.54Ω	5.0nH

In summary, the Spectronics SPX 1527 edge emitter LED has been compared to two types of TI dome LEDs. The comparison has included

- power coupled to a fiber bundle,
- 10-90% rise time and fall time,
- modulation transfer function,
- series resistance, and
- series inductance.

All three types of LEDs tested are remarkably similar. However, the edge emitter structures gives the best overall performance and continues to be the best LED for use in fiber optic data transmission.

In addition to these comparisons it has been shown that large optical modulation depths can be obtained above the 0.707 frequency of an LED by using current overdrive. Also, for pulse or digital signals, both the rise time and fall time of the light output can be significantly decreased by using speed-up networks.

E. PHOTODIODE EVALUATION & COMPARISON

A detailed analysis of photodiodes was presented in Reference 1 which showed that properly designed silicon planar photodiodes were optimum for use in optical data transmission systems. This analysis concluded that photodiodes having a depletion layer width of 100μm would have low capacitance, a rise time of about 1ns, and good high-frequency responsivity for LED wavelengths out to about 940nm.

Silicon photodiodes from several manufacturers have been characterized and evaluated for use in optoelectronic data transmission systems. While the list of photodiodes is not exhaustive, each of the major structural classifications is represented including p-n, p-i-n, and avalanche types. This evaluation shows that no basic new silicon process technology is required for photodetectors to be used in optoelectronic data transmission. However, the evaluation also shows that optimum system performance is obtained only with properly designed and constructed photodiodes. Most of the commercially available photodiodes have one or more serious design and/or construction deficiencies.

The specific components selected for evaluation are:

- Hewlett-Packard 5082-4207 p-i-n photodiode (40mil diameter),
- RCA C30817 avalanche photodiode (30mil diameter)
- Spectronics, Inc. SD 5425 p-n photodiode (50mil diameter),
- Spectronics, Inc. SPX 1615 p-i-n photodiode (50mil diameter),
- Texas Instruments TISL59 avalanche photodiode (30mil diameter),
- Texas Instruments TIXL-79 avalanche photodetector module, and
- United Detector Technology PIN-040A p-n photodiode (40mil diameter).

The hybrid LED and detector modules made by Meret Inc. and distributed by Galileo Electro-Optics were also included in the evaluation. The Galileo designation for the transmitter module is Model 3555971F; the receiver module designation is Model 3555971R.

The SD 5425 and SPX 1615 photodiodes are packaged in TO-46 lens can headers; all of the other photodiodes selected for evaluation are

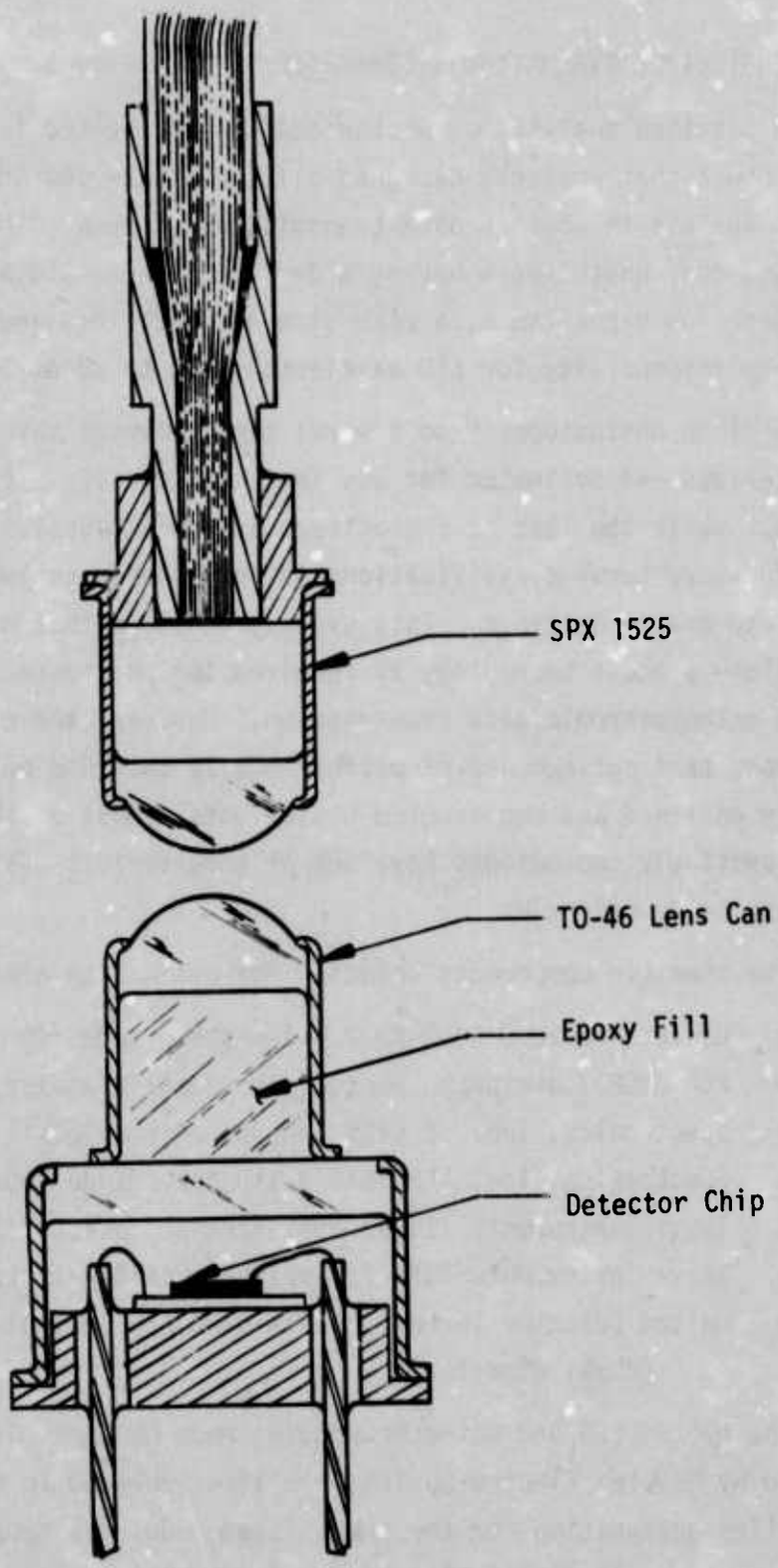

Figure 40. Detector/Fiber Optic Interface
for Photodiode Evaluation

packaged in flat window cans. Because of the distance between the window surface and the silicon chip and the small active area of most of the detectors, it is difficult to obtain efficient coupling to a 0.046 inch diameter fiber optic bundle. This problem has been at least partially solved by adding external lenses to each of the detectors. The external lenses were prepared by filling standard TO-46 lensed cans with epoxy. The resulting thick lenses have a focal length of about 200 mil and a focal point about 40 mil outside the back of the can. When the epoxy filled lenses are cemented on the flat window photodiode cans, the surface of the silicon chip is nominally located at the focus of the lens. Using this approach, the SPX 1525 lens termination was employed in a plugable detector/fiber optic interface shown in Figure 40 in all detector tests. The 46 mil diameter of the fiber optic bundle and the 140 mil focal length of the SPX 1525 combine with the 200 mil focal length of the epoxy filled lens to produce a 65 mil diameter light spot at the plane of the detector surface. An estimate of the interface coupling loss for each detector type is given in the discussion. With the epoxy filled lens cemented into place, there are only two glass/air interfaces in each detector.

1. SD 5425 Performance

The SD 5425 is a p-n junction photodiode manufactured by Spectronics Inc.; Table IX gives a summary of the specifications for this device. This photodiode was used in the Ten-Channel Data Bus Demonstrator[3] and is compatible with the photodiode adapter and other test fixtures and preamps described in Sections IV.A and B. The total capacitance includes about 0.5pF of header capacitance. The responsivity refers only to the high-speed response and the 7.8% front surface reflection loss in the lens is included in the responsivity. When the SD 5425 is interfaced with the SPX 1525 fiber optic lens the optical loss at the plugable interface is about -1.0dB[3].

The test set up of Figure 33 was used to evaluate the slow tail response of the SD 5425 as a function of bias voltage. The LED is

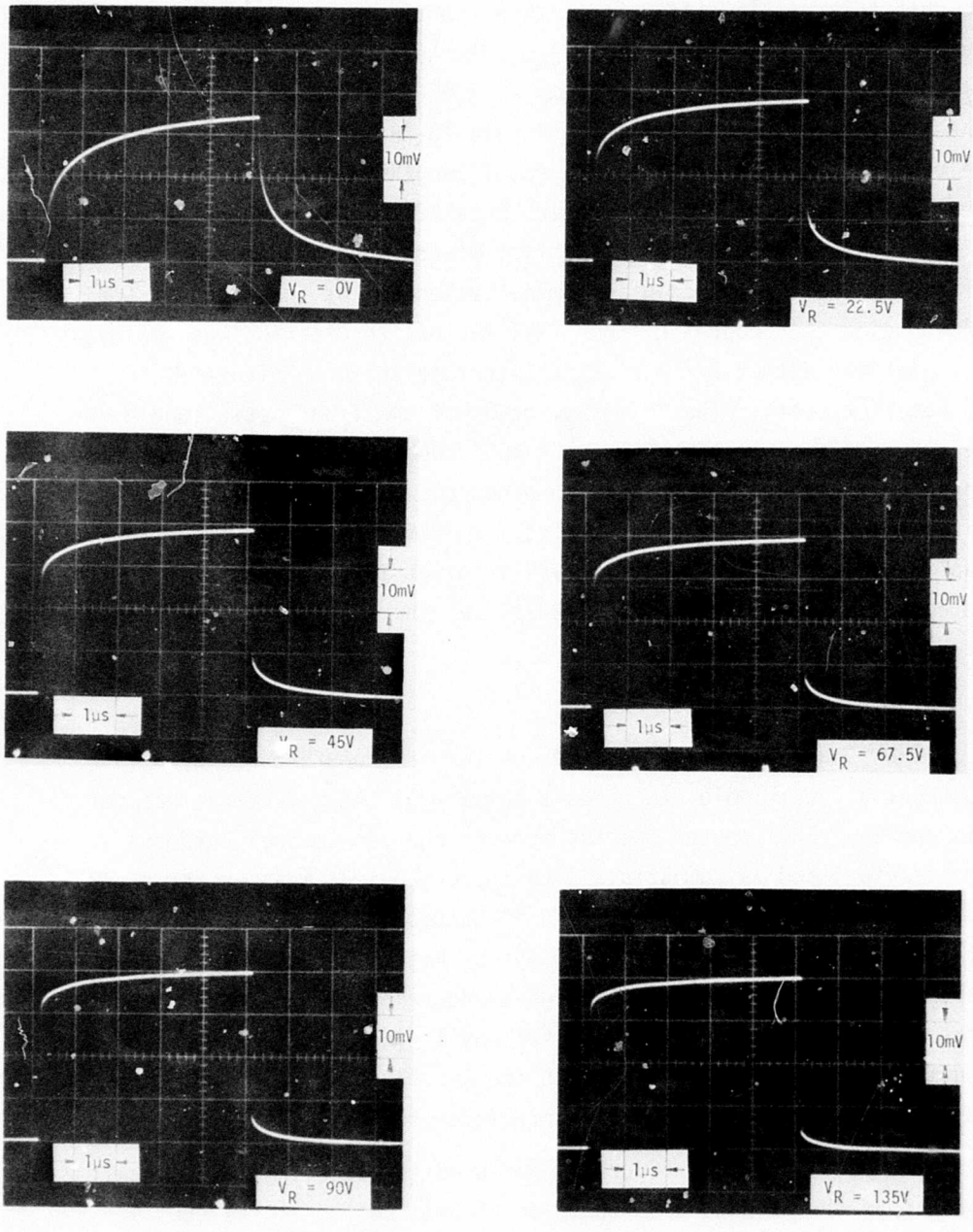

Figure 41. SD 5425 Response Vs Bias at 907nm

TABLE IX. SD 5425-2

DESCRIPTION: P-N Photodiode, TO-46 Header, Lens Can

ACTIVE AREA: .050in Diameter

OPTICAL/ELECTRICAL SPECIFICATION @ 25°C:

	MIN	TYP	MAX
Reverse breakdown voltage @I_R = 10μA	100V	200V	-
Dark Leakage Current @V_R = 90V	-	1.0nA	20nA
Total Capacitance @V_R = 90V, f = 1.0MHz	-	3.5pF	-
Responsivity @ 907nm, 90V	.5A/W	.58A/W	-
Rise Time (10-86%), 907nm, 90V	-	1.0ns	-
Series Resistance @ 90V	-	150Ω	-
Slow tail response, 907nm, 90V	-	12.5%	-

SPX 1527-59 operated at a pulse current of 200mA. The test results are shown in the series of photographs in Figure 41. The 135V pulse response is reproduced in Figure 42. The slow tail response of the detector alone is 7.5% of the total as shown by the trailing edge or "turn-off" portion of the response. The 15% slow tail response observed during the "on" time of the pulse results from the combination of the 7.5% slow-tail response of the detector and an additional 7.5% rise in the output of the LED due to the differential heating effect discussed on page 119. This is also true for each of the photographs in Figure 41; the "turn-off" characteristics represent the slow tail response of the detector alone and the "turn-on" characteristic is the combined effect of the LED and detector slow tail responses. At zero bias the detector slow tail response is about 70% of the total; while at 22.5V it represents only 31% of the total. At higher reverse bias the detector slow tail response drops to 21% at 45V, 15% at 67.5V, 12.5% at 90V and finally about 7.5% at 135V. The preferred operating bias for this photodiode is 90V or greater.

The slow tail response of the detector is the result of light absorbed in the undepleted regions of the silicon chip; this effect is desdribed in detail in Reference 1. The slow tail response of a photodiode can be a major limiting factor in optoelectronic data transmission. At a low data rate, the slow tail response is acceptable because the signal current can reach the full steady state value before the end of the pulse. At medium data rates, the slow tail response begins to introduce intersymbol interference that decreases the available signal current. For high data rates, the slow tail response gives a steady dc response with the fast portion of the response riding on top of the dc level. This condition is undesirable because of both the decrease in the available signal current and the increase in noise that results from full shot noise on the dc response.

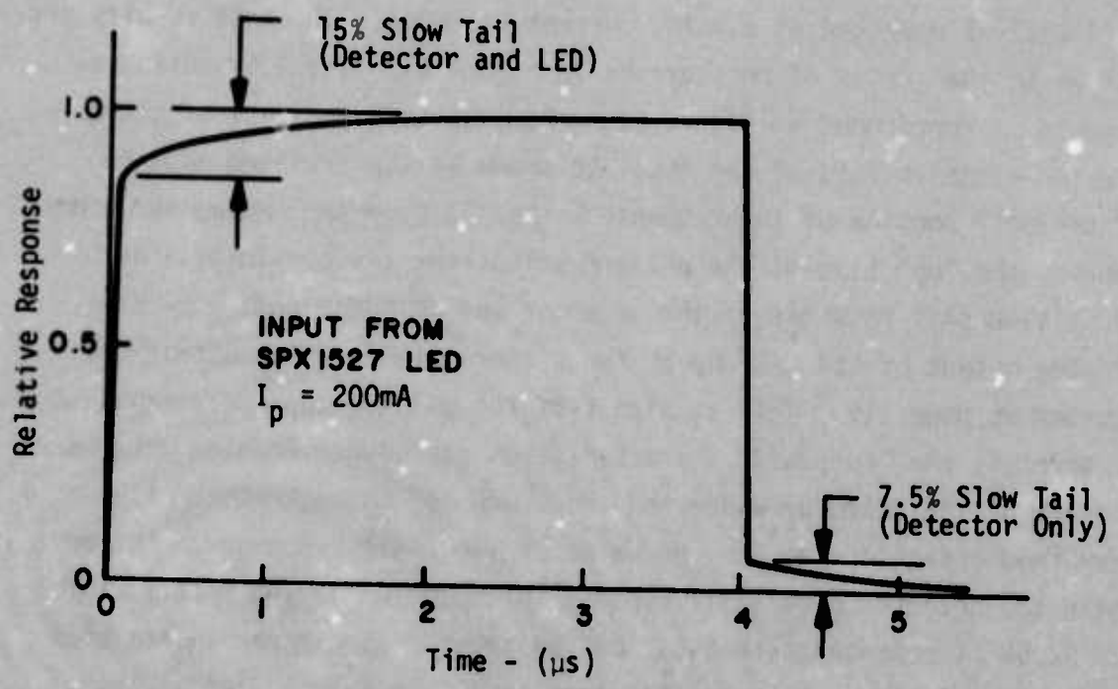

Figure 42. SD 5425 Photodiode Response at 135V Reverse Bias

The "turn off" transient in Figure 41 shows that the slow tail response has a 10-90% rise time of about 2μs. Comparing this to the 10-86% rise time of 1ns given in Table VII gives a 2000/1 ratio between the fast response and the slow tail response. This shows that the data rate that can benefit from the slow tail response of this diode is about 1/2000 times the data rate that can be handled by the high-speed depletion region response. The speed of the slow tail response is determined by the bulk lifetime, wafer thickness and minority carrier diffusion constant. The SD 5425 slow tail response has a speed that is typical of most silicon photodiodes.

The SD 5425 is an acceptable photodiode for most optoelectronic data transmission applications--particularly at data rates below 15M bit/s. The active area is ideally suited for coupling to fiber optic bundles with diameters of 45mil or less. The limitation of this photodiode which tend to degrade performance at high data rates are: high capacitance, high series resistance and a significant slow tail response.

2. SPX 1615 Performance

The SPX 1615 is a p-i-n photodiode manufactured by Spectronics, Inc.; Table X gives a summary of the specifications for this device. The LED measurements using the speed-up network shown in Figure 34 were made using an SPX 1615 photodiode with the amplifier shown in Figure 23. The TO-46 lens can is ideal for coupling to the SPX 1525 fiber optic lens; the coupling loss of this interface is about 1.0dB. An analysis is presented in Appendix I which shows the basis of the 1.1ns rise time at 907nm shown in Table X. This photodiode is designed so that the entire thickness of the wafer is depleted at a reverse bias of 90V. Operation of this detector in full depletion gives minimum capacitance, minimum series resistance, and essentially eliminates the slow tail response at all wavelengths. The test set up of Figure 33 was used to evaluate the slow tail response of the SPX 1615 as a function of bias; the test results are shown in Figure 43. At 22.5V the slow tail response is about 15% of the total

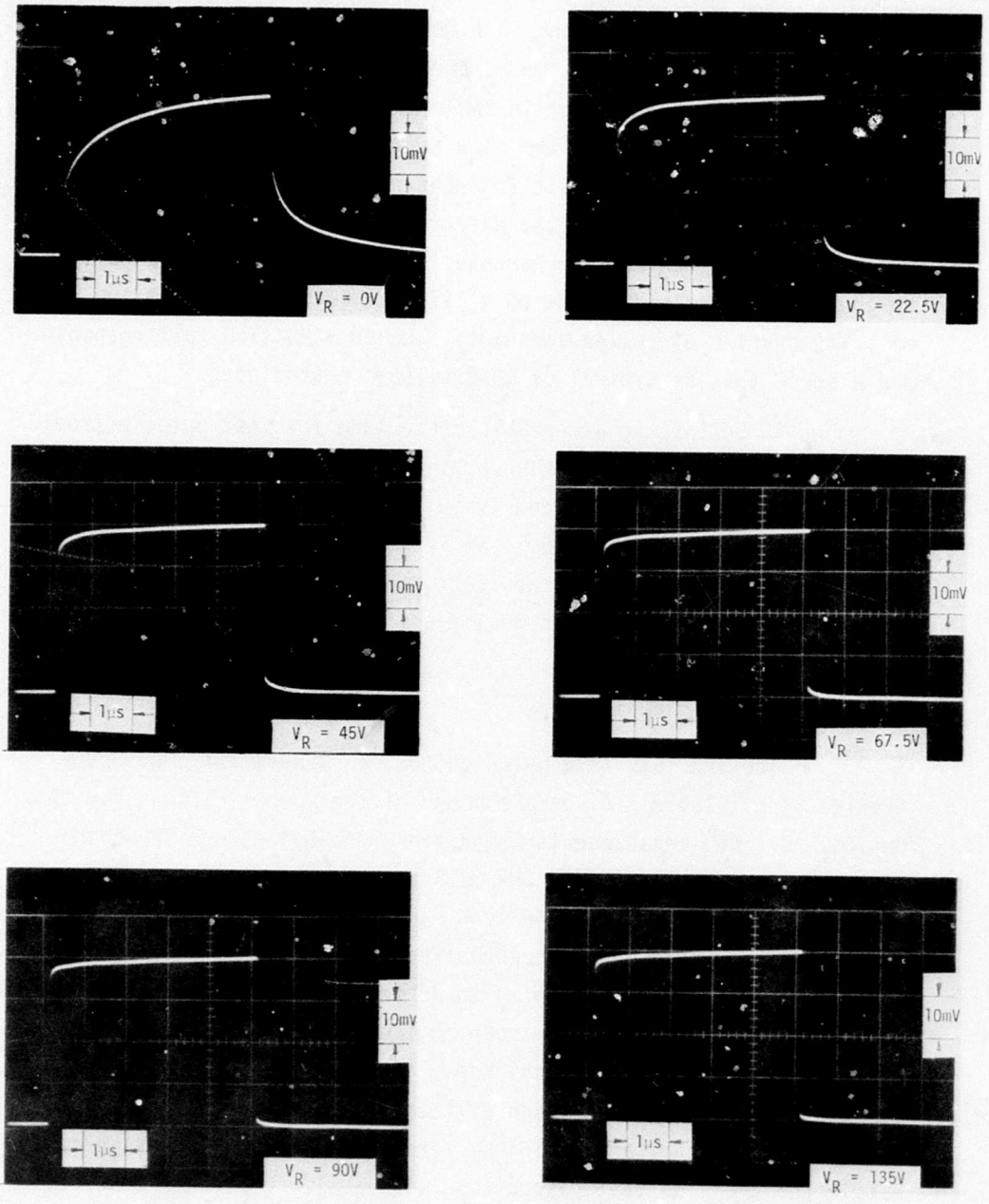

Figure 43. SPX 1615 Response Vs Bias at 907nm

Table X. SPX 1615

DESCRIPTION: PIN Photodiode, TO-46 header, lens can
CHIP THICKNESS: .004in (nominal)
ACTIVE AREA: .050in diameter

OPTICAL/ELECTRICAL SPECIFICATION AT 25°C:

	MIN	TYP	MAX
Reverse breakdown voltage @I_R=10μA	180V	200V	-
Dark leakage current @ V_R=100V	-	1nA	20nA
Total Capacitance @ V_R=100V	-	2.7pF	-
Responsivity @ 907nm	.5A/W	.64A/W	-
Rise time (10-90%) @ 907nm, 100V	-	1.1ns	-
Series Resistance (calc.) @ 100V	-	15Ω	-
Voltage for complete depletion of wafer	-	90V	-
Slow tail response @V_R=90V	-	2.5%	-

and the high-speed response is about 87% of the 90V value. However, since the wafer is only depleted about 2.0 mil, the series resistance is 160Ω and the capacitance is about 4.9pF. At a reverse bias of 90V, the slow tail response is nearly gone, the capacitance is 2.7pF and the series resistance is 15Ω. The small (2.5%) slow-tail response at 90V bias results from light striking the undepleted regions of the surface of the wafer.

The SPX 1615 is near optimum for all optoelectronic data transmission applications. The active area is ideal for coupling to fiber optic bundles with diameters up to 45 mil. For data rates up to 10M bit/s the SPX 1615 may be operated at bias voltages as low as 22.5V. For high data rate systems optimum performance is obtained at a bias voltage of 90V or higher. The photodiode/preamp noise characteristic shown in Equation (26) and Figure 5 are based on the use of an SPX 1615 photodiode at 90V bias.

In Figure 43 the "turn-off" transient for V_R = 135V demonstrates that there is almost no detector slow tail response at that bias voltage. Thus, the "turn-on" transient for V_R = 135V represents the slow tail output of SPX 1527-59 LED operated at a 200mA peak current. This LED

slow tail response is about 12.5% of the total and has a 10-90% rise time of about 3μs. The LED slow tail is only present in the "turn-on" transient because the transient change in absorption in the GaAs chip can only be observed when the junction is emitting light. Since the LED slow tail effects the "turn-on" transient but not the "turn-off" transient it is a nonlinear effect that will give rise to harmonic distortion in analog systems. The LED slow tail response can be reduced by decreasing the thermal resistance of the LED; for a particular LED it can be reduced by lowering the drive current. The detector slow tail response effects the "turn-on" and "turn-off" transients equally and therefore does not introduce nonlinearity. The 20% droop in modulation transfer function between 0.1 and 5.0MHz shown in Figures 36, 37, 38 and 39 is the result of the slow tail response of the LED and the SD 5425 detector used in those measurements.

3. PIN-040A Performance

The PIN-040A is a low-leakage silicon p-n junction photodiode made by United Detector Technology. Table XI gives a summary of the measured and calculated characteristics of this device. The flat window TO-46 header made it necessary to use the epoxy filled lens in the fiber optic interface for this unit. While this photodiode does

Table XI. PIN-040A

DESCRIPTION:	P-N Photodiode, TO-46 header, flat window
ACTIVE AREA:	.040in diameter
OPTICAL/ELECTRICAL CHARACTERISTICS AT 25°C	
Reverse breakdown voltage @I_R = 10μA	90V
Dark leakage current at V_R = 30V	1.0nA
Total capacitance @ V_R = 90V	6.7pF
Responsivity @ 907nm	0.4A/W
Rise Time (0-50%)	<1.0ns
Series resistance @ 90V (estimate)	60Ω
Slow tail response @90V	50%

have a planar diffused junction, there is no oxide on the surface of the diffused p-type layer. The absence of the antireflection coating effect

normally provided by the thermally grown SiO_2 in the active area gives a low value for the responsivity at 907nm. The ohmic contact to the diffused p-type layer is very small--about 1.5 mil X 1.5 mil. This undesirable contact geometry leads to a relatively large series resistance; the capacitance is higher than the SD 5425 even though the area is smaller. The plugable interface loss for the SPX 1525 fiber optic lens is about 5.2dB. Figure 44 shows the 907nm response vs bias characteristic for the PIN-040A. Notice that the "turn-off" transient is the same for all bias voltages. Increasing the reverse bias on this unit has the effect of increasing only the fast response. The 50% slow tail response at the breakdown voltage is not a desirable characteristic. The slow tail response of the PIN-040A (and all other photodiodes tested on this program) will decrease for shorter wavelength.

The PIN-040A is not recommended for use in optoelectronic data transmission systems. The high capacitance, high series resistance, low responsivity and large slow tail response combine to make this component unsuitable. The interface loss using the SPX 1525 is 4.2dB higher than for the SD 5425 or SPX 1615.

4. 5082-4207 Performance

The 5082-4207 is an epitaxial p-i-n planar silicon photodiode made by Hewlett-Packard. Table XII shows the specifications for this photodiode. This device uses the same form of annular contact to the p-type diffused region that is used on the SD 5425 and SPX 1615. The epitaxial chip eliminates most of the series body resistance; however, the use of a thin high-resistance p-type region gives a relatively large value of series resistance. The measured capacitance shown in Table XII is comparable to the SPX 1615 even though the junction area is smaller. Because of the flat window can the epoxy filled lens interface shown in Figure 40 was used with this photodiode. The plugable interface loss with the SPX 1525 fiber optic lens was estimated to be 5.2dB. If a TO-18 lens can were used on this unit the plugable interface loss would be about 2.0dB. The responsivity and rise time of this photodiode have good and useful values at 770nm

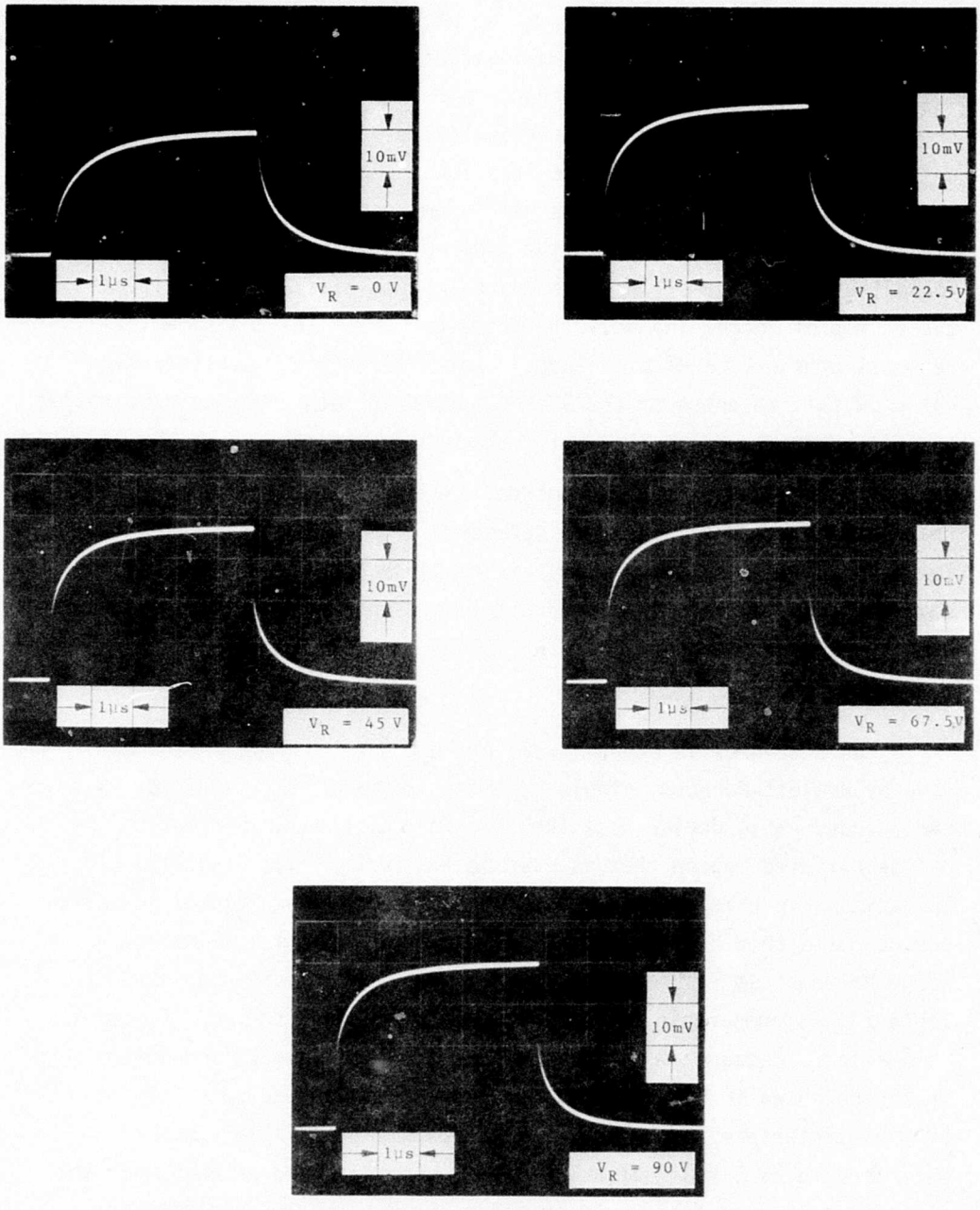

Figure 44. PIN-040A Response Vs Bias at 907nm

Table XII. 5082-4207

DESCRIPTION:	Epitaxial p-i-n photodiode, TO-18 Header, Flat Window
ACTIVE AREA:	.040in diameter

OPTICAL/ELECTRICAL CHARACTERISTICS AT 25°C:

Maximum steady reverse voltage	20V
Peak inverse voltage	200V
Dark leakage current @V_R = 25V	0.5nA
Total Capacitance @V_R = 20V (measured)	2.6pF
Responsivity @ 770nm(Manufacturers Spec.)	0.5A/W
Rise time (10-90%) @ 770nm(Manufacturers Spec)	<1.0ns
Series resistance	50Ω (max)
Slow tail response @ 22.5V, 907nm(Measured)	13%

where they are specified. However, at 907nm the responsivity is down to about 0.33A/W and a 13% slow tail response is present. The response vs bias for the 5082-4207 is shown in Figure 45. The lightly doped n-type epitaxial layer in this photodiode is fully depleted at a bias of 22.5V; the use of larger bias voltage produces a negligible improvement in performance.

The Hewlett-Packard 5082-4207 p-i-n photodiode is useful in many optoelectronic data transmission applications. Its advantages are low capacitance and low bias voltage. Its principal disadvantages are low responsivity, high series resistance and a 13% slow tail response at 907nm. The plugable interface loss with the SPX 1525 is 4.2dB more than for the SD 5425 and SPX 1615.

5. TISL59 and TISL79 Performance

The TISL59 is a p-n junction planar silicon avalanche photodiode made by Texas Instruments, Inc. Table XIII shows the specifications for this photodiode. The silicon wafer uses a guard ring diffusion to eliminate surface breakdown and confine the avalanche multiplication to a .30in diameter region. A flat-window TO-5 header is used for this unit. Both the anode and cathode of the photodiode are isolated from the header; a pin is provided for grounding the

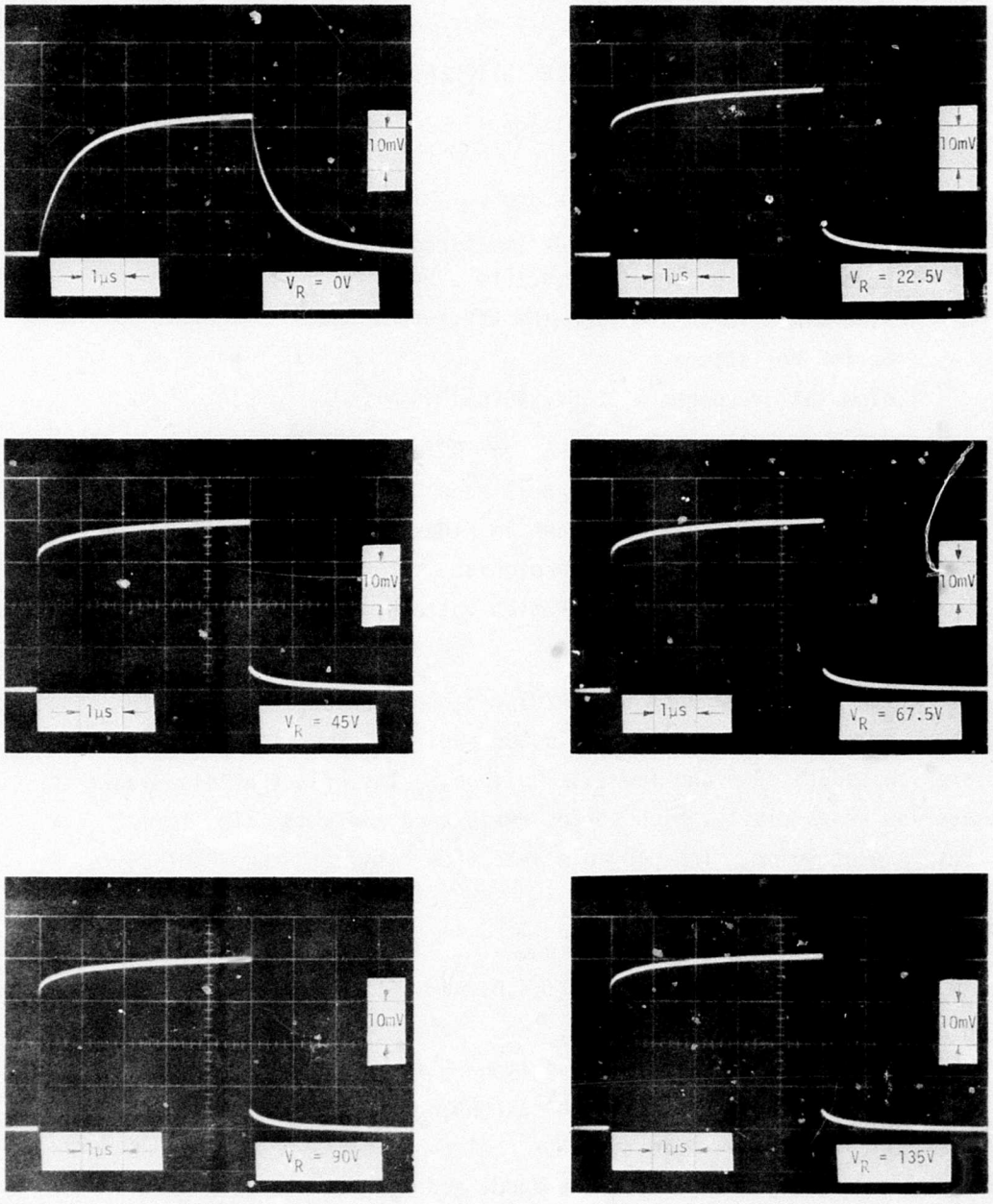

Figure 45. 5082-4207 Response Vs Bias at 907nm

header. Because of the flat window can, the epoxy filled lens interface shown in Figure 40 was used with this photodiode. The plugable interface loss with the SPX 1525 fiber optic lens is estimated to be 7.7dB; this is 6.7dB more than the SPX 1615 interface loss.

Table XIII. TISL59 Avalanche Photodiode

DESCRIPTION: silicon p-n junction avalanche photodiode, TO-5 header, flat window, wafer isolated from header, operating temperature range -65 to +125°C.

ACTIVE AREA: .030in diameter

OPTICAL/ELECTRICAL SPECIFICATION @ 25°C:

		MIN	TYP	MAX
Reverse breakdown voltage @ I_R = 10μA		140V	170V	200V
Dark leakage current @ V_R = 100V.	Bulk	-	20pA	150pA
	Surface	-	10nA	-
Total capacitance @ V_R = 100V, f = 1.0MHz		-	8.5pF	12pF
Responsivity at 907nm, m = 1.	ac	-	.25A/W	
	dc	-	.50A/W	
Gain-bandwidth product at max gain		-	80GHz	-
Series resistance		-	5Ω	-
Gain for sustained avalanche		100	200	-
Slow tail response at 907nm		-	0.5	-

The temperature coefficient of breakdown voltage for the TISL59 is typically 190mV/°C. Thus, an ambient temperature range from -55°C to +125°C requires a bias voltage change of about 34V to maintain constant avalanche gain. This voltage change is only about 20% of the

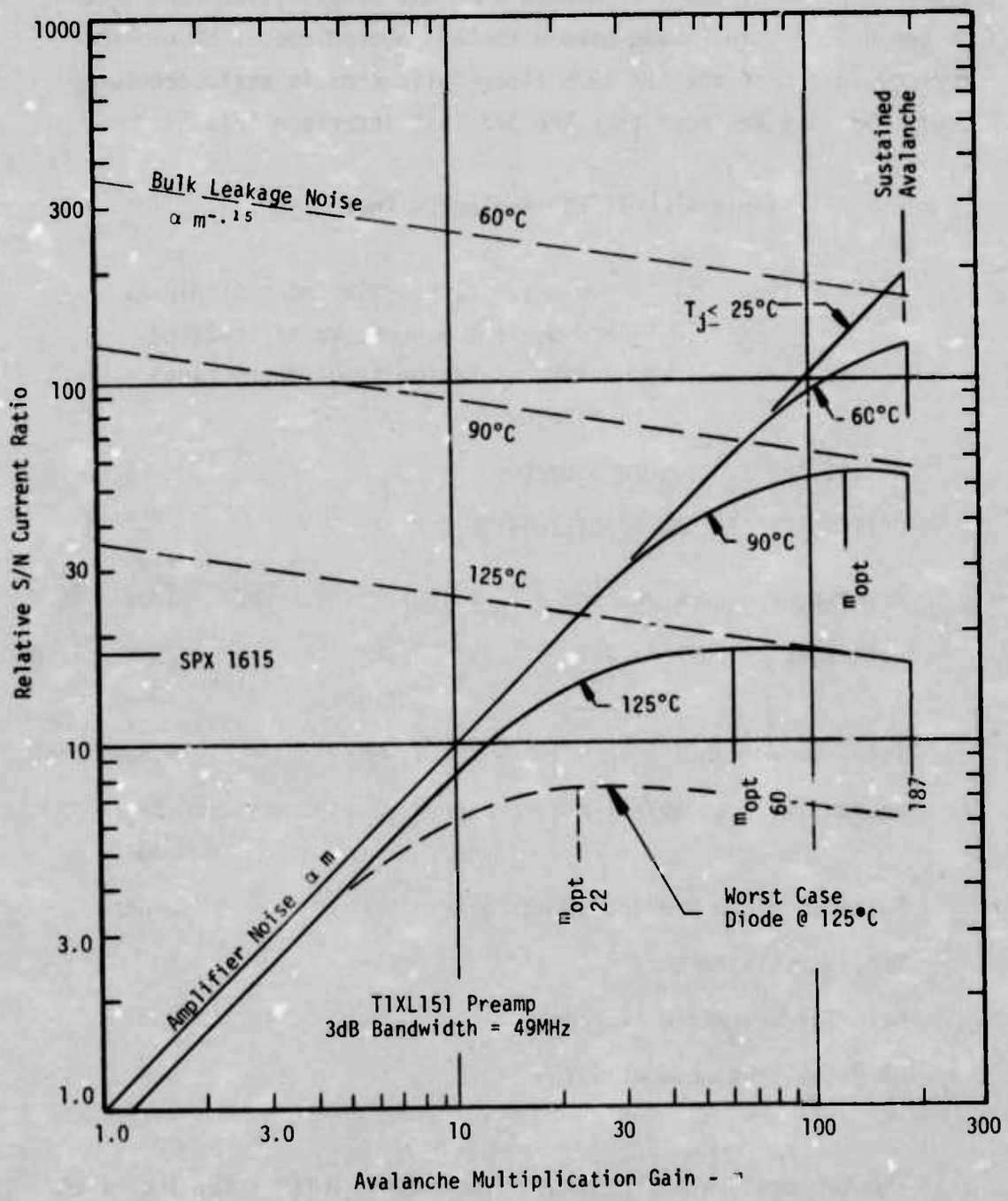

Figure 46. TISL59 S/N Performance

nominal 170V breakdown voltage. A low temperature coefficient of breakdown voltage is typical for the p-n junction guard-ring construction used in the TISL59. This desirable characteristic makes it possible to construct practical voltage regulator circuits that provide constant avalanche gain over the full temperature range -55°C to +125°C.

Avalanche gain, m, in a photodiode is signal gain ahead of the preamp and, therefore, reduces the noise contribution of the preamp. The resulting improvement in S/N as compared to a p-i-n diode is the major performance advantage offered by avalanche gain. Unfortunately, the avalanche process is itself noisy. Increasing the reverse bias voltage from zero first causes the S/N (current ratio) to increase linearly with m as shown in Figure 46. This is followed by a region in which S/N achieves a maximum value at the optimum value of avalanche gain, m_{opt}. For still higher voltage bias, the S/N drops slowly with increasing m. In the TISL59 the S/N for $m > m_{opt}$ varies as $m^{-.15}$. Finally, a bias voltage is reached at which some portion of the junction goes into sustained avalanche breakdown. This condition is characterized by an abrupt increase in avalanche noise which causes a precipitous drop in S/N. As shown in Table XIII the gain for sustained avalanche tends to be different for each diode ranging upward from a minimum value of 100. The device tested on this program has a sustained avalanche threshold of m = 187 at a bias voltage of 162V.

The S/N scale in Figure 46 is a relative scale; however, the S/N improvement at m_{opt} is typical for the TISL59 used with a high performance preamp such as the TIXL151 or the Spectronics, Inc. intermediate bandwidth preamp shown in Figure 24.

In an avalanche photodiode, only the bulk dark leakage current is multiplied by the avalanche gain. The larger surface leakage current shown in Table XIII flows to the diffused guard ring and is not acted on by the avalanche gain. Thus, only the smaller bulk leakage current is important in determining the S/N performance of an avalanche photodiode. Typical leakage current values in Table XIII show that the surface leakage is about 500 times higher than the bulk leakage. As the temperature of the diode is increased above 25°C, both bulk and surface dark leakage currents increase about a factor of 2 for each 10°C; for the range 25°C to 125°C the two components of leakage current will increase by about 1000 times. The effect on S/N is shown in Figure 46. The drop in S/N at 125°C for m = 1 is caused by the increase in surface leakage; the drop in S/N at $m \geq m_{opt}$ is the result of the increase in bulk leakage. At 25°C the bulk leakage is so low (~20pA) that m_{opt} is greater than the sustained avalanche threshold. Therefore, for junction temperature, T_j, between -55°C and 25°C the S/N improvement is proportional to m over the entire useful bias range. At 60°C the bulk leakage is about 200pA and its effect on S/N is significant only for m > 100. At 90°C the bulk leakage is about 2nA and m_{opt} is about 125; the S/N at m_{opt} is about 54 times higher than for m = 1. At 125°C the bulk leakage is about 20nA and m_{opt} is about 60. The S/N at m_{opt} is about 18 times higher than for m = 1; the S/N improvement at 125°C drops to about 17.3 for m = 125.

Figure 46 shows one of the basic limitations of avalanche detectors. If the avalanche gain is held constant at m = 125, then the S/N drops more than 7 times as the temperature goes from -55°C to 125°C. If the detector is biased for an avalanche gain of 60 (m_{opt} at 125°C), then the S/N changes by about 3.3 times for temperatures between -55°C and +125°C. For a worst case system design only the performance at the highest operating junction temperature can be considered. Thus, the considerable S/N improvement offered by

avalanche photodiodes at junction temperatures up to 60°C are not applicable to military avionics systems which require junction temperatures of 125°C. Compared to m = 1, the typical TISL59 shown in Figure 46 has a S/N improvement of 18 times at 125°C. A TISL59 with the maximum bulk leakage of 150pA shown in Table XIII would have a S/N improvement at 125°C of only 7.5 times at m_{opt} = 22.

The utility of the TISL59 avalanche photodiode is further diminished by the low value of ac responsivity at 907nm shown in Table XIII. This ac responsivity of 0.25A/W is caused by the narrow depletion layer width of the TI device and is inherent to the basic structure of the unit. If the TISL59 is constructed to have a greater depletion layer width to provide an ac responsivity of 0.5A/W, the result is an increase in breakdown voltage from 170V to 450V. Comparison to Table X shows that the responsivity of the SPX 1615 is 2.56 times higher than the ac responsivity of the TISL59. The framework of comparison for photodiodes in this report is the plugable optical interface shown in Figure 40; this coupling scheme is based on readily available optical elements and conventional Galileo fiber optic bundles. Within the context of this coupling scheme, the interface loss for the TISL59 is 6.7dB (4.68 times) more than the interface loss of the SPX 1615. The amplifier noise is affected by the photodiode capacitance as shown by Eq(16). Therefore, the amplifier noise levels with the two photodiodes must be included in the S/N comparison. The noise data taken at 25°C in support of Figure 46 used a TIXL151 preamp similar to the one characterized in Section IV.A. The measured rms output noise voltage is 240μV with the TISL59 and 160μV with the SPX 1615. This 1.5 times S/N improvement for the SPX 1615 is consistent with the 2.7pF capacitance from Table X compared to the 8.5pF capacitance of the TISL59 given in Table XIII.

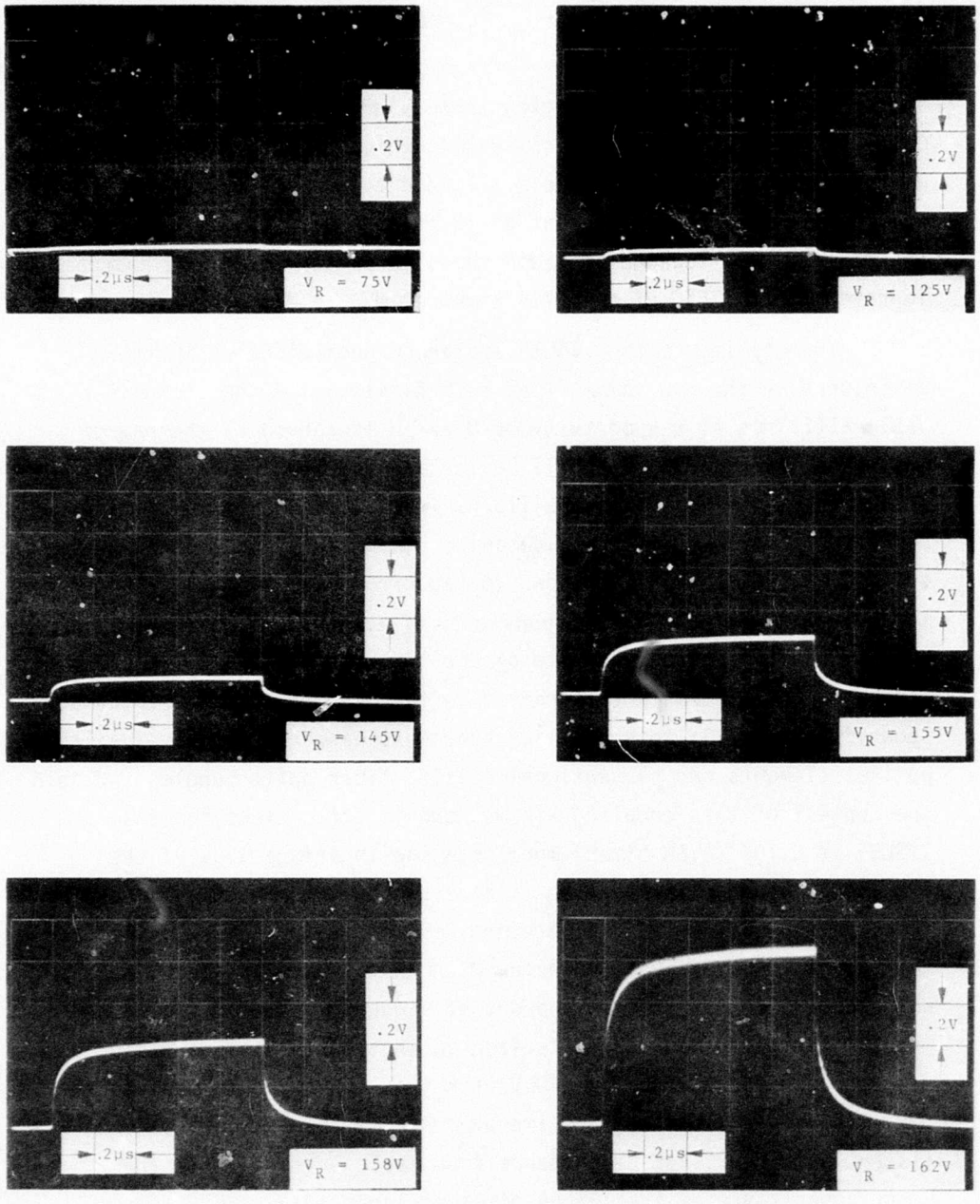

Figure 47. TISL59 Response Vs Bias at 907nm

When the interface loss (4.68 times), responsivity ratio (2.56 times), and noise ratio (1.5 times) are all combined, the total S/N of the SPX 1615 is 18 times higher than the TISL59 for m = 1. This comparison point for SPX 1615 is shown in Figure 46. It should be pointed out that the TISL59 interface loss could be reduced by at least 3.0dB by optimizing the package for that unit.

Figure 46 shows that for a military avionics system requiring a junction temperature of 125°C the S/N of a typical TISL59 is equivalent to the SPX 1615; the worst case TISL59 (150pA bulk leakage at 25°C) is inferior to the SPX 1615 at 125°C. Even at 25°C the S/N of the TISL59 is only 10 times higher than the S/N of the SPX 1615. Based on this performance comparison, the added cost and complexity of the TISL59 avalanche photodiode is not justified in a fiber optic data transmission system.

Table XIII shows that the dc responsivity of the TISL59 at 907nm is 0.5A/W, this value is twice as large as the ac responsivity. This leads to a 50% slow tail response as shown in Figure 47. The fast or ac portion of the rsponsivity has a 10-90% rise time of less than 1ns and the slow tail response has a 10-90% rise time of about 0.5μs. The slow tail response is seen to be independent of bias voltage. The series of response curves shown in Figure 47 all have the same voltage scale; the magnitudes of the output show the relative avalanche gain for each bias voltage. The curve for 162V corresponds to an avalanche gain of 187; this point is just below the threshold for sustained avalanche. Figure 48 shows a plot of avalanche multiplication gain vs. bias for the TISL59 that was evaluated; this curve shows the extremely critical dependence of avalanche gain on bias voltage that is characteristic of these units.

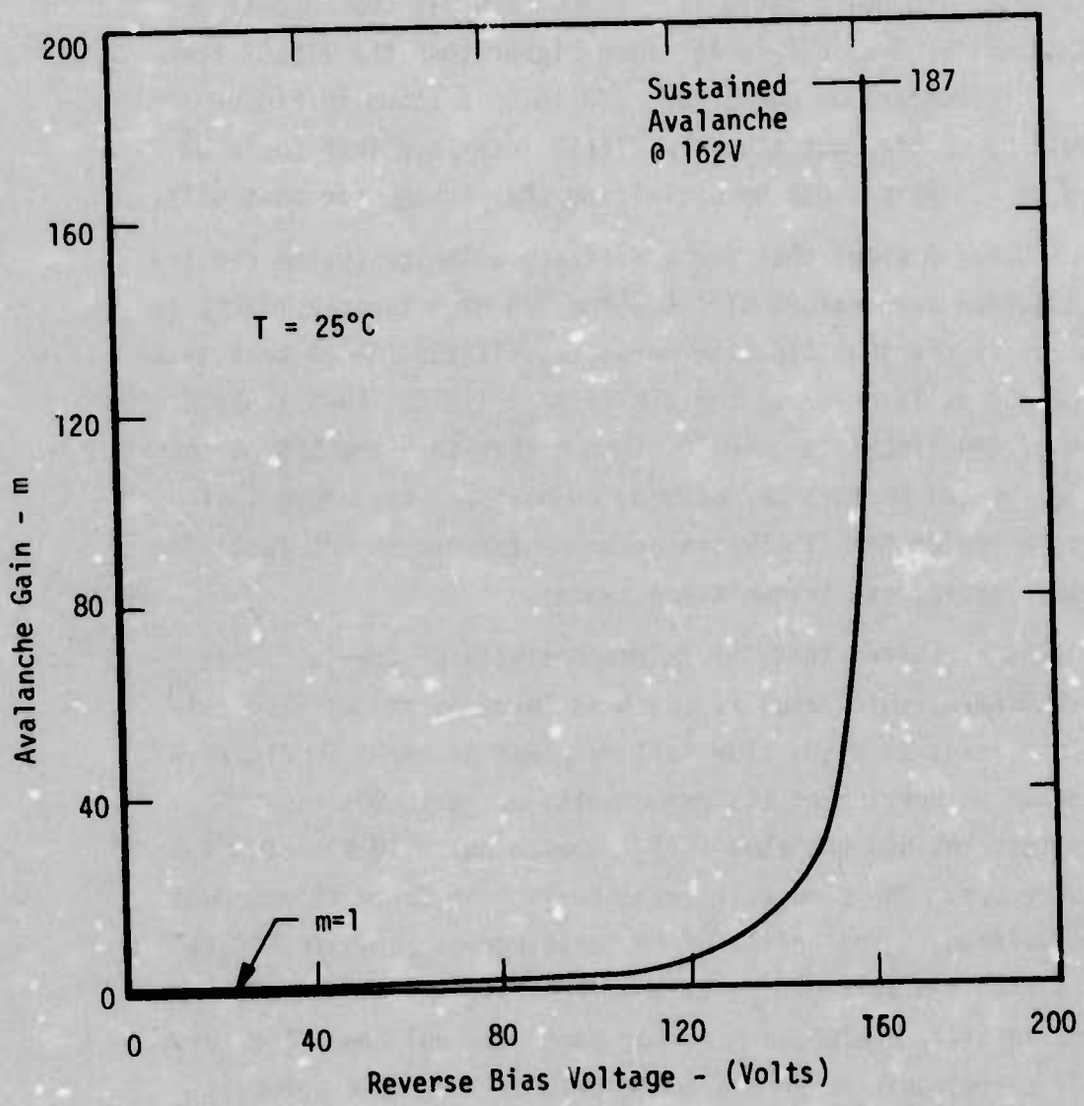

Figure 48. TISL59 Avalanche Gain Vs Bias

An overview of the performance of the TISL59 shows that this avalanche photodiode is not optimized for 907nm wavelength. Furthermore, the relatively high junction capacitance increases high frequency noise and the small junction diameter makes it difficult to couple to .045in diameter fiber optic bundles. A significant improvement in performance results if the TISL59 is operated at a wavelength of 800nm. At this wavelength the ac and dc responsivities are equal at about 0.6A/W and the slow tail response disappears.

The TISL79 is an avalanche photodiode receiver module manufactured and sold by Texas Instruments, Inc. This module includes a TISL59 avalanche photodiode, a TIXL151 hybrid preamp and a regulated power supply to track the breakdown voltage of the photodiode in such a way that the overall gain of the unit is constant with temperature. The measured performance of this module is consistent with the data provided by TI and the performance of the individual components as discussed above. The characteristics of the module provided by TI are presented in Table XIV.

Optical coupling to this module was accomplished with the plugable interface shown in Figure 40. This gives an interface loss of 7.7dB (5.9 times). Thus, for this fiber optic coupling technique the NEP given in Table XIV must be multiplied by 5.9.

$$\begin{aligned} NEP &= (5.9)(1.91 \times 10^{-13})\ WHz^{-\frac{1}{2}} \\ &= 1.13 \times 10^{-12}\ WHz^{-\frac{1}{2}} \end{aligned} \tag{148}$$

This NEP value is 6.7 times better than the expected NEP = $7.6 \times 10^{-12}\ WHz^{\frac{1}{2}}$ based on the TIXL151 noise performance from Figure 25 and the SPX 1615 characteristics given in Table X. The S/N comparison presented in Figure 46 predicts that the S/N of the avalanche module should be 6.9 times higher than the SPX 1615 at

Table XIV. TISL79 Avalanche
Photodiode Module

DESCRIPTION: Optical receiver module including
TISL59 avalanche photodiode
TIXL151 hybrid preamp
regulated power supply for constant gain.

ACTIVE AREA: .030in diameter

OPTICAL/ELECTRICAL SPECIFICATION

		min.	meas.	max.
High Voltage supply @ 1.5mA		240V	240V	255V
Amplifier bias voltage @ 20mA		8.0V	8.5V	9.0V
Photodiode responsivity @ 907nm	ac		.25A/W	
	dc		.45A/W	
Avalanche multiplication gain	-40°C		120	
	+60°C		125	
Transresistance of preamp			5.4kΩ	
Module responsivity @ 907nm	ac		1.69×10^5V/W	
	dc		3.04×10^5V/W	
Output noise voltage	25°C		300μV	
	60°C		300μV	
Noise Equivalent Power	25°C		1.91×10^{-15}WHz$^{-\frac{1}{2}}$	
	60°C		1.91×10^{-13}WHz$^{-\frac{1}{2}}$	
Signal bandwidth, 3dB			55MHz	

25°C and 5.8 times higher at 60°C. Thus, the measured and predicted performance of the module are in good agreement.

Figure 49 shows the time response of the TISL79 avalanche module at two bias voltages corresponding to avalanche gains of 12 and 125. The voltages shown are the external values applied to the voltage regulator and are not the voltages applied to the photodiode. The expected 44% slow tail response is observed at m = 125. At m = 12, the slow tail response is about 50%.

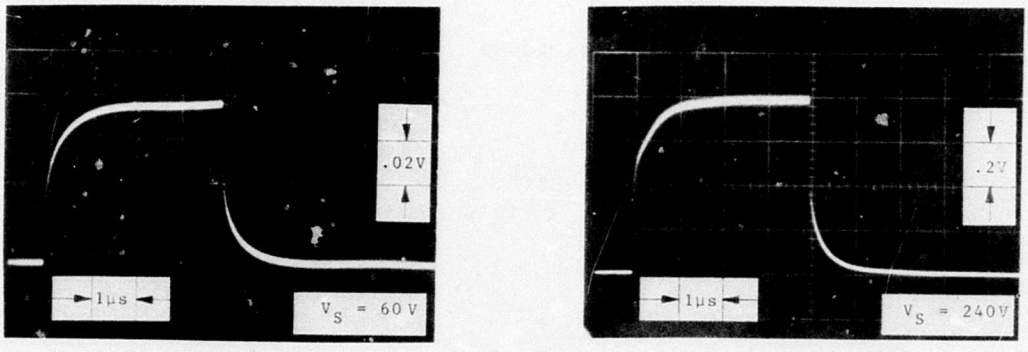

Figure 49. TISL79 Response Vs Bias at 907nm

6. C30817 Performance

The C30817 is a silicon planar avalanche photodiode made by RCA. This device uses the n-p-π-p structure which gives a different set of performance characteristics than the p-n guard-ring structure used by TI. The characteristics of the C30817 are shown in Table XV. A flat window TO-5 header is used for this unit. Both the anode and cathode of the photodiode are isolated from the header; a pin is provided for grounding the header. Because of the flat window can, the epoxy filled lens interface shown in Figure 40 was used with this unit. The plugable interface loss with the SPX 1525 fiber optic lens

Table XV C30817 Avalanche Photodioe

DESCRIPTION: silicon n-p-π-p avalanche photodiode, reach through structure to eliminate slow tail response, TO-5 header, flat window, wafer isolated from header, operating temperature range -40 to +70°C.

ACTIVE AREA: .031in diameter (.08cm)

OPTICAL/ELECTRICAL SPECIFICATION @ 25°C

		Min.	Typ.	Max.
Reverse breakdown voltage		300V	375V	475V
Temperature coefficient of breakdown voltage		-	1.8V/°C	-
Responsivity @ 907nm		.51A/W	.62A/W	-
Data leakage current @ 335V	bulk	-	-	100pA
	surface	-	.1μA	.2μA
Total capacitance @ 335V		-	2pF	4pF
Rise time, 10-90%, 50Ω load		-	2ns	3ns
Series resistance		-	10Ω	15Ω
Avalanche gain @ 335V		100	129	-

is estimated to be 7.4dB; this is 6.4dB (4.4 times) more than the SPX 1615 interface loss. The temperature coefficient of breakdown voltage at 1.8V/°C is 9.5 times higher than the TISL59 and the operating bias voltage for the C30807 is two times higher than the TISL59. For the limited temperature range of -40°C to +70°C the bias voltage must be changed by 200V from 235V to 435V respectively to hold the avalanche gain constant at a typical value of 120. Compared to the room temperature bias of 335V this represents a 60% change as compared to the 20% change required for the TISL50 over a wider temperature range (-55°C to +125°C). The large bias range required by the C30817 is undesirable because it increases the complexity of the required voltage regulator and requires a two times higher power

supply input voltage than the TISL59. Even though this bias characteristic is undesirable, it is inherently related to the n-p-π-p structure and must be tolerated to achieve some of the very desirable performance characteristics associated with this construction.

One of the desirable characteristics of the RCA reach through structure is the elimination of the slow-tail response. Figure 50 shows the response of the C30817 at 907nm as a function of bias. The slow-tail response is eliminated for all bias voltages greater than 150V. This RCA avalanche detector and the SPX 1615 are the only two photodiodes investigated on this program which do not show a significant slow-tail response. The 10-90% rise time of the RCA diode at 335V is typically 2ns. This is adequate for many applications but is slower than both the SPX 1615 and the TISL59.

Another desirable characteristic of the RCA device is the relative insensitivity of avalanche gain to reverse bias voltage shown in Figure 51. This characteristic is inherently related to the large temperature coefficient of breakdown voltage; however, it is useful in laboratory work at constant temperature because it allows the avalanche gain to be set and controlled more precisely. Figure 51 should be compared to the similar curve for the TISL59 shown in Figure 48.

The S/N performance of the C30817 is presented in Figure 52. From Figure 52 the useful range of bias is for $m > 30$; this range is marked in Figure 52. At room temperature the avalanche noise on the bulk leakage is completely negligible and the major effect of avalanche gain is to reduce the preamp noise. At the recommended bias voltage of 335V the avalanche gain is 112. A photodiode with a maximum bulk leakage of 100pA at 25°C will have a bulk leakage of about 2.3nA at 70°C. In this case m_{opt} is near 112 and the S/N improvement is 51 times compared to $m = 1$. The responsivity and capacitance of the C30817 are essentially the

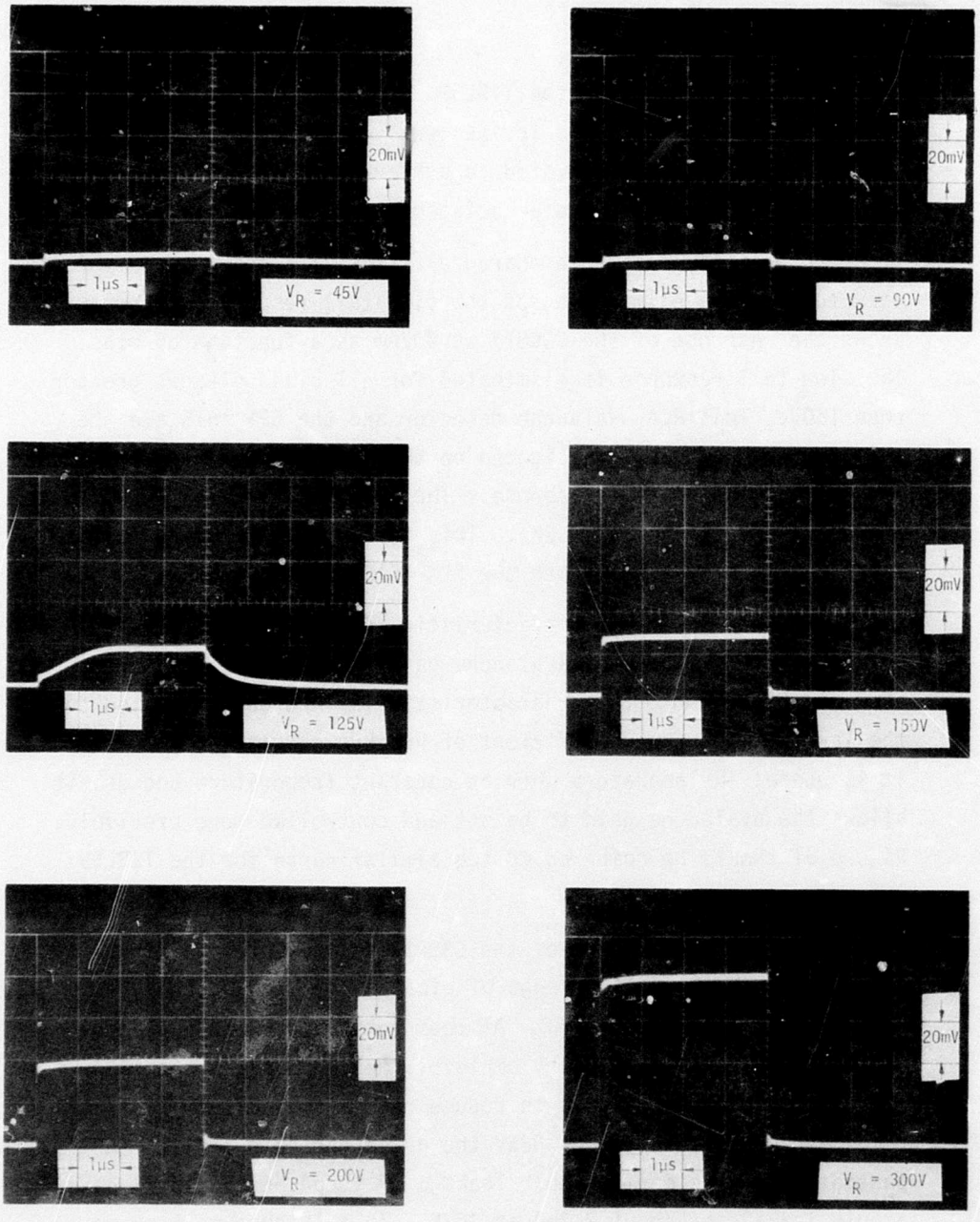

Figure 50. C30817 Response Vs Bias at 907nm

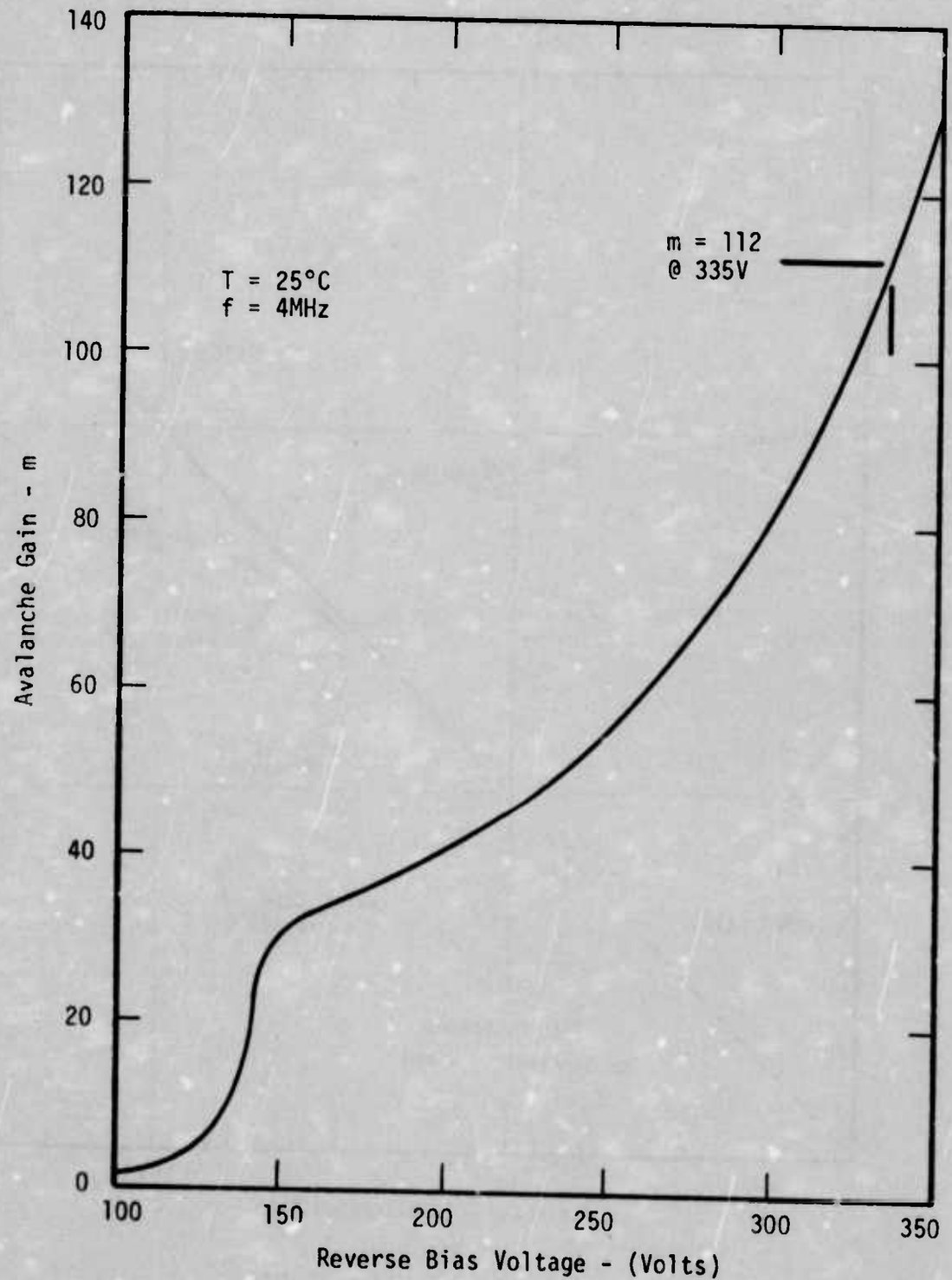

Figure 51. C30817 Avalanche Gain Vs Bias

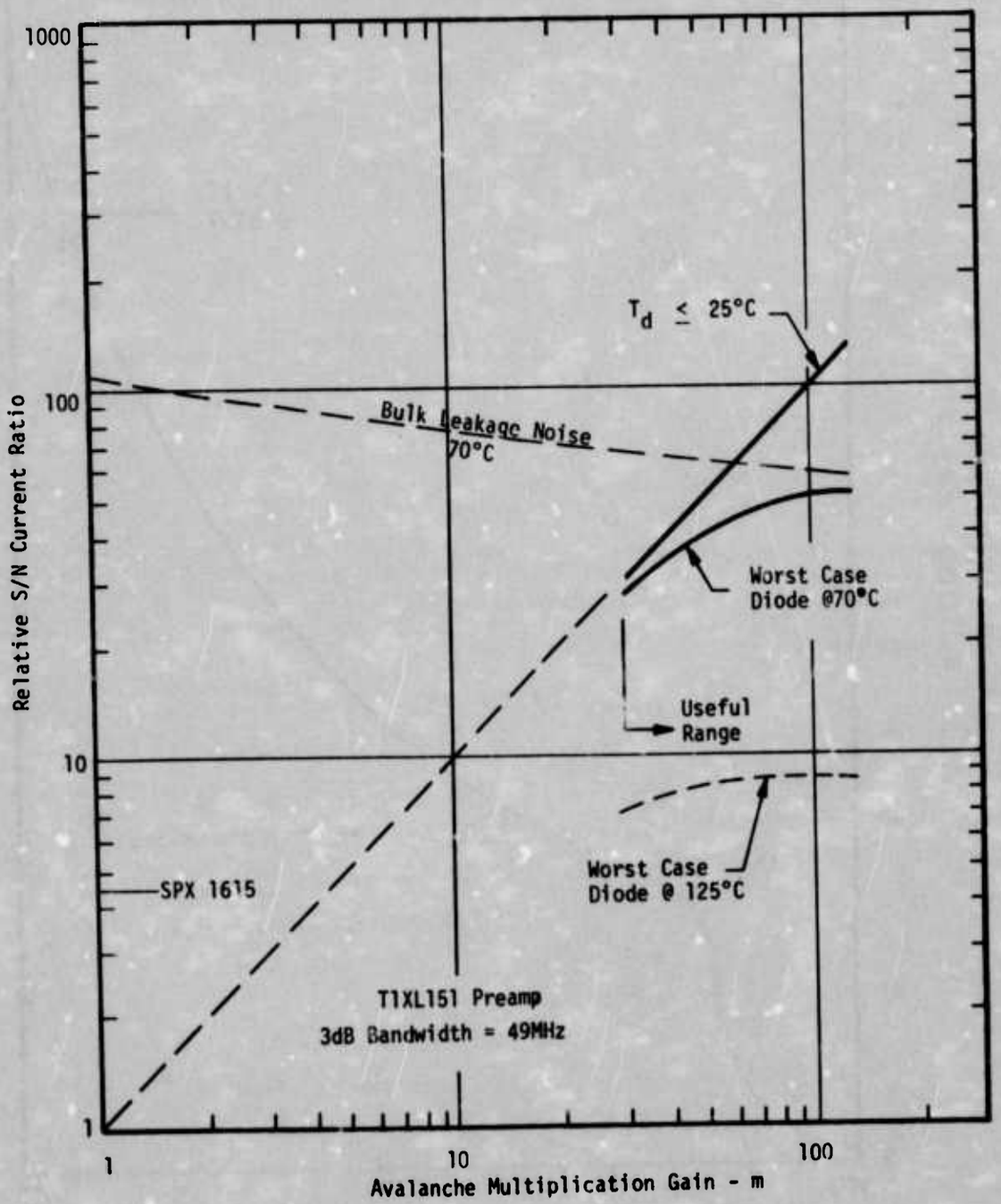

Figure 52. C30817 S/N Performance

same as the SPX 1615. Therefore, no correction factor for these parameters is needed to compare these two photodiodes. The interface coupling loss for the C30817 is 6.4dB (4.4 times) more than the SPX 1615. The S/N for the SPX 1615 is 4.4 times higher than for the C30817 at m = 1; at least 3.0dB of the interface coupling loss of the RCA photodiode could be removed by optimizing the package.

Figure 52 shows that the C30817 S/N for m = 112 and $T_j \leq 25°C$ is about 25 times higher than the SPX 1615. Comparing Figure 46 and Figure 52 shows that at the same avalanche gain, the S/N of the C30817 is 4.1 times higher than for the TISL59. The worst case C30817 operated at 70°C has a S/N that is 11.6 times higher than the SPX 1615. If the worst case C30817 could be operated at 125°C the S/N at m = 112 would be 2 times higher than for the SPX 1615 or the typical TISL59.

The RCA data sheet supplied with the C30817 gives a room temperature NEP of 1×10^{-14} $WHz^{\frac{1}{2}}$ at 907nm and 335V. However, when the avalanche photodiode is combined with the TIXL151 hybrid preamp and the plugable optical interface, the NEP of the optical receiver is significantly lower. At 335V the overall responsivity of the C30817 to the 907nm light from the fiber optic lens is

$$\frac{mR}{4.4} = \frac{(112)(62A/W)}{4.4} = 15.8A/W \qquad (149)$$

From Eq (143) the input noise current of the TIXL151 is

$$i_{nT} = 30nA \qquad (143)$$

From Eq(29) the equivalent noise bandwidth of the TIXL151 is

$$\Delta f_a = 2.48\, f_e = (2.48)(49\text{MHz})$$

$$\Delta f_a = 122\text{MHz} \tag{150}$$

Combining Eqs (143), (149) and (150) gives the NEP of the receiver

$$\text{NEP} = \frac{4.4 i_{nT}}{mR(\Delta f)^{\frac{1}{2}}}$$

$$= \frac{30\text{nA}}{(15.8\text{A/W})(122\text{MHz})^{\frac{1}{2}}} \tag{151}$$

$$= 1.72 \times 10^{-13}\ \text{WHz}^{\frac{1}{2}}$$

Figure 5 shows a theoretical NEP with an SPX 1615 photodiode of

$$\text{NEP} = 4.3 \times 10^{-12}\ \text{WHz}^{\frac{1}{2}} \tag{152}$$

The ratio of Eq(152) to Eq(151) shows that the RCA avalanche photodiode/preamp has an NEP that is 25 times better than the SPX 1615/preamp NEP. This result is in good agreement with the S/N performance presented in Figure 52.

An overall review of the performance of the C30817 avalanche photodiode shows a number of desirable characteristics including

- low series resistance,
- low capacitance
- no slow tail response,
- high responsivity at 907nm, and
- avalanche gain relatively insensitive to bias voltage.

However, this photodiode is not packaged in an optimum manner for coupling to .045in diameter fiber optic bundles and the maximum operating junction temperature of 70°C severely limits its usefulness in military avionics applications which often require 125°C junction temperatures. In addition, the rise time is a factor of two slower than a p-i-n photodiode (SPX 1615) at 1/3 to 1/4 the bias voltage and the large temperature coefficient of breakdown voltage adds to the complexity of the voltage regulator needed to control the avalanche gain. Based on this evaluation, the C30817 is recommended for laboratory use and in special applications in the commercial temperature range of -40°C to +70°C. This avalanche photodiode is not recommended for general use in military fiber optic data transmission systems.

7. Galileo Link Performance

Galileo Electro Optics markets a single channel fiber optic digital data transmission link. This system consists of a transmitter module, a terminated fiber optic bundle and a receiver module shown in Figure 53.

The transmitter module, designated model 3555971F, is contained in a stainless steel housing designed for bulkhead or panel mounting. Power and input signal are supplied through the wire leads extending from the unit. The heart of the transmitter is a hybrid LED/driver mounted in a flat window TO-5 header. This hybrid circuit is similar to the MLT327 made by Meret Inc. of Santa Monica, California. The LED driver is an integrated circuit wafer with 6 gates in parallel. The combined gate outputs drive a 20mil x 20mil flat geometry LED chip in series with an RC speed-up network. The RC network consists of a deposited resistor and a chip capacitor in parallel. The LED chip is mounted near the center of the package but no lens or focusing element is used in the transmitter.

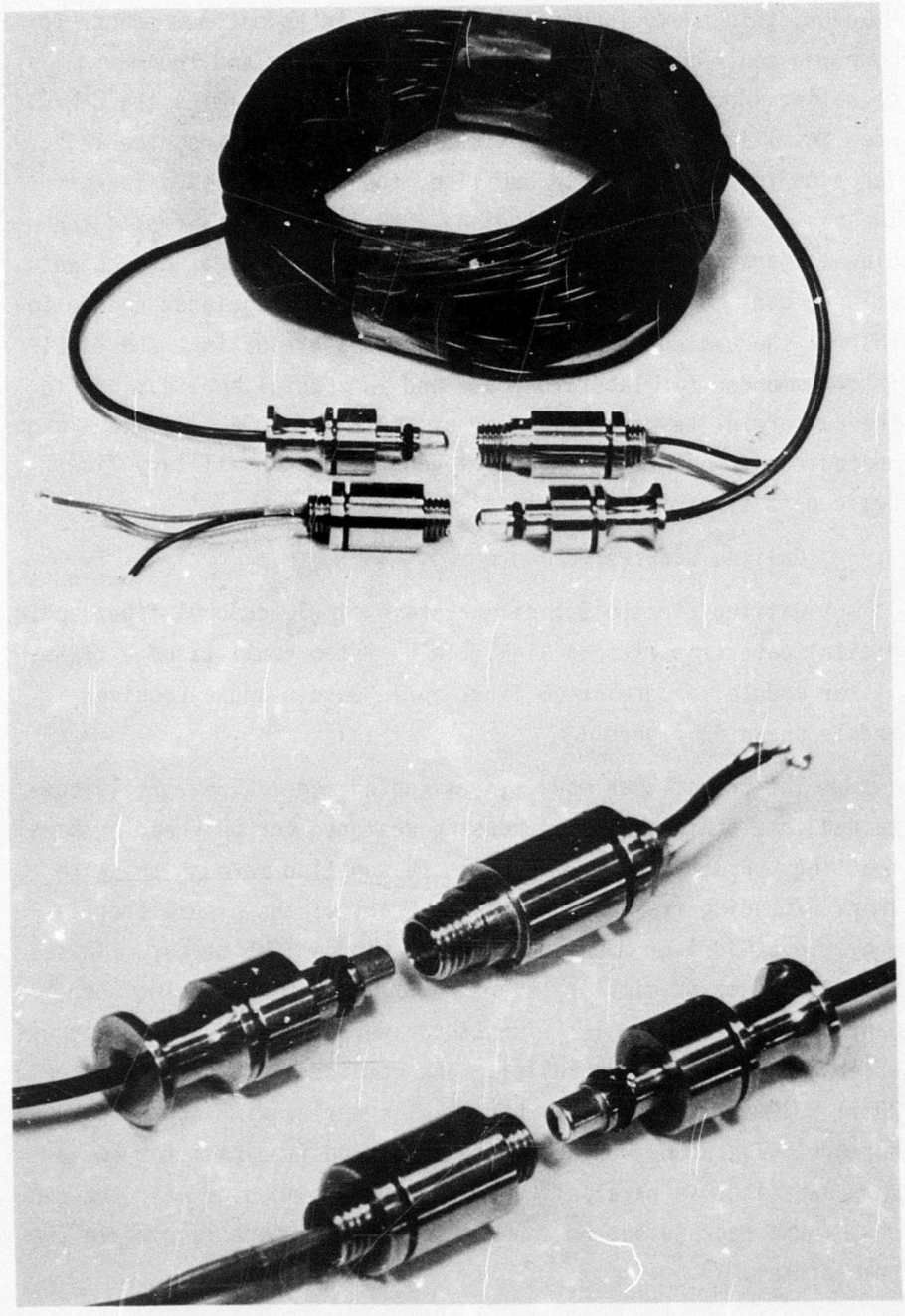

Figure 53. Galileo Data Transmission Link

The transmitter has three leads

Black = ground
Red = +5.5V (153)
Blue = pulse input

The instruction sheet received with the unit requires that an external 50Ω resistor be connected between ground and the pulse input. The current drain on the 5.5V supply is 20mA in the rest condition when no pulses are applied to the pulse input. The driver is rated for 50% maximum duty cycle. Due to the speed-up capacitor in series with the LED, the total current required with input pulses applied increases with pulse repetition rate. For 50% duty cycle above 5 MHz the operating voltage should be reduced to avoid excessive heating due to the speed-up capacitor. No attempt was made to measure the LED output power. However, the MLT327 has a specified peak power of 4mW.

The measured 10-90% rise time and fall time of the light from 3555971F transmitter is

$$t_r = 56\text{ns} \quad (154)$$

$$t_f = 42\text{ns} \quad (155)$$

The receiver module, designated model 3555971R, is also contained in a stainless steel housing designed for bulkhead or panel mounting. Power and output signal connections are provided through three wire leads extending from the unit

Black = ground
Red = +15V (156)
Yellow = signal out

The power supply lead must be bypassed to ground with an external 0.1μF capacitor. The circuit draws 5-6mA from the positive supply. The output offset voltage is 1.3V and the output will drive dc loads as small as 500Ω.

The heart of the receiver module is a hybrid photodiode/preamp mounted in a TO-5 flat window can. This hybrid circuit is similar to the MDA425 made by Meret Inc. The silicon planar photodiode is mounted in the center of the window. The active area of the detector is 59mil x 118mil; no lens or focusing element is used in the receiver. The photodiode chip is mounted on a metalized ceramic disc that covers the visible aperture of the flat window TO-5 can. A shunt feedback preamp is located under the detector ceramic and is not visible from outside the header. The preamp input terminal is not available in the detector module; thus, it is not possible to independently evaluate the detector responsivity and preamp transresistance. The measured 10-90% rise time and fall time of the 3555971R receiver module output are

$$t_r = 48\text{ns} \tag{157}$$

$$t_f = 52\text{ns} \tag{158}$$

The measured 3dB frequency of the receiver is 8.0MHz and the rms output noise voltage with no light on the detector is

$$e_{on} = 160\mu\text{V} \tag{159}$$

The information and instruction sheet supplied with the detector module did not specify an external filter cut-off for noise measurement and none was intentionally provided. When the detector module is optically driven from the fiber optic bundle provided with the system, the voltage responsivity of the receiver is

$$R_V = 7.2 \times 10^3 V/W \tag{160}$$

There is some doubt as to the effective noise bandwidth of the receiver. However, if Eq(29) is assumed to be correct for this receiver the noise bandwidth is

$$\begin{aligned} \Delta f_a &= 2.48 f_e \\ &= (2.48)(8MHz) \\ &= 19.8MHz. \end{aligned} \tag{161}$$

Combining Eqs (159), (160) and (161) gives the effective NEP of the Galileo receiver module when driven by the Galileo lens terminated fiber optic bundle

$$NEP = \frac{e_n}{R_V(\Delta f_a)^{\frac{1}{2}}}$$

$$= \frac{160\mu V}{(7.2 \times 10^3 V/W)(19.8MHz)^{\frac{1}{2}}} \tag{162}$$

$$NEP = 5.0 \times 10^{-12} WHz^{-\frac{1}{2}}$$

A 50ft fiber optic cable was purchased as part of the data transmission system. This cable is made from a conventional 45mil diameter Galileo fiber optic bundle with black PVC jacket. The ends of the cable are terminated using precision ferrules and a TO-46 size fiber optic lens very similar to the SPX 1525 termination shown in Figure 40. Stainless steel connector bodies are provided on each end of the fiber optic cable. These connectors are threaded to form a locking interface with the transmitter and

receiver modules. An o-ring is located just behind the fiber optic lens to insure a good mechanical fit at the plugable optical interfaces with the transmitter and receiver.

The data transmission system composed of the transmitter module, fiber optic cable and receiver module produces the output signal waveform shown in Figure 54. The top trace shows the output waveform on a time base of 1.0μs/division; the lower trace is an expanded view of the intensified portion of the upper trace. The time base for the lower trace is 50ns/division. The 10-90% rise time for the composite system is 70ns and the peak-to-peak output is 11mV. The 70ns rise time indicates a maximum square wave frequency of about 5MHz. Since the uncompensated preamp in the receiver has an output drift of about 5mV/°C the receiver is not suitable for use in direct coupled systems; a temperature change of 2.2°C causes an output drift equal to the peak-to-peak signal. If the output of the receiver is ac coupled to the next stage, the drift does not cause a problem. However, the ac coupled system must use Manchester coded signals and the data rate is limited to 5Mbit/s.

The voltage responsivity of Eq (160) and the 11mV output signal gives a total power out of the fiber optic lens of

$$P_2 = \frac{11mV}{7.2 \times 10^3 V/W} = 1.53\mu W \tag{163}$$

Assuming that the LED output power is

$$P_1 = 4mW \tag{164}$$

As specified by Meret Inc. for the MLT327 the total attenuation in this system is

$$a_T = \frac{1.53\mu W}{4mW} = 3.8 \times 10^{-4} \quad (-34.2dB) \tag{165}$$

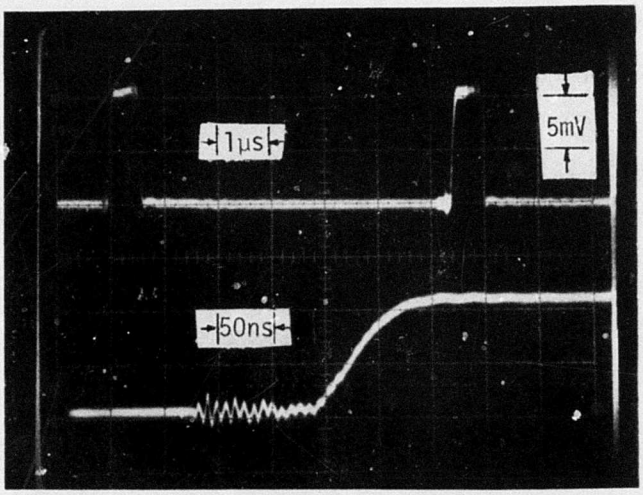

Figure 54. Output Waveform of Galileo Data Transmission Link

For typical Galileo fiber optic bundles the attenuation is about 0.18dB/ft; thus, the 50ft cable length gives an attenuation of about 9dB. This leaves a combined loss of 25.2dB for the plugable interfaces at the transmitter and receiver. Probably 4.2dB of this loss is at the receiver interface which leaves a 21dB loss for the transmitter interface. The plugable optical interfaces used in the SPX 1629, SPX 1631 and SPX 1633 shown in Appendix IV have a total loss of about 9dB with 1.6dB at the receiver and 7.4dB at the transmitter. These are the same basic interfaces used in the Ten-Channel Data Bus Demonstrator[3] built by Spectronics Inc. for AFAL.

The output signal shown in Figure 54 has a S/N current ratio of 34.4; this assumes the threshold level is set at one half of the peak output. For a bit error rate less than 10^{-8}, the value of S/N must be 5.62 or greater. Thus, the Galileo system will operate satisfactorily with 6.12 times less optical signal at the receiver.

The additional allowable attenuation is 7.8dB which coresponds to 43ft of additional fiber optic bundle (at 0.18dB/ft) or a total cable length of 93ft.

Based on this investigation, the Galileo data transmis·ion link is recommended for laboratory demonstrations using Manchester coded signals with an ac coupled receiver and data rates up to 5Mbit/s. The Galileo transmitter and receiver modules will probably not find wide use in military avionics systems or commercial equipment.

F. GALILEO FIBER OPTIC BUNDLES

Extensive measurements have been made on Galileo K2K fiber optic bundles. This characterization of the fiber bundles provides information needed to properly design and predict the performance of passive directional couplers and multiterminal data buses. It also provides information for improving the design of LED/fiber optic interfaces. The 45mil diameter Galileo fiber optic bundle was selected for evaluation because it is inexpensive and readily available. Also, the bundle diameter and NA are suitable for coupling to non-coherent LEDs and photodiodes. While only one fiber bundle type has been investigated, the various characteristics and phenomena that have been studied are present to some degree in all glass fiber optic bundles. The measurement techniques developed are applicable to all types of fiber optic bundles.

The Galileo 45mil diameter fiber optic bundles contain 285 clad glass fibers with a nominal fiber diameter of 2.5mil. The core/fiber diameter ratio is about 19/21. The core is a high-index lead glass with an index of refraction of 1.625 while the cladding is a barosilicate glass with index of refraction of 1.48. The limiting NA of these fibers is 0.66. At Spectronics, Inc. the ends of the fiber bundles are terminated using the SPX 1523 precision ferrule which has a reamed ID of 46.5mil. The end transmission of a typical

termination is about 61%; this includes both front surface reflection losses and packing fraction losses.

In the first fiber optic bundle evaluation, SPX 1527-59 was coupled to various lengths of Galileo fiber optic bundle with the LED/fiber optic interface shown in Figure 55. This interface was developed for the Ten-Channel Data Bus Demonstrator[3] and is also used in the SPX 1629 LED adapter shown in Appendix IV. The fiber optic bundle lengths are 1ft, 4ft, 10ft, 35ft, 100ft, and 150ft. The four shorter cables are from the same batch of fiber optic bundles; the 150ft cable is from a different batch and has slightly lower attenuation than the other four.

Figure 30 shows the far field radiation pattern of SPX 1527-59. This plot and all other radiation patterns shown in this report were run using the Spectronics, Inc. Model 170 Radiation Pattern Plotter. The radiation pattern is a plot of radiant intensity vs. angle from the axis. Figure 56 shows the launch cone (radiation pattern) of the light coupled to the fiber optic bundle. The cross section drawing in Figure 56 indicates the way the measurement was made; the test set up for Figures 30 and 56 is shown in Figure 29. The test set up used for measuring the far field radiation pattern at the exit end of a fiber optic bundle is shown in Figure 57. Figures 58 through 63 show the far field radiation pattern at the exit end of the fiber optic bundles of the specified lengths. The two curves plotted in each figure were taken in two orthogonal planes to provide a measure of the uniformity of the radiation pattern.

The void in the center of the launch cone is clearly displayed in Figure 56. Figures 58-63 show the effect of scattering and mode coupling in the glass fibers; the longer the cable the more the center of the pattern is filled in and the less the exit end radiation pattern resembles the launch cone at the input end. The 100ft and 150ft radiation patterns approach the equilibrium exit end radiant intensity

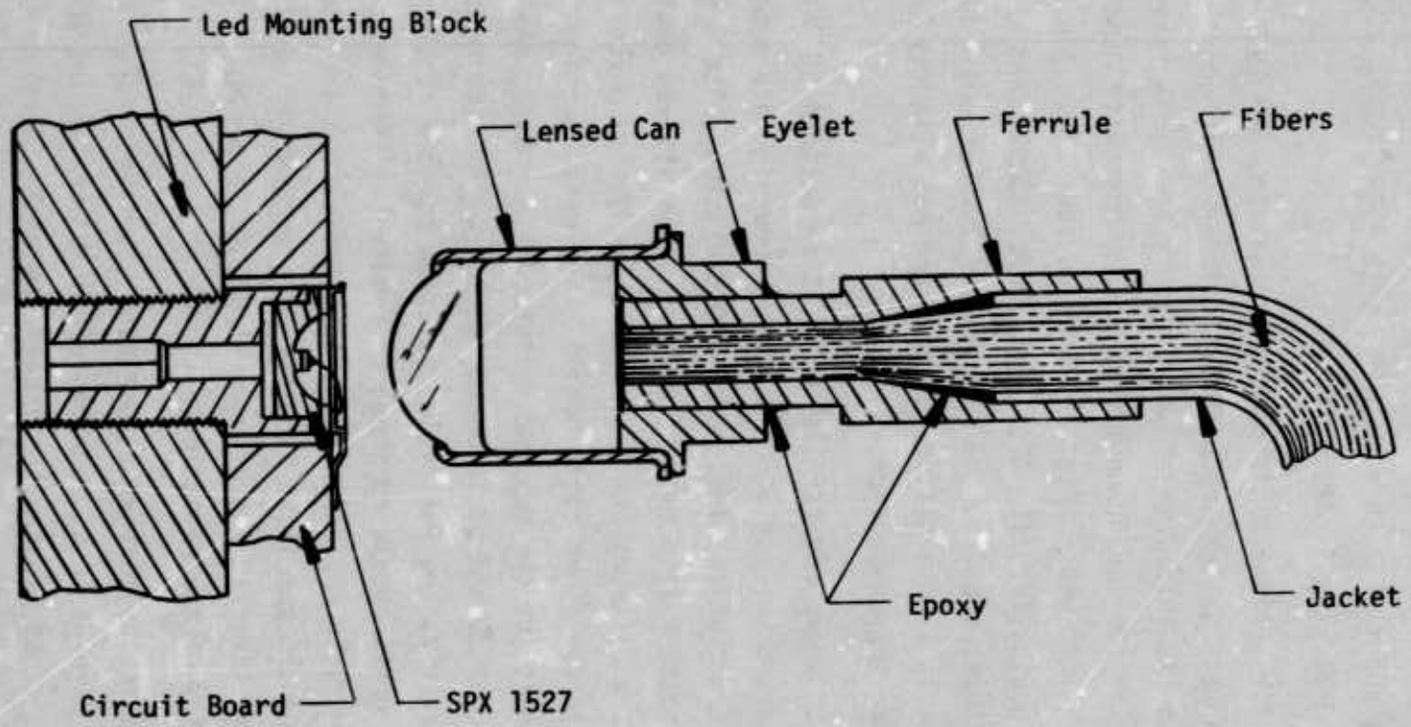

Figure 55. LED/Fiber Optic Interface

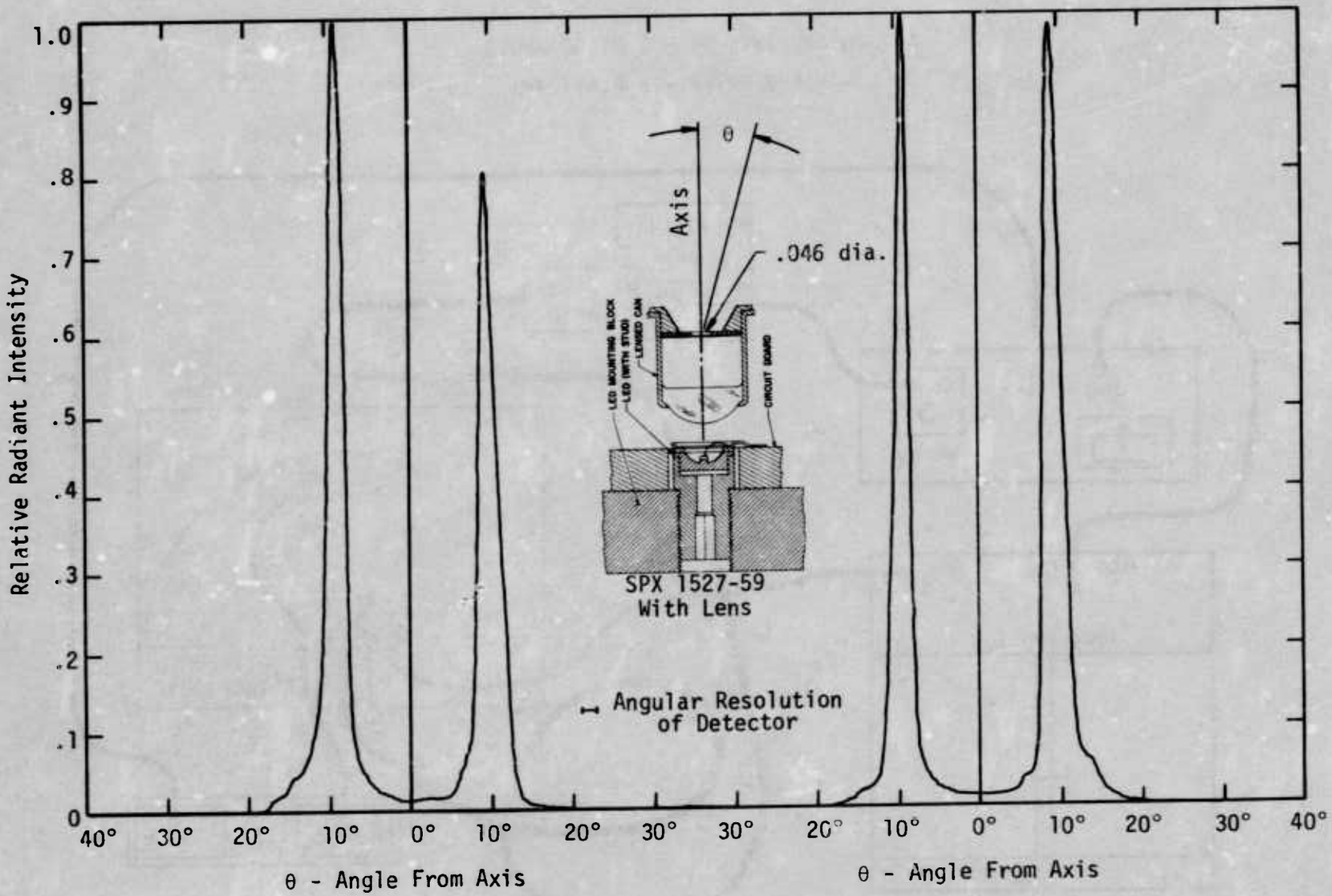

Figure 56. Far Field Launch Cone for SPX 1527/Lens Interface

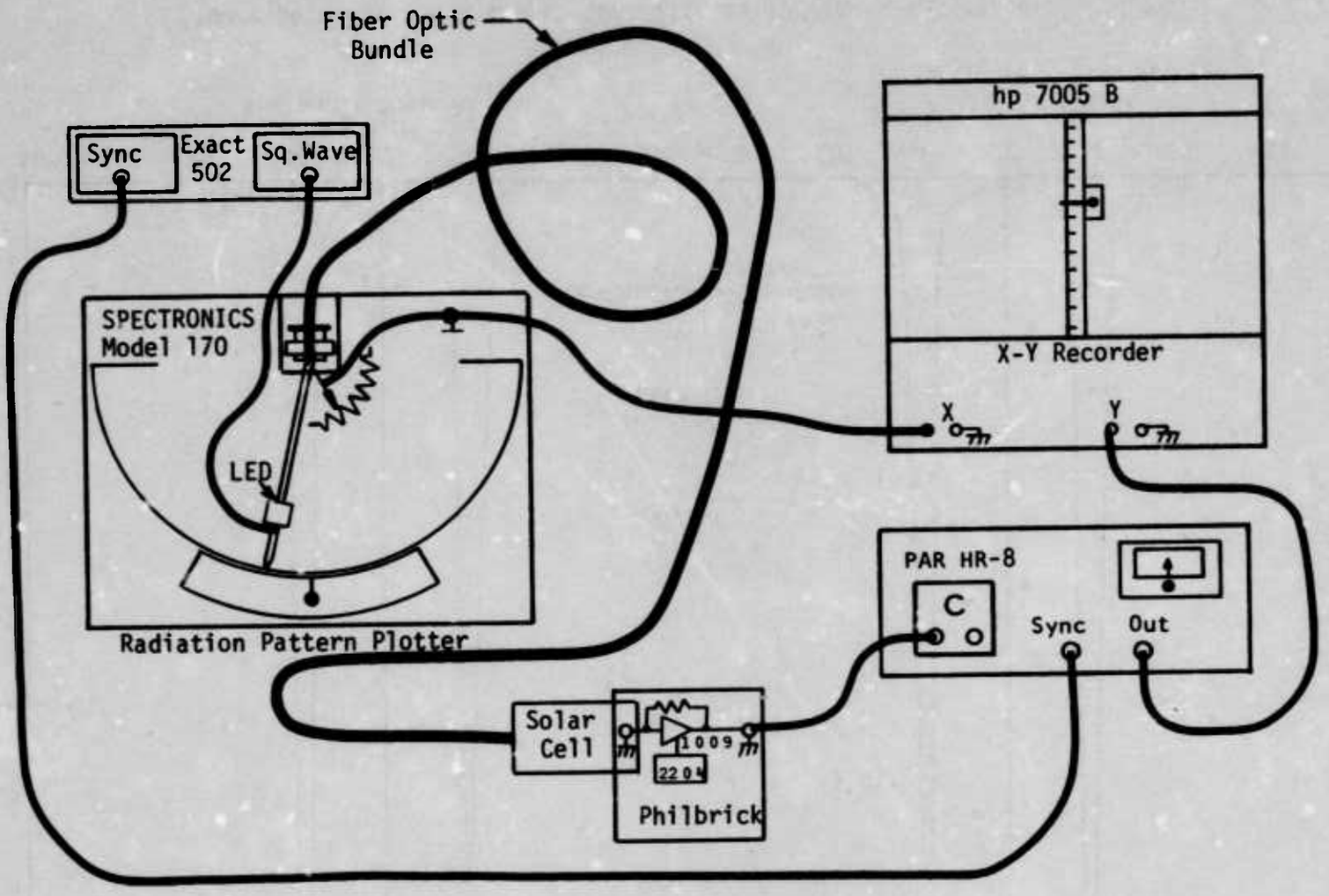

Figure 57. Far Field Radiation Pattern
Fiber Optic Bundle Test Set Up

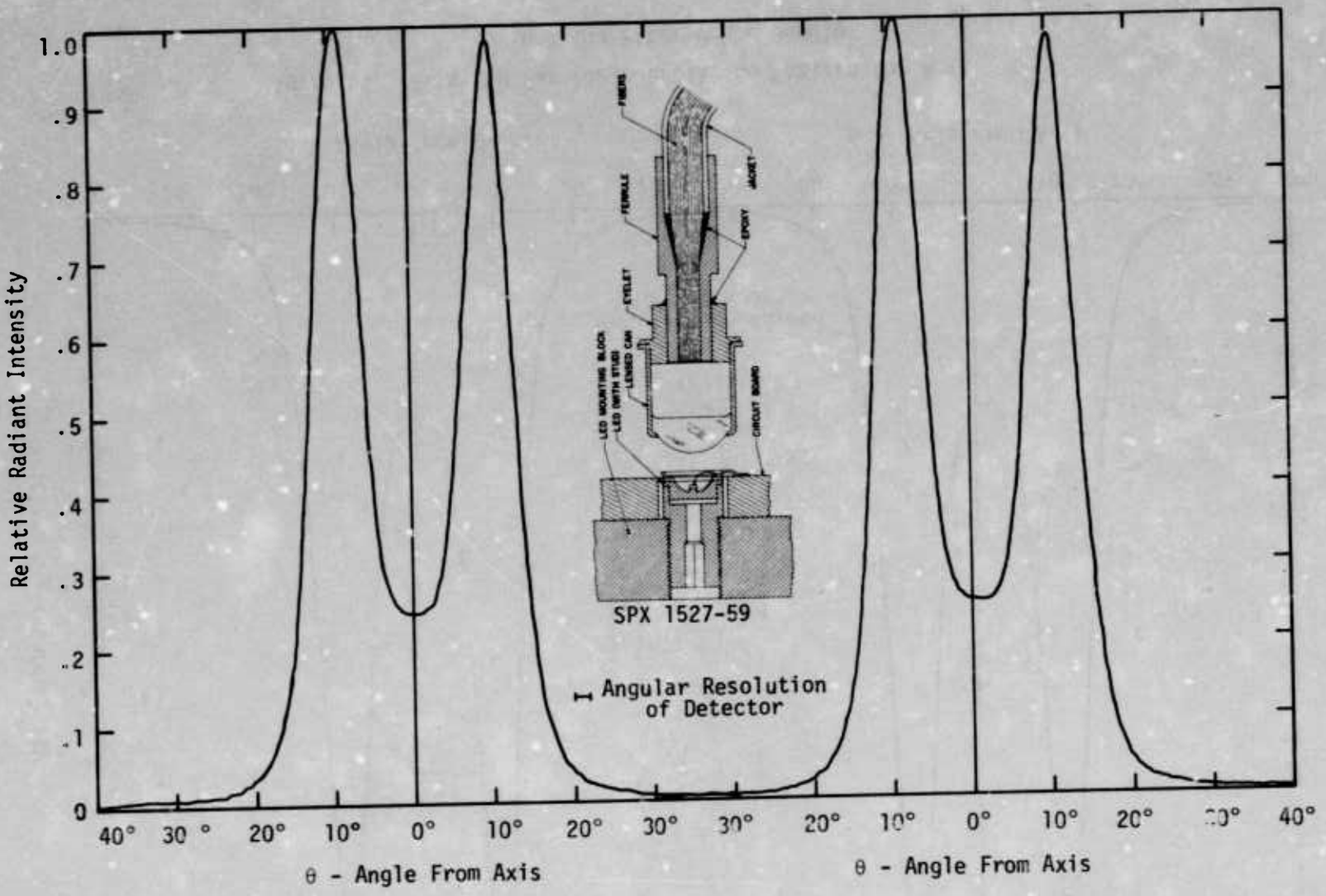

Figure 58. Exit End Far Field Radiation Pattern for 1ft Galileo Fiber Optic Bundle

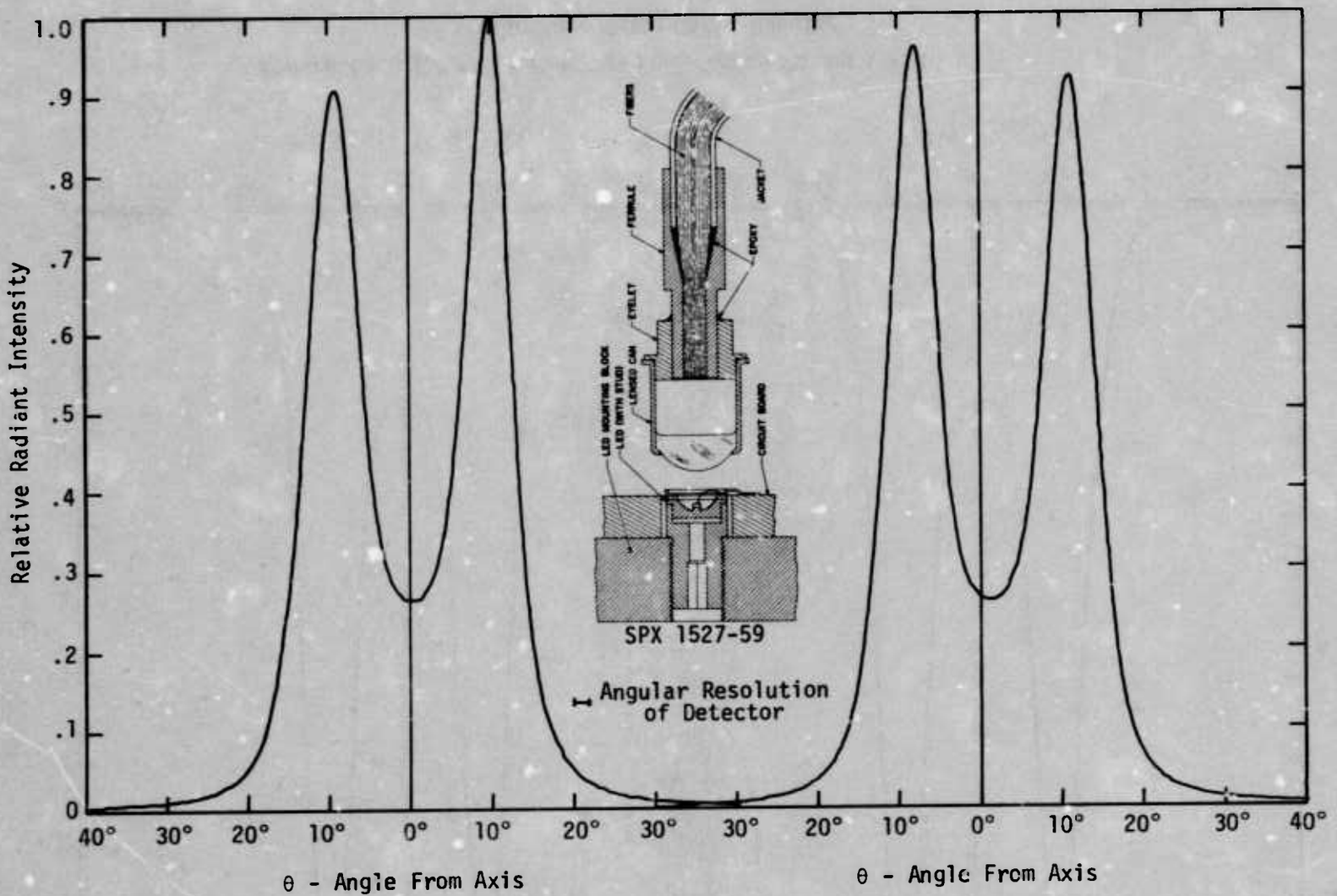

Figure 59. Exit End Far Field Radiation Pattern for 4 ft Galileo Fiber Optic Bundle

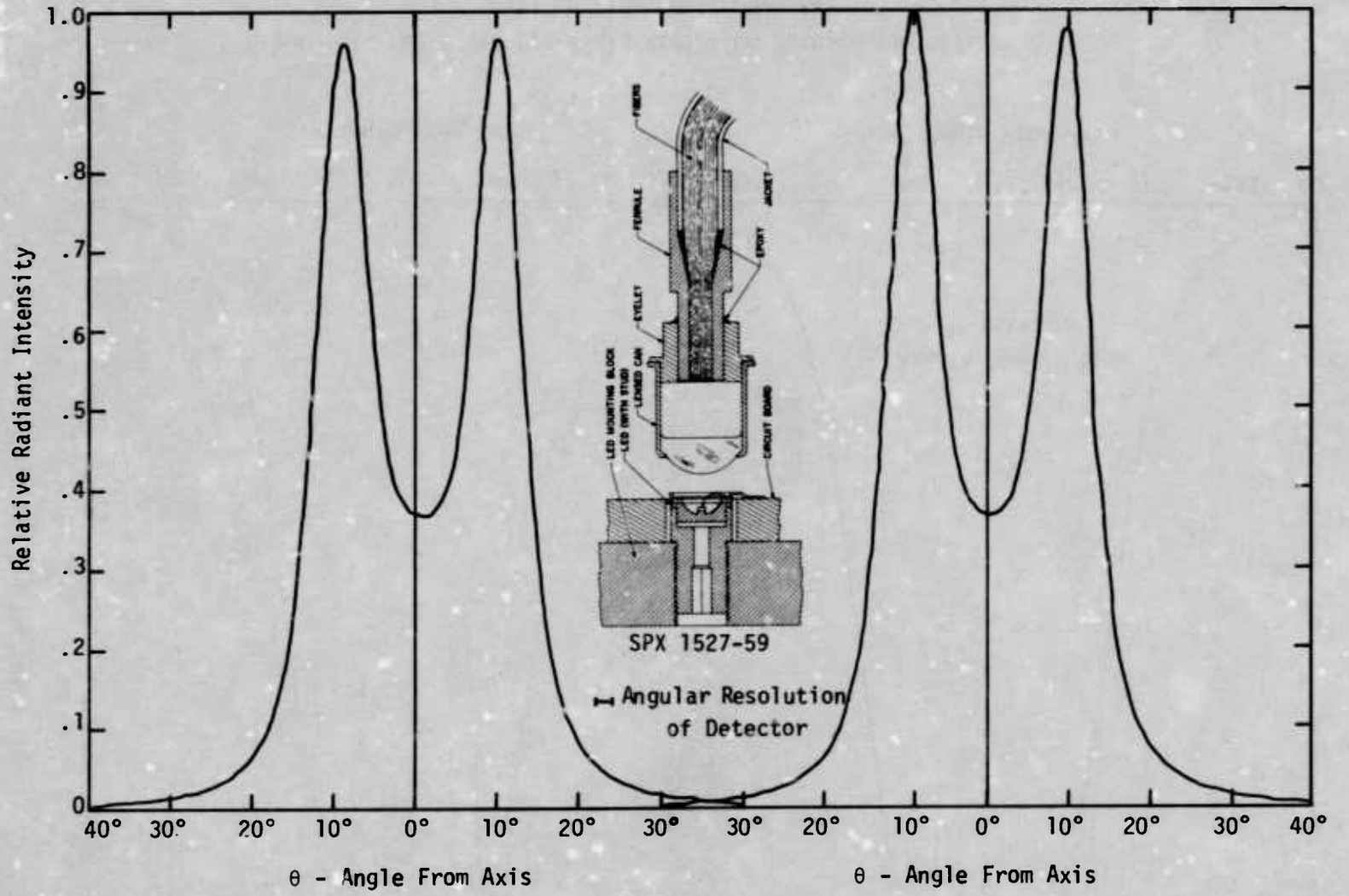

Figure 60. Exit End Far Field Radiation Pattern for 10ft Galileo Fiber Optic Bundle

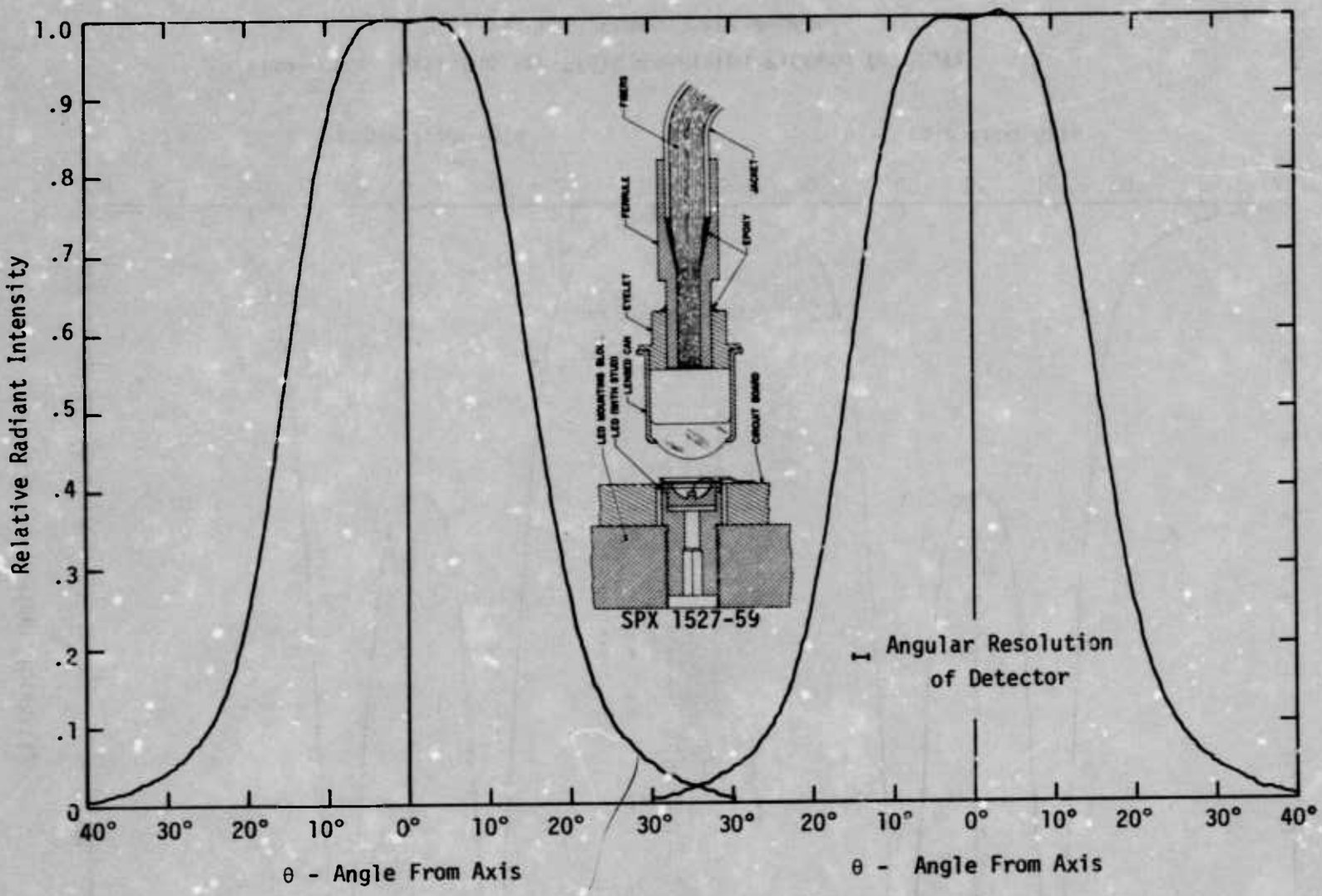

Figure 61. Exit End Far Field Radiation Pattern for 35ft Galileo Fiber Optic Bundle

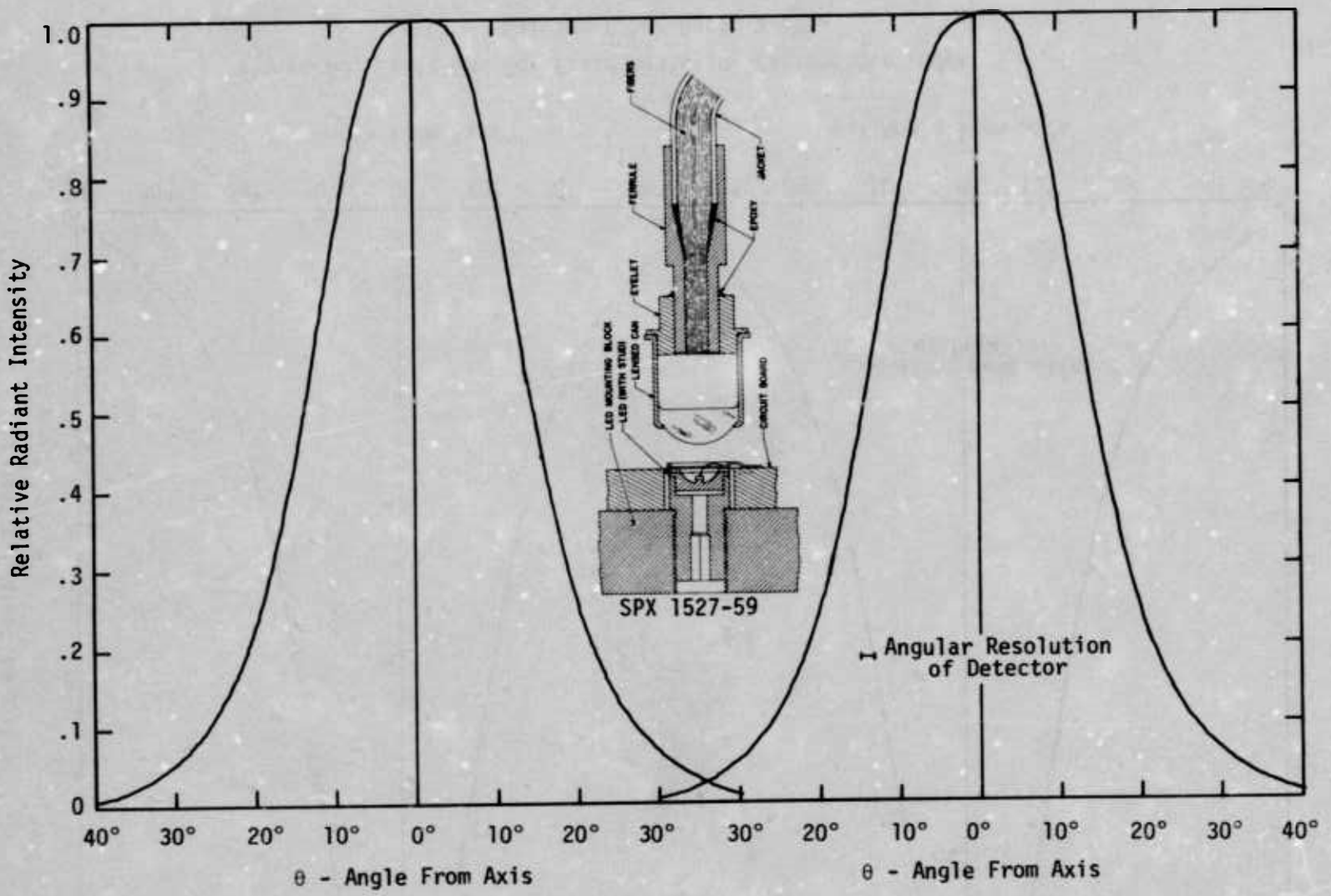

Figure 62. Exit End Far Field Radiation Pattern for 100ft Galileo Fiber Optic Bundle

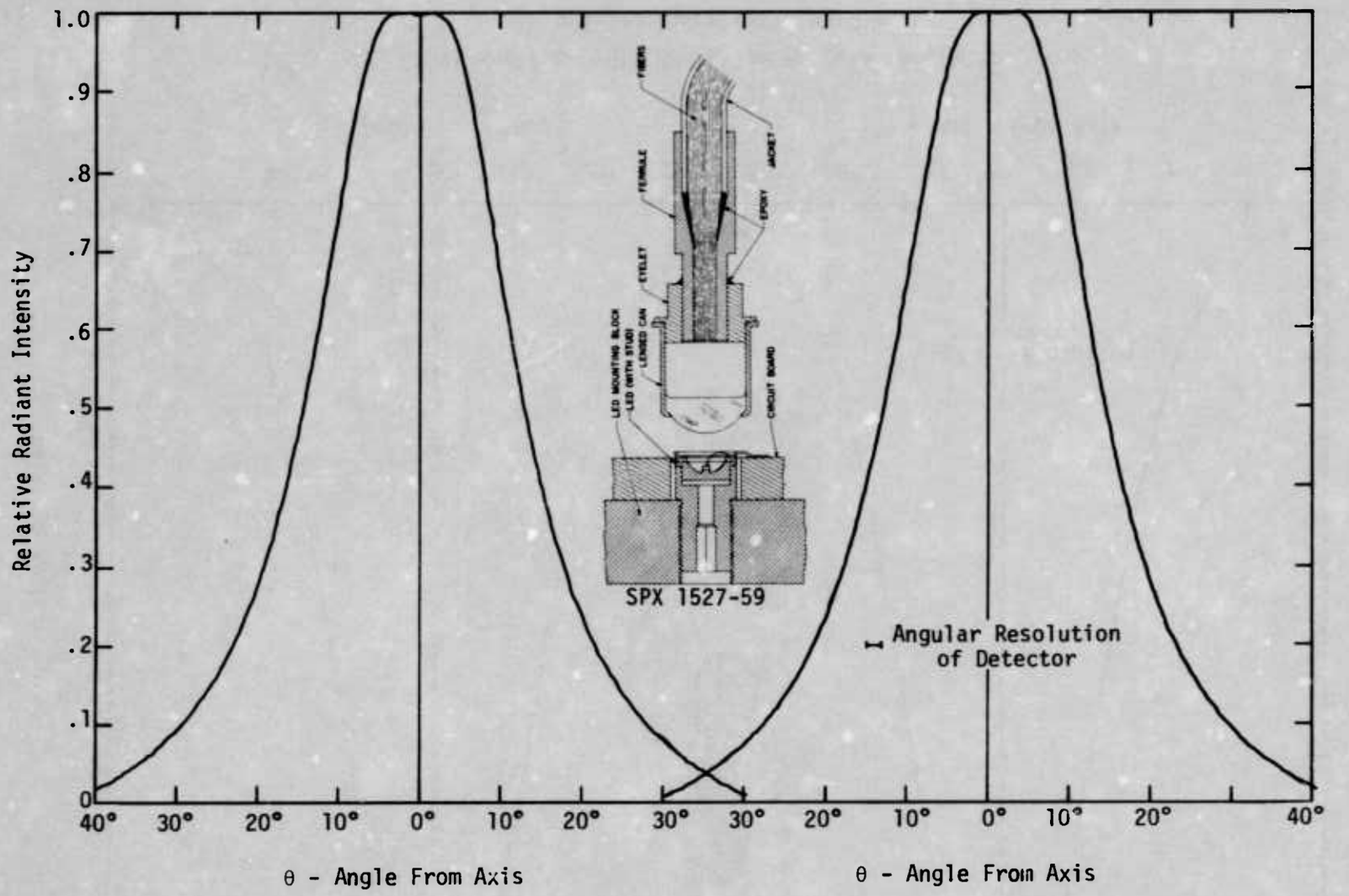

Figure 63. Exit End Far Field Radiation Pattern for 150ft Galileo Fiber Optic Bundle

distribution. Note that the half angle of the launch cone (Figure 56) is <14° and that the half angle of the exit end radiation pattern is ≤14° (NA=0.24) for all cable lengths shown. Figure 64 shows a composite radiation pattern for the 4ft, 10ft, 35ft and 100ft cables. These curves were all run at the same gain setting to display both the attenuation and scattering loss.

Another set of exit end far field radiation patterns was run for the various cable lengths without the lens on either termination using a very narrow launch cone (∿1° half angle) centered at various launch angles in 5° increments. This test set up used two Model 170 Radiation Pattern Plotters. This family of curves is presented in Figures 65-70. Due to the low signal level with the 100ft and 150ft cables the curves in Figures 69 and 70 were traced twice to average out the noise. For the short cables, the peaks in the exit pattern occur at the launch angle; whereas, in the long cables the major effect of the launch angle is to change the attenuation. Notice that even though the light is launched into the fiber optic bundle in a narrow pencil beam it exits in a uniform cone.

Figure 71 shows the test set up used to measure the launch angle characteristics presented in Figures 72-77. These plots are similar to the two preceding sets except that in this case, a large area silicon solar cell is used as a detector on the exit end of the cable. These curves show the dependence of NA on fiber bundle length and are useful for determining the effectiveness of various LED radiation patterns for coupling to fiber optic bundles. The 4ft cable in Figure 73 shows 18% coupling at 41° (NA=.66); the rapidly decaying tails in this figure that extend beyond 41° are probably due to scattering from imperfections in the polished surface at the entrance end of the fiber optic bundle. Again, the launch angle characteristic of the long fibers is very similar to the exit end far field radiation patterns shown in Figure 63 and 70.

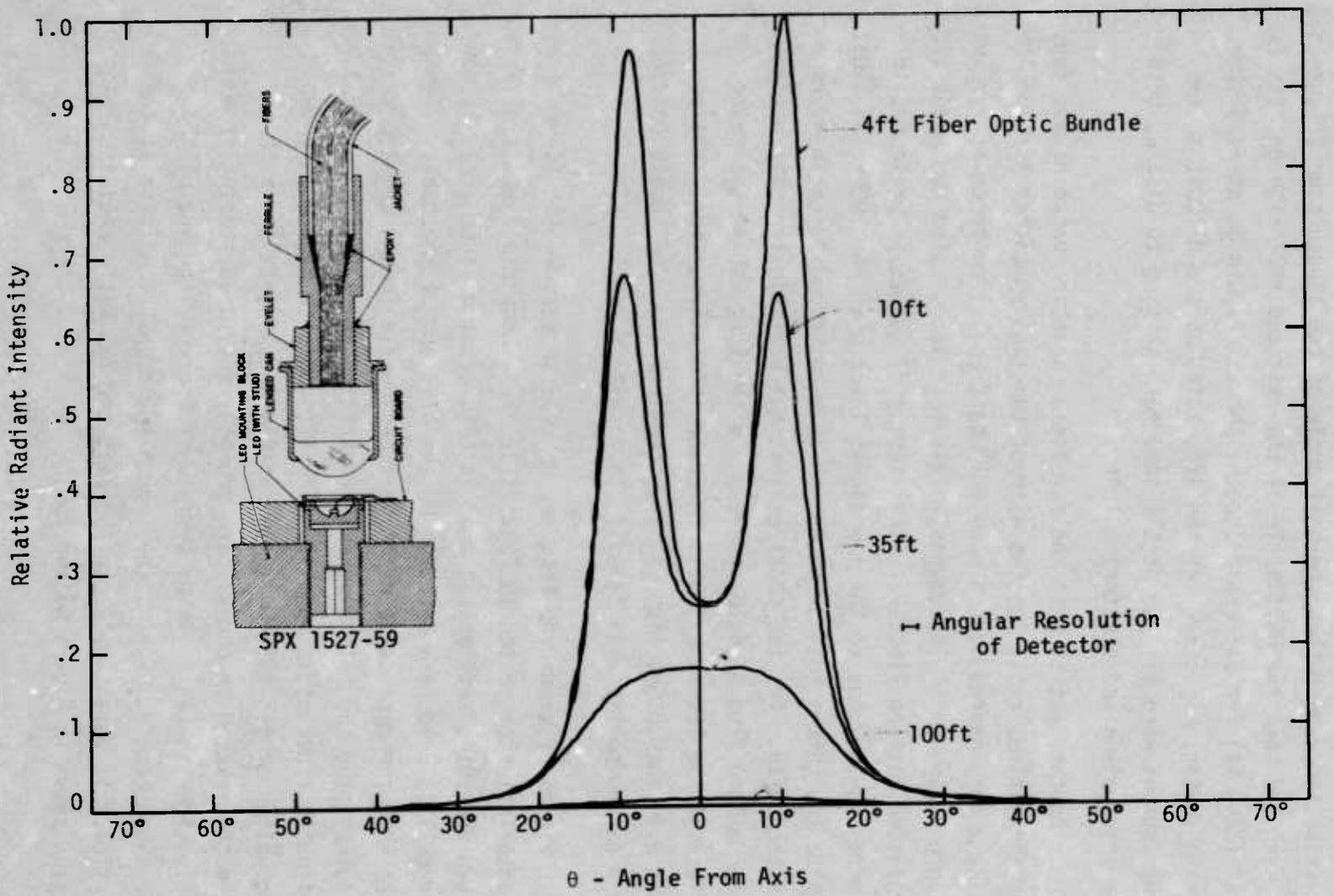

Figure 64. Composite Exit End Far Field Radiation Pattern for Galileo Fiber Optic Bundles

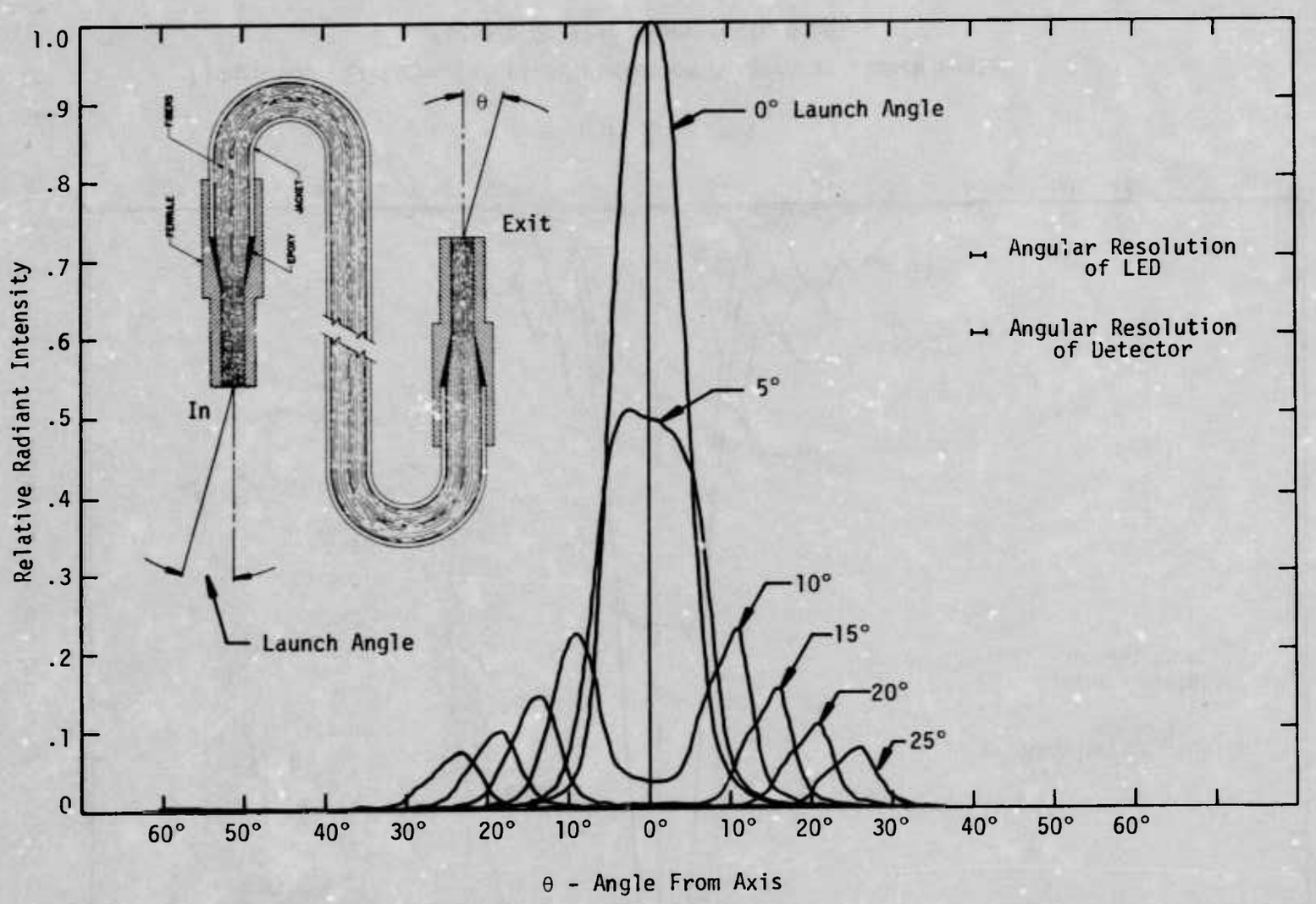

Figure 65. Exit End Far Field Radiation Pattern Vs Launch Angle for 1ft Galileo Fiber Optic Bundle

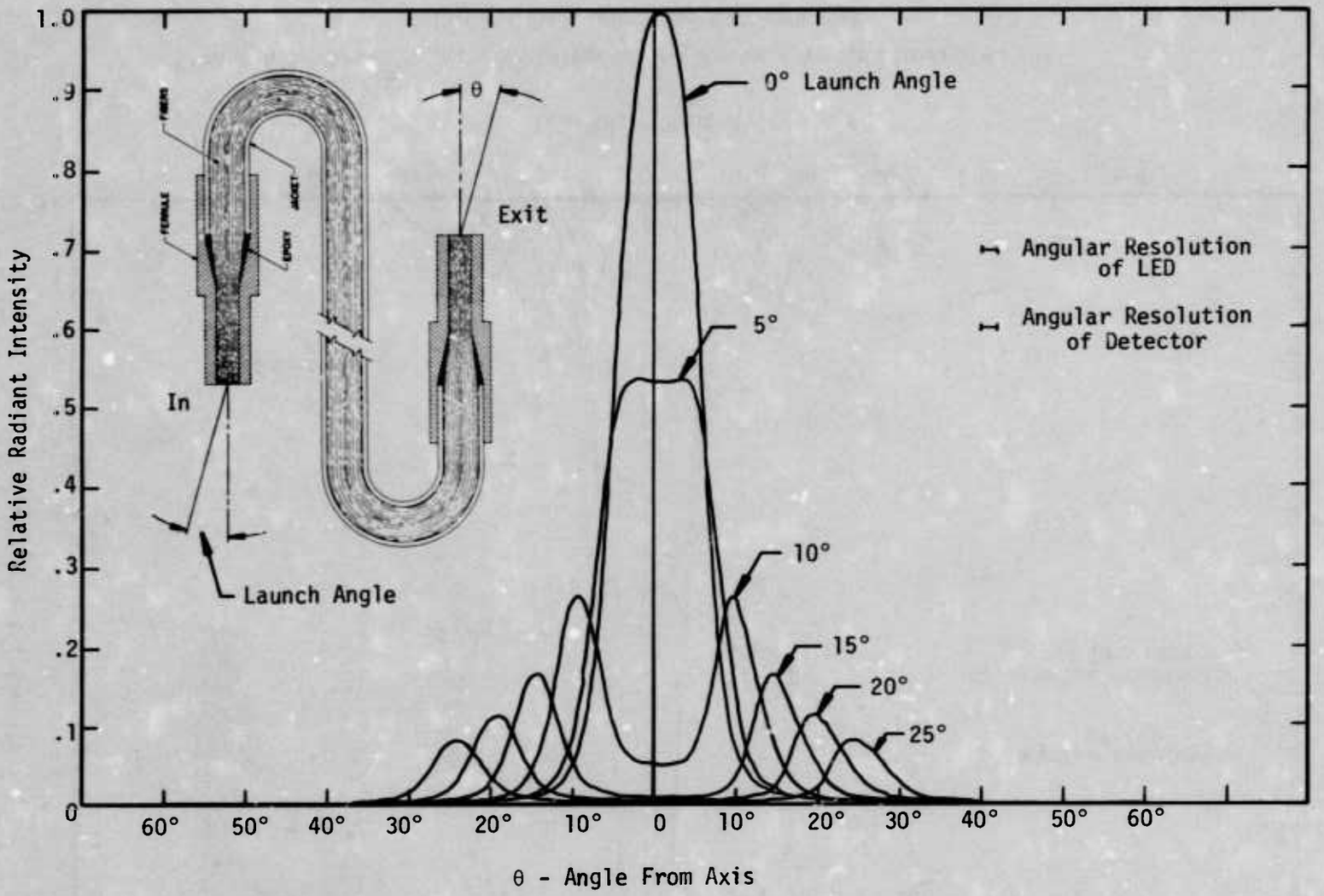

Figure 66. Exit End Far Field Radiation Pattern Vs Launch Angle for 4ft Galileo Fiber Optic Bundle

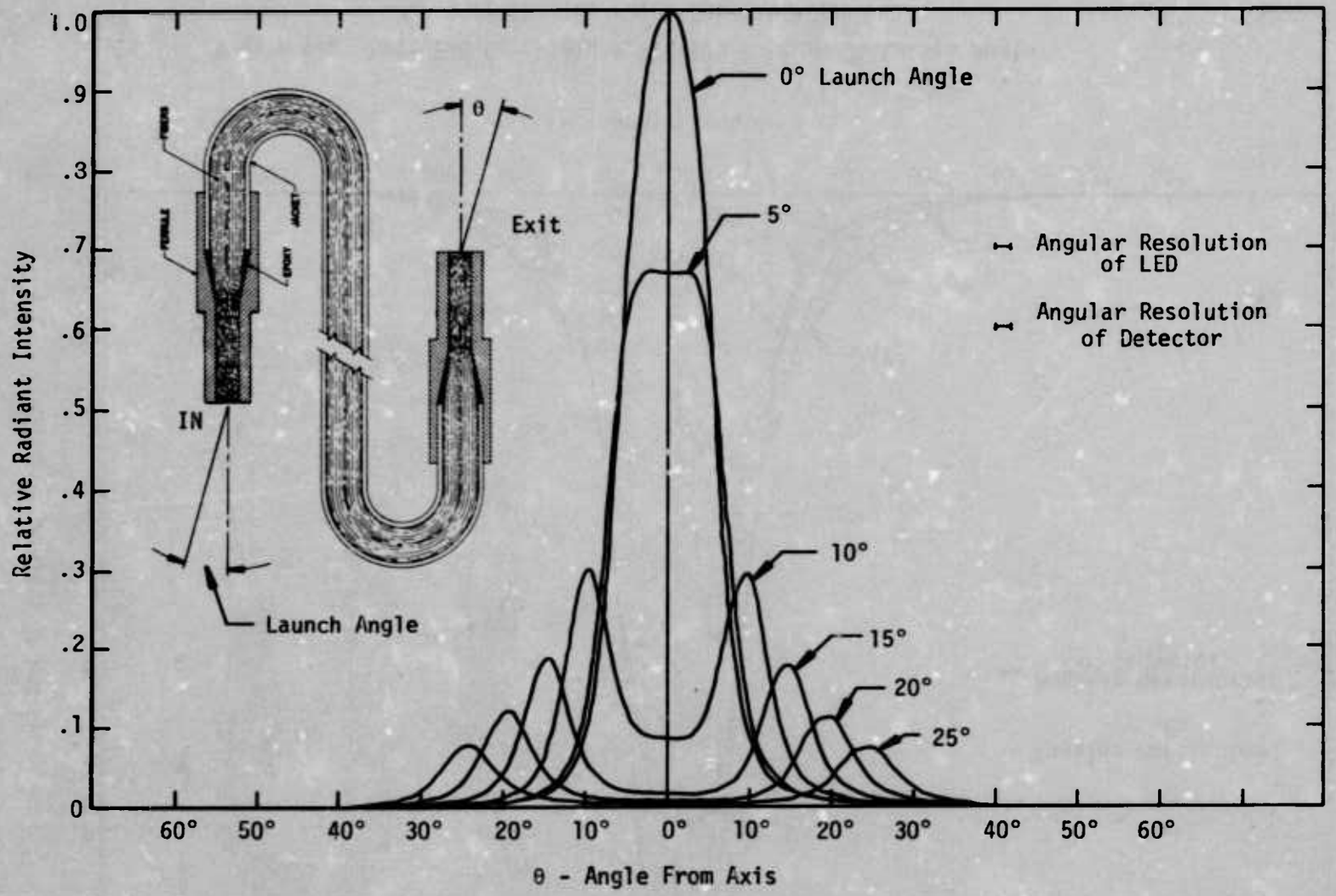

Figure 67. Exit End Far Field Radiation Pattern Vs. Launch Angle for 10ft Galileo Fiber Optic Bundle

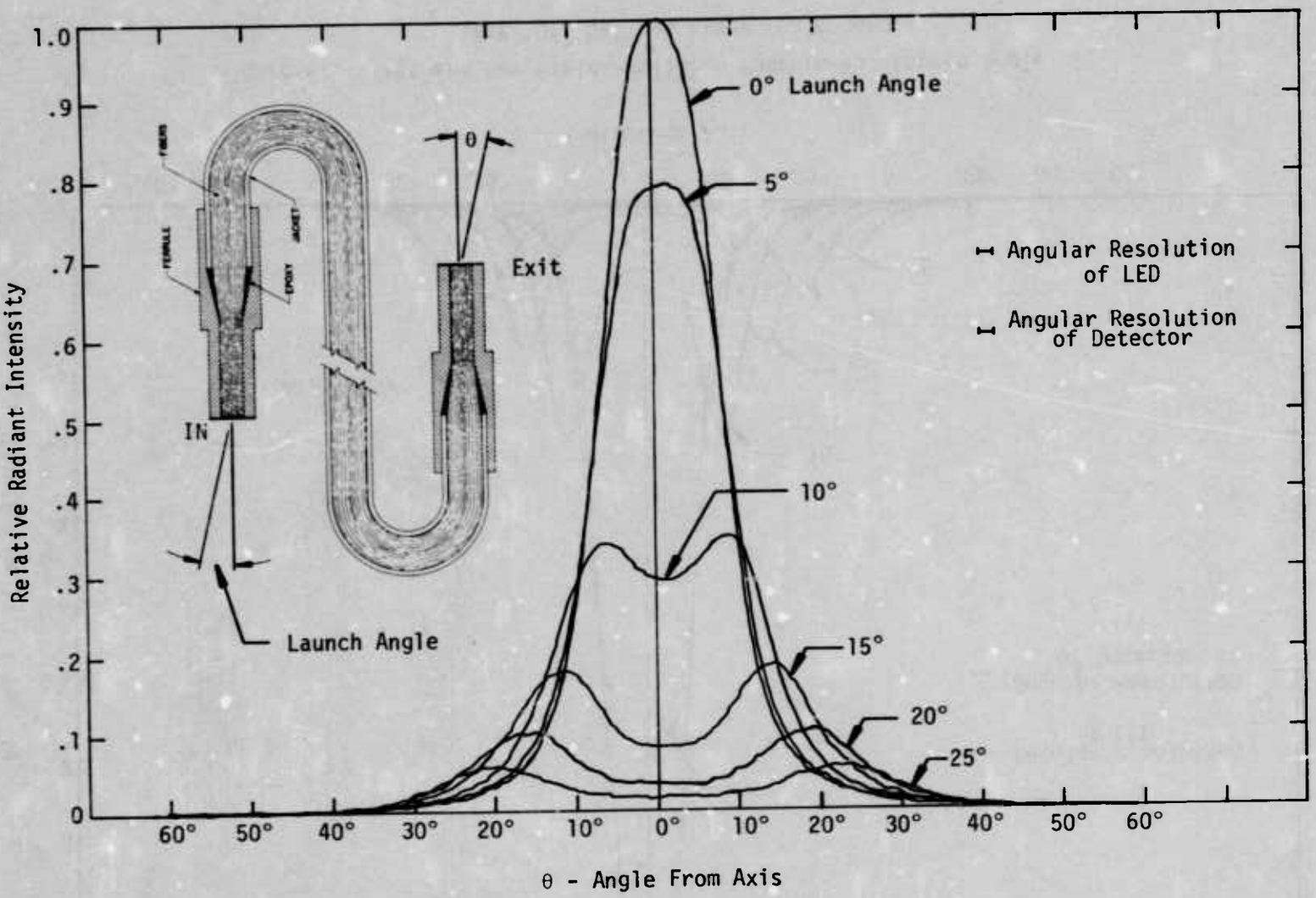

Figure 68. Exit End Far Field Radiation Pattern Vs Launch Angle for 35ft Galileo Fiber Optic Bundle

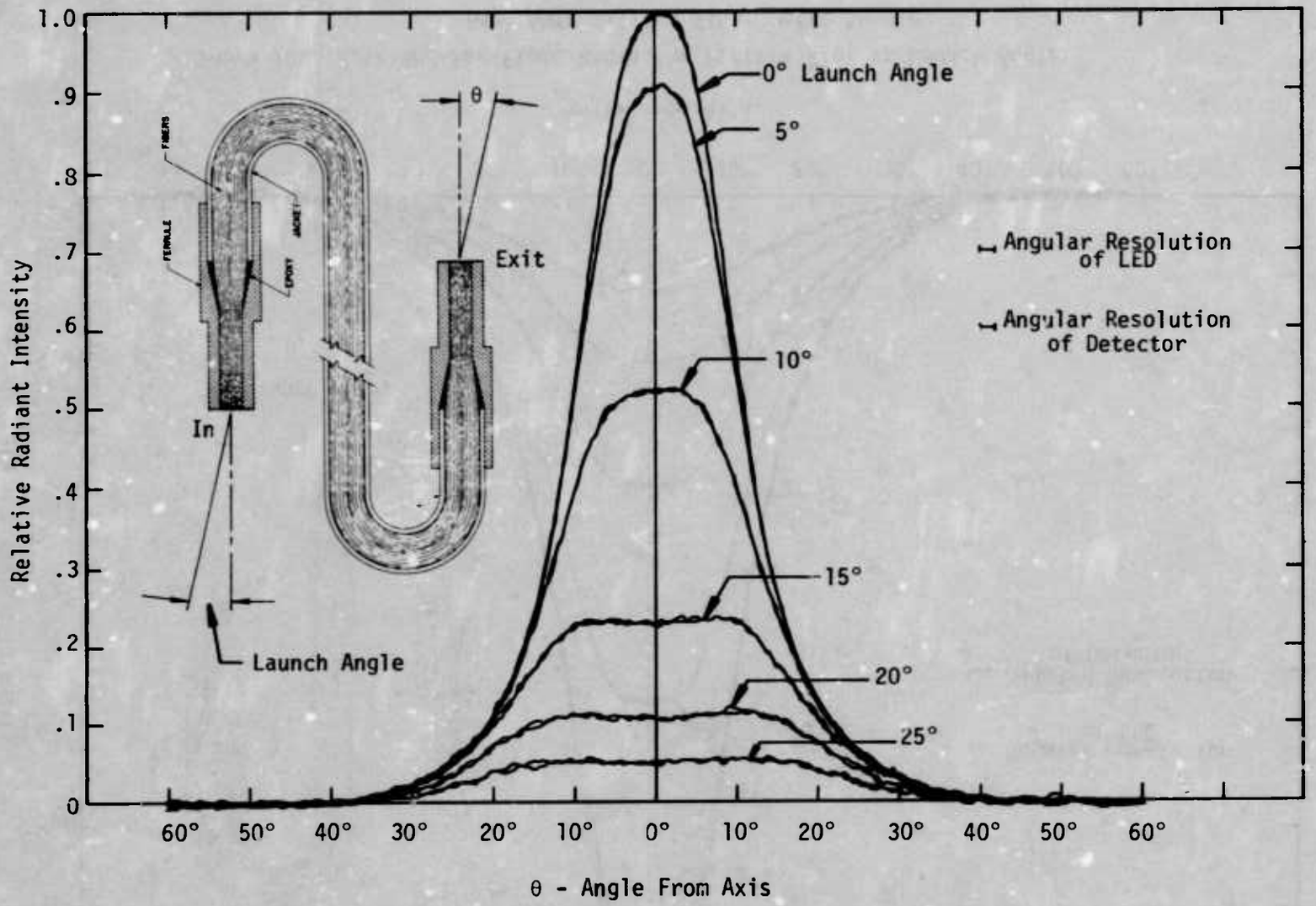

Figure 69. Exit End Far Field Radiation Pattern Vs Launch Angle for 100ft Galileo Fiber Optic Bundle

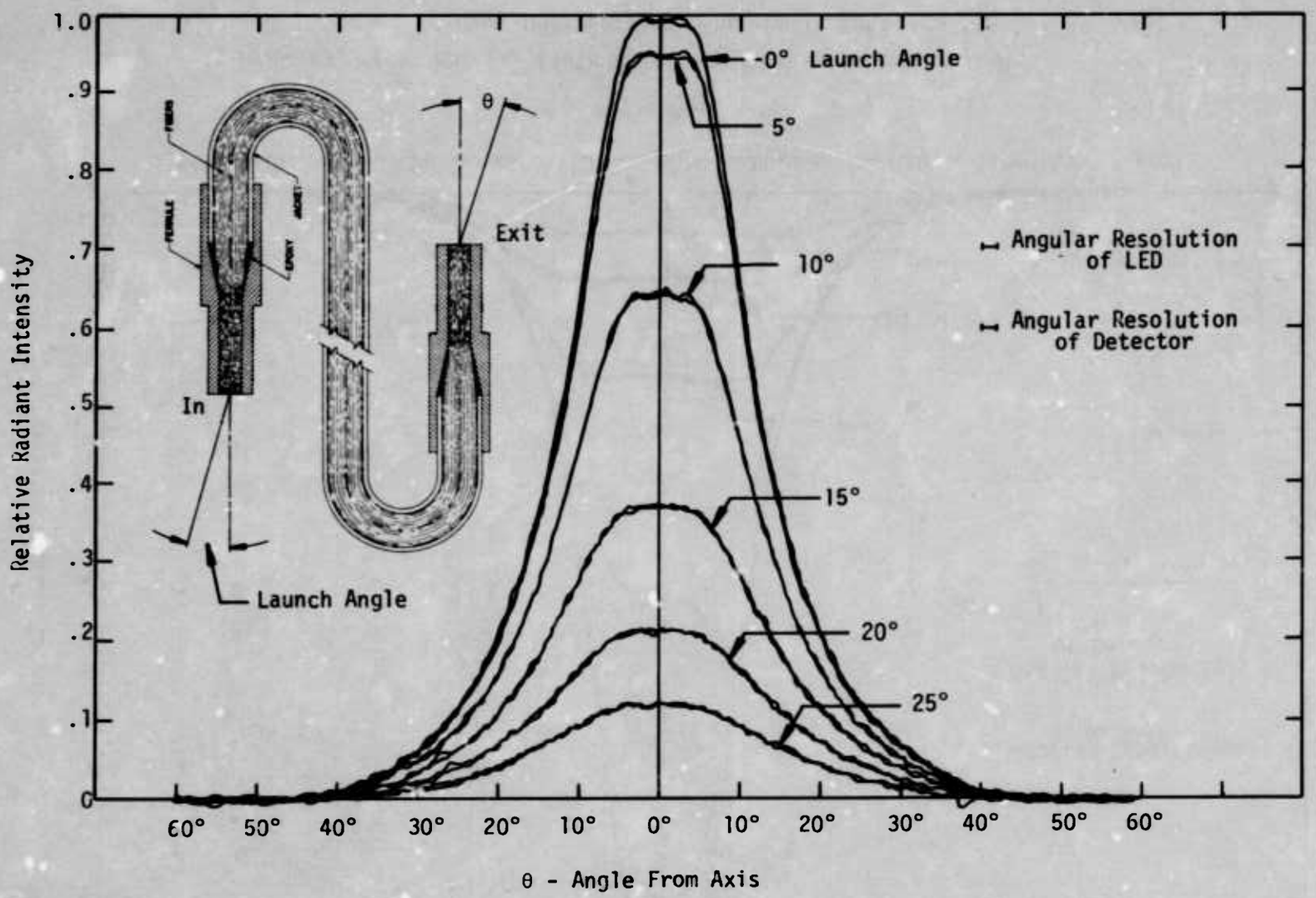

Figure 70. Exit End Far Field Radiation Pattern Plot Vs Launch Angle for 150ft Galileo Fiber Optic Bundle

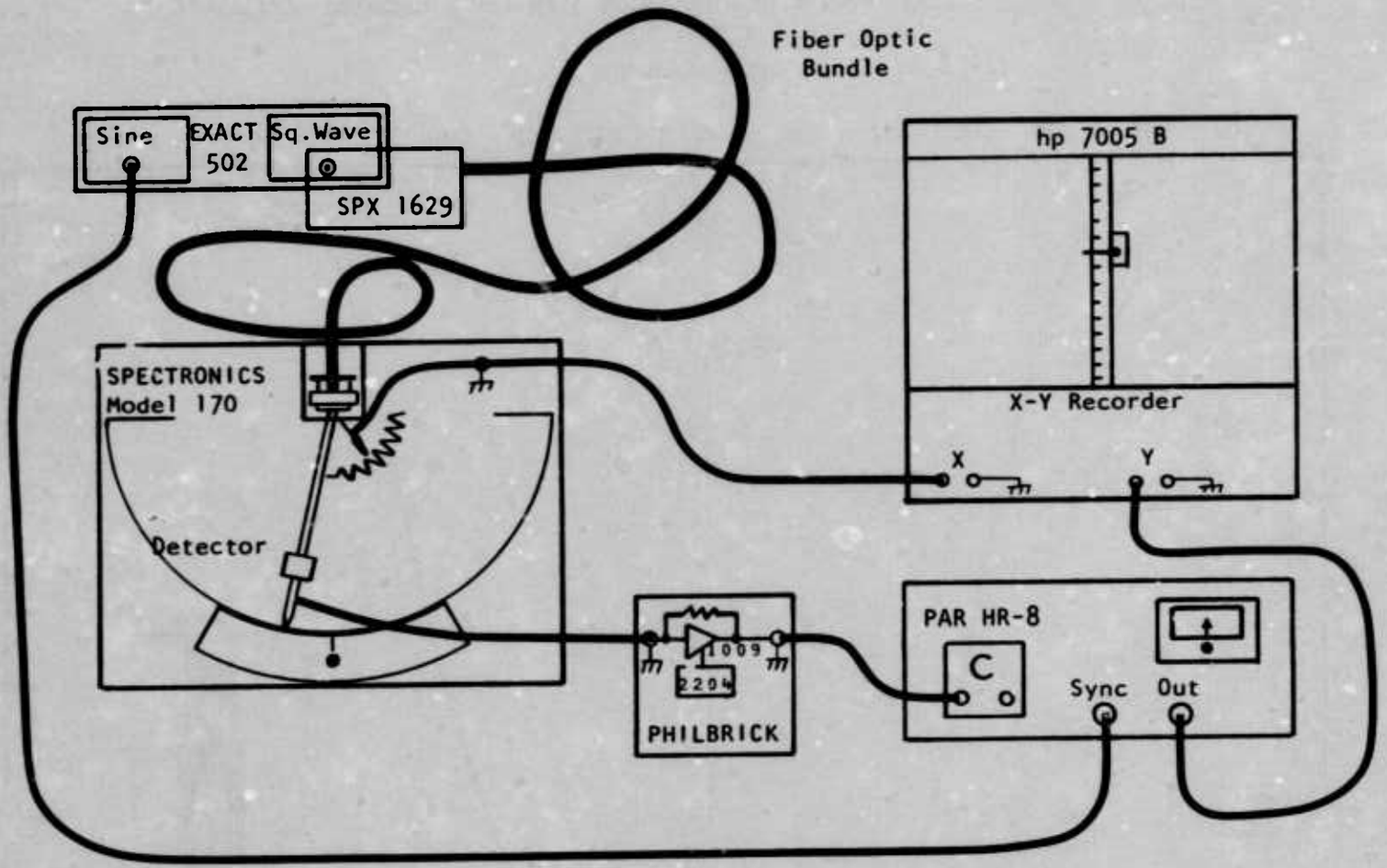

Figure 71. Detector Power Vs Launch Angle
Fiber Optic Bundle Test Set Up

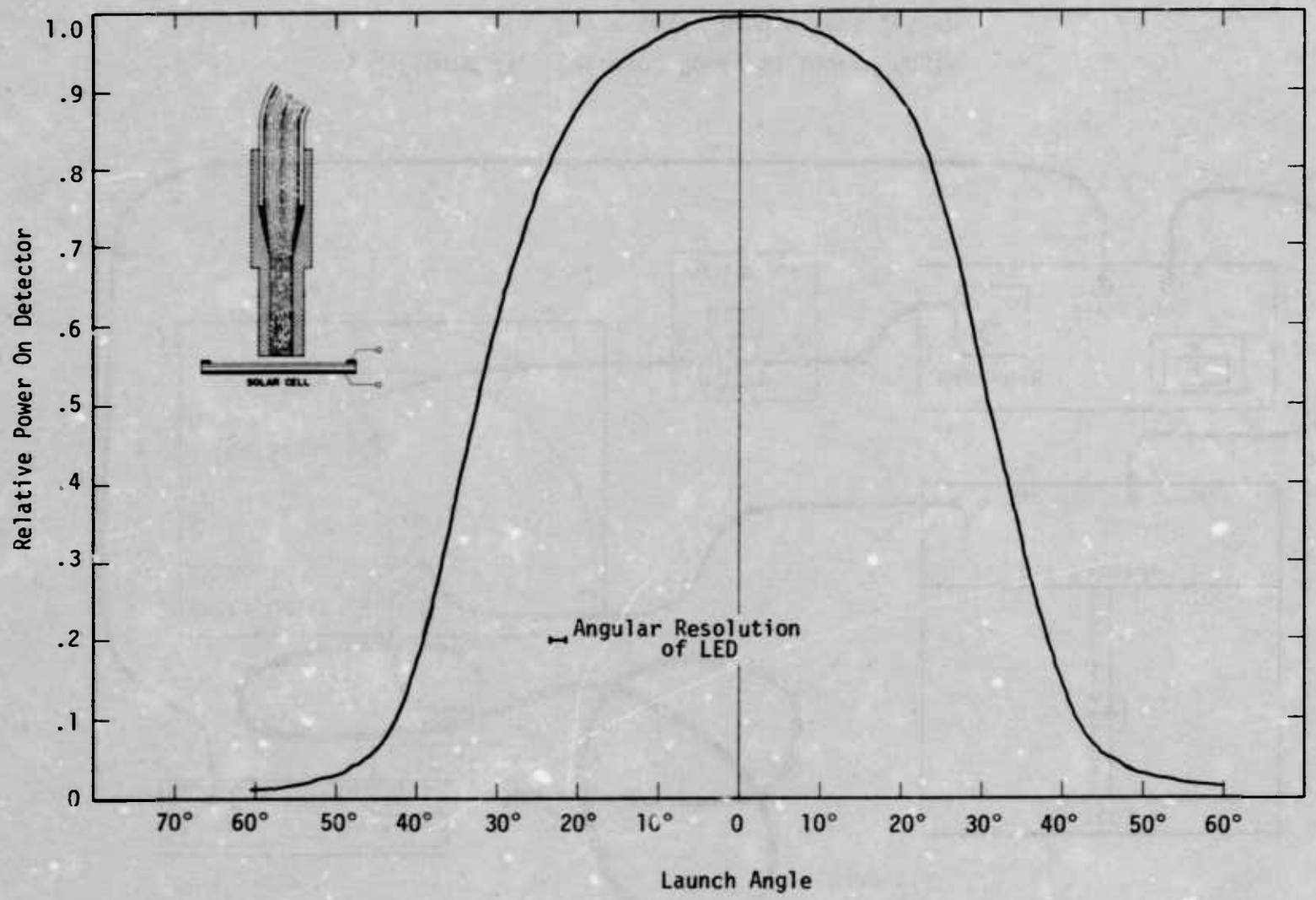

Figure 72. Detector Power Vs Launch Angle With Solar Cell for 1ft Galileo Fiber Optic Bundle

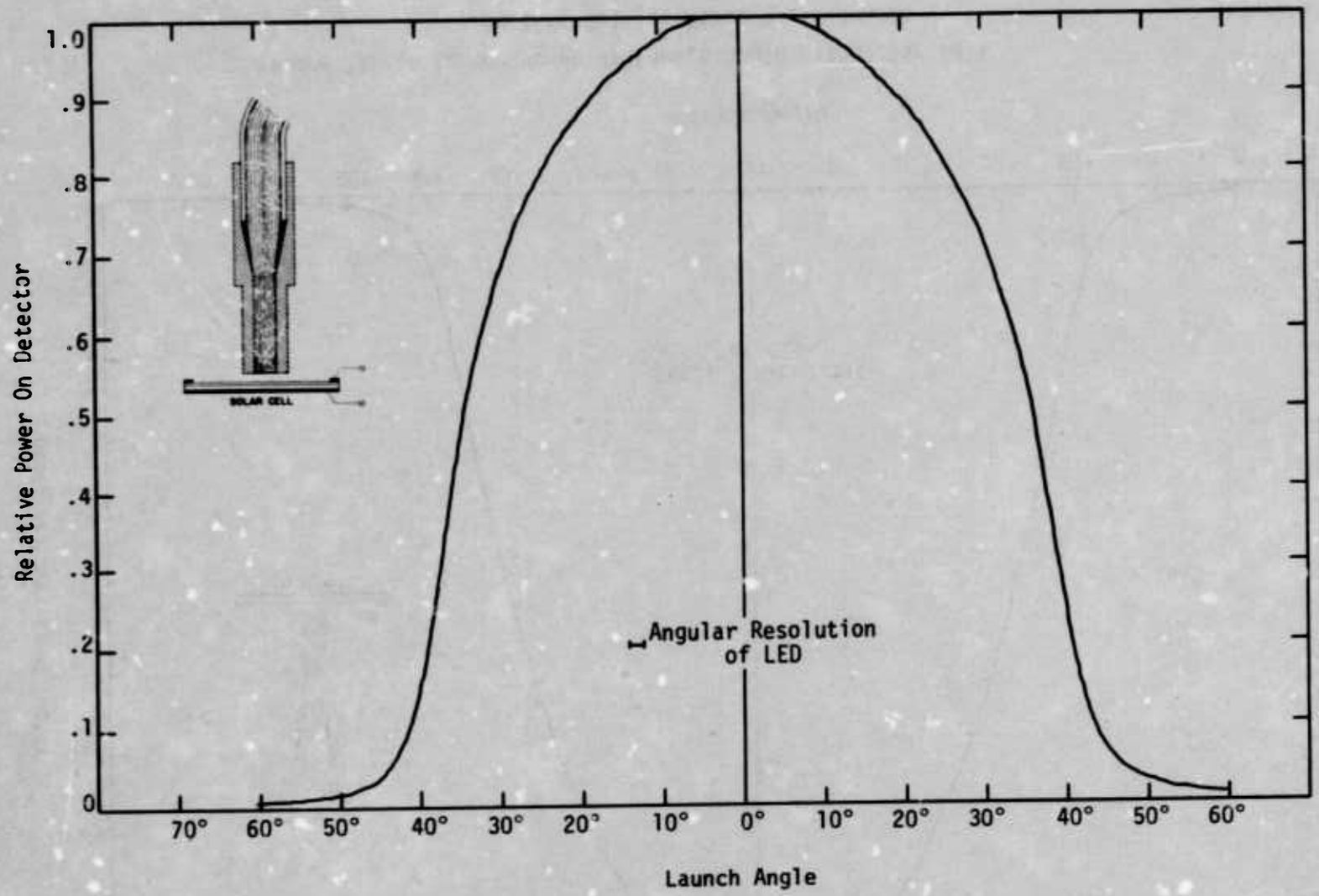

Figure 73. Detector Power Vs Launch Angle With Solar Cell for 4ft Galileo Fiber Optic Bundle

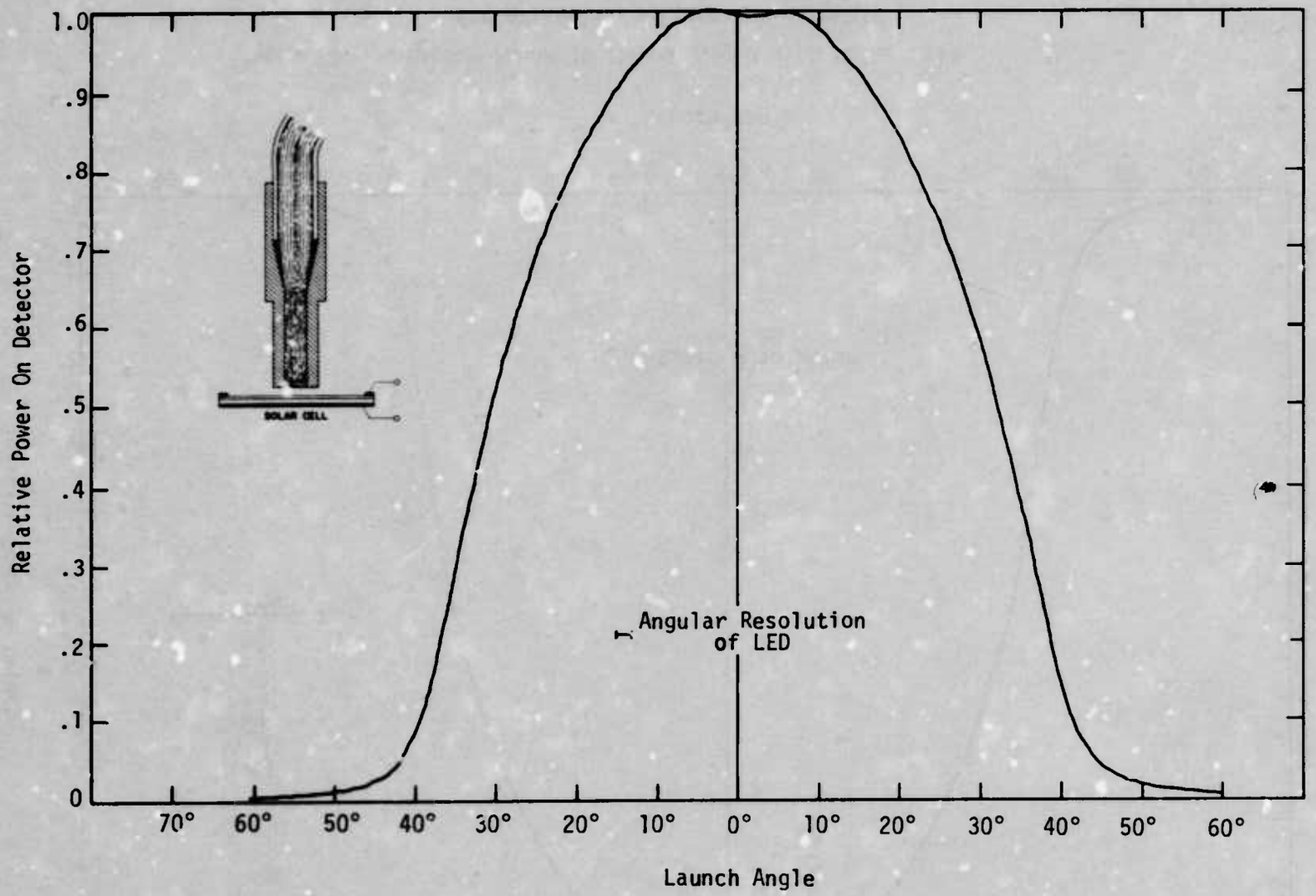

Figure 74. Detector Power Vs Launch Angle With Solar Cell for 10ft Galileo Fiber Optic Bundle

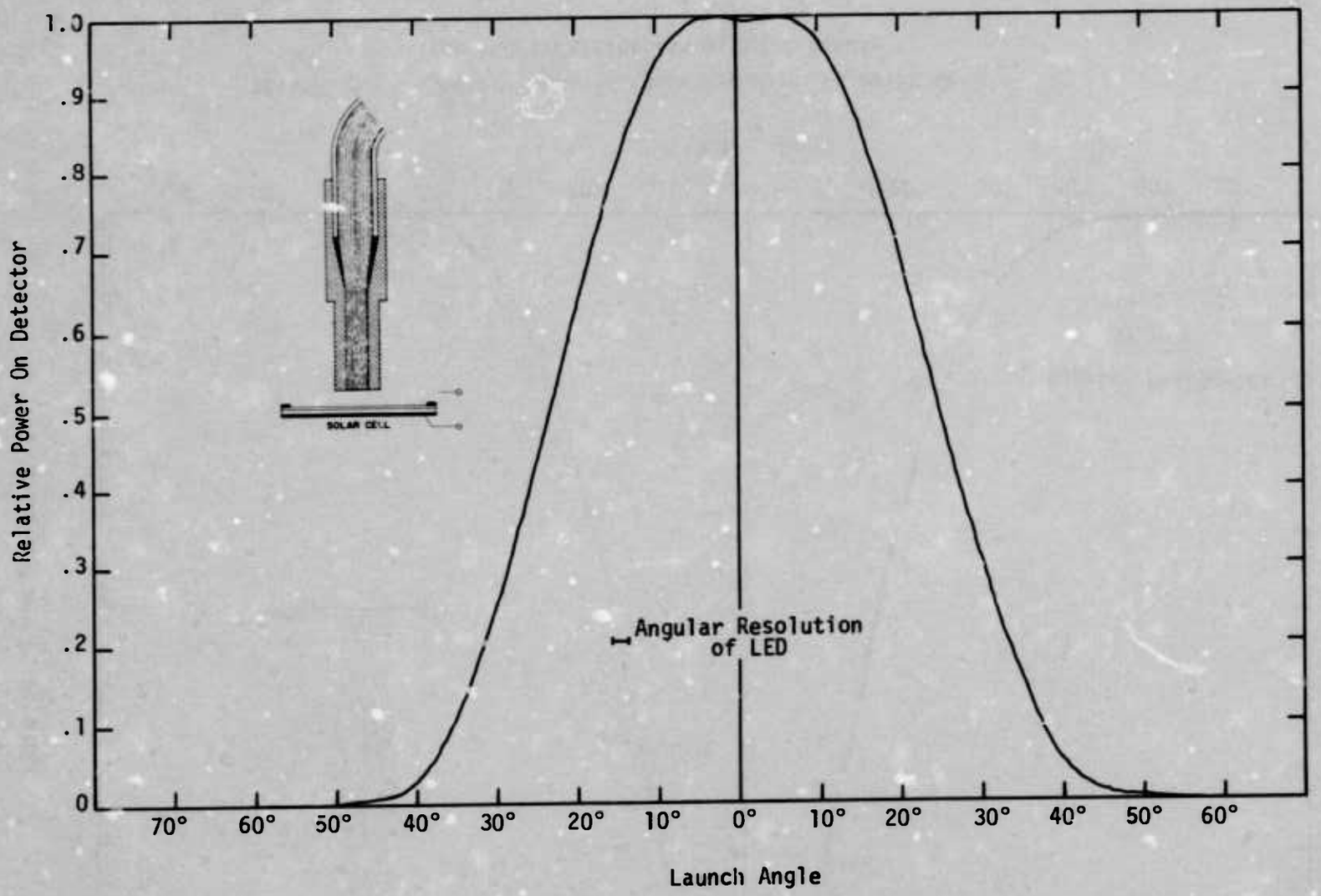

Figure 75. Detector Power Vs Launch Angle With Solar Cell for 35ft Galileo Fiber Optic Bundle

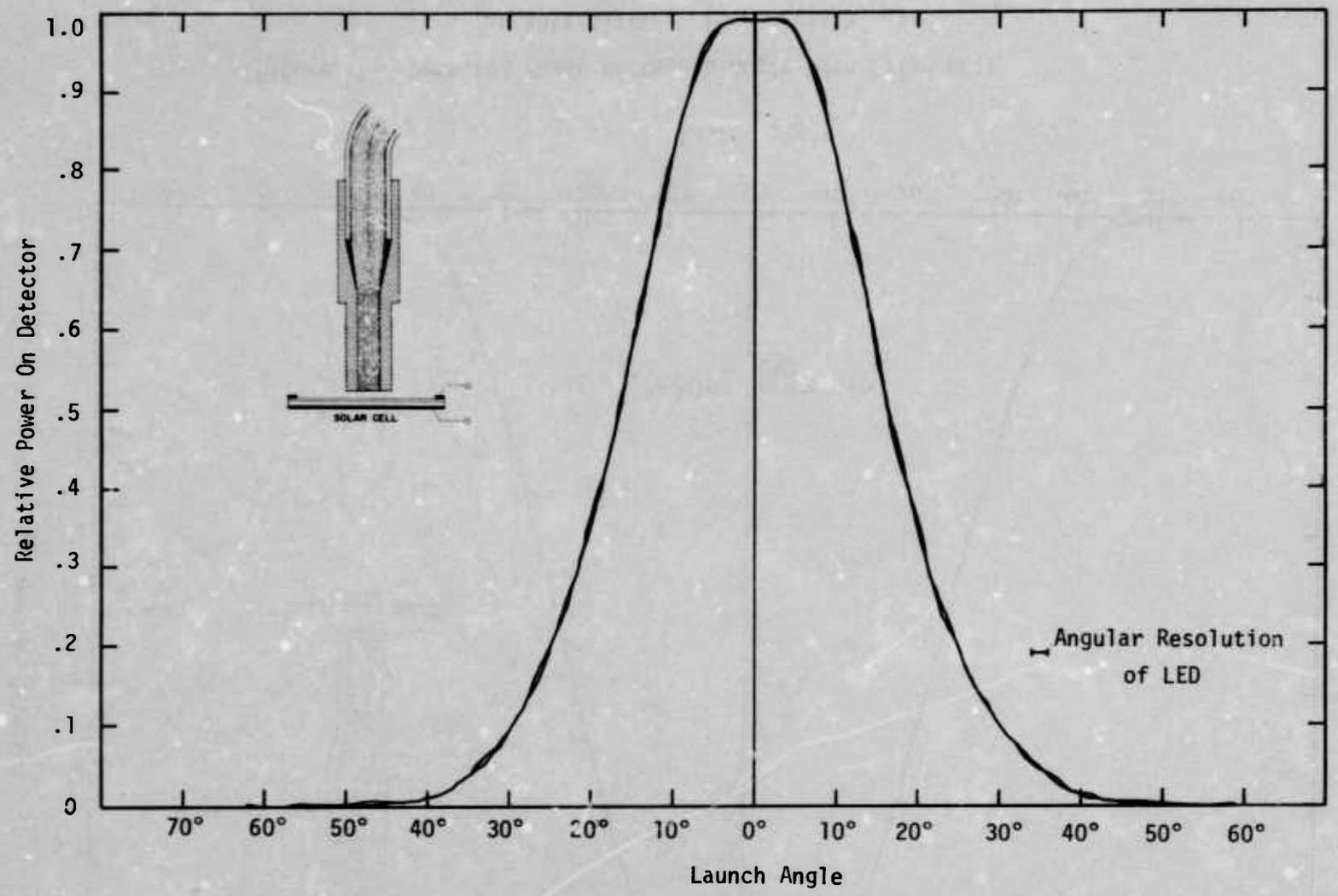

Figure 76. Detector Power Vs Launch Angle With Solar Cell for 100ft Galileo Fiber Optic Bundle

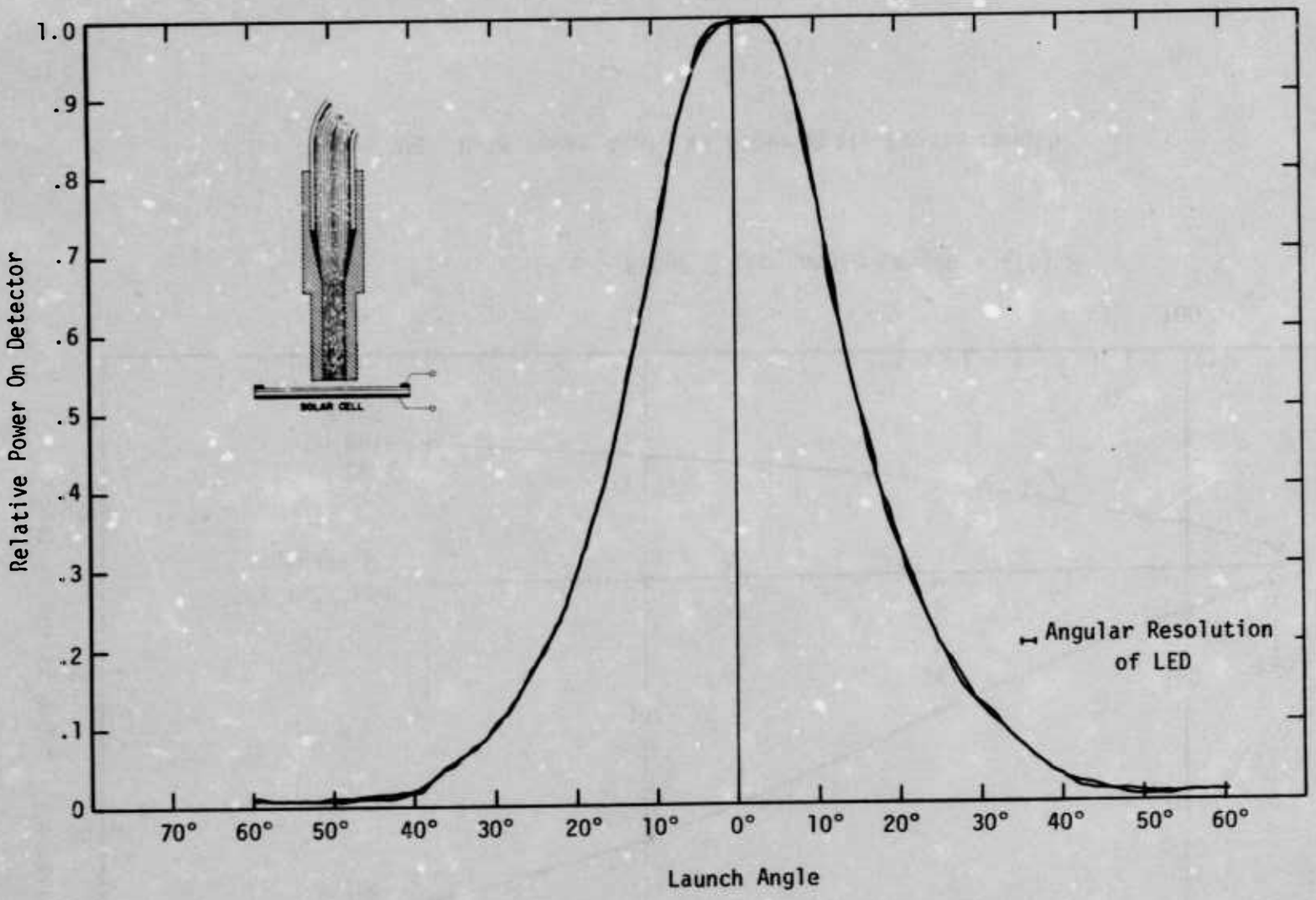

Figure 77. Detector Power Vs Launch Angle With Solar Cell for 150ft Galileo Fiber Optic Bundle

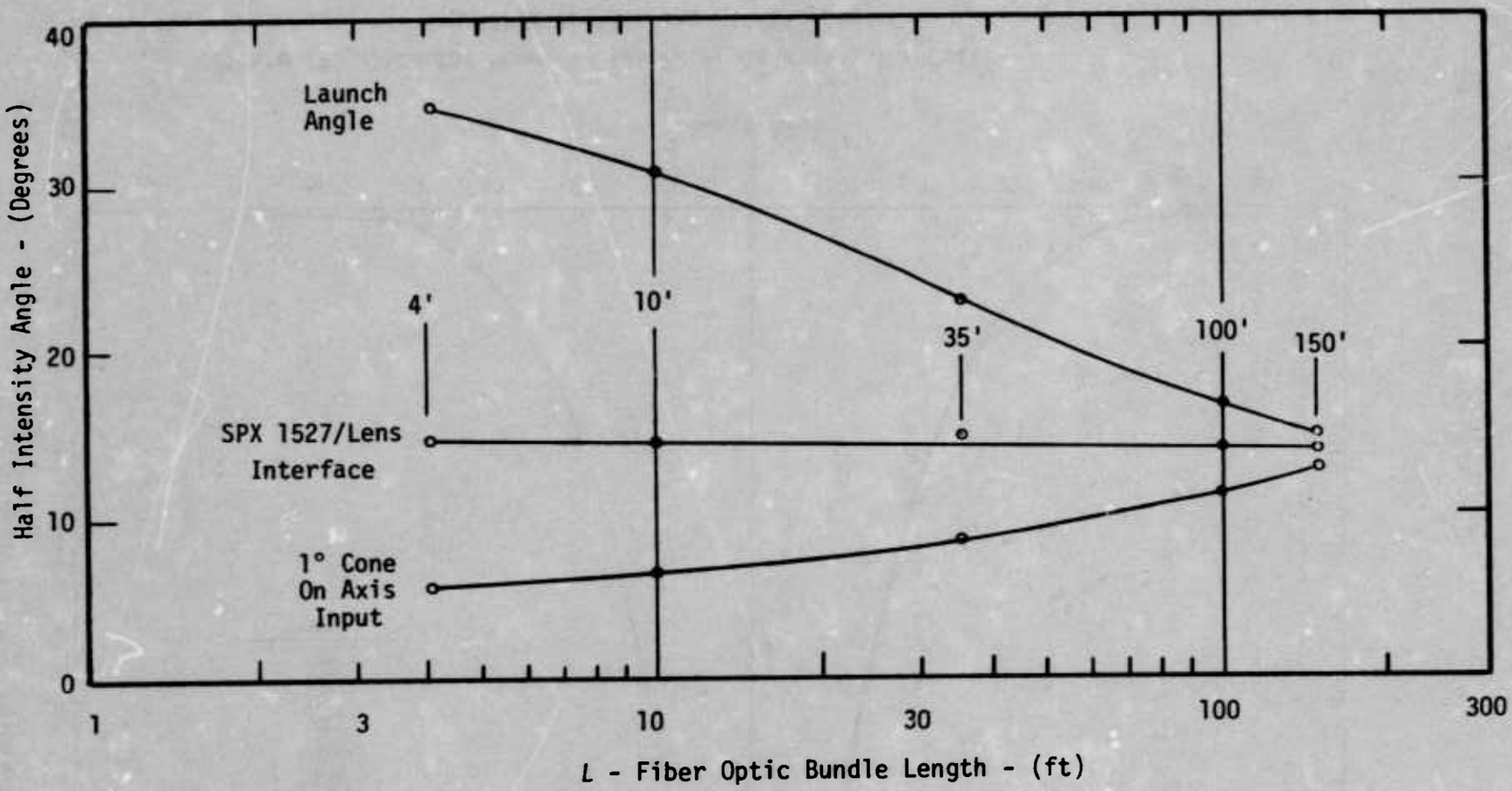

Figure 78. Half Power Angle Vs Fiber Optic Bundle Length

Figure 78 is a plot of the half intensity angle vs. length for the three sets of curves presented in this section. The top curve is the transmission NA or launch angle plot. The middle curve is the exit end pattern plot for the SPX 1527/Lens interface shown in Figure 55. The bottom curve is the far field exit end pattern plot for a 1° half angle cone input on axis. All three curves tend to the same half intensity angle at L = 150ft. Inspection of Figure 63, 70 and 77 shows that not only are the half intensity angles close to the same but the plots themselves are nearly the same at all angles. Thus, for L = 150ft the exit end radiation pattern is independent of the launch condition. Furthermore the launch angle or transmission characteristic has the same shape as the exit end radiation pattern. This means that the rays propagating down the fiber have become almost completely scrambled in 150ft and the angular distribution of radiant intensity has reached an equilibrium condition. Based on Figure 78 the scrambling length, L_s, of Galileo fiber optic bundles is about 150ft.

For lengths less than L_s, the pulse distortion follows the geometrical model give by[1]

$$\Delta t = \left(\frac{NA_\phi}{2n_2}\right)^2 \frac{2n_2}{c} L \qquad (166)$$

where L is the length ($L \leq L_s$),

NA_ϕ is the numerical aperture of a uniformly filled launch cone ($0 \leq NA \leq 0.24$),

c is the velocity of light in vacuum,

n_2 is the index of refraction of the core glass ($n_2 = 1.625$), and

Δt is the length of the ramp at the exit end of the fiber for a step function input.

For a scattering length of 150ft, and NA = .24 the pulse distortion is

$$\Delta t = 2.66\text{ns} \tag{167}$$

For fiber optic bundles longer than L_s the complete scrambling of trajectories (delay times) causes the pulse distortion to increase as $L^{\frac{1}{2}}$ as shown in Eq (168)

$$\Delta t = \left(\frac{NA_\phi}{2n_2}\right)^2\left(\frac{2n_2}{c}\right)\sqrt{L_s\ L} \tag{168}$$

At present the attenuation in the Galileo fiber optic bundles is so great (0.6dB/m) that lengths greater than L_s have little practical value. Therefore, over the useful range, the pulse distortion in the Galileo fiber optic bundles will follow Eq (166).

The ideal radiation pattern for an LED in a data bus is the exit end radiation pattern of a fiber bundle of length L_s. An LED with this ideal radiation pattern insures that the angular distribution of the optical energy, NA_ϕ, is the same at all parts of the bus. Based on the half intensity angle, the SPX 1527/lens interface shown in Figure 78 comes close to meeting this condition for the Galileo fiber bundles. Unfortunately the SPX 1527/lens interface has a large void in the center of the launch cone as shown in Figure 56. From Eq (134) the preferred length for scrambler rod is dependent on NA_ϕ. Thus, when the LEDs on a data bus all have the ideal radiation pattern, the scrambler rods will have the same effect on light from a short fiber and light from a long fiber. When NA_ϕ is constant the fiber optic attenuation is a constant. In point-to-point fiber optic data transmission systems where scrambler rods are not used, the attenuation can be reduced by using a highly collimated LED with a smaller half intensity angle than the ideal radiation pattern.

The bottom curve in Figure 78 shows that when a 1° half angle cone is coupled into a 4ft fiber optic bundle, the light at the exit end has a half angle of 5°. This measurement has been repeated with a fiber optic bundle 1ft long with the same result. Direct microscopic examination of the polished terminations on these bundles has shown that this effect is due to a significant region of graded index of refraction in the core near the core/cladding interface. This graded-index region may be observed by viewing one end of a fiber bundle with a low power microscope while the other end is illuminated with white light at an angle of about 45° to the axis of the termination. Under these conditions, the light from the central region of the core of each fiber will lie outside the NA of the microscope objective lens; thus, the center of the fibers will be dark. However, the index gradient near the core/cladding interface will refract the light into the microscope objective and the outer edge of the core will light up as shown in Figure 79. Comparing the width of this lighted region to the cladding thickness shows the graded region to be 4-5μm thick. The presence of this graded layer may explain the lower loss for rays near the optical axis of the fibers and the shape of the equilibrium angular distribution of light in long fibers. For small angle rays, this graded index interface gives a gradual ray bending effect like that in a self-focusing fiber. However, since the graded region does not extend all the way across the fiber, the time dispersion characteristics will be largely the same as for a clad fiber without grading. The 5° angle spread observed for this phenomenon suggests that the change in core index in the graded region is about 0.2% or from 1.625 to 1.62175.

The graded index region discussed here lies entirely inside the core/cladding interface as observed under front surface illumination as described above. Under certain lighting conditions, the lighted ring can be very bright with sharp contrast to the dark

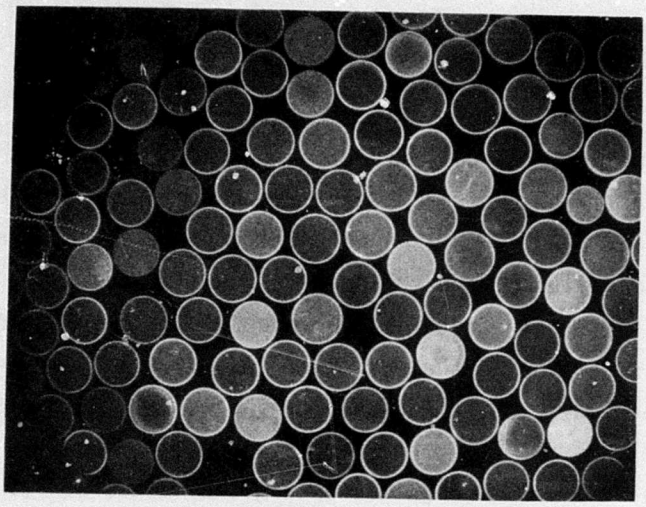

Figure 79. Galileo Graded Index Region

central region of the core. Observation of this phenomenon should not be interpreted as light transmission in the cladding glass. In most cases, the epoxy used in a conventional termination has an index of refraction between 1.49 and 1.62 which is higher than the index of the cladding glass. Thus, the epoxy used in the termination effectively couples light out of the cladding glass at each end of a fiber optic bundle and optical transmission through the cladding glass is negligible.

The relatively small value of scattering length (L_s = 150ft) of the Galileo fiber optic bundle suggests that much of its optical loss is due to scattering phenomena rather than absorption. The fact that the NA decreases so rapidly with fiber length suggests that most of the scattering centers are at the core/cladding interface rather than in the bulk of the core. This causes the wide angle rays to be attenuated more rapidly than the axial rays because the wide angle rays undergo more reflections at the core/cladding interface. Since the attenuation seems to be dominated by scattering, significant improvements in performance can be expected if the scattering centers at the core/cladding interface can be removed.

Corning low-loss fiber optic bundles have attenuation factors less than 0.03dB/m at 907nm. However, these bundles have small diameter (25mil) and low NA (0.14) and are therefore difficult to couple to LEDs.

The new plastic clad-fused silica core fibers offer the most promise for use in optoelectronic data transmission in avionic systems. These fibers have attenuation of 0.1dB/m or less at 907nm and NA between 0.3 and 0.4. The maximum operating temperature is greater than 125°C and the fibers are more radiation hard than Corning low loss. As these new fibers become more readily available, they should be evaluated using the techniques described in this section.

SECTION V

CONCLUSIONS

Optoelectronic data transmission is based on the use of light emitting diodes (LEDs), multimode flexible fiber optic bundles and silicon photodiodes. This optoelectronic technology offers an information transmission capability that is consistent with military requirments and potentially superior to wire techniques. The optoelectronic interface is suitable for use in both high data rate digital data buses and wide band analog channels. Thus, this emerging technology offers a viable means of responding to the increasing bandwidth requirements of new avionics systems. The purpose of this continuing study has been to evaluate and characterize non-coherent optical components, devices and techniques in order to discover and define the factors that limit the performance of optoelectronic data transmission systems. Particular emphasis has been given to those phenomena and effects which impose design and performance constraints that are different from the familiar constraints found in wire systems.

Presently available optoelectronic components are capable of data rates in excess of 100Mbit/s with a bit error rate of 10^{-8}. LED development can result in a 10 times improvement in basic LED speed and a 6 to 10 times improvement in LED efficiency. These improvements are needed more to simplify LED drive circuits than to achieve higher data rates. With the speed of present GaAs LEDs the driver circuits become very complex and inefficient. Higher efficiency LEDs could result in transmission over greater distances. However, it is more likely that the higher efficiency will be used to reduce drive current requirements and thereby further simplify the LED driver circuit and increase the life of the LED.

A. TASK SUMMARY

The conclusions of the various analyses performed on this study are summarized briefly below.

Optoelectronic Signaling and Detection - The characteristics of optoelectronic signaling and detection are discussed in detail. The constraints imposed by the unipolar nature of optical signals are discussed in conjunction with the problems of clock recovery and synchronization in a data bus. A thorough analysis of the photodiode/preamp interface is presented. The Spectronics, Inc. suboptimum detection scheme is described and compared to a matched filter detector for the existing non "white" noise case. The two detection schemes are essentially equivalent. A circuit technique to increase the signal bandwidth of an LED by up to 10 times is presented. This increase in bandwidth is achieved at the expense of power efficiency and complexity of the driver circuit.

Data Bus Structure - The analysis of data bus structures is expanded to include the radial data bus. Comparison of in-line and radial data bus systems shows a clear performance advantage for the radial structure. Circular and square scrambler rods are discussed and an approximate technique for designing scrambler rods is presented.

Optoelectronic Components - Several discrete component and hybrid preamps are characterized and compared to theory. A technique is presented for achieving approximate drift cancellation without increasing noise. A number of test adapters are described and characterized. These test adapters are then used to evaluate LEDs and photodiodes. An LED driver circuit is presented which uses the speed-up technique developed on this program. The circuit functioned properly but the expected performance could not be achieved because of inductance in the transistor package in series with the emitter lead. A search for adequately packaged transistors in continuing. Spectronics, Inc. edge emitter LEDs are compared to two kinds of dome LEDs made by Texas Instruments. The three types

of GaAs LEDs have comparable bandwidth, series inductance, and series resistance. The SPX 1527 edge emitter consistently couples both a larger power and a larger fraction of its total power to a 45mil diameter fiber optic bundle. Part of this result is due to the lower internal efficiency of the domes tested. If the dome efficiency is normalized, the edge emitter is 27% better than one dome and 12% worse than the other. The edge emitter structure offers better tolerance control and is more amenable to volume manufacture than the dome. An SPX 1527 LED achieved a 1.1ns rise time with a speed-up network; the high-frequency modulation transfer of both dome and edge-emitter LEDs falls off as $f^{-\frac{1}{2}}$, it is shown that large optical modulation depths can be obtained at frequencies above the LED cut-off frequency by using current overdrive. A total of 4 photodiodes, two avalanche photodiodes, an avalanche photodetector module and a hybrid data transmission system are characterized and compared. The SPX 1615 p-i-n photodiode gives the best overall performance in most data transmission applications. The two different types of avalanche photodiodes each offer superior performance in certain special cases. The performance advantages of avalanche photodiodes tend to be offset by the increased cost and circuit complexity associated with their use. A detailed characterization of the transmission properties of Galileo fiber optic bundle is presented. The ideal radiation pattern for a data bus LED to be used with Galileo fiber optic bundles is defined as the exit end far field radiation pattern of a fiber optic bundle longer than the scrambling length. The new plastic clad-fused silica core fiber optic bundles meet all of the requirements of optoelectronic data transmission systems. This fiber has $0.3 \leq NA \leq 0.4$ which offers ease of coupling to LEDs, the attenuation is less than 100dB/km, a maximum operating temperature above 125°C, and the best radiation tolerance of any fiber reported.

Radiation Effects - Appendix V is devoted entirely to a study of radiation effects. It begins with general background information and terminology of the interaction of radiation with matter. It also covers radiation damage effects in the specific materials of optoelectronic data transmission systems. The presentation then turns to radiation effects on the specific components of the optical system and concludes with a summary of radiation damage threshold values and failure modes for optical system peripheral circuitry such as digital and linear integrated circuits.

A radiation analysis of a typical 30m optoelectronic data transmission channel with a data rate of 10Mbit/s is presented. This analysis shows that the transient absorption of the fiber optic bundle following a pulse of ionizing radiation causes the most severe degradation of system performance. The plastic clad-fused silica core fibers show the best radiation tolerance of any fiber reported - better even than the all plastic fibers. Also, the fused silica core fibers show their highest radiation tolerance at longer wavelengths (900nm) and are therefore ideal for use with existing GaAs LEDs and silicon photodiodes.

B. RECOMMENDATIONS

The technologies of diffused junction GaAs LEDs and silicon planar p-i-n photodiodes are well advanced and presently capable of supporting an optoelectronic data transmission system activity. Comparing the two technologies, silicon is much further advanced and no basic technology development is required. Silicon photodiode component development will be required to insure optimum performance in the variety of system environments that will be encountered. Component development and manufacturing activity is needed in GaAs to optimize LED performance and insure compliance with environmental and reliability requirements of military applications. Continued research in GaAlAs and InGaAs LEDs is needed to achieve an anticipated improvement of 10 times in both speed and power output compared to present GaAs LEDs.

Development activity on fiber optic bundles should emphasize the plastic clad-fused silica core technology. Additional radiation damage measurements are needed. Transient absorption measurements should be extended to pulse doses of 10^7 rad and recovery times of 5 seconds. Fiber optic research should continue to search for new approaches to multimode fiber optic bundles that will give better performance than the plastic clad-fused silica core technology.

The greatest need of optoelectronic data transmission at this time is the identification and definition of systems that can profitably use this emerging technology.

APPENDIX I

FREQUENCY RESPONSE OF THE SPX 1615 PIN PHOTODIODE

TABLE OF CONTENTS

A. INTRODUCTION

In defining the maximum data rate limitations for a wide-band data transmission system, it is imperative that accurate high-frequency modeling of the components comprising the system be performed. For optoelectronic data transmission systems, the components which must be considered are the LED, fiber bundle and photodiode detector. This investigation is concerned with the high-frequency performance of the SPX 1615 PIN photodiode detector portion of the system.

Electron and hole drift velocities do not reach the saturation limit in the SPX 1615 under conventional operating voltage of 90 volts (I-layer reach-through condition). Instead ∿90% of the electric-field region in the depletion layer is of strength characteristic of field dependent (non saturated) mobility and ∿10% is characteristic of a constant, low-field mobility. Also, the electron and hole mobility values are not equal to one another at any given position in the depletion layer. An accurate representation of carrier mobility characteristics must be included for a meaningful model for the frequency response of the SPX 1615.

This investigation utilizes realistic values for hole and electron mobilities in the depletion layer and a theoretical expression for the impulse response of the SPX 1615 to incident 907nm photons is thereby dervied. A Fourier transformation of the impulse response equation is then performed to obtain the frequency response of the SPX 1615. Also the rise time of the photo-generated pulse is obtained from the impulse response.

B. DERIVATION OF THE IMPULSE RESPONSE

The electric field E in the depletion layer of a p-n junction diode is given as a function of position x by

$$E = \frac{2\,V(W - x)}{W^2} \tag{169}$$

where V = applied voltage

W = depletion layer width

The intrinsic layer (I layer) in the SPX 1615 is not, in fact, intrinsic but rather is lightly doped n-type ($\rho_n \simeq 400\Omega$-cm). However, it is customary to refer to this lightly doped n-type layer as the I layer. For the SPX 1615 the I-layer width is 10^{-2} cm (4mil). At a bias of 90V the depletion layer width, W, reaches through the I layer width and the E field in the depletion layer is shown in Figure 80. Photo-generated electron-hole pairs in the depletion layer experience a drift velocity v given by

$$v = \mu E \tag{170}$$

where μ is the carrier mobility and is field dependent for E greater than $\sim 10^3$ V/cm. The electron mobility can be modeled as[15]

$$\mu_n = \frac{\mu_o E_c}{E + E_c} \tag{171}$$

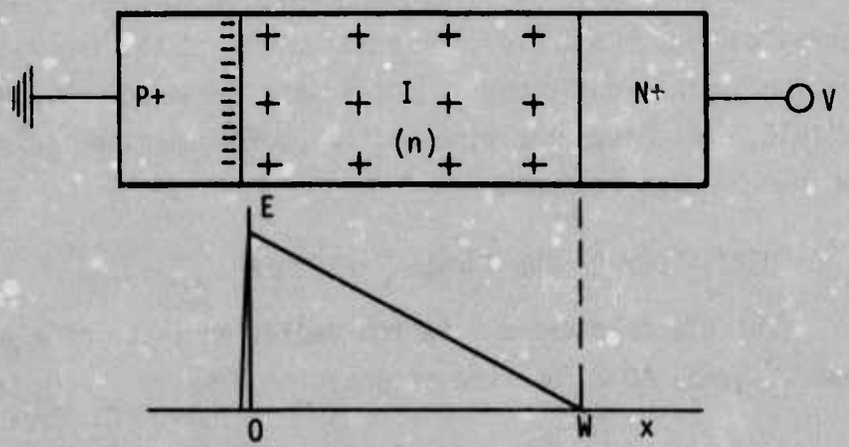

Figure 80. Electric Field Representation in the PIN Diode at Reach-Through Bias Condition

where $\mu_o = 1400 cm^2/Vs$

$E_c = 1.0 \cdot 10^4 V/cm$

The hole mobility μ_p will be assumed to have the same field dependence as that for electrons and represented as

$$\frac{\mu_n}{\mu_p} = 2.8 \tag{172}$$

Electron drift velocity in the depletion layer can then be obtained from Eqs (110) and (171) as

$$v = \frac{\mu_o E_c}{E + E_c} E \tag{173}$$

Then utilizing Eq (169),

$$v = \frac{dx}{dt} = \left[\frac{\mu_o E_c}{\frac{2V}{W^2}(W - x) + E_c} \right] \cdot \left[\frac{2V}{W^2}(W - x) \right] \tag{174}$$

which yields

$$dx \left[1 + \frac{W^2 E_c}{2V(W - x)} \right] = \mu_o E_c dt \tag{175}$$

The equation of motion for electrons photo-generated at x = 0 (Figure 80) can be obtained by integrating Eq (175)

$$\int_0^x \left(1 + \frac{W^2 E_c}{2V(W - x)} \right) dx = \int_0^t \mu_o E_c dt \tag{176}$$

which becomes

$$x - \frac{E_c W^2}{2V} \ln\left(\frac{W - x}{W}\right) = \mu_o E_c t \qquad (177)$$

When the SPX 1615 is operated in the reach through condition as shown in Figure 80, then V = 90V, W = 10^{-2} cm and Eq (177) becomes

$$x - \frac{1}{180} \ln (1 - 100x) = 1.4 \cdot 10^7 t \qquad (178)$$

Equation (178) is the equation of motion for electrons generated at x = 0 as they traverse the depletion layer.

For electrons originating at any point $x = a_1$ in the I layer, Eq (175) can be integrated as

$$\int_{a_1}^{x} \left(1 + \frac{W^2 E_c}{2V(W - x)}\right) dx = \int_0^t \mu_o E_c dt \qquad (179)$$

which becomes

$$(x - a_1) - \frac{1}{180} \ln \left[\frac{10^{-2} - x}{10^{-2} - a_1}\right] = 1.4 \cdot 10^7 t \qquad (180)$$

Similarly for holes

$$(x - a_1) - \frac{1}{180} \ln \left[\frac{10^{-2} - x}{10^{-2} - a_1}\right] = \frac{1.4 \cdot 10^7 t}{2.8} \qquad (181)$$

Eqs (178), (180), (181) yield position (x) as a function of time, and velocity $(\frac{dx}{dt})$ as a function of position for carriers drifting in the E field of the depletion region.

The time-dependent impulse response for electron current, I_n, can then be derived from a knowledge of $\frac{dx}{dt}$ since

$$I_n = \frac{nq}{W}\left(\frac{dx}{dt}\right) \tag{182}$$

where q = charge on the electron

n = number of released electrons/cm^2 (a function of the number of quanta absorbed per unit path length in the x direction).

Similarly, the time-dependent impulse response for hole current, I_p, can be obtained from

$$I_p = \frac{pq}{W}\left(\frac{dx}{dt}\right) \tag{183}$$

where p = number of released holes/cm^2 (a function of the number of quanta absorbed per unit path length in the x direction).

The total current, I_t, is given by

$$I_t = I_n + I_p \tag{184}$$

The impulse photoresponse of the SPX 1615 can be obtained by coupling the above results to the following model. Consider photon absorption in the I layer of the SPX 1615 when the I layer is divided into 11 segments as shown in Figure 81. The total current is obtained by summing the electron and hole contributions originating in the eleven sigments of the I layer. To clarify the technique utilized in the calculation, consider the current impulse response resulting

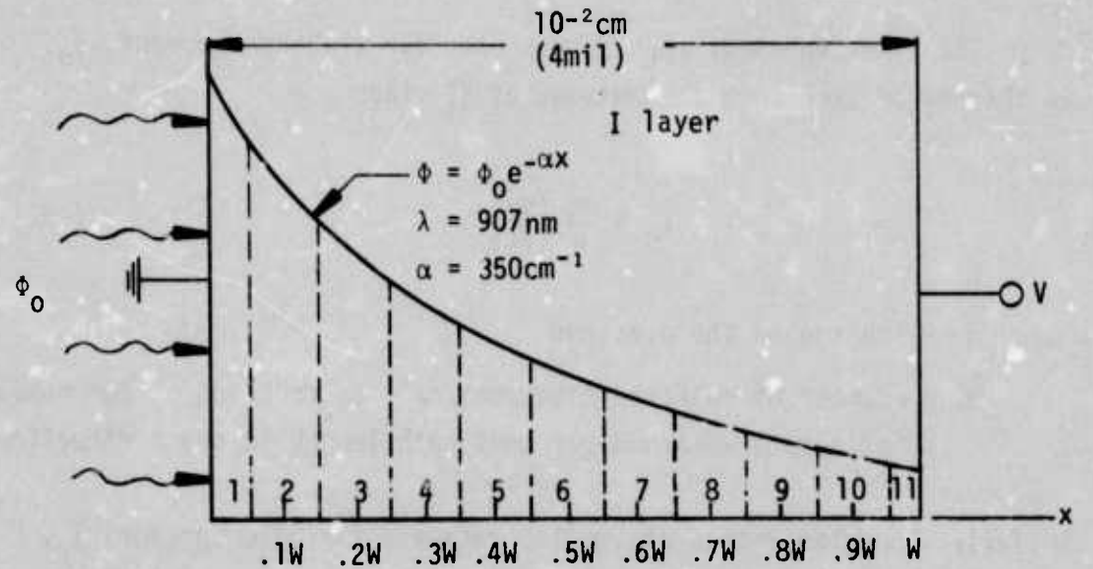

Figure 81. Photon absorption in the I layer of the SPX 1615

from photoabsorption in the fourth segment of Figure 81. Table XVI can be constructed using Eqs (180)-(183) and the photon absorption characteristic shown in Figure 81.

The results of Table XVI are summarized in graphical form in Figure 82 where impulse current response for electron-hole pair generation in segment 4 of Figure 81 is plotted. Similar calculations were performed for segments 1-11 and the results combined to yield the total electron and hole impulse current components. These results are summarized and then combined to obtain the total impulse current response in Figure 83.

From Figure 83 it is observed that the impulse resonse can be written in equation form as

$$I_*(t) = \frac{-at}{b} + a \qquad (185)$$

Table XVI. Impulse Response Contribution from Segment 4 of Figure 81

(source strength = $0.121\Phi_o$)

x (mils)	t (ns)	$v=\frac{\Delta x}{\Delta t}$ (cm/s)	$I_{normalized}=\frac{.121v}{10^7}$
Electron current, I_n			
1.2	0	$.76\times10^7$	.091
1.6	0.132	$.70\times10^7$	.083
2.0	0.276	$.63\times10^7$	.076
2.8	0.621	$.43\times10^7$	.065
3.2	0.850	$.31\times10^7$	.052
3.6	1.140	$.16\times10^7$	.041
3.8	1.490	$.09\times10^7$	.017
Hole current, I_p			
1.2	0	$.27\times10^7$	.033
.8	0.370	$.29\times10^7$	.035
.4	0.710	$.30\times10^7$	.036
.1	1.040	$.31\times10^7$	.037
0	1.120	$.32\times10^7$	.038

where $a = 1.035$ normalized current units

$b = 1.7\cdot10^{-9}$s

In obtaining Eq (185), the exponential portion of the electron-current component has been neglected. Since this remnant of current represents less than 8% of the total impulse response current, this approximation is considered to be justified both in terms of required accuracy and resulting simplicity of further analysis.

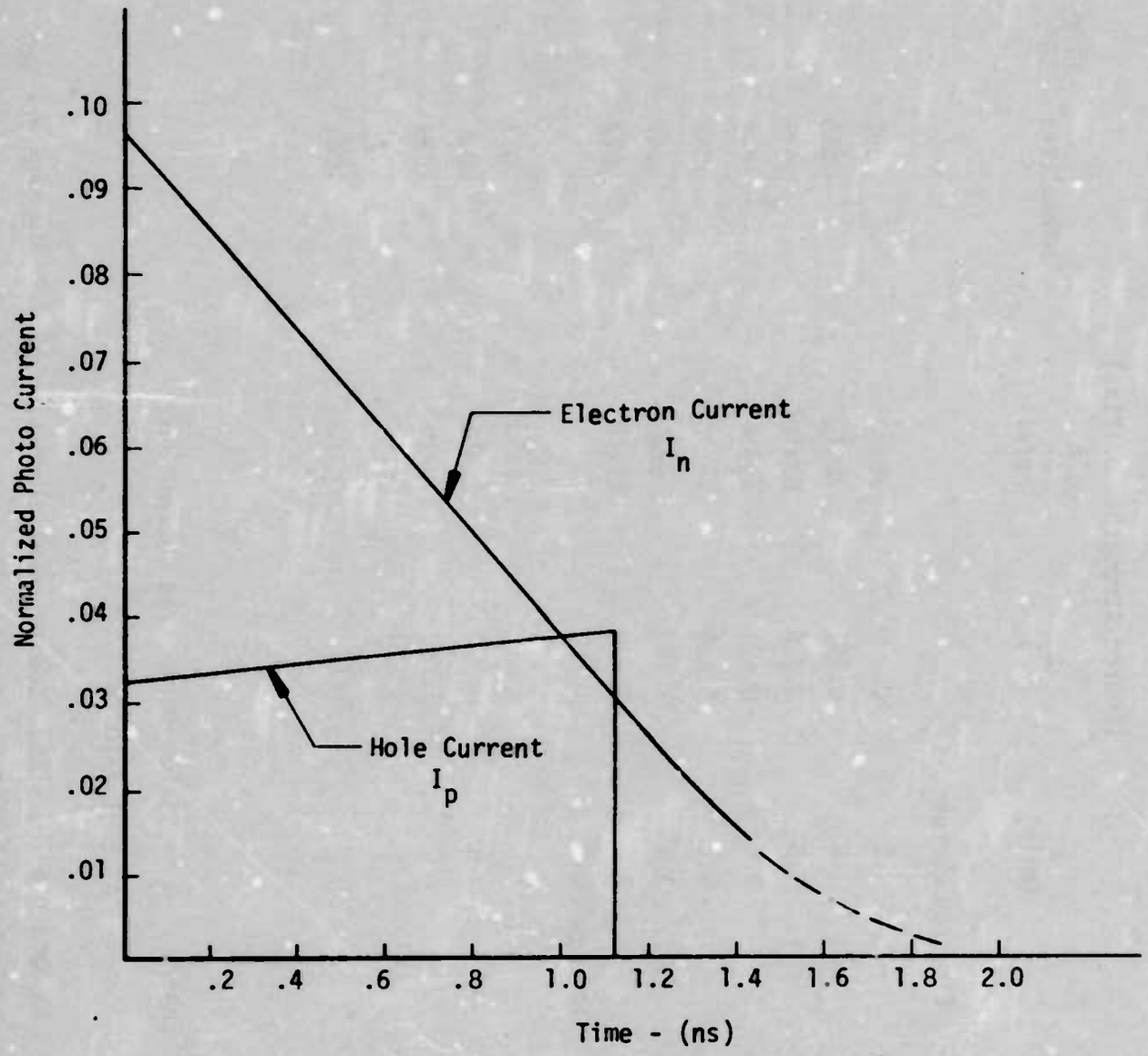

Figure 82. Impulse Response of Electron and Hole Current Components Initiated in Segement 4

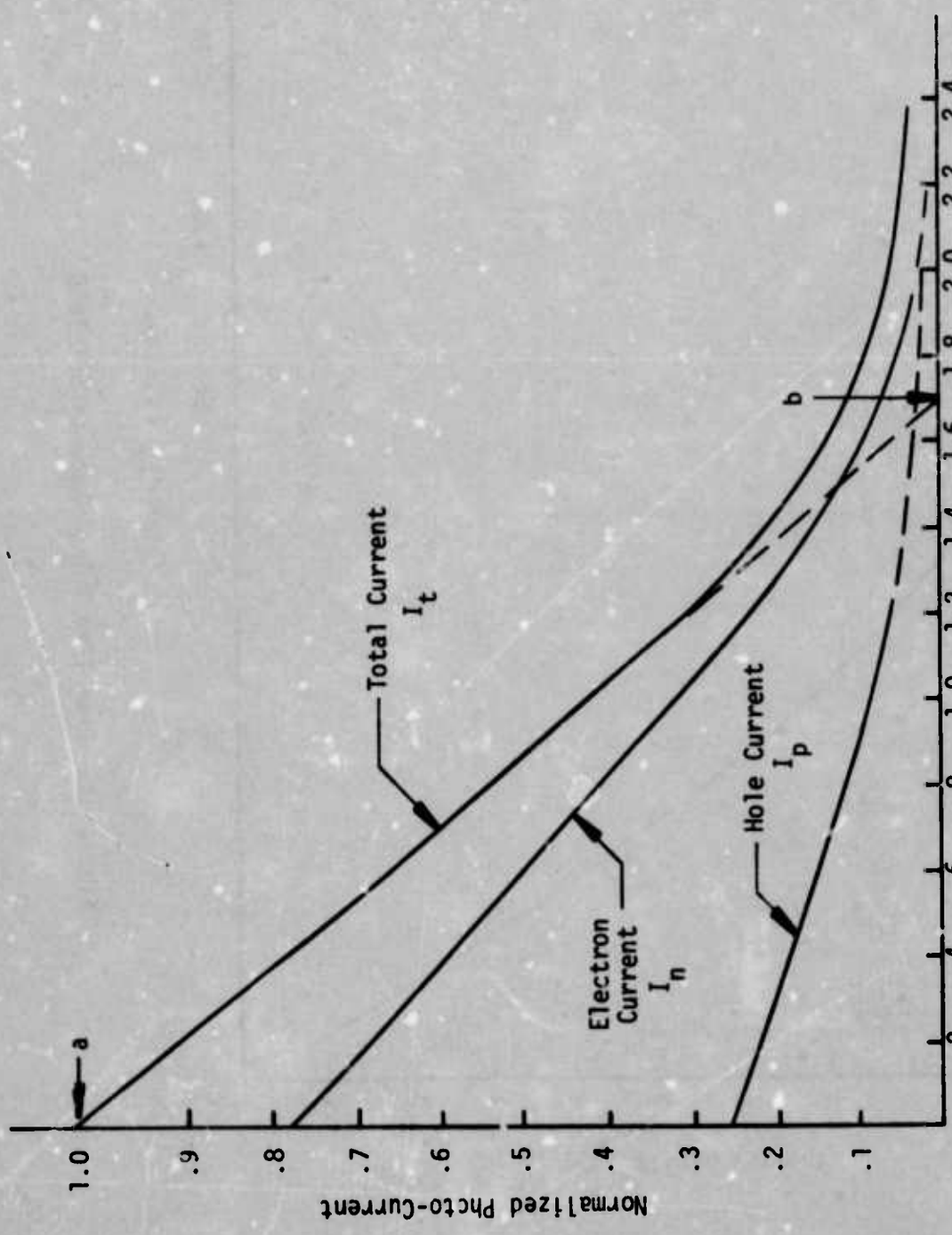

Figure 83. Total Impulse Response Current

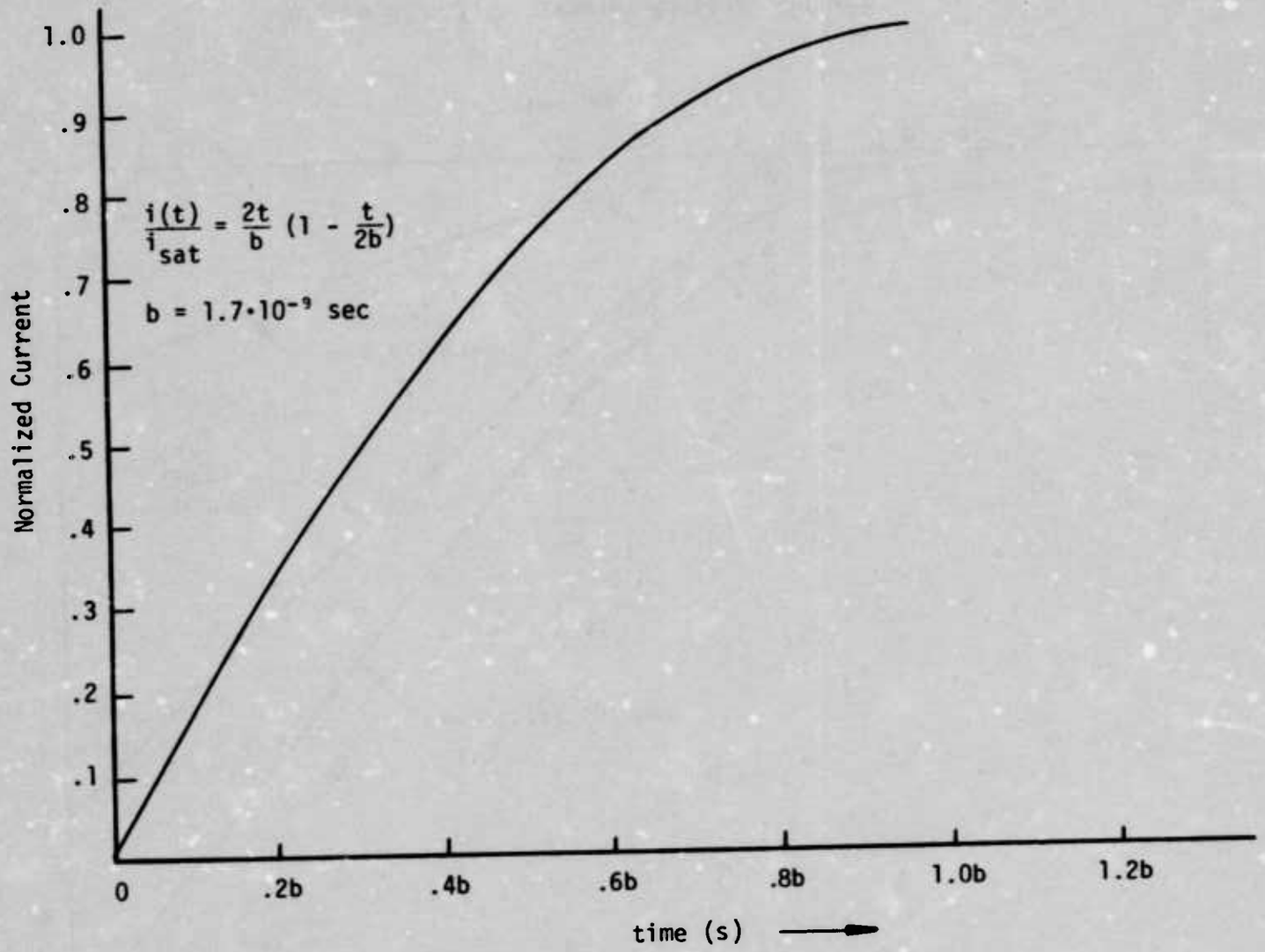

Figure 84. Rise Time Pulse Shape of SPX 1615

C. RISE TIME

The pulse response of the SPX 1615 can be determined mathematically by integrating the impulse response given by Eq (185). Thus

$$i(t) = \int_0^t I_t dt = \int_0^t \left(\frac{-at}{b} + a\right) dt \quad \text{for } t \leq b \qquad (186)$$

then

$$i(t) = \frac{-a}{b}\frac{t^2}{2}\Bigg|_0^b + at\Bigg|_0^b \qquad (187)$$

and,

$$i(t) = at\left(1 - \frac{t}{2b}\right) \quad \text{for } t \leq b \qquad (188)$$

From Eq (188) i(t) saturates at t = b and,

$$i_{sat} = \frac{ab}{2} \qquad (189)$$

Then

$$\frac{i(t)}{i_{sat}} = \frac{2t}{b}\left(1 - \frac{t}{2b}\right) \qquad (190)$$

From Eq (190) the 10% - 90% rise time of the pulse response is determined as

$$t_r = 1.07 \cdot 10^{-9} s \qquad (191)$$

The rise time "pulse shape" as derived from the impulse response with the above considerations is summarized in graphical form in Figure 84.

D. FREQUENCY RESPONSE

Fourier transformation of the impulse response from the time domain to the frequency domain yields the frequency response for the system under consideration [8,16].

$$F(\omega) = \int_{\infty}^{\infty} f(t)e^{-j\omega t}dt \tag{192}$$

Thus for the SPX 1615 from Eq (185)

$$I(\omega) = \int_{0}^{b} \left(\frac{-at}{b} + a\right)e^{-j\omega t}dt \tag{193}$$

which yields when integrated

$$I(\omega) = \frac{a}{b\omega^2}(1 - \cos\omega b) + j\frac{a}{b\omega^2}(\sin\omega b - \omega b) \tag{194}$$

As $\omega \to 0$, the low frequency value of $I(\omega)$ is given by

$$I(\omega) \to \frac{ab}{2} \tag{195}$$

Then normalizing Eq (194) to the low-frequency value of $\frac{ab}{2}$, the integral Eq (193) becomes

$$\frac{2}{ab}\int_{0}^{b}\left(\frac{-a}{b}t + a\right)e^{-j\omega t}dt = \frac{2}{\chi^2}\left[1 - \cos\chi\right] + j\frac{2}{\chi^2}\left[\sin\chi - \chi\right] \tag{196}$$

where $\chi = 2\pi fb = \omega b$

Eq (196) is in the form of, Re $I(\omega)$ + jIm $I(\omega)$ and the magnitude of the spectrum of $I(\omega)$ can be obtained from

$$\left|I(\omega)\right| = \sqrt{\left[\text{Re } I(\omega)\right]^2 + \left[\text{Im } I(\omega)\right]^2} \tag{197}$$

The phase spectrum can be determined from

$$\theta(\omega) = \tan^{-1}\left[\frac{\text{Re } I(\omega)}{\text{Im } I(\omega)}\right] \tag{198}$$

Solutions to Eq (196) and Eq (197) were obtained with the aid of an HP65 desk calculator and are plotted in Figure 85 as $|I(f)|$ and $\theta(f)$.

The results of Figure 85 indicate that the SPX 1615 photodiode has a 3dB cut-off frequency of

$$f_{3dB} = \frac{.56}{b} \tag{199}$$

and since $b = 1.7 \cdot 10^{-9}$ (Figure 83),

$$f_{3db} = \frac{.56}{1.7 \cdot 10^{-9}} = 330\text{MHz} \tag{200}$$

It is further noted that both the magnitude and phase of the frequency response are well-behaved functions similar to those characteristics of a simple RC network.

E. CONCLUSIONS

The results of Figures 84 and 85 can be utilized to discuss the high-frequency performance of the SPX 1615 photodiode in an opto-electronic data transmission system. From Eq (191) the 10 - 90% rise

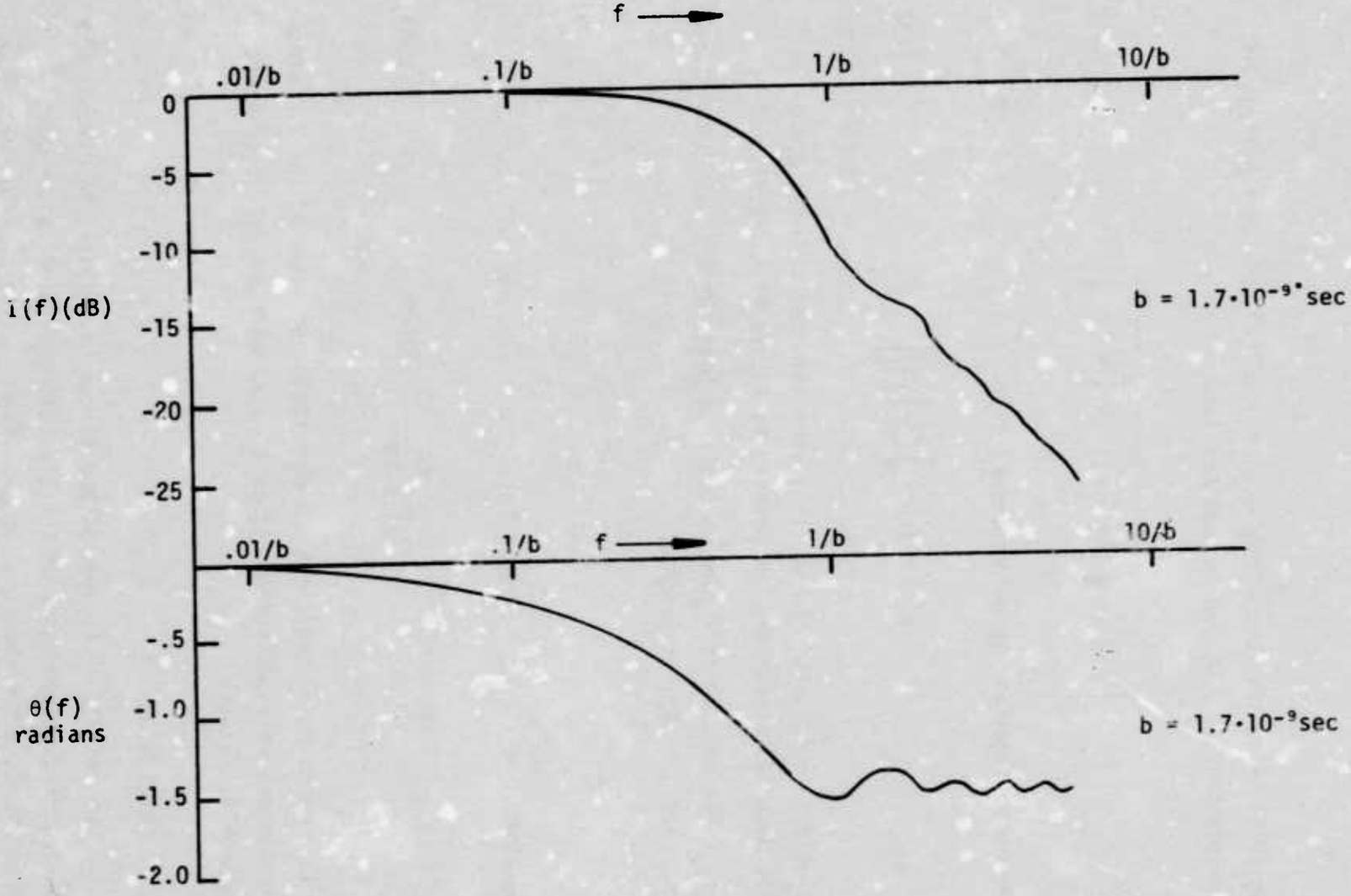

Figure 85. Magnitude and Phase of SPX 1615

time, t_r, of the device has been determined to be

$$t_r = 1.07\text{ns} \tag{191}$$

This gives an effective detector time constant, τ_d of

$$\tau_d = \frac{t_r}{2.2} = 0.49\text{ns} \tag{201}$$

The obtained 3db cut-off frequency of 330MHz (Figure 85) implies an information detection capacity of ∿300 to ∿600Mbit/s for this diode depending on coding technique, synchronization and recovery requirements. Operated at reach-through bias (V=90V) and a wavelength of 907nm, the SPX1615 photodiode exhibits well behaved transient and frequency response characteristics.

APPENDIX II

IN-LINE UNIFORM DUPLEX DATA BUS

In an in-line data bus, the T couplers are connected with flexible fiber optic bundles as shown in Figure 86. As optical signal moves down the bus it must pass through the terminations at each end of the fiber optic bundles. Thus, the transmission of the terminations is an important parameter in determining system performance. Section III describes T couplers and defines various coupling, transmission and quality factors that describe coupler performance. In this analysis of an in-line data bus, the transmissions of the fiber optic terminations are included explicitly as separate factors apart from the losses and quality factors associated with the T couplers. This approach was used so that the resulting expressions would be more generally applicable and not limited to a specific construction technique. It allows system performance to be predicted from the separate characteristics of the independent parts.

For purposes of analysis, an in-line data bus of N stations uniformly distributed along a total length L will be considered. This configuration gives the correct result for a worst case condition of transmission between opposite ends of the data bus, and typical results for all intermediate path lengths. The average fiber optic attenuation between adjacent stations, a_o, is given by

$$a_o = \exp\left[\frac{-\alpha L}{N-1}\right] \tag{201}$$

where L is the total length of the bus, and

α is the loss coefficient of the fiber optic bundle.

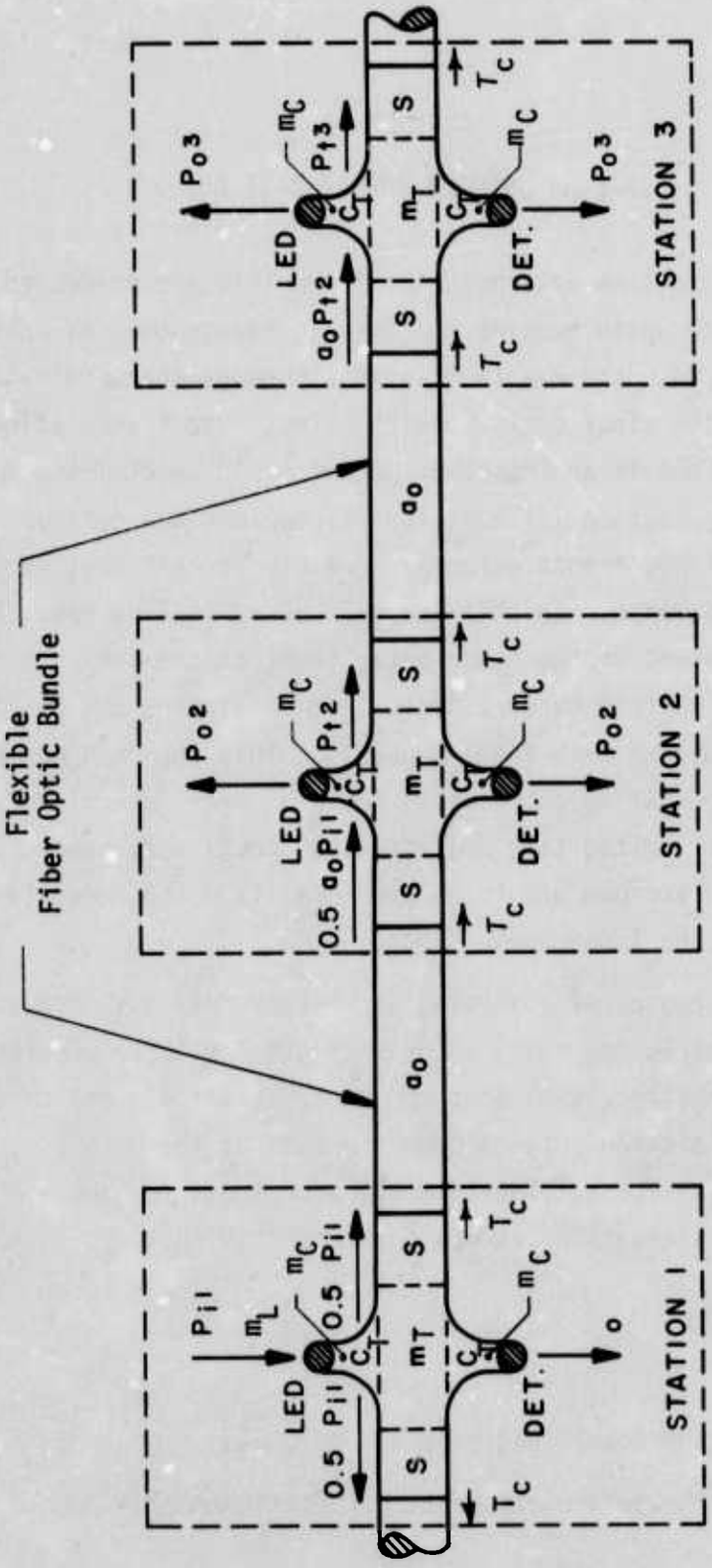

Figure 86. Signal Power Relationships in an In-Line Data Bus

When optical power is coupled into a fiber optic bundle, it is attenuated by the transmission of the input termination T_c given by Eq (104). As the light transits the fiber between stations it is attenuated by a_o given in Eq (202). As the light leaves the exit end of the fiber optic bundle a portion is reflected at the core/air interface; the fraction of light transmitted is $T_c = (1 - R_c)$ given by Eq (106). Thus, the transmission of an average fiber optic bundle that interconnects two stations is

$$a_o T_c T_c = a_o (1 - R_c)^2 \, GR_a \tag{203}$$

The symbols a_o, T_c, and T_c are shown on Figure 86.

The signal power relationships in the in-line duplex data bus when station 1 is transmitting are shown in Figure 86. When an optical power, P_{i_1}, is emitted by the LED of station 1, the power on the LED port is $m_L P_{i_1}$, where m_L is the LED quality factor defined by Eq (91). The power coupled out at the detector port of station 2, P_{o_2}, is given by

$$P_{o_2} = \left[m_L m_C^2 C_T \right] \left[a_o T_c T_c \right] \frac{P_{i_1}}{2} \tag{204}$$

The coupling quality factor, m_C is defined by Eq (89)

$$m_C = \frac{\text{(power at detector port)}}{\text{(power into scrambler area attributed to detector port)}} \tag{89}$$

the coupling factor, C_T, is defined by Eq (86)

$$C_T = \frac{\text{(scrambler area attributed to detector port)}}{\text{(area of the scrambler)}} \tag{86}$$

and $a_o T_c T_c$ is the total attenuation of the fiber optic bundle between station 1 and station 2 given by Eq (203). Referring to Eq (204), the term m_C enters once in the LED side arm of station 1 and again in the detector side arm of station 2. Front surface reflection losses at the scrambler input of station 2 are by definition included in m_C. The factor of $\frac{1}{2}$ in Eq (204) describes the split of the LED power between the two directions of transmission on the data bus.

The power transmitted to the output port of station 2, P_{t_2}, is

$$P_{t_2} = \left[m_L m_C^2\right]\left[a_o T_c T_c m_T\ (1-2C_T)\right]\ \frac{P_{i_1}}{2} \tag{205}$$

where m_T is the transmission quality factor of the T coupler given by Eq (87)

$$m_T = \frac{T_T}{1 - 2C_T} \tag{87}$$

The signal at the detector port of station 3 is

$$P_{o_3} = \left[m_L m_C C_T\right]\left[a_o^2 T_c^2 T_c^2 m_T (1-2C_T)\right]\ \frac{P_{i_1}}{2} \tag{206}$$

and the power transmitted to the output port of station 3 is

$$P_{t_3} = \left[m_L m_C^2\right]\left[a_o T_c T_c m_T (1-2C_T)\right]^2\ \frac{P_{i_1}}{2} \tag{207}$$

For station N, the power at the detector port as a fraction of the input power is

$$\frac{P_{oN}}{P_{i_1}} = \left[\frac{a_o T_c T_c m_L m_C^2 C_T}{2}\right]\left[a_o T_c T_c m_T (1-2C_T)\right]^{N-2} \tag{208}$$

Equation (208) is the worst case power ratio, R_{PT}, given in Eq (115) in Section III.C. This worst case power ratio can be maximized by setting the derivative of R_{PT} with respect to C_T equal to zero, and solving for the optimum value of C_T. Inspection of Eq (208) shows that R_{PT} is of the form

$$R_{PT} = K_1 C_T \left(1-2C_T\right)^{N-2} \tag{209}$$

where K_1 is a constant given by

$$K_1 = \left[\frac{a_o T_c T_c m_L m_C^2}{2}\right]\left[a_o T_c T_c m_T\right]^{N-2} \tag{210}$$

From Eq (209)

$$\frac{dR_{PT}}{dC_T} = K_1\left[\left(1-2C_T\right)^{N-2} - (2C_T)(N-2)\left(1-2C_T\right)^{N-3}\right] \tag{211}$$

Setting Eq (211) equal to zero gives

$$(1-2C_T) - (2C_T)(N-2) = 0 \tag{212}$$

which defines the optimum value of C_T given in Eq (116)

$$C_{opt} = \frac{1}{2(N-1)} \tag{116}$$

From Eq (116), C_{opt} is dependent only on the number of stations on the bus. Specifically, this means that the optimum value of C_T is independent of all of the factors included in the constant K_1, Eq (210). Equation (116) is a very general result with no limiting assumptions or approximations.

The use of the optimum coupling factor in an in-line data bus gives the maximum value of the worst case power ratio. This maximum value of R_{PT} is determined by substituting Eq (116) into Eq (115). The results is shown in Eq (117)

$$R_{PT}\Big|_{max} = \left[\frac{a_o T_c T_c m_L m_C^2}{4(N-1)}\right]\left[\frac{a_o T_c T_c m_T (N-2)}{(N-1)}\right]^{N-2} \tag{117}$$

The worst case dynamic range encountered at the various detectors in the in-line data bus occurs when station (N-1) transmits to station N followed by a transmission from station 1 to station N. This worst case dynamic range, D_{RT}, is equal to the ratio of the output power at station 2 to the output power at station N when station 1 is transmitting.

$$D_{RT} = \left[\frac{1}{a_o T_c T_c m_T (1-2C_T)}\right]^{N-2} \tag{213}$$

The value of D_{RT} when the coupling factor is C_{opt} is obtained by substituting Eq (116) into Eq (213). The result is presented in Eq (118)

$$D_{RT}\Big|_{opt} = \left[\frac{1}{a_o T_c T_c m_T}\left(\frac{N-1}{N-2}\right)\right]^{N-2} \tag{118}$$

APPENDIX III

IN-LINE TAPERED DUPLEX DATA BUS

Because all of the passive couplers are identical in the uniform data bus shown in Figure 86, the end unit termination absorbs 93.3% of the signal power on the bus at that point. This waste of useful signal power can be eliminated by tailoring the coupling factors of the duplex couplers depending on the position of a particular station on the data bus. Figure 87 shows one half of an open line duplex data bus using graded coupling factors. Station 9 represents the midpoint of the data bus. The coupler at station 9 is a symmetrical duplex coupler like Figure 15. The couplers at station 1 (and 17 not shown), couple out all of the signal power remaining on the bus at that point; these end couplers are not duplex. The coupling factors in Figure 87 were calculated using a recursion formula developed for Ref 1 which gives the optimum values of the two way coupling factors all along the data bus. For the tapered duplex data bus, the optimum set of coupling factors will result in equal optical signal power at each detector port on the data bus.

Again, the stations will be assumed to be uniformly spaced along the data bus so that the fiber optic attenuation a_o can be represented by Eq (202) in Appendix II. The transmission of an average fiber optic bundle that interconnects two stations is given by Eq (203) in Appendix II.

The signal power relationships in the in-line tapered duplex data bus are basically the same as for the uniform data bus shown in Figure 86. However, the subscript T has been dropped and numerical subscripts used to denote the station; the parameters m_L, m_C, m_T, T_C and T_C are assumed to have the same value for all couplers. Thus, T_1 denotes station 1 and C_N denotes station N. The tapered data bus

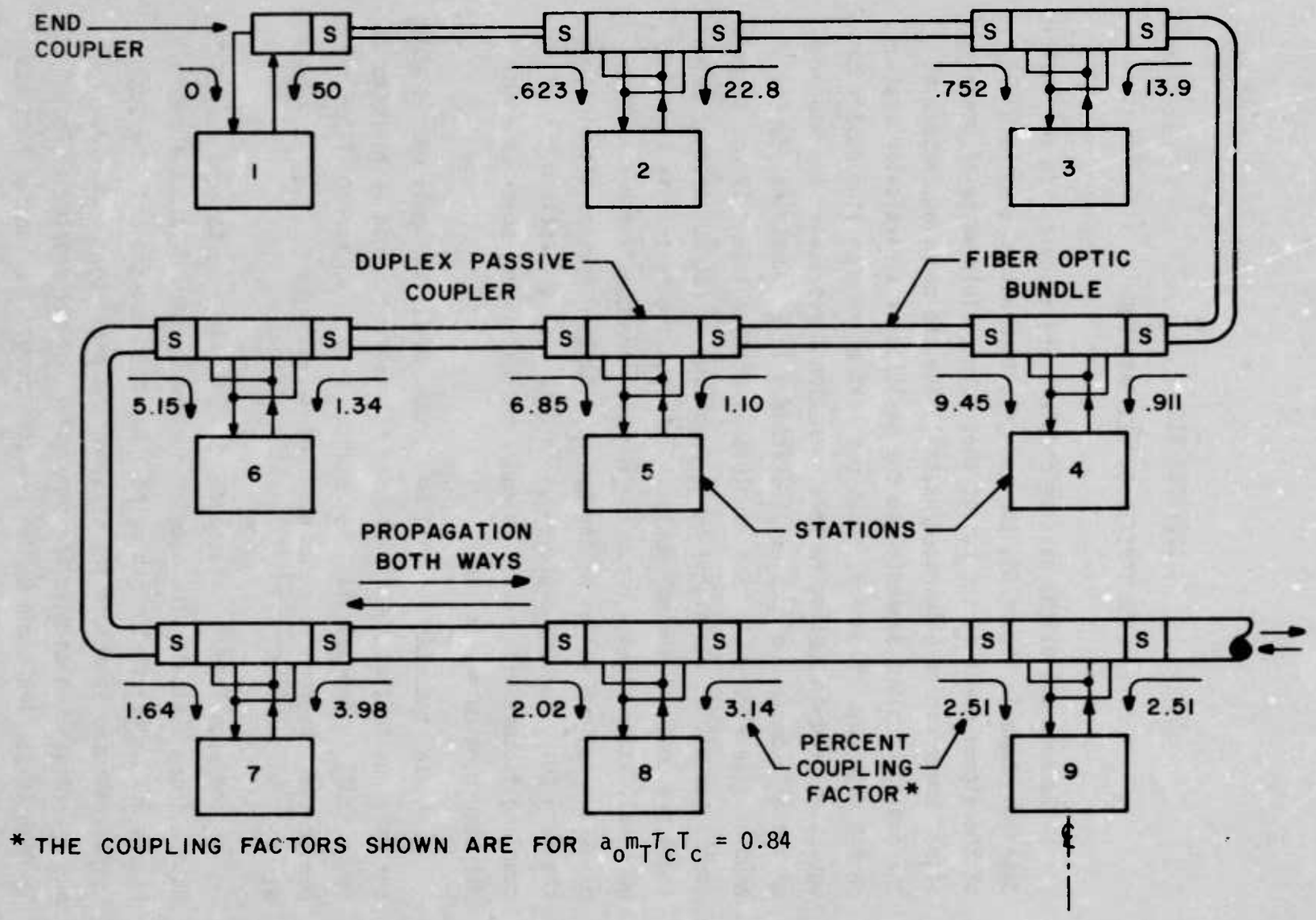

Figure 87. Tapered Duplex Data Bus

is always symmetrical about the center. For an odd number of stations, the passive coupler at the center station is symmetrical. For an even number of stations, the point of symmetry falls between two stations, and none of the passive couplers are symmetrical.

The open line data bus of Figure 87 can be converted to a loop system by combining stations 1 and 17, and making that combination the central master unit. This gives the reliability advantage gained by relaying through the central master unit if the data bus is broken.

When an optical power P_{i_1} is coupled into the bus at station 1, the power at the detector port of station 2, P_{O2}, is given by

$$P_{O_2} = \left[m_L m_C^2 C_2\right]\left[a_o T_c T_c\right] P_{i_1} \tag{214}$$

The coupling quality factor, m_C is defined by Eq (89) and the coupling factors C_1 through C_N are defined by Eq (86) at each end of each coupler.

The power transmitted to the output port of station 2, P_{t_2}, is

$$P_{t_2} = \left[m_L m_C\right]\left[a_o T_c T_c m_T\ (1-2C_2)\right] P_{i_1} \tag{215}$$

where m_T is the transmission quality factor of the T coupler given by Eq (87). At station 3 the output powers are

$$P_{O3} = \left[m_L m_C^2 C_3\right]\left[m_T(1-2C_2)\right]\left[a_o T_c T_c\right]^2 P_{i_1}$$

$$P_{t^3} = \left[m_L m_C\right]\left[(1-2C_2)(1-2C_3)\right]\left[a_o m_T T_c T_c\right]^2 P_{i_1} \tag{216}$$

At station N the output powers are

$$P_{oN} = (a_o T_c T_c)(a_o m_T T_c T_c)^{N-2}(1-2C_2)(1-2C_3)\cdots(1-2C_{N-1})C_N \tag{217}$$

$$P_{tN} = 0$$

Because of symmetry, station N is identical with station 1 and

$$C_N = 0.5 \tag{218}$$

The coupling factors may be optimized by setting $P_{o2} = P_{o3} = \cdots P_{oN}$ and solving for the ratios of the coupling factors on adjacent stations. Thus, from $P_{o_2} = P_{o3}$ comes

$$\left[m_L m_C^2 C_2\right]\left[a_o T_c T_c\right] = \left[m_L m_C^2 C_3\right]\left[m_T(1-2C_2)\right]\left[a_o T_c T_c\right]^2 \tag{219}$$

which gives

$$C_3 = \frac{1}{a_o m_T T_c T_c}\ \frac{C_2}{1-C_2} \tag{220}$$

In general, for any station k where $k \neq 1$

$$c_k = \frac{1}{a_o m_T T_c T_c}\ \frac{C_{k-1}}{1-2C_{k-1}} \tag{221}$$

and at station N

$$C_N = 0.5 = \frac{1}{a_o m_T T_c T_c}\ \frac{C_{N-1}}{1-2C_{N-1}} \tag{222}$$

from which

$$\frac{2C_{N-1}}{1-2C_{N-1}} = a_o m_T T_c T_c \tag{223}$$

Solving for 2 C_{N-1} gives

$$2C_{N-1} = \frac{a_o m_T T_c T_c}{1 + a_o m_T T_c T_c} \tag{224}$$

Equation (221) states that

$$2C_{N-1} = \frac{1}{a_o m_T T_c T_c} \quad \frac{2C_{N-2}}{1-2C_{N-2}} \tag{225}$$

Solving Eq (225) for $2C_{N-2}$ gives

$$2C_{N-2} = \frac{2a_o m_T T_c T_c C_{N-1}}{1 + 2a_o m_T T_c T_c C_{N-1}} \tag{226}$$

Substituting the value of $2C_{N-1}$ from Eq (224) gives

$$2C_{N-2} = \frac{(a_o m_T T_c T_c)^2}{1 + (a_o m_T T_c T_c) + (a_o m_T T_c T_c)^2} \tag{227}$$

For convenience in notation let

$$a_o m_T T_c T_c = T_{tp} \tag{228}$$

Using Eq (228) and applying Eq (221) for each station in turn gives a general expression for the coupling factors

TABLE XVII

Coupling Factors For

An N Station Tapered Data Bus

Station	C (left)	C (right)
1	0	0.5
2	$\frac{0.5(T_{tp})^{N-2}(1-T_{tp})}{1-(T_{tp})^{N-1}}$	$\frac{0.5T_{tp}}{1+T_{tp}}$
3	$\frac{0.5(T_{tp})^{N-3}(1-T_{tp})}{1-(T_{tp})^{N-2}}$	$\frac{0.5(T_{tp})^{2}(1-T_{tp})}{1-(T_{tp})^{3}}$
**********		
k	$\frac{0.5(T_{tp})^{N-k}(1-T_{tp})}{1-(T_{tp})^{N+1-k}}$	$\frac{0.5(T_{tp})^{k-1}(1-T_{tp})}{1-(T_{tp})^{k}}$
**********		
N-2	$\frac{0.5(T_{tp})^{2}(1-T_{tp})}{1-(T_{tp})^{3}}$	$\frac{0.5(T_{tp})^{N-3}(1-T_{tp})}{1-(T_{tp})^{N-2}}$
N-1	$\frac{0.5T_{tp}}{1+T_{tp}}$	$\frac{0.5(T_{tp})^{N-2}(1-T_{tp})}{1-(T_{tp})^{N-1}}$
N	0.5	0

$$2C_{N-j} = \frac{(T_{tp})^j}{1 + T_{tp} + T_{tp}^2 + \cdots + (T_{tp})^j} \qquad (229)$$

where $j \neq N$. In the context of this notation, $C_1 = 0$ because there is no transmission to the left of station 1. Another useful form of Eq (229) is

$$2C_k = \frac{(T_{tp})^{N-k}}{1 + T_{tp} + T_{tp}^2 + \cdots (T_{tp})^{N-k}} \qquad (230)$$

where $k \neq 1$; again $C_1 = 0$.

The recursion formula stated in Eqs (229) and (230) was developed for uniform response at all detectors when optical power is transmitted at station 1. This represents only one half the coupling factors on the data bus. However, the symmetry of the bus requires that the same set of coupling factors must apply for the other side of each of the couplers starting from station N back to station 1, and that uniform signals will result at all detectors when station N transmits.

For an N station data bus, with station 1 on the left and station N on the right, the two coupling factors for each station are shown in Table XVII. The equation for the sum of a finite geometric progression has been used to simplify the form of the Cs. Throughout this analysis it is assumed that the power from the LED is coupled onto the bus and distributed uniformly over all the fibers in the bundle by the scrambler. However, the LED ports are constructed exactly like the detector ports. Therefore, the power from each LED is split between the two directions of propagation as the ratio of the right and left coupling factors shown in Table XVII. It can be shown that the worst case unbalance in the LED power split occurs for stations 2 and N-1; for these stations the power coupled to stations 1 and N respectively

is about $(1 + T_{tp})$ times greater than the power coupled toward the center of the bus.

In order to keep the detector response about the same for all LEDs, it is also necessary to reduce the LED "on" current progressively toward the center of the data bus. The greatest value of the current reduction factor, F_{CR}, is at the center of the data bus and is approximately

$$F_{CR} = 2\left[1 - (T_{tp})^{\frac{N+1}{2}}\right]\left[T_{tp}\right]^{\frac{N-1}{2}}, \quad N \text{ - odd}$$

$$= \left[1 + T_{tp} - 2(T_{tp})^{\frac{N+2}{2}}\right]\left[T_{tp}\right]^{\frac{N-2}{2}}, \quad N \text{ - even} \tag{231}$$

The highest LED "on" current occurs in stations 1 and N; therefore, the detector resonse to transmissions from these two stations constitute the worst case for signal power ratio. Since all detectors response equally when these two stations transmit, the worst case photodetector fractional power may be evaluated from Eq (214).

$$R_{PT} = \frac{P_{o2}}{P_{i1}} = \frac{a_o m_L m_C T_C T_C}{2} \; \frac{(a_o m_T T_C T_C)^{N-2}\,(1 - a_o m_T T_C T_C)}{1 - (a_o m_T T_C T_C)^{N-1}} \tag{120}$$

Eq (120) is equivalent to Eq (115) for the uniform in-line data bus. The coupling factors for the 17 station tapered in-line data bus shown in Figure 87 were calculated for

$$a_o m_T T_C T_C = 0.84 \tag{232}$$

Using Eq (232) $m_C = 0.558$ and $m_T = .9$ the current reduction factor -Eq (231)- is $F_{CR} = 0.4$ for the center (9th) station, and the worst case fraction detector power ratio from Eq (120) is

$$\text{TD} \qquad R_{PT} = 5.82 \times 10^{-3} \qquad (-22.35\text{dB}) \qquad (233)$$

Equation (232) is a very optimistic value using $a_o = 0.748$ for Rank fiber from Table II and $m_T T_C T_C = 0.452$ from Table I gives

$$a_o m_T T_C T_C = 0.338 \qquad (-4.71\text{dB}) \qquad (234)$$

which gives from Eq (231) for the center station of an 8 station bus.

$$F_{CR} = 0.08 \qquad (235)$$

and from Eq (120) with $m_C = 0.558$ and $m_T = 0.884$ for an 8 station bus

$$\text{TD} \qquad R_{PT} = 6.16 \times 10^{-5} \qquad (-42.11\text{dB}) \qquad (236)$$

The worst case dynamic range for the tapered bus is the same as the worst case unbalance in the power split. Therefore, the value of D_{PT} is

$$D_{PT} = \frac{P_{O_1}}{P_{O_3}} = 1 + a_o m_T T_C T_C \qquad (237)$$

Using Eq (234) gives

$$D_{PT} = 1.338 \tag{238}$$

APPENDIX IV

FIXTURE DATA SHEETS

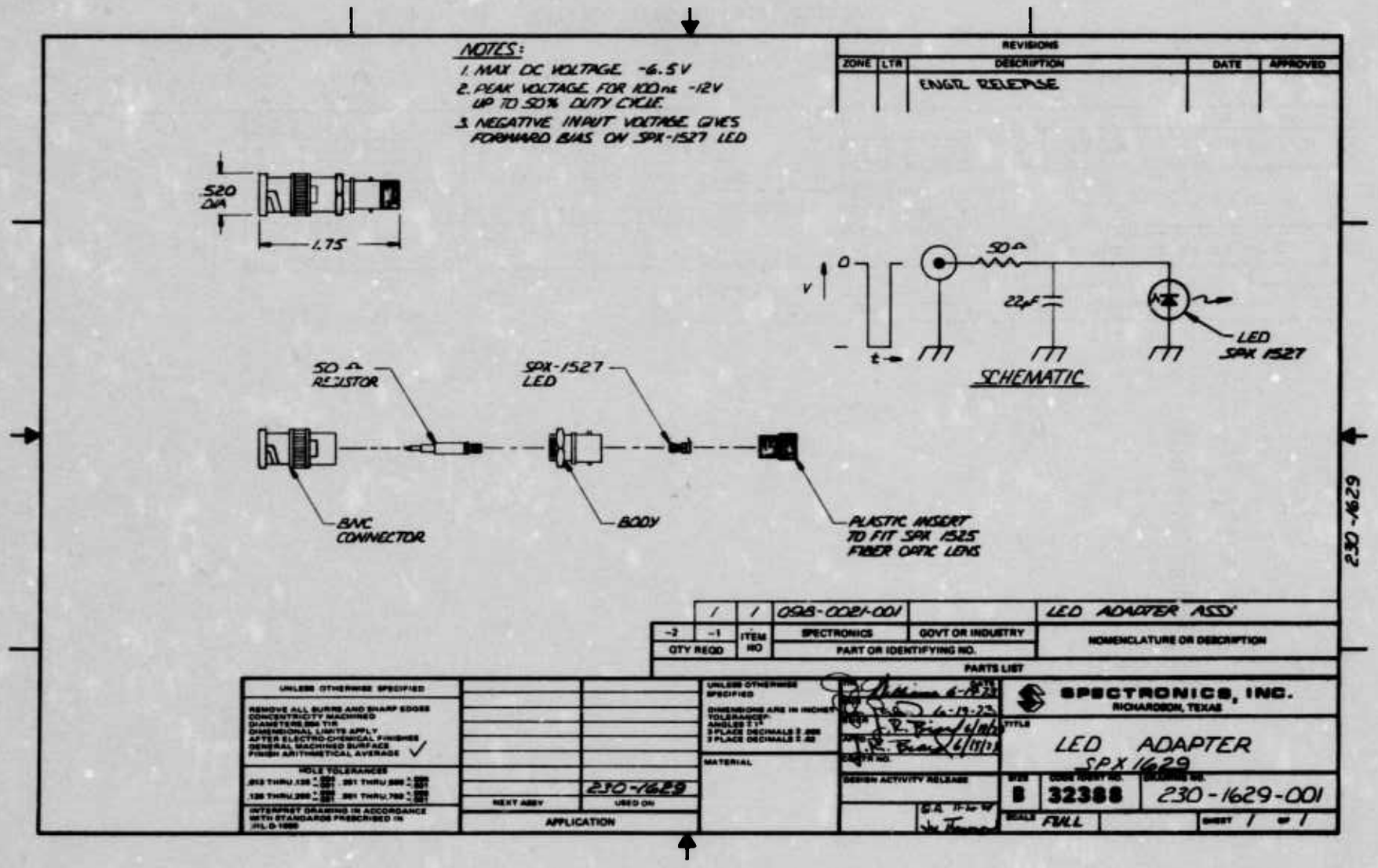

Figure 88. SPX 1629 LED Adapter

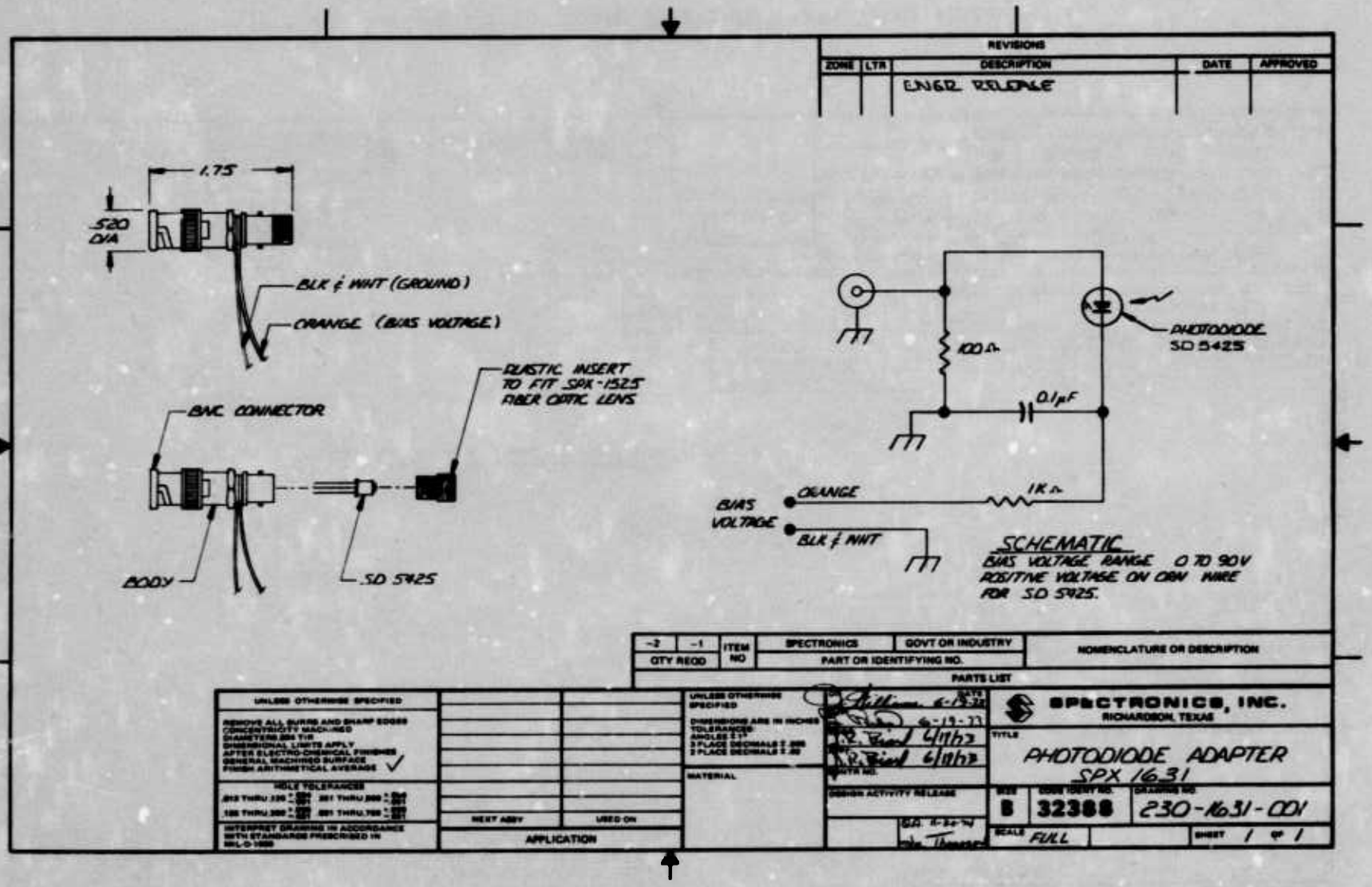

Figure 89. SPX 1631 Photodiode Adapter

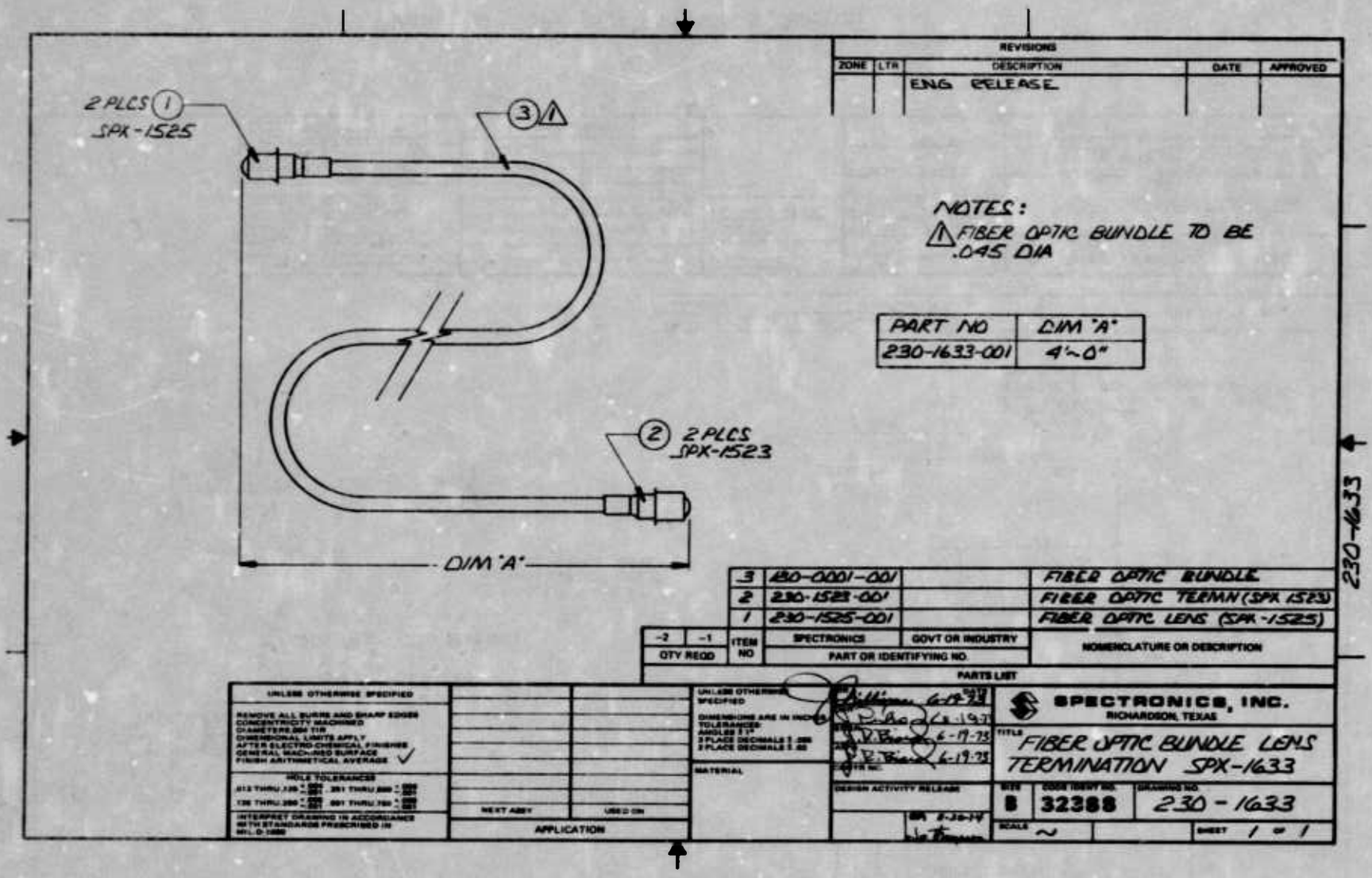

Figure 90. SPX 1633 Fiber Optic Bundle With Lens Termination

APPENDIX V

AN INTRODUCTION TO RADIATION EFFECTS

ON ACTIVE AND PASSIVE OPTICAL COMPONENTS

TABLE OF CONTENTS

TABLE OF CONTENTS (continued)

LIST OF SYMBOLS

SYMBOL	DEFINITION	UNIT
A_j	Junction area	cm^2
c	Damage constant	rad^{-1}
C	Junction capacitance	F
D	Dose in rad (Si)	rad
D_n	Diffusivity of electrons	cm^2/s
E	Electric field in PIN diode	V/cm
E	Energy, general	ergs
E_i	Incident electron energy	eV
E_f	Final energy of electron	eV
E_{PE}	Kinetic energy of photoelectron	eV
EMI	Electromagnetic interference	V/m
ESR	Electron spin resonance	--
g	Electron-hole pair generation rate	$cm^{-3}s^{-1}$
I_d	Drift current component	A
I_{gen}	Generation current in depletion-layer region	A
$I_g(\Phi)$	Generation current as a function of neutron fluence	A
K	Neutron damage constant	cm^2/s
K_N	Damage constant	cm^2/s
K_γ	Gamma-ray damage constant	rad^{-1}
L_n	Electron diffusion length	cm^{-1}
n_i	Intrinsic carrier concentration	cm^{-3}

LIST OF SYMBOLS (continued)

SYMBOL	DEFINITION	UNIT
N_D	Concentration of donor impurities	cm^{-3}
Δp	Excess carrier (hole) concentration	cm^{-3}
p_n	Concentration of holes in an n-type semiconductor	cm^{-3}
p_{no}	Concentration of holes in an n-type semiconductor in equilibrium	cm^{-3}
q	Magnitude of electronic charge	C
R	Radiation intensity, dose rate	rad/s
T	Transmission (transmissivity)	--
t_p	Radiation pulse duration	s
V	Applied voltage	V
W	Depletion layer width	cm
W_t	Junction thickness	cm

LIST OF GREEK SYMBOLS

α	Decay constant	--
ε_o	Permittivity of free space = $8.86X10^{-14}$	F/cm
ε_{Si}	Dielectric constant of silicon = 12	--
η	External quantum efficiency	--
η_o	Pre-irradiation external quantum efficiency	--
κ	Electron-hole pair generation rate in silicon, $4.3 \cdot 10^{13}$ pairs/cm^3-rad (Si)	$cm^{-3}rad^{-1}$
μ	Carrier mobility	$cm^2/V\text{-}s$

LIST OF SYMBOLS (continued)

SYMBOL	DEFINITION	PAGE
μ	Linear absorption coefficient	cm^{-1}
ρ	Electrical resistivity	ohm-cm
σ	Cross section, general	cm^2
σ_t	Total cross section	cm^2
τ	Minority carrier lifetime	s
τ_o	Initial lifetime	s
τ_N	Non-radiative lifetime	s
τ_{No}	Pre-irradiation non-radiative lifetime	s
τ_R	Radiative lifetime	s
Φ	Neutron fluence	cm^{-2}

SECTION I
INTRODUCTION

Fiber-optic data transmission systems are presently being considered for use in military communication systems. These systems offer a number of inherent advantages in comparison to twisted pair or coaxial cables. Advantages include: improved RFI-EMI characteristics, elimination of cross talk, large bandwidth, light weight, electrical isolation between circuits and general insensitivity to EMP.

In military applications, fiber-optic communication systems will be required to operate during and after exposure to nuclear radiation. The performance of the various components of a fiber-optic system is, however, degraded on exposure to nuclear radiation. In fact, the study of radiation effects on glasses (one component of the optical data transmission system) has been the subject of extensive investigations during the past 30 years. Radiation damage effects in silicon and gallium arsenide have also been the subject of lengthy investigation. As a result, a vast amount of information is available to form a basis for understanding and predicting radiation effects on optical system components. Although this information exists, the continued evolvement of new fiber materials and device designs of light emitter and detector semiconductor structures continues to generate new developments in system radiation hardening. As a result, this field of endeavor is at a new height of intensity and sophistication with rapid advances being made during the past few years.

This investigation comprises an effort to provide both a foundation for understanding radiation effects in fiber optic system components as well as a summary of present state-of-the-art system design consideration for radiation hardness. The study begins with general

background information and terminology of the interaction of radiation and nuclear particles with matter. The presentation then turns to radiation effects in semiconductor devices and fiber optic bundles. The final sections deal with radiation damage in LEDs, PIN photodiodes, fiber optic bundles, digital integrated circuits and linear integrated circuits. A limited system analysis is then performed based on the data (both transient and permanent) which has been gathered for components and fibers. Recommendations are made for profitable areas of continued study.

SECTION II

INTERACTION OF RADIATION AND NUCLEAR PARTICLES WITH MATTER

A. DEFINITIONS

Following is a list of definitions which will prove useful in the study of radiation and nuclear-particle damage on solid-state optical components.[17,18]

A -- the symbol for mass number, the sum of the neutrons and protons in a nucleus. It is the nearest whole number to an atom's atomic weight. For example, the mass number of cobalt-60 (^{60}Co) is 60.

Absorbed dose -- When ionizing radiation passes through matter, some of its energy is imparted to the matter. The amount of energy absorbed per unit mass of irradiated material is called the absorbed dose, and is measured in rads.

Absorber -- any material that absorbs or diminishes the intensity of ionizing radiation. Thermal-neutron absorbers such as boron and cadmium are used in control rods for reactors. Concrete and steel absorb gamma rays and neutrons in reactor shields. A thin sheet of paper will absorb or attenuate alpha particles and low-energy beta particles.

Absorption -- the process by which the number of particles or photons entering a body of material is reduced by interaction of the particle or radiation with the material.

Activation -- the process of making a material radioactive by bombardment with neutrons, protons, other nuclear particles, or high-energy photons.

Alpha particle (α) -- a positively charged particle made up of two neutrons and two protons bound together and therefore identical to the nucleus of a helium atom. It is the least penetrating of the three common types of radiation (alpha, beta, gamma) emitted by radioactive material.

Angstrom ($\mathring{A}$) -- 10^{-8} centimeters

Annihilation radiation -- the radiation produced when a positron recombines with an electron. The commonest process of destruction is one in which a positron unites with a free or loosely bound electron and both disappear, their entire energy passing away in the form of 2 photons each having energy of 0.51 MeV. The two photons are emitted at 180° with respect to one another.

Atomic weight -- the mass of an atom relative to other atoms. The present-day basis of the scale of atomic weights is carbon with an arbitrarily assigned weight of 12.

Barn -- $10^{-24}cm^2$ is the unit of cross section (σ) and is the measure of the probability that a nuclear interaction will occur. For example, to describe the interaction of fast neutrons with a semiconductor material, the number of interactions per cubic centimeter per second is equal to $N\sigma\phi$ where N = number of target atoms/cm^3 and ϕ = incident neutron flux (number of neutrons crossing a cm^2 of target area per second).

Beta particle -- an elementary particle emitted from a nucleus during radioactive decay. A negatively charged beta particle (β^-) is identical to an electron. A positively charged beta particle (β^+) is called a positron.

Bremsstrahlung -- electromagnetic radiation produced by the sudden deceleration of a moving electron is described by the German term bremsstrahlung (braking radiation). This form of radia-

tion has its origin when a moving electron approaches very close to the positively charged nucleus and suffers a drastic energy loss. The loss in energy will appear as a photon with energy $E = h\nu$.

Cadmium ratio -- is used to describe the energy distribution of a flux of neutrons. It is approximately equal to the ratio of flux component below the cadmium cutoff to the flux component above the cadmium cutoff. The cadmium cutoff occurs at 0.4 ev. At energies above the cadmium cutoff, the neutron capture cross section drops off rapidly; below this energy, the capture cross section is high. The cadmium ratio is often used to define the relative hardness of a neutron flux or beam.

Cerenkov radiation -- light emitted when charged particles pass through a transparent material (e.g., fiber optics) at a velocity greater than that of light in the material. The number of quanta emitted per wavelength interval is proportional to $1/\lambda^3$. The Cerenkov light is found predominantly at the blue end of the visible spectrum.

Cobalt 60 source -- an intense gamma-ray source used in radiotherapy and for the study of radiation damage in solids. Each disintegration of ^{60}Co involves the emission of 1 beta particle and 2 gamma rays given by the following decay scheme. In most cobalt 60 sources the beta particle is purposely absorbed and only gamma radiation is emitted.

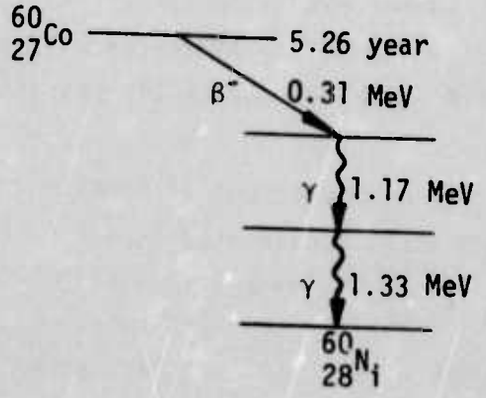

Compton electron -- the electron which is ejected by an incident photon from an unbound state in the atom. This is essentially a "two-body" elastic collision between the incident photon and free electron. The incident photon scatters at a given angle and reduced energy while the Compton electron is propelled at a given energy and angle. The Compton effect is one of the three ways photons lose energy upon interaction with matter.

Cross Section -- the probability of occurrence per nuclide, per unit time, per unit flux of a particular collision process, such as the elastic scattering of a particle through a certain angle or the absorption of a particle by a given nuclear process, etc.

Curie -- the quantity of any radioisotope which has a disintegration rate of $3.7 \cdot 10^{10}$/s.

Dose -- a measure of the radiation field to which a material is subjected. It should be expressed in terms of the interaction of the field with a reference material, e.g., silicon. Dose is expressed in rads or Roentgen (R,r).

Dose rate -- the radiation dose delivered per unit time and measured for example in terms of rads per second (rad/s).

Electromagnetic radiation -- radio waves, heat waves, light waves, gamma-rays, photons are all examples of electromagnetic radiation. They all travel with a velocity $c = 3 \cdot 10^{10}$ cm/s in a vacuum. Energy given by $E = h\nu$ where h = Planck's constant = $6.63 \cdot 10^{-27}$ erg-s, and ν = frequency of the radiation.

Electron volt (eV) -- the amount of kinetic energy gained by an electron when it is accelerated through a potential difference of 1 volt. It is equivalent to $1.6 \cdot 10^{-12}$ erg. It is a unit of energy.

Fission -- the splitting of atoms of uranium, plutonium, etc. into two atoms (fission fragments) with release of neutrons and an enormous amount of energy. (Mass of the two fission fragments is less than the fissioning atom).

Fluence -- the time-integrated flux rate, e.g., the total number of incident neutrons that cross a square centimeter of target area during the exposure time; the units are cm^{-2}.

Flux (neutron) -- a measure of the intensity of neutron radiation. It is the number of neutrons passing through 1 square cm of a given target in 1 second; the units are $cm^{-2}s^{-1}$.

Fusion -- the release of energy obtained by forming one heavier atom (e.g., $^{3}_{2}He$) plus a neutron from two lighter atoms (e.g. $^{2}_{1}H$). Mass of the heavy atom and the neutron is less than the sum of the two lighter atoms.

Gamma (γ) ray -- a high-energy, (defined herein to be $\geq$ 0.1 MeV) short-wavelength electromagnetic radiation. Gamma rays have their origin within the nucleus of an atom.

Ionization -- the process of removing one or more electrons from atoms or molecules thereby creating ions. Nuclear radiation can cause ionization.

Isotope -- atoms composed of nuclei with the same number of protons (Z) but different number of neutrons and hence different mass numbers (A) are called isotopes.

keV -- one thousand electron volts ($1.6 \cdot 10^{-9}$ ergs).

Linear absorption coefficient (μ) -- a characteristic coefficient that expresses the efficiency with which material absorbs ionizing radiation. It appears for example in the equation $I = I_0 e^{-\mu x}$

where I is the dose per unit area remaining after penetrating x cm of material thickness and I_0 is the incident dose rate per unit area.

Luminescence -- emission of light produced by the action of electrical, chemical, incident radiation, or any other cause except high temperature (which produces incandescence).

MeV -- one million electron volts ($1.6 \cdot 10^{-6}$ ergs).

Neutron -- an uncharged particle having a mass slightly larger than the proton. The neutron and the proton are the fundamental building blocks of all nuclei.

Thermal neutrons are in thermal equilibrium with their environment, generally considered to be those whose energy is less than approximately 0.1 keV. At room temperature the most probable energy of thermal neutrons would be 0.025 eV.

Epithermal neutrons have energies greater than thermal neutrons.

Epicadmium neutrons have energies above the cadmium absorption cutoff (approximately 0.4 eV).

Slow neutrons have energies in the range 0 - 1000 eV.

Intermediate neutrons have energy in the range 10^3 to $5 \cdot 10^5$ eV.

Fast neutrons have energy greater than ~10 keV. Most damage to semiconductor components of interest is caused by fast neutrons.

Nucleon - proton or neutron (which are the fundamental building blocks of all nuclei).

Nuclide -- a general term applicable to all atomic forms of the elements. Nuclides comprise all the isotopic forms of all the elements.

Pair production -- when the energy of an incident photon is greater than 1.02 MeV, the photon can be absorbed in the material through the mechanism of pair production (production of an

electron and a positron). If the photon has excess of 1.02 MeV, the excess energy is shared between the positron and electron, thus:

$$h\nu = 1.02 \text{ MeV} + E_+ + E_- \qquad (239)$$

Pair production is one of the three ways photons lose energy upon interaction with matter.

Photoelectron and Photoelectric Effect -- the electron which is ejected from one of the electron shells of an atom when a photon of energy $h\nu$ collides with an atom. Energy (E) of the photoelectron is given by:

$$E = h\nu - \text{binding energy of electron} \qquad (240)$$

All of the energy of the incident photon is expended in the photoelectric process. The photoelectric effect is one of the three ways photons lose energy upon interaction with matter.

Photon (Gamma-ray or X-ray) -- a bundle of energy which travels in wavepacket form at the velocity of light, $c = 3 \cdot 10^{10}$ cm/s. Energy is described as $E = h\nu$ where h = Planck's constant $= 6.63 \cdot 10^{-27}$ erg-s and frequency $\nu = c/\lambda$ where λ = wavelength of the radiation. Photons are referred to almost interchangeably as quanta, gamma rays, X-ray, or light waves. A general relation between energy of the photon in electron volts (eV) and wavelength λ in nanometers is:

$$E(eV) = \frac{1,243}{\lambda(nm)} \qquad (241)$$

Positron -- a positively charged electron with charge + e = $1.6 \cdot 10^{-19}$ coulombs.

Proton -- an elementary particle with single positive charge, (the nucleus of a hydrogen atom). The proton and neutron are the fundamental building blocks of all nuclei.

Rad -- that quantity of nuclear or ionizing radiation that releases 100 ergs of energy in a gram of given material. The material must be specified when using the term. Because silicon is a common reference material, (Si) is often designated in terms of the "dose" expressed in rads.

Roentgen (R,r) -- a term specifying the amount of ionizing (gamma or X-) radiation that produces $2.083 \cdot 10^{9}$ ion pair/cm^3 in air at S.T.P. The rate of energy release is expressed in roentgens per unit time.

X-ray -- a penetrating form of electromagnetic radiation emitted when the inner oribtal electrons of an excited atom return to their normal state (characteristic X-rays) or by the bremsstrahlung process. X-rays are non-nuclear in origin.

Z -- The atomic number of an atom. Z is equal to the number of protons in the nucleus. The un-ionized atom has Z electrons surrounding the nucleus.

B. INTERACTION OF X-RAYS AND GAMMA-RAYS WITH MATTER

The basic series of events which transpire in the interaction of radiation (photons) with matter will now be considered. If a slab of material thickness Δx is placed in the path of a beam of X- or gamma radiation, a number of photons will be removed from the beam. The number ΔI will depend directly on the number of incident photons I and on the thickness Δx. Mathematically, ΔI is equal to the product of μ, I and Δx so that

$$\Delta I = -\mu I \Delta x \tag{242}$$

where μ, the constant of proportionality, is called the linear absorption coefficient and is expressed in units of cm^{-1}. The linear absorption coefficient μ depends in a complicated way upon the atomic number Z of the absorbing material and energy E of the radiation, but for given values of Z and E, μ has a definite value. The negative sign is necessary to Eq (242) because as Δx increases, the number of photons in the beam decreases.

Rearranging Eq (242) and integrating gives

$$\int_{I_0}^{I(x)} \frac{\Delta I}{I} = -\int_0^x \mu dx \tag{243}$$

$$\ell n\left(\frac{I(x)}{I_0}\right) = -\mu x$$

$$I(x) = I_0 e^{-\mu x} \tag{244}$$

where

I_0 = incident radiation intensity at $x=0$.

$I(x)$ = radiation intensity at position x in the material.

The absorption of X- or gamma rays is thus said to be exponential. Extensive tables for the linear absorption coefficient μ are to be found in the literature.[19]

Let us now define the methods by which photons are absorbed in matter and resulting motion imparted to electrons. The processes by which these interactions take place are:

- Photoelectric effect
- Compton process
- Pair production

1. Summary of the Photoelectric Effect

The photoelectric effect involves an interaction between a photon and a bound electron within the various electron shells of the atom. In the interaction, the photon disappears and all of its energy is imparted to the resulting photoelectron and the photoelectron binding energy within the atom. The kinetic energy E_{PE} of the photoelectron is therefore:

$$E_{PE} = h\nu - \text{binding energy of the electron} \qquad (245)$$

The photoelectric cross section per atom and hence the accompanying linear absorption coefficient varies as $\left(\frac{1}{h\nu}\right)^3$ (i.e., inverse E^3 dependence). The absorption coefficient per atom of material varies with atomic number as $\sim Z^4$. From the Z dependence, note that photoelectric absorption will be about 25 times more effective per atom in GaAs than in Si. For semiconductors, the effect plays a dominant role in the energy range 1 keV to 100 keV.

2. Summary of the Compton Process

The Compton process involves an interaction between a photon and a free or "unbound" electron within the material. In each photon collision with the electron some energy is scattered and some absorbed; the amount depending on the angle of collision and the

energy of the photon ("billiard ball" type collision). The photon does not disappear in the Compton process. On the average, the fraction of energy transferred to kinetic energy of the electron per collision process increases with increase in photon energy. Since the Compton process is one involving free electrons, all materials absorb essentially the same amount of radiation per electron. On an atomic basis each electron in the atom scatters independently and the Compton absorption coefficient per atom is proportional to the atomic number Z. The cross section for Compton interaction varies as 1/E where E is the energy of the incident photon. For the interaction of photons with semiconductors in the energy range -- 200 keV to 10 MeV, Compton absorption is much more important than either the photoelectric or pair-production process.

3. Summary of Pair Production

Pair production involves the interaction between a photon and a nuclear charge. When a photon passes near the nucleus of an atom and is subject to the strong electric field of the nucleus, it may disappear as a photon and become a positive and negative electron pair. The threshold is 1.02 MeV (the sum of the rest mass of the electron and positron expressed in units of energy, MeV). The absorption of the photon per atom involved in pair production increases approximately as Z^2. The energy dependence for photon absorption varies as $\sim E$, where E is the incident photon energy. Pair production becomes the most important type of absorption for photon energies above ~10 MeV.

C. INTERACTION OF ELECTRONS WITH MATTER

When an electron penetrates the surface layer of a given material it suffers many collisions before it loses all of its energy. Two fundamentally different energy loss mechanisms occur. They are referred to as collision losses and radiation losses. Both processes are complicated if studied in detail, but can be understood in part without the introduction of advanced quantum mechanics.

Collision losses are of two types:

1) Collision of the incident electron with atomic electrons of the material results in excitation or ionization of the atom which in turn results in generation of quanta (X-rays, light waves, heat, etc.). The electrons ejected from the atom often have enough energy to produce excitation and ionization of other atoms. The collision cross section for this process varies as $\sim Z^2$. The average energy of the electron expended in generating an ion pair in air by this mechanism is about 33 eV. Approximately 3 to 4 eV is expended by an electron per hole-electron pair generated in semiconductor materials.

2) Direct collision of the incident electron with atoms results in atomic displacement. This type of collision produces defects in the lattice structure of semiconductors and crystalline insulators. From application of classical concepts of conservation of energy and momentum, it can be shown that the onset energy threshold of the incident electron for this process in silicon is $\sim$250 keV.

Radiation loss occurs when an electron approaches very close to the nucleus of an atom. In this case the electron is made to partially orbit around the nucleus by the strong attraction between the positive nucleus and the incident negative electron. The electron will recede from the atom with reduced energy. The loss in energy will appear as a photon with energy $h\nu$ and the primary electron will recede with final energy E_f given by:

$$E_f = E_i - h\nu \tag{246}$$

where E_i = incident energy of the electron. The resulting radiation of energy $h\nu$ is called bremsstrahlung radiation. It arises from the decleration of the electron. At low energies this interaction is very unlikely but at high energies it becomes more probable than energy loss by collision interactions. The cross section per atom

for electron energy loss to bremsstrahlung radiation varies as Z^2 and is proportional to E.

The rate of electron energy loss to collisions decreases with increase in energy; whereas, the rate of electron energy loss increases with energy for radiation effects (generation of bremsstrahlung). Production of bremsstrahlung dominates that of collision loss at energies greater than 10 MeV.

In general, electrons of a given energy have far less penetrating power (range) in material than do quanta or neutrons of the same energy. Ranges of electrons in materials are finite and are defined in the literature in terms of incident electron energy versus range in g/cm^2 for the given material. Ranges of neutrons and quanta exhibit an exponential dependent characteristic absorption.

D. INTERACTION OF FAST NEUTRONS WITH MATTER

The uncharged nature of the neutron makes it behave very differently in its transit through matter than does that of radiation or charged particles. Charged particles and photons can exert electric forces capable of ionizing atoms through which they pass and are also capable of interacting with positively charged nuclei. The neutron, however, can experience a force only when it comes within extremely close range of a nucleus. The ratio of the neutron beam intensity after traversal of a sample of thickness x with n number of atoms/cm^3 and total cross section σ_t to the incident intensity is defined as the transmission T and is given by:

$$T = e^{-n\sigma_t x} \tag{247}$$

The interaction of the neutron with a nucleus may be regarded as a collision, which may be either elastic or inelastic. We will limit our discussion of the subject to elastic collisions of fast neutrons

since they are the types of collisions which induce radiation damage in semiconductors and fiber optics.

Fast neutrons ($E > 10\,keV$) experience elastic collisions with nuclei of matter. In an elastic collision, the classical conservation of energy and momentum laws apply, and a portion of the energy of the striking neutron is transferred to the struck nucleus. The cross section for elastic collissions for fast neutrons increases with increasing mass number A roughly in the same manner as the geometrical cross section of a sphere whose volume increases proportionally to the number of particles contained therein. Elastic scattering cross sections for fast neutrons are in the ~1 to 10 barn range.

In semiconductors and glasses the greatest cross section for fast neutrons is elastic scattering resulting in displaced atoms and primary knock-on atoms which are capable of causing ionization. The displaced atoms cause defects in the lattice of semiconductors and crystalline insulators and lead to permanent damage effects in these materials.

E. EMP DEFINITION

A significant portion of the energy released during a nuclear detonation appears as an electro-magnetic pulse having the same frequencies as commercial radio and military systems equipment. The effect is of importance to the designer concerned with radiation effects on electronic systems.[20,21,22] Two mechanisms are believed to generate the EMP from a nuclear detonation. They are:

- Compton-electron production, and
- Generation of hydromagnetic waves.

The first mechanism, that of Compton electron production, is created as the initial symmetrical distribution of gamma radiation from the nuclear explosion collides with electrons, atoms and molecules of the surrounding air. The resulting Compton electrons move

rapidly away from the center of the blast and generate an electromagnetic wave. The electromagnetic signals are emitted in the first few milliseconds after the burst and have a very broad-banded radio-frequency spectrum. From the system designer's standpoint, the signals can be handled as a severe case of radio noise and ordinary precautions taken against this type of noise.

The second effect, generation of hydromagnetic waves, is created by the "field-displacement" effect. A property possessed by all plasmas is the tendency to exclude a magnetic field such as that of the earth from its interior. The expanding plasma of weapon residues thus causes a distortion of the earth's magnetic field. As a result of the interaction between the geomagnetic field and the charged particles in the expanding plasma and in the very tenuous, ionized surrounding gases, the disturbance propagates away from the burst region as a hydromagnetic wave. This is a slowly moving magnetic field of great penetration power, and the system engineer must utilize high-permeability shielding to reduce its magnitude to acceptable values at the system level. Cabling must be protected and standard techniques for reduction of induced voltages must be utilized. The "field-displacement" mechanism is believed to be especially important at very high altitudes where the air density is low and the expansion of the plasma is not impeded by the atmosphere.

A typical high level EMP has an intensity of $\sim 10^6$ volts per meter. This is $\sim 10^7$ times as intense as fields created by EMI sources in a typical metropolitan area. Fortunately, immunity to many of the effects of EMP is realized by utilizing an electronic system coupled with fiber optics. The fibers are effective insulators which eliminate the possibility of such fundamental EMP source detection mechanisms as "ground loops", etc.

SECTION III

RADIATION DAMAGE IN SEMICONDUCTORS

A. INTRODUCTION

The radiation damage effects to be discussed in this section are permanent* and remain after all transient ionization has decayed[23,24,25]. The permanent damage which predominantly affects the electrical properties of semiconductor materials is the creation of vacancies and interstitials in the crystalline structure. These defects are created when an atom is displaced from its lattice site and leaves a vacancy. The atom comes to rest in a position outside the lattice and is referred to as an interstitial. The vacancy-interstitial pair is defined as a Frenkel defect.

Atoms are displaced from their lattice sites by incident fast neutrons, energetic electrons, or by knock-on interstitials (secondaries traveling through the crystal). Approximately 15 eV of energy must be imparted to an atom to remove it from its lattice site. From conservation of energy and momentum theorems, this implies that a threshold energy of ~200 eV is required for incident neutrons and ~250 keV for incident electrons. Because the momentum of a photon is so small, Frenkel defects arise during high-energy photon bombardment by means of the secondary processes of photo-electron, Compton-electron, or pair-production interaction with the

---

*Transient radiation effects resulting from pulse exposure of the semiconductor to ionizing radiations such as X- and gamma rays are also important. The excess charge carriers (electron-hole pairs) created by incident ionizing radiation are capable of producing excess currents and voltages in a semiconductor device. These transient effects disappear as the electron-hole pairs recombine or are swept out of the device by imposed electric fields. Transient radiation effects in semiconductor devices will be separately considered in each of the sections pertaining to the components comprising the fiber-optic data transmission system.

atoms of the crystal. The resulting Frenkel defects occur in localized clusters around the primary knock-on point. Other events such as thermal spikes and transmutation of the semiconductor atoms generate second-order effects on the electrical characteristics of semiconductors and will be neglected in this discussion.

Frenkel defects give rise to energy levels in the forbidden gap, thereby changing the electrical characteristics of the semiconductor crystal. The defect generation rate and position of the energy levels have been shown to be dependent upon certain pre-irradiation properties of the crystal such as oxygen content and defect density.[26] The damage levels in all cases lie close to the center of the forbidden gap and are located well below the Fermi level in n-doped semiconductors and well above the Fermi level in the p-doped crystals. These crystal defects and their corresponding energy levels induce the following permanent (if annealing effects are neglected) changes in the electrical properties of semiconductor materials:

- Decrease the minority-carrier lifetime,
- Reduce the effective doping level (increase resistivity) by means of majority carrier removal, and
- Degrade carrier mobility.

B. MINORITY-CARRIER LIFETIME

Frenkel defects act as recombination centers (traps) which decrease the lifetime of minority carriers[27]. The minority-carrier lifetime is inversely proportional to the trap density and the increase in trap density is proportional to the neutron fluence. The relationship can be expressed as

$$\frac{1}{\tau} = \frac{1}{\tau_0} + K\Phi \qquad (248)$$

where τ_o = pre-irradiation minority carrier lifetime

K = neutron damage constant

Φ = neutron fluence

Eq (248) can also be written as

$$\tau = \frac{\tau_o}{1 + \tau_o K \Phi} \tag{249}$$

which shows the decrease in lifetime as the neutron dosage increases. K depends on such factors as type and energy of the bombarding particle, nature of the semiconductor (whether silicon or gallium arsenide), and upon impurities in the lattice such as oxygen. An order of magnitude value for the damage constant K for silicon is 10^{-7} s^{-1} $(neutrons/cm^2)^{-1}$.

C. MAJORITY-CARRIER REMOVAL

Although reduction of minority-carrier lifetime is the most commonly encountered origin of permanent radiation damage in semiconductors, induced changes in conductivity can also result. Since the Fermi level lies between the energy levels induced by Frenkel defects and the energy band which contains the majority carriers (the conduction band in n-doped and the valence band in p-doped crystals) there is a trapping effect on the majority carriers. For example, in n-doped crystals, the trap levels are below the Fermi level and, therefore, have a high probability of being occupied by electrons. The electrons which fill these traps come from the doping impurities which would normally have supplied electrons to the conduction band. The trapping of these electrons decreases the effective majority-carrier doping concentration (carriers are removed) and results in an increase in the crystal's resistivity.

Carrier removal by trapping of majority carriers becomes important if the number trapped is appreciable in relation to the total impurity concentration. The extent of the effect can be defined in terms of increase in resistivity ρ through the concept of carrier removal rate $\frac{\Delta N_D}{\Delta \Phi}$. Thus:

$$\rho = qu \left[N_D - \left(\frac{\Delta N_D}{\Delta \Phi} \right) \Phi \right]^{-1} \qquad (250)$$

where q = electron charge

μ = mobility

N_D = doping level

The semiconductor crystal tends toward intrinsisity as the radiation dosage increases. The carrier removal rate $\frac{\Delta N_D}{\Delta \Phi}$, however, varies with the number of carriers left to trap; otherwise, the resistivity in Eq (250) would increase to infinity and then become negative. In reality, the removal rate approaches zero as the number of free carriers approaches the intrinsic concentration. For silicon starting resistivity in the 1-10 ohm-cm range the initial carrier removal rate is about 4 per incident fast neutron per cm^2 for reactor source neutrons of average energy $\sim$1 MeV [28].

D. MOBILITY DEGRADATION

Carrier mobility is less sensitive to radiation damage than is minority-carrier lifetime or conductivity. The finite mobility in a crystal at low temperature arises from electron scattering by fixed charged scattering centers. The interaction of electrons with lattice vibrations limits mobility at high temperatures so that radiation has little effect in this latter case. The onset of fast neutron fluence levels which begins to degrade mobility is in the region of $\sim 10^{17}/cm^2$

whereas minority carrier lifetime degradation and majority carrier concentration change begin to take place at neutron fluences of $\sim 10^{12}/cm^2$.

SECTION IV

RADIATION DAMAGE IN SILICA FIBERS

Theory and experiment of the defect solid state form the basis for understanding and categorizing radiation effects in silica and other vitreous fibers. The state-of-the-art is not, however, as nearly advanced for the field of radiation effects on these materials as it is for semiconductors. To establish a basis for analysis of radiation effects on the simplest of the vitreous fibers, silica, we must first focus attention on radiation effects in somewhat similar structures which are considerably more elementary and which have received a great amount of attention during the past 30 years. These structures are the alkali halides (also referred to as ionic crystals)[29,30].

Ionic crystals are generally transparent insulators, many having elementary structure such as found in NaCl and CsCl. Understanding of the radiation sensitivity of the alkali halides has been advanced through study of color centers within these materials. Perhaps the most often referred to defect which gives rise to color centers in ionic crystals is the so called F center. The F center in NaCl, for example, is a negative ion vacancy Cl^- with an electron occupying the vacancy site and the Cl^- positioned interstitially within the crystalline lattice. The electron and its quantum mechanical system at the vacancy site give rise to a characteristic absorption band which, in turn, imparts color to the crystal -- hence the term color center.

The fact that the single crystalline alkali halides are essentially completely ionic in their atomic bonding plays a centeral role in interpreting structure-sensitive radiation effects in these crystals. It is reasonable, therefore, to ask with what rigor

can we apply ionic crystal defect concepts to amorphous materials such as silica? Rationale for applying these principles, in somewhat over-extended generality, can be developed by considering the materials in the following sequential order:

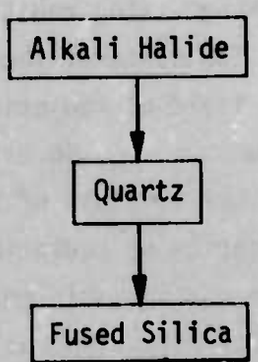

From X-ray studies[31] it has been shown that:

- The alkali halides exhibit ionic bonding.
- Single crystalline quartz bonding is about "halfway" in content between purely ionic and purely covalent bonding.
- The "local" arrangement of the atoms of amorphous silica is very similar to that of quartz, e.g.:
  - The average Si-O distance in silica is 1.62Å in close agreement with 1.60Å in quartz.
  - The average number of oxygens around each silicon atom in silica is four in close analogy to quartz.

Thus, the amorphous silica may be pictured as a random distribution of SiO_4 groups interlocked via oxygens which belong to two adjacent tetrahedra. Radiation properties which depend on localized environment should be very similar in the crystalline and in the amorphous forms while those which depend on long-range correlations are expected to differ greatly.

A linkage, tenuous as it may be, does therefore exist between the material properties of amorphous silica and the alkali halides through single crystalline quartz[32]. The terminology, methods of experimental investigation (ESR, optical absorption, etc.), and theoretical concepts developed for the defect solid state of the alkali halides have not only been applied to silica but have been extended to other vitreous forms of glass. It should be expected, however, that in making the foregoing extensions that the amorphous glasses will exhibit far more complex physical defect characteristics than those of the single-crystalline alkali halides.

As to the nature of defects in silica, one must further rely on analogy to ionic crystals since no theoretical calculations have been made from which the probability of occurrence, stability, mobility, etc. of defects can be judged. The elementary defects are:

Impurities	Oxygen vacancies	Silicon vacancies
Dislocations	Oxygen interstitials	Silicon interstitials

Again from analogy with ionic crystal defects we might expect the following electron redistributions around the above 6 defects which would lead to light absorption in silica (light attenuation in silica fibers).

Si (interstitial) traps electrons	O (interstitial)traps holes
Si (vacancy) traps holes	O (vacancy) traps electrons

As for radiation effects, the following mechanisms are considered important for inducing damage in silica fibers:

- Atomic displacement produced by elastic collisions with fast neutrons or high-energy electrons. In SiO_2, the simplest result of such interactions is the creation of vacancies and interstitials of both silicon and oxygen.

- Thermal or displacement spikes. The thermal agitation set up in the wake of fast particles may rapidly heat a small volume of the material to a very high temperature followed by rapid quenching. This can result in highly disordered regions in the solid.
- Production of color centers at existing defects by means of trapping of radiation released electrons. The electrons are released by incident gamma or electron ionizing irradiations.

The above considerations serve as a useful guide, but the system is of course more complex if the silica is non-stoichiometric, i.e., contains impurities [33], excess silicon, excess oxygen, etc. The situations where other vitreous fiber optic materials are employed such as the lead glasses, the soda lime glasses, etc., introduce further intricacies in the analysis of radiation effects and the defect solid state. Data concerning radiation effects on these and other fiber optic materials are presented in Section VI*.

Included in Section VI* are discussions of both permanent and transient induced absorption in the fiber resulting from radiation damage. Luminesence effects which occur in the fiber <u>during</u> radiation can confuse or obliterate communication information and are also considered.

*In this Appendix

SECTION V

RADIATION EFFECTS ON PIN DIODES

A. INTRODUCTION

A silicon PIN diode[34], Figure 91, is used in optoelectronic data transmission systems as the sensor for LED output signals which have been transmitted through multimode glass fibers. The PIN diode is operated under reverse bias in order to collect the

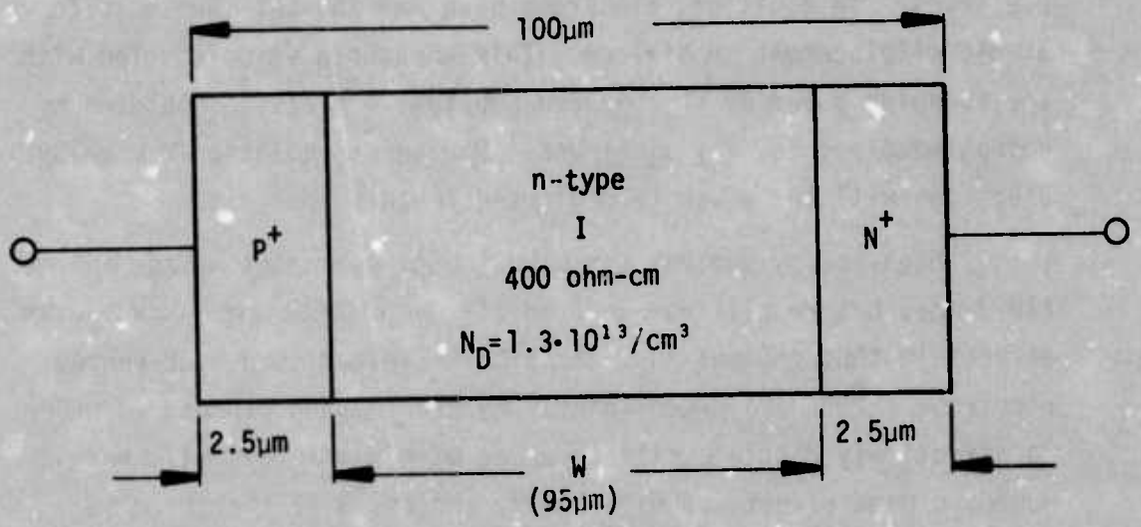

Figure 91. The SPX 1615 PIN Diode

ionization in the I layer created by the light output from the optically-coupled LED. Operation of the PIN diode considered herein is in the fully-depleted mode, i.e., the depletion layer reaches through (punches through) the I region from P^+ to N^+ interface. Operating voltage is, however, held below the avalanche breakdown condition. Since the PIN diode is operated under reverse bias in

these optoelectronic applications, the analysis will be directed only to the response of the reverse characteristics to permanent and transient radiation effects. For specificity, these results will be related to the SPX 1615 PIN diode photodetector.

The permanent effects (introduction of lattice defects) are induced by fast neutron fluxes. Permanent effects can also be generated by high-energy electrons, but since the PIN diode is encapsulated in a metal package (TO-46, for example) electron radiation is shielded in part from the silicon die and the accompanying radiation damage becomes package dominated. The 10mil metal wall thickness of the package will effectively stop ~0.6 MeV electrons. In addition, electrons have an ~250-keV threshold for atomic displacement in silicon. This threshold value coupled with the stopping power of the package provides effective shielding to approximately 1 MeV for electrons. Permanent radiation damage by electrons will therefore be neglected in this analysis.

High-energy photons can also induce permanent damage in the PIN diode, but recall from Section II* that these are second-order effects in that photons must first be converted into high-energy electrons (>250 keV) predominantly by the Compton process in order to effectively displace silicon atoms within the crystal. Permanent damage effects of high-energy photons will therefore be neglected.

Transient radiation effects[35] of high-energy photons will, however, be considered. Exposure to high-energy photons creates (through the photoelectric, Compton or pair-production process) excess electrons and holes in the I layer of the PIN diode. These excess carriers cause temporary changes in the behavior of the PIN diode which return to pre-irradiation conditions after the radiation is removed. During the radiation interval, however, current

*In this Appendix

flow in the reverse-biased PIN diode can be orders of magnitude greater than that of nominal leakage current. This radiation-generated current can interfere with the normal signal processing and interpretation of data flow through the optical fiber for detection at the PIN diode. These transient radiation effects in the PIN diode will therefore have a large impact on fiber-optic system performance.

B. PERMANENT DAMAGE

1. Introduction

The permanent effects of radiation damage on PIN diodes are summarized in Figure 92. PIN diode response to permanent radiation damage has been investigated in detail during the past 15 years [36-39]. The resulting response can now be predicted with a fair amount of accuracy. The major effect that will be considered in this category of radiation damage is that of permanent increase of leakage current resulting from radiation induced minority carrier lifetime degradation. Fortunately, minority carrier lifetime degradation does not alter the internal quantum efficiency since the PIN diodes under consideration operate in the fully depleted mode where internal quantum efficiency is independent of minority carrier life time.

2. Radiation Induced Leakage Current

Silicon PIN diode leakage current (dark current) at a fixed reverse bias voltage is identifiable as generation current in the space-charge (depletion-layer) region and is given by[40]:

$$I_{gen} = \frac{1}{2} q \frac{n_i}{\tau} WA_j \qquad (251)$$

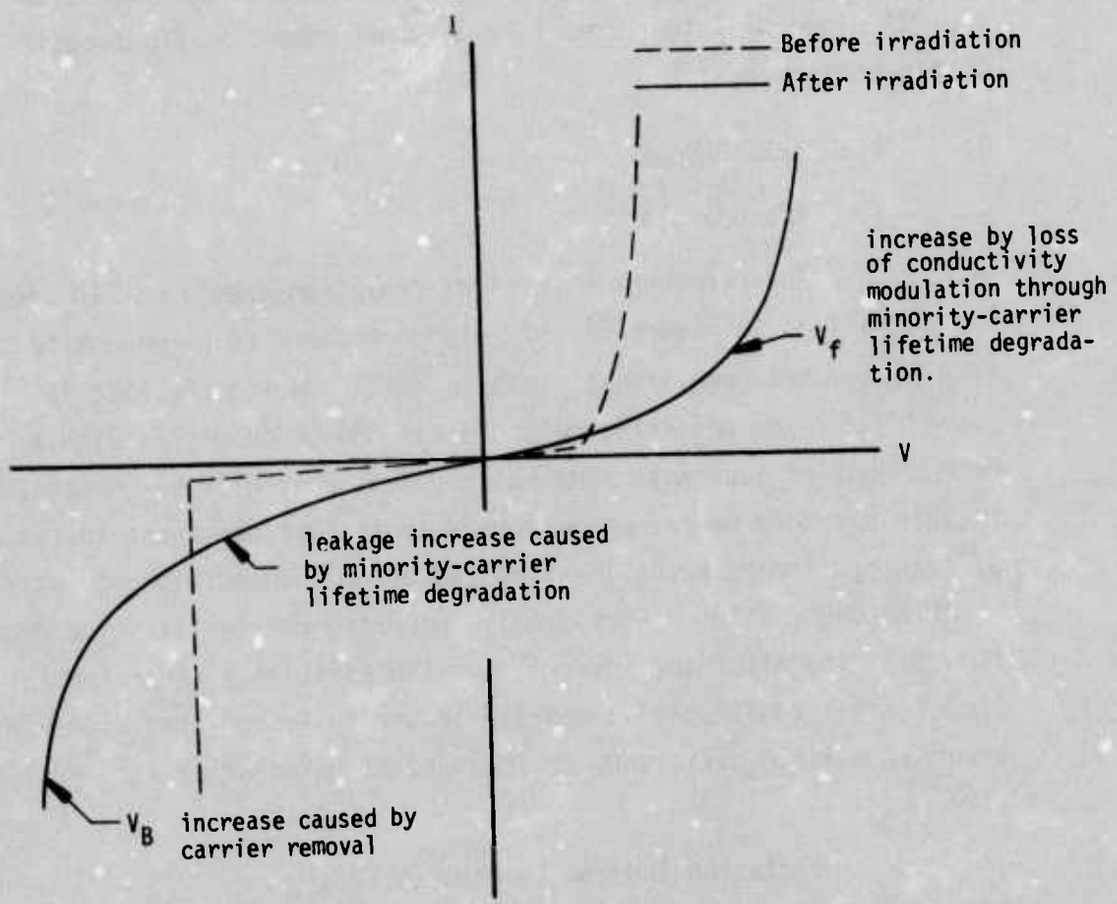

Figure 92. PIN Diode I-V Characteristic Response to Permanent Radiation Damage Effects

where:

q = $1.6 \cdot 10^{-19}$ C

n_i = intrinsic carrier concentration for silicon ($1.45 \cdot 10^{10}/cm^3$ at room temperature)

W = depletion layer width

A_j = junction area

τ = minority-carrier lifetime

From Section III* the minority-carrier lifetime is a function of neutron fluence and is given by:

$$\frac{1}{\tau} = \frac{1}{\tau_o} + K\Phi \tag{252}$$

where:

τ_o = initial lifetime

$K \sim 10^{-7}$ sec^{-1} (neutrons/cm^2)$^{-1}$

Φ = neutron fluence

Eq (252) can be written as:

$$\tau = \frac{\tau_o}{1+\tau_o K\Phi} \tag{253}$$

The dark current can then be expressed as a function of neutron fluence by combining Eq (251) and Eq (253) so that:

$$I_{gen}(\Phi) = \frac{1}{2} q \frac{n_i}{\tau_o} WA_j(1+\tau_o K\Phi) \tag{254}$$

*In this Appendix

A quality PIN diode will have the following pre-irradiation parameters

$$\tau_o = 50 \text{ s}$$

$$D_n = 30 \text{ cm}^2/\text{s}$$

$$L_n \sim 15\text{mils, where } L_n = \sqrt{D_n \tau_o}$$

For calculation purposes consider an SPX 1615 PIN diode as shown in Figure 91 operated in full depletion such that W = 95μm. Then for a junction area of 0.0126 cm^2 (50mil diameter) the pre-irradiation value of dark current can be calculated from Eq (254) as:

$$I_{gen} = 2.7\text{nA @ T} = 27°\text{C} \tag{255}$$

The dark current of the PIN diode provides a shot-noise signal input to the pre-amplifier to which the PIN diode is connected. As shown in this report (Figure 5, p. 22), the equivalent input noise current (bias current) is linearly proportional to the data-bit rate. When the PIN diode leakage current reaches a value equal to the input base bias current of the pre-amplifier, the input noise will be increased by 3dB. We will arbitrarily consider the noise increase of 3dB as an upper bound on the permissible radiation damage effects which can take place in the I-V characteristics of the PIN diode.*

---

* For a system designed to operate in a nuclear environment, allowance must be made for radiation degradation of the components comprising the system. In the case of the PIN diode, this degradation takes place in the form of increased dark current and associated shot noise. The allowance that must be made in this case is to apply more signal power to the detector than is required to achieve the desired signal-to-noise ratio prior to degradation of the photodiode. The amount of excess signal that is required must be determined individually for each specific application. In order to quantify this effect, a factor of 2 (3dB) excess signal is chosen herein for numerical demonstration of the magnitude of this effect.

It has further been shown[1] that for a 7.5Mbit/s system, the input bias current to the first stage of the detector pre-amplifier is 1μA. Also, the input current scales linearly with bit rate and has a value of 20μA at a data bit rate of 150Mbit/s. Using these concepts coupled with the 3dB constraint for radiation damage effects on the PIN diode, a nomograph (Figure 93) can be constructed which defines the radiation tolerance of the PIN diode as it is utilized in the optoelectronic data-transmission system. In preparing the nomograph, it is assumed that the PIN diode dark current is dominated by I_{gen} given by Eq (254). The approximation that I_{gen} doubles for every 10°C increase in temperature is also utilized in obtaining the results of Figure 93.

C. TRANSIENT RADIATION EFFECTS[41-43]

In PIN diodes where transient ionization effects are particularly important, the excess carriers created by ionization will be capable of producing excess currents and voltages until the generated carriers disappear through eventual electron-hole recombination or are swept out of the I region by the presence of the electric field. For steady-state irradiation where equilibrium is reached and where there is no current-density gradient, the excess minority carrier concentration Δp is given by

$$\Delta p = p_n - p_{no} = g\tau \tag{256}$$

where

p_n = concentration of holes in an n-type semiconductor

p_{no} = concentration of holes in an n-type semiconductor at equilibrium

g = generation rate of electron-hole pairs due to absorbed radiation (electron-hole pairs/cm^3-sec)

τ = minority carrier lifetime

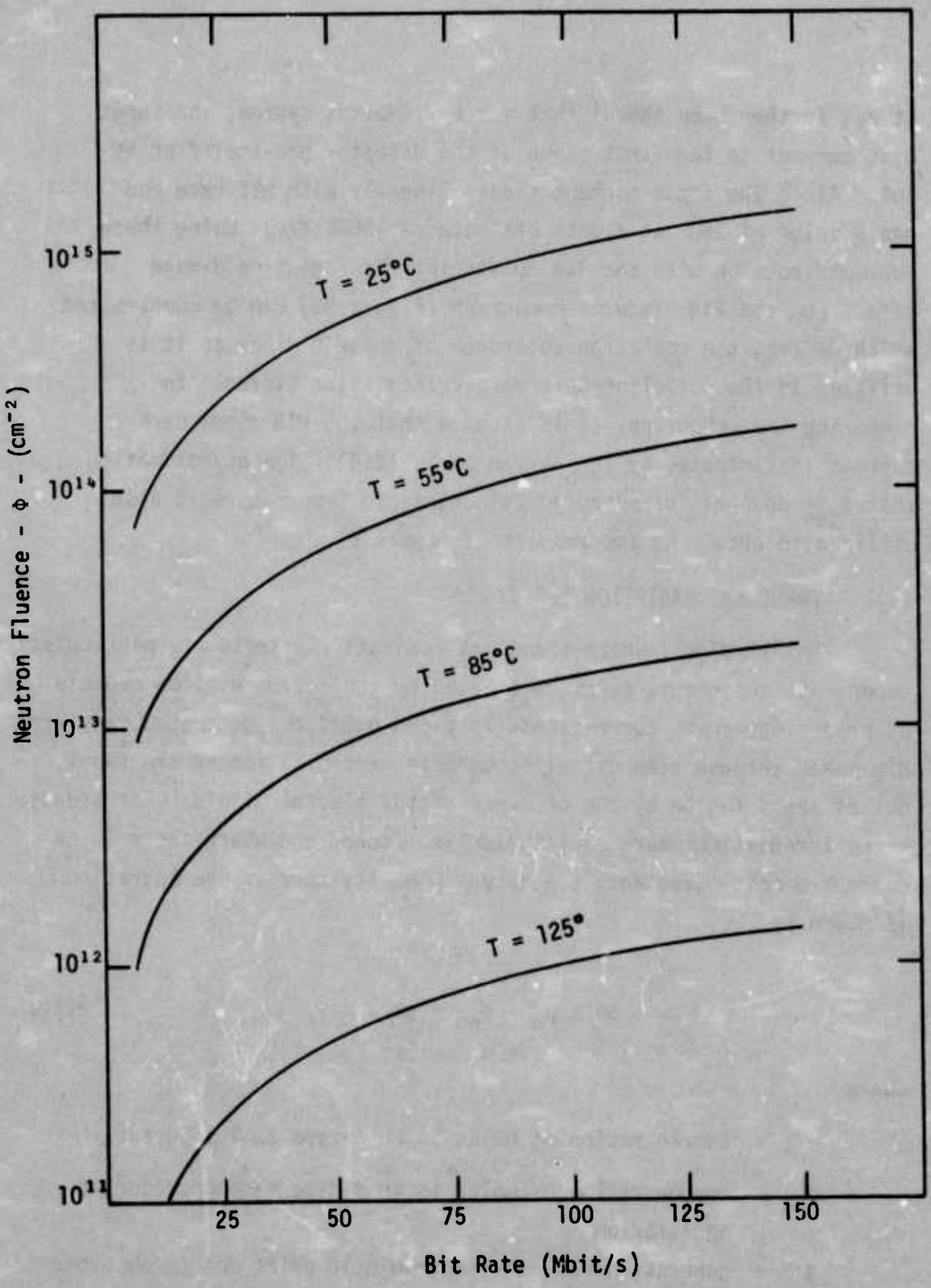

Figure 93. PIN Diode Radiation Tolerance as a Function of Transmission Bit Rate (Theory)

Two processes cause motion of the generated excess carriers and give rise to current flow in the PIN diode. The first process is due to the presence of the electric field and results in drift current. Typical junction transit times for carriers producing drift current in semiconductor devices are 0.1ns to 10ns. The second process is due to diffusion of the carriers in the presence of a carrier concentration gradient and results in diffusion current. The components of diffusion current are considerably slower than those of drift current and are typically 10ns to 1.0ms.

For the case of the PIN diode operated in the fully depleted mode (reach-through condition), diffusion currents become of secondary importance and transient radiation effects can be defined in terms of the drift current component only. Thus for a drift condition with I-layer transit time at ~ 1.0ns (short compared to the transient radiation pulse length, t_p) the short-circuit current I_d is given by

$$I_d = qgA_jW \tag{257}$$

where:

q = electron charge ($1.6 \cdot 10^{-19}$ C)

g = electron-hole pair generation rate = κR. For silicon[38], R = radiation intensity (rads/sec) and $\kappa = 4.3 \cdot 10^{13}$ pairs/cm^3-rad.

A_j = junction area

W = depletion-layer width

Then for the specific case of the SPX 1615 PIN diode:

A_j = .0126 cm^2

W = 95μm

and from Eq (257)

$$I_d = (1.6 \cdot 10^{-19})(4.3 \cdot 10^{13})(.0126)(95 \cdot 10^{-4}) = 8.2 \cdot 10^{-10} \text{A/rad-s}^{-1} \quad (258)$$

The generated current pulse in the SPX 1615 would appear as shown in Figure 94.

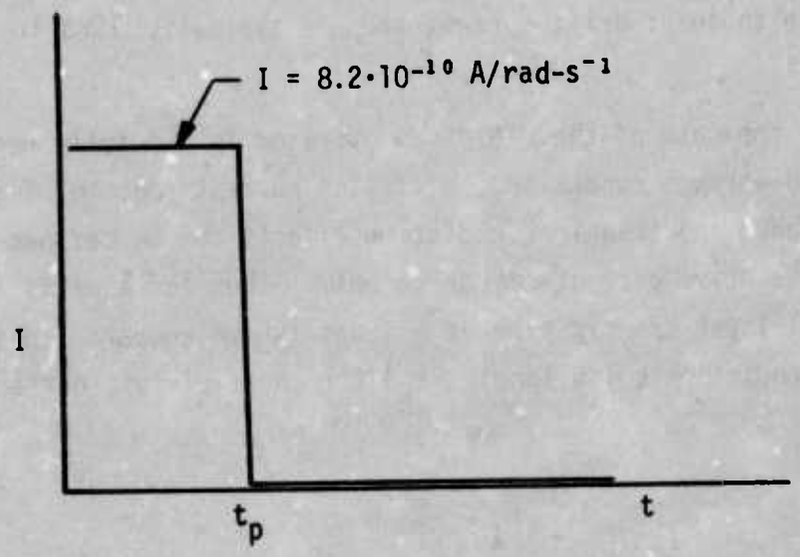

Figure 94. SPX 1615 Response to Transient Ionizing Radiation of Constant Amplitude and Time Duration t_p

It is of interest to calculate the transient radiation flux level in the PIN diode which would be disruptive to data interpretation for a given fiber-optic system. As an example, consider a system comprised of 150ft of Galileo fiber having attenuation of .2dB/ft. Assume that 1 milliwatt of power is coupled into the fiber from the LED and that the responsivity of the PIN diode is 0.5A/W. Then a 30dB signal loss occurs in the fiber and the resulting signal current flow in the PIN diode for this system is

$5 \cdot 10^{-7}$ A. If we assume that a transient radiation induced signal in the PIN diode equal to one fourth that of the peak-to-peak signal amplitude of a data pulse can be experienced without introducing an error in the data, then an incident transient radiation pulse of intensity, $R \leq 1.5 \cdot 10^{2}$ rad/s can be tolerated as calculated from Eq (257).

Similar calculations can be performed on other fiber-optic systems. Further consideration of these effects will be presented in an overall system study of radiation effects in Section X*.

D. MISCELLANEOUS RADIATION EFFECTS

1. Avalanche Breakdown Voltage (V_B)[40]

Radiation induced majority-carrier removal will serve to <u>increase</u> the avalanche-breakdown voltage of a conventional p-n diode. This effect has its origin in the reduction of electric field resulting from effective decrease of the doping levels in the junction by radiation-induced majority-carrier removal.

For the PIN diode considered herein, operation is in the reach-through mode (I layer of width W is fully depleted). The average electric-field, $\bar{E}$, in the I layer is given by

$$\bar{E} = \frac{V}{W} \tag{259}$$

For the abrupt P^+n and N^+n junctions characteristic of the PIN diode shown in Figure 91, W will remain essentially constant during radiation exposure because of the presence of the heavily doped P^+ and N^+ regions. These regions will not experience appreciable carrier removal until the neutron fluence exceeds values of $> 10^{17}/cm^2$. Electric field at a fixed bias will therefore remain constant and V_B will essentially be independent of neutron fluence for conventional exposures.

---

*In this Appendix

2. Junction Capacitance[40]

Capacitance of the conventional p-n junction at a given reverse voltage will decrease because of radiation-induced majority-carrier removal. This is caused by the increase of depletion-layer width for a given reverse voltage as the effective doping levels decrease on exposure to radiation.

For the PIN diode operated in the reach-through mode, capacitance is given by:

$$C = \frac{A_j \varepsilon_o \varepsilon_{Si}}{W} \tag{260}$$

and is independent of doping level. The P^+ and N^+ regions which serve as the boundaries of W will not move until neutron fluence values exceed $10^{17}/cm^2$. Capacitance of the PIN diode will therefore be independent of radiation effects at conventional exposure levels

3. Series Resistance

Series resistance of the PIN diode is primarily determined by the resistance generated in the P^+ and N^+ regions shown in Figure 91. Again, because of the heavy doping in the P^+ and N^+ regions, carrier removal effects will not become important until Φ exceeds $10^{17}/cm^2$. Onset of mobility degradation will take place at $\Phi \sim 10^{17}/cm^2$. Until these levels of neutron fluence are reached little if any increase should be expected in the series resistance of the reverse-biased PIN diode.

4. Quantum Efficiency

Quantum efficiency of the PIN diode of Figure 91 operated fully depleted with ohmic contacts close to the depletion region is to first order independent of electron or hole diffusion length. In this case, absorption of all incident quanta takes place only in the

I layer and minority carriers are drifted across the I layer by the electric field and collected at the device terminals. The quantum efficiency should therefore be independent of neutron radiation damage for PIN diodes of the type shown in Figure 91.

SECTION VI
RADIATION EFFECTS ON GaAs LEDS

A. INTRODUCTION

The p-n junction light-emitting diodes (LEDs)[44] summarized in Table XVIII exhibit 10-90% rise times of less than 20 nanoseconds, operate without special cooling, have small size, low cost, rugged construction and are well suited for data-bus use.

Table XVIII. LED Components for Data Bus Use

GaAs (Zn-Si) zinc diffused
InGaAs (single heterostructure)
GaAlAs (single heterostructure)

The LEDs summarized in Table XIX are not generally used for data-bus applications and hence will not be considered in the discussion of radiation effects[45,46].

Table XIX*. LED Components Not Suited for Data Bus Use

LED	Comment
$GaAs_{1-x}P_x$	not reliable, too inefficient
GaAs(Si-Si)	too slow
GaP	too inefficient

*Although plastic fibers in general appear promising from a radiation hardness standpoint, they suffer an intolerably high inherent loss factor at 900nm. In the vicinity of 700nm, however, the plastic fibers have an acceptable inherent loss factor of only ~0.7dB/m and thus can perform the fiber-optic function in this latter wavelength range. The GaAsP LEDs defined in Table XIX can be fabricated to radiate in the 700nm range. They unfortunately possess the physical deficiencies defined in Table XIX and high-performance LEDs with radiation wavelengths compatible to plastic fiber optics are not available. Basic material limitations presently indicate that a high-data rate plastic fiber/LED-based military system will not be achieved.

Attention is therefore directed toward defining radiation-damage effects on the particular devices summarized in Table XVIII. The information pertaining to these effects will be somewhat rudimentary since extensive documentation and a comprehensive understanding of radiation-damage effects on III-V LEDs is not yet available.

B. PERMANENT RADIATION EFFECTS ON GaAs (Zn-Si) LEDs

1. Response to Gamma Irradiation

Investigations of the decrease in external quantum efficiency of light output of coherent and incoherent GaAs diodes has been attributed to the introduction of nonradiative defect centers which decrease the minority-carrier lifetime.[49-51]. The effect has been quantified by Share et-al[52] for radiation effects on closely compensated LEDs whose p-n junction regions are formed with Zn and Si, respectively. These diodes were fabricated by diffusing zinc into n-type, silicon-doped GaAs, $N_D = 1.5 \cdot 10^{18}/cm^3$. Light was emitted from the p region and the number of p-radiative centers was considered to be approximately $4 \cdot 10^{16}/cm^3$. Response to gamma-ray radiation damage can be summarized as:

a. Degradation of radiative lifetime, τ_R.

The light-generating mechanism is apparently more strongly affected by ^{60}Co gamma rays than by fast neutrons. For example, Share et-al[52] find that at gamma-dose levels of 10^8 rads (Si), the external quantum efficiency drops off almost exponentially (a factor of 300); whereas, the minority-carrier lifetime τ only decreases slightly (by a factor of 7). The large reduction in efficiency with gamma dosage accompanied by the small decrease in carrier lifetime indicates that the decrease in efficiency is not solely due to a decrease in minority carrier lifetime. The radiative lifetime is found to increase as:

$$\frac{1}{\tau_R} = \frac{1}{\tau_{Ro}} e^{-cD} \qquad (261)$$

where:

τ_R = radiative lifetime

τ_{Ro} = pre-irradiation radiative lifetime

D = dose in rads (Si)

c = Damage constant expressed in {rads (Si)}$^{-1}$

A c value for these diodes is found to be

$$c = 4 \cdot 10^{-8} \{\text{rads (Si)}\}^{-1} \tag{262}$$

b. Degradation of non-radiative lifetime, τ_N.

The effect of gamma dose on the non-radiative lifetime is given in analogy to Eq (248) by

$$\frac{1}{\tau_N} = \frac{1}{\tau_{No}} + K_\gamma D \tag{263}$$

where:

τ_N = non-radiative lifetime

τ_{No} = pre-irradiation non-radiative lifetime

K_γ = Damage constant expressed in {rads (Si) sec}$^{-1}$

The K_γ value for these diodes is found to be:

$$K_\gamma = 2.1 \{\text{rads (Si) s}\}^{-1} \tag{264}$$

The fractional degradation in external quantum efficiency produced by incident ^{60}Co gamma rays is

$$\frac{\eta}{\eta_o} = \frac{\tau_{No} + \tau_{Ro}}{\tau_N + \tau_{Ro} e^{cD}(1+\tau_{No} K_\gamma D)} \tag{265}$$

where

η = external quantum efficiency

η_o = pre-irradiation external quantum efficiency

and all other terms and coefficients have been defined.

2. Response to Neutron Irradiation

The total minority carrier lifetime τ can be expressed in terms of the radiative lifetime τ_R and the non-radiative lifetime τ_N as[53]

$$\frac{1}{\tau} = \frac{1}{\tau_R} + \frac{1}{\tau_N} \tag{266}$$

for exposure to neutrons, Eq (266) reduces to

$$\frac{1}{\tau} = \frac{1}{\tau_o} + K_N \Phi \tag{267}$$

where

I_o = pre-irradiation minority carrier lifetime

Φ = neutron fluence

K_N = Damage constant expressed in cm^2/s

A K_N value for these diodes is found to be

$$K_N = 12 \cdot 10^{-6} cm^2/s \tag{268}$$

The fractional degradation in external quantum efficiency induced by fast neutrons is given by

$$\frac{\eta}{\eta_o} = \frac{1}{(1 + \tau_o K_N \Phi)^{3/2}} \tag{269}$$

where all terms have been previously defined.

3. Summary of Response to Neutron and Gamma Irradiation (Permanent Damage Effect)

The above results indicate that the data can be fitted to a model in which gamma radiation introduces the following 2 defects which contribute to degradation of light output:

- Defects are introduced which act as non-radiative recombination centers resulting in a decrease in non-radiative lifetime.
- Defects are introduced which reduce the number of active recombination centers on the p-side of the junction. This has the effect of increasing the radiative lifetime. A low concentration of active radiation centers such as found in the Zn - Si diodes ($4 \cdot 10^{16}/cm^3$ Zn) is probably a necessary prerequisite for observing such an effect. The precise physical explanation for the effect, however, is presently undetermined.

The neutron-induced defects are primarily non-radiative in character since the reduction in efficiency can be explained by a decrease in minority-carrier lifetime.

Finally, from the data of Share et-al[52], it is to be noted that the external quantum efficiency is down by 50% at a ^{60}Co gamma dose of $\sim 10^7$ rads, Eq (265). A neutron fluence of $\sim 10^{13} cm^2$ is required to reduce the external quantum efficiency by 50%, Eq (269).

C. TRANSIENT RADIATION EFFECTS ON GaAs (Zn-Si) LEDs

A transient pulse of ionizing radiation incident on an LED will produce electron-hole pairs in and about the region of the p-n junction of the device. The resulting ionization will generate a current flow in a direction such as to forward bias the device. If the radiation

burst is of sufficient intensity (rad/s), the forward current flow will be large enough to generate a light output signal from the LED which will be disruptive to the normal flow of data in the fiber-optic system.

Let us calculate the ionizing radiation intensity required to generate the spurious signal from the LED. For the calculation assume that a type SPX 1775 LED is subjected to the ionizing radiation pulse and that forward current flow in the device of I_f= 50mA will generate the interfering signal. Then

$$I_f = qgA_jW_t \tag{270}$$

where

q = electron charge ($1.6 \cdot 10^{-19}$ C)

g = electron-hole pair generation rate

$$g = \frac{R(100\text{ergs/g})\,(\text{density of GaAs})}{(3\text{eV/ion-pair})(1.6 \cdot 10^{-12}\text{ergs/eV})}$$

R = dose (rad/s)

A_j = junction area = $50 \cdot 10^{-6}\text{cm}^2$ for the SPX 1775

W_t = junction thickness = $1.6 \cdot 10^{-3}$cm for the SPX 1775

Then substituting the appropriate values for the SPX 1775 LED into Eq (270) yields

$$50 \cdot 10^{-3} = \frac{(1.6 \cdot 10^{-19})(R)(100)(5.3)(50 \cdot 10^{-6})(1.6 \cdot 10^{-3})}{(3)(1.6 \cdot 10^{-12})} \tag{271}$$

and,

$$R = 3.5 \cdot 10^{10}\text{rad/s} \tag{272}$$

Thus an incident ionizing radiation pulse of intensity equal to $3.5 \cdot 10^{10}$ rad/s will generate a spurious light output signal from the SPX 1775 which will be disruptive to true data flow in the fiber-optic system.

SECTION VII

RADIATION EFFECTS ON FIBER OPTICS

A. INTRODUCTION

Recent investigations have demonstrated that substantial light transmission losses may arise in multimode glass fibers exposed to ionizing radiation[54,55]. In addition, generation of luminescence in the optical fiber during and immediately following the irradiation produces erroneous signals and in extreme cases can result in photodetector damage in optical systems[56]. This section summarizes results of radiation damage measurements which have been performed on both high- and low-loss fibers used in present-day optical systems and also on some of the other relevant bulk glasses and plastic fibers. A review of radiation hardening methods for fiber optics is also included.

If the optical system is to function in a radiation environment, radiation effects must be taken into account in component selection so that system sensitivity is not degraded and false signals are not introduced in the system. For typical LED transmitting powers and receiving system sensitivities, the total optical loss in the system can be about 45dB for a bit-error ratio of 10^{-6} to 10^{-8}. Optical losses have their origins in:[55]

10dB Loss
- 1) Coupling loss between LED and fiber,
- 2) Reflectivity loss at the ends of the fiber,
- 3) Packing-fraction loss due to the difference between total fiber bundle area and fiber-core area.

4) Inherent losses in the fiber material caused by absorption and scattering processes. The inherent loss can be defined in terms of the composition as follows:

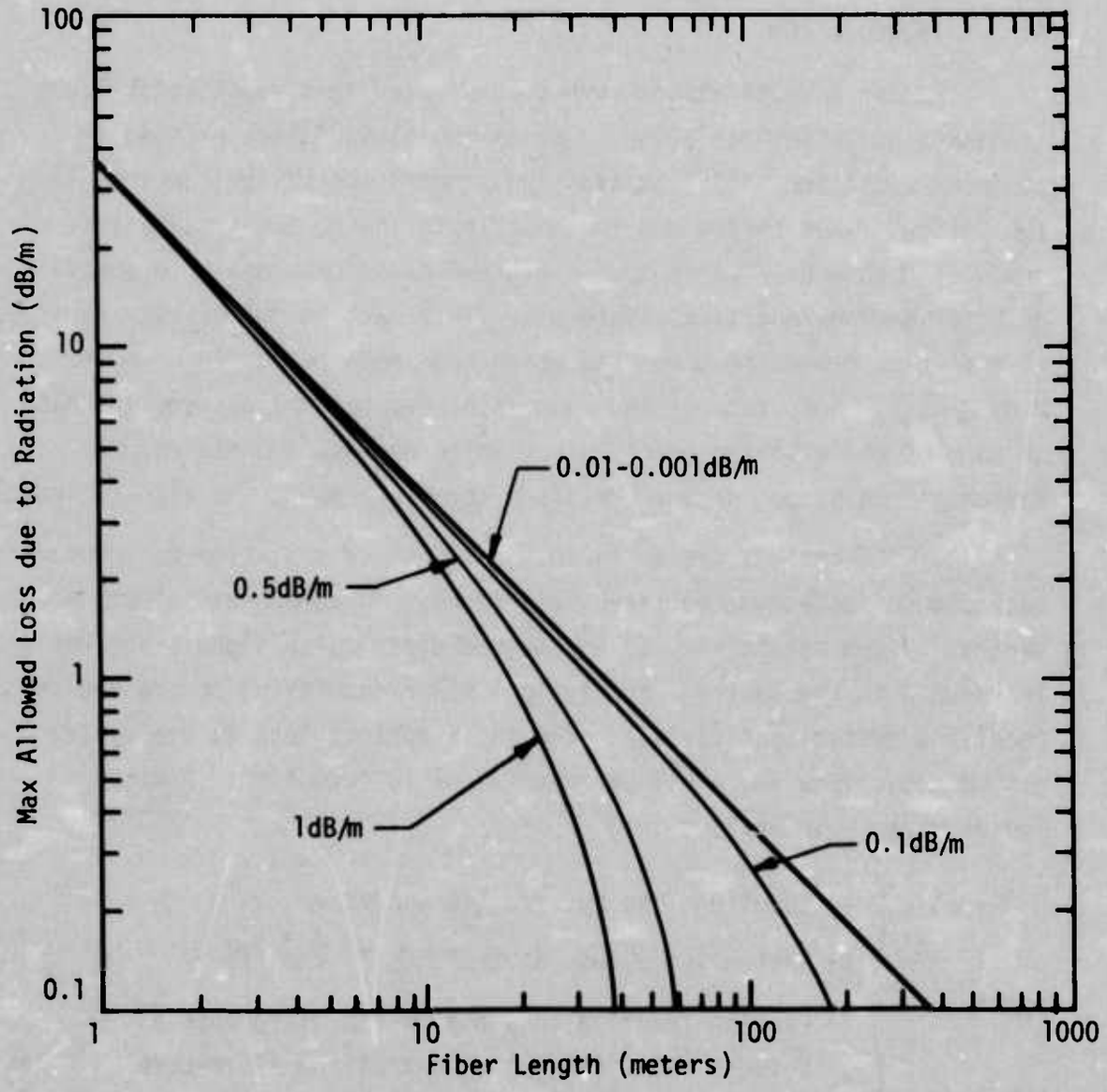

Figure 95. Maximum Allowable Radiation-Induced Absorption vs Fiber Length for Various Values of Inherent Loss

Material	Inherent Loss
Pure and some doped fused silicas	0.001-0.01dB/m
Best multicomponent glasses and some other doped glasses	0.1dB/m
Most commercially available fibers	0.5dB/m
Doped multicomponent glasses and plastics	1dB/m

5) Losses due to absorption centers induced by radiation damage.

Since a loss of ∿10dB is contributed by items 1 through 3 above, losses of ∿35dB can be expended in items 4 and 5. The maximum allowed loss due to irradiation (dB/m) can be expressed in terms of fiber length (meters) if the remaining 35dB loss is distributed between the inherent loss and radiation damage loss. The results are plotted in Figure 95 for the four levels of inherent loss defined in the fourth item above.

B. FIBER RESPONSE TO X- AND GAMMA RADIATION (PERMANENT DAMAGE)

Incident X- or gamma-rays produce energetic electrons in glass which dissipate their energy by formation of electron-hole pairs. Of those holes and electrons captured at the quasi lattice imperfections in the glass, some result in optical absorption[57]. Also, the irradiation energy (if high enough) may result in the production of defects and these defects when populated with holes and electrons may further contribute to absorption of light in glass fibers.

Most of the commercially available optical fibers (∿1dB/m inherent loss) consist of a high-index lead-silicate glass core clad with lower-index borosilicate glass. Radiation-induced loss versus wavelength for one of these fibers (Corning-5010) is shown in Figure 96[54]. The results summarized in Figure 96 are typical of the response exhibited by many of various fibers to high-energy photon exposure. Characteristics to be noted are:

- Increasing doses of ^{60}Co gamma-rays produce a general increase in induced absorption toward shorter wavelengths. Induced absorption results from color-center formation in the ultra-violet, visible, and near infra-red regions.
- The absorption bands near 400nm and 650nm are thought to be hole centers characteristic of silicate glasses[58].
- Absorption loss is approximately linear with dose for the values recorded in the range of 200 - 10,000 rads over a spectral distribution of 500nm to 1.15μm.
- Substantial fading of the radiation included absorption occurs with time at room temperature, c.f. insert of Figure 96. To avoid inconsistencies in reporting <u>permanent damage</u> effects introduced by absorption centers with short lifetimes, approximately 24 hours must be allowed between irradiation and subsequent redetermination of the optical absorption spectrum.

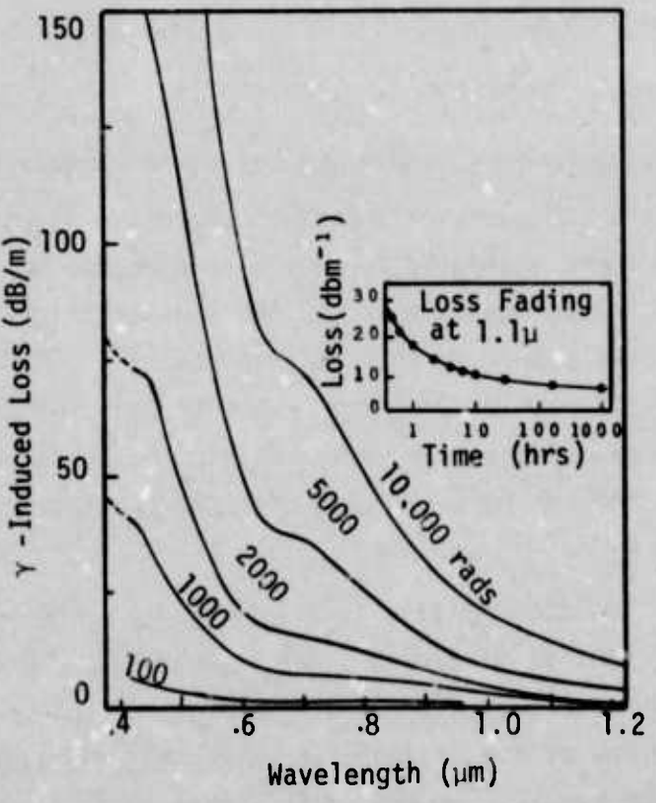

Figure 96. ^{60}Co Gamma-ray Induced Absorption Loss in Corning Type 5010 Fibers

Table XX summarizes reported values[55,59] for radiation-induced loss in several commercial fibers and relevant glasses at a wavelength value appropriate to systems discussed in this report, viz 900nm. The data of Table XX can be used in conjunction with the information summarized in Figure 95 for treatment of system design situations. For example, Corning 5010 fibers suffer a permanent absorption loss of 2.5dB/m on expose to 1.0 k/rad of radiation thereby limiting fiber length to 10 meters in system application at this radiation level. In contrast, 10-meter long Corning low-loss (SiO_2(Ge): SiO_2) fibers can withstand approximately 5000 k/rad of radiation for equivalent system performance based on linear extrapolation of radiation damage constant given in Table XX.

C. FIBER RESPONSE TO FAST NEUTRONS (PERMANENT DAMAGE)

Pioneering investigations[60,61,62] of neutron radiation damage effects on crystalline and fused silica were performed in the late 1950's. The nature of the work involved discovery of radiation induced absorption bands, wavelength location of the bands, discovery of optical and thermal bleaching (fading) of the bands, Gaussian curve fitting to the resolved bands, and establishing models of band formation. Perhaps one of the most important basic discoveries of the time was that when samples are subject to fast-neutron irradiation, color centers are produced which subsequently are activated (become colored) by ionizing radiation.

The early investigations were performed with neutron fluences greater than $10^{18}/cm^2$ which are at least six orders of magnitude higher than those of present interest for long fiber-optic cables. The optical materials of that time were also limited in their variety of compositions. In addition, many of the studies were concentrated on the absorption bands as they developed in the ultraviolet. Thus although these efforts are not of pragmatic value to the design of radiation hardened fiber-optic systems, experimental techniques were developed and data were obtained which provide a foundation for the

Table XX . Inherent Loss and Gamma Radiation Induced Loss of Selected Fibers and Glass (^{60}Co-Gamma)

Manufacturer	Type and Composition	Form	Inherent Loss (dB/m @ 900nm)	Radiation Damage Permanent Loss (dB/m-k rad @ 900nm)
Valtec	101	Fiber	.1	3.4
Corning	5010 (Pb-silicate	Fiber	0.5 - 1	2.5
Galileo	K2-K-350 (Pb-silicate)	Fiber	0.5 - 1	1.9
Owens Corning	130 (Ba-Silicate)	Fiber		1.0
Electro Fiber Optics	LF5/R6	Fiber	0.5 - 1	0.75
Corning	SiO_2(Ti): SiO_2	Fiber		0.45
Bendix	PR_3/K	Fiber	0.5 - 1	0.3
Corning	7971 ULE (Ti-Silicate)	Bulk		0.29
American Optical	UK50/EN-1	Fiber	0.5 - 1	0.1
Owens Corning	X-4048B	Bulk		0.04
Owens Corning	X-4115	Bulk		<0.01
NRL	SiO_2 - B_2O_3	Bulk	.01	0.004
Bell Labs	SiO_2: B_2O_3 - SiO_2	Fiber	.01	0.0027
Corning	SiO_2(Ge):SiO_2	Fiber	.01	0.0009
NRL	Soda Lime (.1% Ce)	Bulk	.1	.001
Int. Fiber Optics	Polystyrene	Fiber	0.5 - 1	0.0002
Heraeus-Schott	Suprasil 1	Bulk	.1	<0.00001

concentrated research efforts which are needed on present-day fiber optics.

Neutron radiation damage data for fiber optics is much more limited in availability than is that of damage effects from ^{60}Co gamma rays. The recent work of Maurer et-al[63]; however, indicates that the spectral response of absorption loss induced by fast neutrons (E = 14MeV) is similar in shape to that resulting from fiber exposure to ^{60}Co gamma rays, c.f. Figure 95. In general, the radiation induced changes are large at short wavelengths and decrease monotonically to very small effects at longer wavelengths. Maurer et-al[63] measured twenty-five to fifty-meter sections of multimode high-silica glass fibers in their original state at Corning Glass Works and then subjected them to irradiation at USAECOM, Fort Monmouth. The samples were returned to Corning for transmission measurements. Results indicated that a 14MeV neutron fluence of $1.4 \cdot 10^{12}/cm^2$ induced an attenuation of $\sim$0.02dB/m at 900nm in these fibers.

Other data pertaining to neutron induced loss in various fibers has recently been obtained from the Sandia Laboratories at Livermore, California[64]. Their results are summarized in Table XXI. The 1MeV neutrons used in the experiment are derived from a polonium-beryllium source. Although the data of Table XXI are preliminary and should be used with caution until formally published, it would appear that the equivalence of permanent damage generated by fast neutrons and ^{60}Co gamma rays is given very approximately for the lead silicate glasses as

$$3 \cdot 10^{10} \text{neutrons/cm}^2 \text{ @ 1MeV} \simeq 1.0\text{k rad of } ^{60}\text{Co gammas} \qquad (273)$$

Further complications in interpreting the data of Table XXI arise in that saturation effects in neutron radiation damage (non-linear response) have been observed[64].

Table XXI. Inherent Loss and Fast-Neutron Radiation
Induced Loss of Selected Fibers
for 1.0MeV Neutrons

Manufacturer	Type and Composition	Form	Inherent Loss (dB/m @ 900nm)	Radiation Damage Permanent Loss $\phi = 10^{10}/cm^2$ (dB/m @ 900nm)
Bendix	K2K	fiber	1	∿0.8
Corning	SiO_2(Ge): SiO_2	fiber	0.1	∿0.05
Schott	Suprasil	fiber	0.03	∿0.05
Int. Fiber Optics	Polystyrene	fiber	30	∿0.01
Dupont	Crofon (PMMA)	fiber	30	∿0.01

It is realized that fast neutrons create atomic displacement with resulting generation of defects. Electron and hole excitation by ionizing radiation followed by trapping of electrons and holes at the defects creates the light absorbing color centers. It is not obvious then as to the degree by which neutron damage to the fibers enhances the damage sensitivity to ensuing X-rays and gamma rays. Clearly, further neutron-damage experiments are required on fiber optics.

D. TRANSIENT RADIATION EFFECTS

Some military and civilian communication systems may be subject to exposure to ionizing radiation fields of various intensities. It is therefore of importance to characterize the transient response of optical fibers to bursts of ionizing radiation. Two transient characteristics are observed. They are luminescence and decay of characteristic absorption spectra in the irradiated fiber.

1. Luminescence

Generation of luminescence in optical fibers during pulsed irradiation is indicated by a detectable light level in the fibers which is in excess of the pre-irradiation value. For fiber optic data links operating in a pulsed radiation environment, luminescence detected by broad-band silicon photodetectors acts as a source of false signals and may represent possible transient interference on the communications system. The effect has been studied in some detail[55,59] and it has been found that the luminescent intensity during pulsed irradiation is large enough to interfere with signal detection in typical applications. Data have been obtained for X-ray and electron exposure rates from 10^3 to $\sim 10^{12}$ rad/s. Pulse duration was typically 50ns.

Characteristics of the induced luminescence can be summarized as follows:

- The intensity of luminescence is proportional to the instantaneous rate of dose deposition in the fiber.
- The most prominent feature of luminescent spectra is the increase in emission intensity toward shorter wavelengths.
- Luminescence is caused primarily by Cerenkov radiation of electron origin. Threshold energy for electrons is greater than 200 keV for glass with index of refraction ≈1.5 for producing Cerenkov output.
- Processes such as electron-hole recombination also contribute to luminescence.
- Luminescence is observed only during the irradiation pulse [55]. An exponential decay with characteristic constant of ∿170μs has, however, been observed for luminescence in certain glasses[59].
- The intensity of luminescence is greater during electron irradiation than during X-ray excitation for the same dose. (X-rays must be converted into high energy electrons by the Compton process, etc. in order to generate Cerenkov radiation.)

It is concluded that even in an optimistic evaluation including filtering, luminescence generated during a pulsed irradiation can interfere with signal processing and detection in many applications unless special circumvention or lock-out techniques are employed[55]. The electronic recognition of valid Manchester data code and parity check should be particularly effective in nullifying the system response to luminescence generated by the radiation pulse.

2. Decay of Characteristic Absorption Spectra

The transient nature of defect centers in glass has been recognized for many years. An example of these effects is found in the fading of radiation induced coloration in glass dosimeters[65]. Time spans of hours to days were of interest for dosimeter glasses. For fiber optic data systems, we are interested in the range extending from hundreds of microseconds to several hours following exposure to ionizing radiation. In a previous section of this report, radiation induced absorption spectra are considered to be permanent twenty-four hours after the conclusion of exposure. We will continue to make this assumption concerning permanent damage, although in reality thermal untrapping processes continue indefinitely. It will be found that the radiation induced transient absorption is typically orders of magnitude larger than the radiation induced permanent absorption.

Following is a summary of experimentally determined decay characteristics of radiation induced absorption spectra:

- The high-loss fibers, following pulse irradiation, show substantially more radiation induced loss than the low-loss fibers.
- Measured decay rates are similar following both pulsed electron and X-radiation. Both the magnitude and shape of the peak transient absorption spectra are substantially the same for equivalent doses of electrons and X-rays.
- The magnitude of the peak transient absorption is, in most glasses, approximately linear with dose for exposures up to ~50 k rad. Above that dose level, saturation effects become dominant.
- The magnitude of the peak transient absorption spectrum is different from the permanent absorption spectrum for a given material. For example, the absorption spectrum of Corning low-loss fibers

Table XXII. Fiber Transient Response

Fiber Type	Pulse Dose Electron or Gamma-Ray (rad)	Fiber Length For 35dB Optical Attenuation at 900nm at Indicated Time After Electron or Gamma-Ray Pulse (meters)			
		t = 100μs	t = 1s	t = 5s	t = 1min
Typical lead-silicate Inherent loss = 1dB/m	100 3000 10^6	10 .46 .0014	15 .87 .0027	-	18 1.3 .0038
BTL SiO_2: B_2O_3-SiO_2 Inherent loss = .01dB/m	100 3000 10^6	3000 66 .2	3400 500 1.5	-	3500 1100 4.9
Corning Low Loss SiO_2(Ge): SiO_2 Inherent loss = .01dB/m	100 3000 10^6	220 450* 8 17* .02 .05*	2900 450 1.6	-	3300 1400 7
Corning I-279 Inherent loss = .01dB/m	100 3000 10^6	1300** 70** .2**	-	-	-
Crofon - PMMA all plastic Inherent loss = 1dB/m†	100 3000 10^6	33* 12* .6*	-	-	-
Schott Vitreous Silica plastic clad Inherent loss = .1dB/m††	100 3000 10^6	290* 100* 4.5*	350* 280* 40*	350* 300* 55*	

* Data of Mattern, Watkins, Skogg, Brandon and Barsis[55]
† Analysis performed at 700nm
** Data of J. A. Wall[66]
†† Optical Absorption is nonlinear with dose[55].

measured 24 hours after ^{60}Co gamma irradiation appears as the tail of a band centered at the shorter wavelengths, with negligible absorption above 600nm. In contrast, the transient spectrum in the same material peaks near 500nm with a monatonically decreasing tail extending beyond 900nm.

The fading of the transient absorption spectrum follows a power law (i.e., fading $t^{-\alpha}$). The recovery data can thus not be explained by a conventional model involving the characteristic expenential decay of thermally stimulated release of trapped charge.

To obtain an appreciation of what transient decay implies for a real system, Table XXII shows the maximum lengths which could be used for some representative fibers at a transmission wavelength of 900nm if a 35dB radiation loss could be tolerated in the fiber link. The results of Table XXII are obtained from the data of Sigel et-al[59], Mattern et-al[55], and Wall[66]. From the results of Table XXII it would appear that for reasonable recovery times, the entire optical data link will be dominated by transient effects in the fibers. Recovery times of several minutes may be required with accompanying system shut down in order to establish adequate recovery of the fibers and proper system performance. Here again, electronic recognition of valid Manchester data code and parity check should be effective in nullifying the system response to the radiation pulse.

E. RADIATION HARDENED FIBER OPTICS

Research for protecting fiber optics material against radiation has been initiated. In one of the investigations[54], the application of the conventional glass window radiation protection method of cerium doping has been employed. High purity soda lime silicate glass of composition 0.75 SiO_2, 0.2 Na_2O, and 0.05 CaO was prepared without

cerium, with 0.001% mole $CeO_{1.5}$ and with 0.01% $CeO_{1.5}$. Figure 97 shows the relative response of the three glasses following a $5 \cdot 10^7$ rad dose. In the visible and near IR, substantial radiation hardening has been achieved. Protection by trivalent cerium has been found to be successful if optical losses arise from hole-center absorption bands. This approach to radiation protected lead-silicate glasses is also being pursued by Acharekar[67].

The result of another recent study[68] has shown that the radiation response of silica, germania and doped silica can be altered by controlling the ambient atmosphere during heat treatment. If there are oxygen vacancies in the glass, the concentration of E' defects may be decreased and the fiber radiation hardened by heat treatment in an oxygen atmosphere. In addition, high-temperature annealing in argon may be used to relieve strained bonds. This latter technique has been used to decrease the radiation sensitivity observed in Corning 7943, Suprasil, and Dynasil 1000[68].

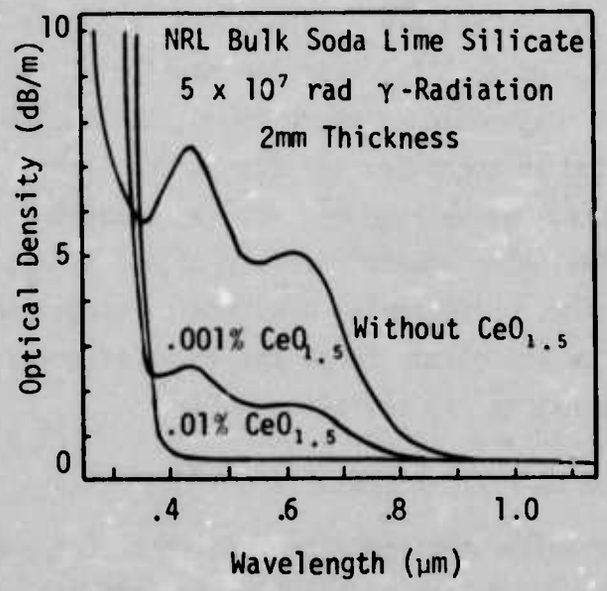

Figure 97. Radiation hardening of soda lime silicate glass with cerium-oxide doping.

There have been indications that hydroxyl content has an inhibiting effect on the formation of radiation induced absorption centers in vitreous silica[69]. It has therefore been proposed that OH radicals reside at oxygen sites, preventing the formation of oxygen vacancies and E' defects during irradiation. In conflict with the latter, however, is the physical characteristic that silica for fiber optics must be prepared with low OH content to prevent optical absorption in the infrared by OH harmonic bands. It may therefore be advantageous to seek alternate methods for lowering the intrinsic absorption near 900nm. One such method would be the exchange of deuterium for hydrogen in the hydroxyl concentration thereby shifting predominant 950nm band to 1,340nm while at the same time maintaining a high deuterated "hydroxyl" content. Recent measurements[70] indicate that under appropriate conditions, this procedure would be practical for glass fibers.

SECTION VIII

RESPONSE OF COUPLERS TO THE RADIATION ENVIRONMENT

Passive optical couplers will typically use scrambler rods made from the same type of glass as the core glass of the fiber optic bundles used in the system. Flexible side arms in the couplers will employ the same type fiber optic bundle as is used in the system. With the construction technique reported in Ref 2, the passive couplers use unclad solid glass scrambler rods that are surrounded and held in place by a low-index silicone or epoxy resin which also acts as a cladding layer. Based on this approach, the nuclear radiation resistance of the passive coupler is expected to be equal to or better than an equivalent length of the corresponding fiber optic bundle.

With the lead glass/borosilicate glass fibers (Galileo, Rank, American Optical and Pilkington), the plastic cladding used in the coupler will give superior performance to the borosilicate glass cladding used in the fiber optic bundles. This same situation applies to couplers made for Corning low-loss fiber. With the plastic clad-fused silica fibers, the couplers and fiber-optic bundles should have equivalent radiation resistance. Since these fibers and couplers use undoped SiO_2, they are expected to give the best radiation resistance of any of the approaches considered.

All-plastic fiber bundles and couplers based on DuPont's Crofon fibers will provide nuclear radiation resistance that is better than the lead-silicate fibers but worst than the plastic clad-fused silica fibers. This approach has not been considered because plastic fiber optic bundles require LEDs with a wavelength of less than 700nm and high-performance LEDs in this wavelength range are not available. Basic material limitations seem to indicate that a suitable plastic-fiber LED for high data rate applications will not be achieved.

SECTION IX

RADIATION RESISTANCE OF INTEGRATED CIRCUIT COMPONENTS

A. INTRODUCTION

The radiation exposures that can cause failure of semiconductor devices cover an exceedingly wide range. In general, the most sensitive devices degrade sufficiently to cause circuit malfunction at fluences of 10^{12} fast neutrons/cm^2. Diodes and transistors can be selected, however, to provide adequate resistance to fluences of 10^{14} fast neutrons/cm^2.

Although radiation-damage effects in discrete bipolar devices have been detailed[71], there is presently a dearth of published information pertaining to radiation effects on standard, commercially available digital and linear integrated circuits (ICs). An attempt will be made, however, to summarize the radiation resistance of ICs since these components will be used in peripheral circuits serving solid-state optical data transmission systems. Definition of the radiation hardness, of IC components is therefore needed in order to assess the overall radiation resistance of the optical system.

B. DIGITAL INTEGRATED CIRCUITS

Permanent radiation damage of digital ICs primarily affects the parameters of fanout and propagation delay. Olson et-al[72] have reported on radiation response of the RSN54L series of radiation hardened TTL digital ICs. These circuits feature dielectric isolation, thin film resistors, and photocurrent compensation. The foregoing technical innovations harden the devices mainly with respect to transient radiation effects. The RSN54L gates were found to be within full electrical specifications at a total neutron fluence of $1.4 \cdot 10^{14}$ n/cm^2 (1 MeV average) and a total electron (17 MeV) fluence equivalent to 10^8 rad (Si).

The gamma-ray transient failure threshold was found to be $3 \cdot 10^9$ rad(Si)/s.

The above data coupled with published information[73,74,75] provide the basis for an estimate that standard bipolar digital IC components should be fairly insensitive to neutron fluences up to 10^{13} n/cm^2, electron and gamma-ray exposure to 10^7 rads and transient exposure of $\sim 10^7$ rad/s.

C. LINEAR INTEGRATED CIRCUITS

Permanent radiation damage effects on linear ICs degrade parameters such as open loop gain, input resistance, and offset voltage. Only limited experimental information pertaining to these effects has been reported in the literature[76]. From the published data and basic comparisons of digital to linear circuit operation, it is estimated that standard linear ICs should be relatively insensitive to neutron fluences up to $\sim 10^{12}$ n/cm^2, electron and gamma-ray exposure of $\sim 10^6$ rads and transient exposure of $\sim 10^5$ rad/s.

SECTION X

SYSTEM ANALYSIS AND CONCLUSIONS

This section presents an overall view of nuclear radiation effects on a state-of-the-art optoelectronic data transmission system. The system performance is drawn from the analysis and measurements presented in other sections of the report. The effects of various kinds of nuclear radiation are evaluated using data and concepts presented in this appendix. The radiation analysis covers four different types of fiber optic bundle; pulse transient and permanent effects are considered. The system performance in different radiation environments is discussed and conclusions and recommendations are presented.

A. SYSTEM DEFINITION

Recent component development has resulted in improved LEDs and detectors for use in optoelectronic data transmission systems and data buses. The SPX 1775* LED is an hermetically sealed edge emitter designed for a plugable interface with 23 to 46mil diameter fiber optic bundles. This GaAs LED delivers a total output power of about 2.75mW at a bias of 100mA. The GaAs edge emitter wafer used in this LED is the same as used in the SPX 1527 described in Section IV.D. in the body of this report. The improved package of the SPX 1775 gives a thermal resistance of 100°C/W which eliminates much of the LED slow tail response. It also eliminates the need for a lens termination on the fiber optic bundle and provides minimum LED/fiber optic interface loss.

The SPX 1777* is an hermetically sealed silicon planar PIN photodiode that is also designed for a plugable interface with 23

*The SPX 1775 and SPX 1777 photodiode were developed for the Naval Avionics Facility at Indianapolis on Contract N00163-73-C-0544.

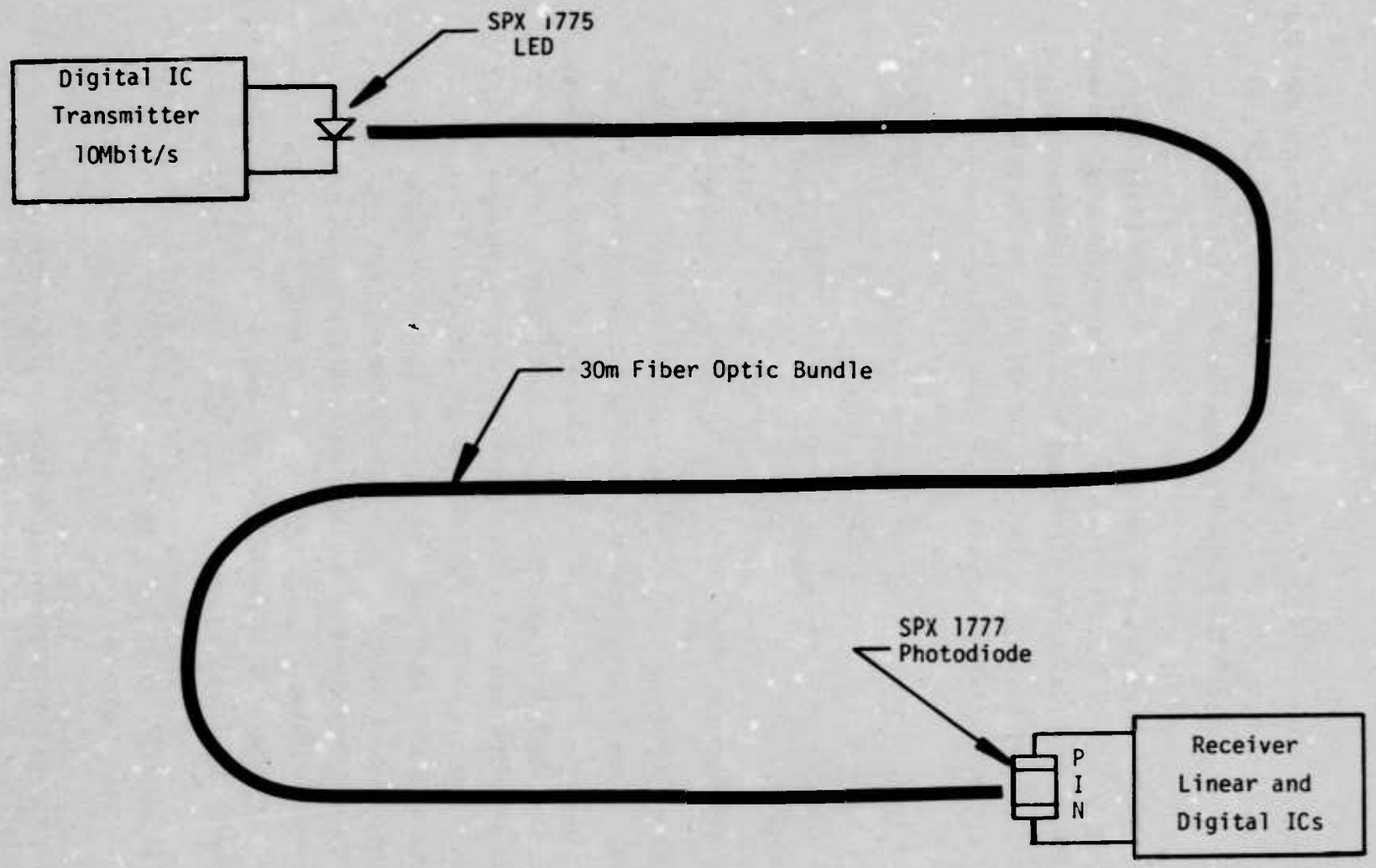

Figure 98. Optoelectronic Data Transmission System

to 46mil diameter fiber optic bundles. This silicon detector uses the same PIN photodiode chip as the SPX 1615. Therefore, the SPX 1615 analyses presented in Appendix 1 and Section V of this appendix as well as the measured characteristics in Section IV.E.2 in the body of the report are applicable to the SPX 1777. The package design of the SPX 1777 eliminates the need for a lens termination on the fiber optic bundle and reduces the detector/fiber optic interface loss to a minimum. The measured responsivity of the SPX 1777 is 0.5A/W including all interface losses.

The system selected for analysis is a 10Mbit/s (Manchester) data transmission link as shown in Figure 98. The system consists of a digital IC transmitter, an SPX 1775 LED, 30m of fiber optic bundle, an SPX 1777 photodiode, a receiver using both linear and digital ICs.

The four types of fiber optic bundles selected for study are listed in Table XXIII. Additional information on these fiber optic bundles is presented in Table III.

For 10Mbit/s Manchester data, the preamp 3dB frequency, f_e, from Eq (5) is 8.1MHz. Allowing 2.5 times more bandwidth for synchronization and clock recovery, the required 3dB bandwidth is 20MHz. From Eq (20) an optimized 20MHz preamp has an input noise current of 8.9nA. Combining this preamp with the SPX 1777 photodiode with a responsivity of 0.5A/W gives a required optical signal power of 17.8nW at the exit end of the fiber optic bundle for S/N = 1. For a bit error rate of 10^{-8} including clock errors and data errors the required S/N is about 5.75. For 2.5 times excess bandwidth, the fractional response of the amplifier is 1.0; thus, from Eq (35) the required steady-state power at the exit end of the fiber bundle is 206nW. For an SPX 1775 LED with a total 907nm output power of 2.75mW, the maximum allowable attenuation of the optical system is

$$\text{maximum attenuation} = \frac{206\text{nW}}{2.75\text{mW}} = 7.5 \cdot 10^{-5} \qquad (-41.25\text{dB}) \qquad (274)$$

Table XXIII. System Definition

Fiber Manufacturer	Fiber Type	End Loss	Fiber Attenuation	Excess Signal
Galileo	lead-silicate	3.3dB	17.7dB	20.25dB
Pilkington	lead-silicate	8.3dB	3.0dB	29.95dB
Schott	SiO_2 plastic clad	8.6dB	3.0dB	29.65dB
Corning	SiO_2(Ge): SiO_2	12.9dB	0.9dB	27.45dB

Table XXIII shows how this maximum attenuation is distributed in the system for each of the four fiber optic bundle types. The end losses represent measured values for the Galileo, Pilkington and Corning fibers and a calculated value for the Schott fiber. This calculation assumed that the Schott fiber optic bundle consisted of 19 fibers each having a 4mil diameter core and numerical aperture of 0.3. The fiber attenuation was calculated for each bundle type using the specified 30m length and the attenuation factors given in Table III. The excess signal column in Table XXIII specifies the ratio between the actual power at the exit end of the fiber optic bundle and the required minimum power:

$$\text{excess signal} = 10 \log \left[\frac{\text{actual signal}}{206\text{nW}} \right] \tag{275}$$

For each fiber type, the sum of the end loss, fiber attenuation and excess signal is the maximum allowable attenuation of 41.25dB.

The design philosophy for implementing radiation hard opto-electronic data transmission systems begins with seeking the largest possible value of excess signal. This quantity alone defines the amount of S/N degradation that can be allowed and still meet the error rate specification. When the S/N degrades more than this amount the error rate increases dramatically. The S/N can degrade due to

1) decrease in LED output power,
2) increase in fiber bundle attenuation,
3) increase in receiver noise,
4) decrease in receiver gain,
5) light generated in the fibers by ionizing radiation, and
6) response of the LED, photodiode and ICs to ionizing radiation.

Items 1) thru 4) can in principle be either permanent or transient sources of degradation. However, the annealing effects associated with the degradation of the LED, photodiode and ICs are very slow at ordinary temperatures (hours-weeks) compared to the response time of an aircraft. Thus, the degradation of the LED and PIN photodiode must be treated as permanent. Fiber optic bundles exhibit both transient and permanent increases in attenuation, item 2), and the transient effects can decay significantly in times less than 1.0s. Items 5) and 6) comprise a third category of distrubance in the system. This is the direct response of the semiconductor devices and fiber optic bundle to ionizing radiation such as high energy electrons, X-rays and gamma rays. In this analysis and discussion this type disturbance will be referred to as the nuclear pulse response of the system to distinguish it from the permanent and transient effects.

The two lead-silicate fiber types are included in this analysis to demonstrate the impact of the pre-irradiation fiber loss on the hardness of the system. The Galileo fiber has lower end loss than the smaller diameter Pilkington bundle but this is more than offset by the higher attenuation of the Galileo fiber; the Pilkington system has 9.7dB more excess signal than the Galileo system. The Schott system has about the same end loss and fiber attenuation as the Pilkington system. Comparison of these systems will show the basic difference between the lead-silicate and SiO_2 fibers in a nuclear radiation environment. This emphasizes the other major consideration in the design philosophy of radiation hard optoelectronic data transmission systems; namely, to construct the system using the best radiation hard components available. The Corning system in Table XXIII has high end loss and very low fiber attenuation. The excess signal is only 2.2dB less than for the Schott system. The Corning fiber, with its germanium doped SiO_2 core offers a different set of characteristics in the nuclear radiation environment.

B. SYSTEM PERFORMANCE

The system performance in various nuclear radiation environments is presented in Table XXIV. The three classes of system performance degradation that are considered are

- permanent degradation,
- transient degradation, and
- nuclear pulse response.

The remainder of this system performance section will be devoted to a detailed discussion and explanation of the data presented in Table XXIV.

1. Permanent Degradation

Permanent degradation of the system is caused by both high-energy neutrons and ionizing radiation (high-energy electrons, X-rays and gamma rays). In Table XXIV the ionizing radiation is represented by gamma rays. The permanent degradation is dependent on the total integrated dose and usually is independent of dose rate. For the nuclear radiation enviornment of an aircraft, the total dose could be received in a single short pulse of high dose rate.

For the Galileo fiber, the system bit error rate will be at 10^{-8} after a dose of $8.4 \cdot 10^{9}/cm^{2}$ 1.0MeV neutrons or a dose of 355 rad of ^{60}Co gamma rays. At these low dose levels there is no significant change in the LED, photodiode, linear ICs or digital ICs; all of the permanent damage is in the Galileo fiber optic bundle. Any dose larger than the values shown will cause a dramatic rise in the bit error rate. The Galileo fiber has very poor nuclear radiation hardness.

The Pilkington fiber is also based on lead-silicate glass and, therefore, has much the same nuclear radiation degradation characteristics as the Galileo fiber. The Pilkington system has

Table XXIV. Optoelectronic 10Mbit/s Data Transmission System Performance in Nuclear Radiation Environment

Fiber Manufacturer	Excess Signal	Permanent		Transient*		Nuclear Pulse
		Total Dose		^{60}Co Gamma		
		1MeV Neutrons (n/cm^2)	^{60}Co Gamma (rad)	Dose (rad)	Out Time --	Dose Rate (k rad/s)
Galileo	20.25dB	$8.4 \cdot 10^9$*	355*	100	27min	--
Pilkington	29.95dB	$1.24 \cdot 10^{10}$*	525*	100	20s	--
Schott	29.65dB	$1.98 \cdot 10^{11}$†	5 x 10^7**	10^6	0.3s	29††
Corning	27.45dB	$1.83 \cdot 10^{11}$	10^6	$3 \cdot 10^5$	1.9min	17.5††

* Dominated by fiber optic bundle.

† Photodiode a 14% effect at 125°C.

** LED is 50% effect and fiber optic bundle is 50% effect.

†† Dominated by PIN Photodiode.

9.7dB more excess signal and is, therefore, harder than the Galileo system. For the Pilkington system, the permanent damage threshold for a bit error rate of 10^{-8} is $1.24 \times 10^{10}/cm^2$ 1.0MeV neutrons or 525rad ^{60}Co gamma. Compared to the Galileo system, the permanent damage thresholds are not increased by a factor of 9.33 (9.7dB) but are increased by the ratio of the excess signals (in dB) which gives a factor of 1.479. The lead-silicate Pilkington fiber has very poor nuclear radiation hardness.

The Schott plastic clad-fused silica core fiber has the highest permanent damage thresholds shown in Table XXIV. For this system the error rate is 10^{-8} after a dose of $1.98 \cdot 10^{11}/cm^2$ 1.0MeV neutrons or 50M rad of ^{60}Co gammas. From Eq (23) the optimum emitter current in the 20MHz preamp input transistor is 326μA; for a common emitter current gain of 100 the dc base current is 3.25μA. For the optimized preamp, the total mean square input noise current is about equal to 2 times full shot noise on the dc base current; this is also equal to full shot noise on two times the dc base current. Thus, the mean square input noise current of the receiver can be represented by shot noise on a dc current of 6.5μA. For detector degradation to cause a S/N problem, the dark current of the detector must rise to a value of the order of 6.5μA. From Eq (253) the Schott system neutron fluence threshold of $1.98 \cdot 10^{11}/cm^2$ causes the detector lifetime to drop from 50μs to 25μs - a factor of 2 permanent degradation. From Eq (254), this change in lifetime will cause the dark current to double; at 27°C, the dark current will rise from 2.7nA to 5.4nA; 5.4nA is negligible compared to the equivalent noise current of 6.5μA. Thus, the Schott system neutron fluence threshold, which is the highest value in Table XXIV, causes a negligible permanent degradation in the PiN photodiode. If the temperature is raised to 125°C after neutron irradiation, the dark current of the photodiode will increase by

10^3 times to 5.4μA which is not negligible compared to 6.5μA. The S/N of the receiver at 125°C will be degraded by a factor of 1.14 (.56dB). In general, Table XXIV refers to operation at 25°C; however, if the Schott system is required to operate at 125°C the neutron fluence threshold drops to $1.74 \cdot 10^{11}/cm^2$. Thus, even for the Schott fiber, the SPX 1777 neutron degradation @ 125°C is only 14% of the degradation in the fiber optic bundle. Diffused junction GaAs LEDs like the SPX 1775 are tolerant to fast neutron fluences of $10^{12}/cm^2$, standard digital ICs are tolerant to $10^{13}/cm^2$ and monolithic linear ICs are tolerant to $10^{12}/cm^2$. Thus, none of these components causes a significant performance degradation at a fast neutron fluence of $1.98 \cdot 10^{11}/cm^2$.

The ionizing radiation permanent damage threshold for the Schott system of 5×10^7rad ^{60}Co gamma produces equal permanent degradation in the Schott fiber and the SPX 1775 LED. The fully depleted PIN silicon photodiode is not degraded by ionizing radiation. The standard digital ICs are tolerant to gamma doses of 10^7rad. In order to match the $5 \cdot 10^7$rad threshold, special radiation hardened ICs may be required. Monolithic linear ICs are tolerant to gamma doses of only 10^6rad. In order to match the $5 \cdot 10^7$rad threshold imposed by the fiber and LED, special hybrid linear ICs will be required.

The Schott plastic clad-fused silica core fiber has the highest (best) permanent damage threshold values of any reported fiber. Even so, the permanent damage threshold of the system is dominated by the Schott fiber.

The 1.0MeV neutron permanent damage threshold of the Corning low-loss fiber system is $1.83 \cdot 10^{11}/cm^2$. This value is less than the corresponding value for the Schott fibers only because of the ratio of excess signal values for the two systems. The neutron damage constants are the same for both fiber types. As in the Schott fiber system, the detector degradation will be noticeable at 125°C

but not at room temperature. All other components in the Corning system are unaffected by the fast neutron fluence of $1.83 \cdot 10^{11}/cm^2$.

The Corning fiber is more susceptible to damage by ionizing radiation than the Schott fiber. Thus, the ^{60}Co gamma permanent damage threshold of the Corning system is 10^6rad (50 times lower than for the Schott fiber). At this dose there is less than 10% degradation in the LED; all other components in the Corning system are tolerant to gamma doses of 10^6rad.

The permanent damage thresholds of the Corning fiber are higher (better) than for the lead-silicate fibers, but not as high as for the Schott fibers. The permanent damage threshold of the Corning system is dominated by the fiber optic bundle.

Permanent damage in the fiber optic bundles is caused by the creation of color centers; the absorption loss is greater (worse) at short wavelength. This is the case for both glass and plastic fibers. The tentative neutron data of Barsis[64] presented in Table XXI suggests that plastic fiber has a lower permanent damage threshold than Schott fiber at 900nm. However, the plastic fibers are useless at 900nm due to high intrinsic absorption. At 700nm, where the plastic fibers are useful (0.5dB/m), the neutron permanent damage constant for the plastic fibers is expected to be equal to or greater than that for Schott fibers at 900nm. For gamma-ray induced permanent damage, the Sandia Report[55] shows that the Schott glass at 900nm is far superior to the plastic fiber at 700nm. Based on these observations, the most fruitful area for research on radiation hard fiberoptic bundles (permanent damage) is in the fused silica core fibers at 900nm and not in the plastic fibers at 700nm. This conclusion is further reinforced by the anticipated difficulty of achieving a high performance LED at 700nm.

2. Transient Degradation

Transient degradation of the system is dominated by the transient absorption induced in the fiber optic bundle by a pulse of ionizing radiation represented by the ^{60}Co gamma-ray dose shown in Table XXIV. In order to observe the effect of the transient recovery of the fiber bundle after the pulse, it is necessary that the pulse dose be less than the permanent damage threshold for each fiber type. Otherwise the system will be permanently degraded and never return to an acceptable mode of operation. Based on this condition a pulse dose of 100rad was selected for the two lead-silicate fibers, 10^6rad for the Schott fiber and $3 \cdot 10^5$rad for the Corning low-loss fiber. The column in Table XXIV labeled "out time" designates the lapsed time following the indicated pulse before the system begins to operate at an error rate of less than 10^{-8}. It is anticipated that out time in the range of 1s to 5s represents the maximum that can be tolerated in a military aircraft.

Both the Galileo and Pilkington fibers have very low pulse dose thresholds and slow recovery during the transient. This behavior is characteristic of all lead-silicate fibers. Following a pulse of 100rad of ^{60}Co gamma rays, the Galileo system will be nonfunctional for 27min and the Pilkington system will be non functional for 20s. The advantage in the Pilkington system is entirely due to the larger value of excess signal. Both of these systems are unacceptable for use in a military pulse radiation environment.

The Schott fiber gives the best transient performance of any fiber reported. Following a ^{60}Co gamma-ray pulse of 10^6rad, the Schott system will be nonfunctional for only 0.3s. The Schott fiber not only has a high pulse dose threshold but it also shows a much more rapid transient recovery than the lead-silicate fibers. The 0.3s out time of this system can probably be tolerated by most military avionics systems provided adequate fail safe mechanisms are designed into the terminal units in the data transmission system.

The radiation characteristics of the Schott fiber used to compute the values in Table XXIV were extrapolated from the Sandia Report[55]. Unfortunately, the peak transient absorption data presented for this fiber extend only to 600k rad at 800nm and 47k rad at 900nm; the transient measurements extend only to 1μs at 800nm and 0.1s at 470nm with no data at 900nm. The extrapolation to high dose levels is made even more difficult by the fact that the peak transient absorption saturates at higher dose levels. The transient recovery extrapolation at 900nm is compatible with data available[59] on BTL silica core fiber. The 900nm peak transient absorption extrapolation is compatible with the 800nm data out to 600k rad. More transient measurements need to be performed on the Schott fiber; the data should be extended to higher doses and longer times.

The Corning low-loss fiber has a lower pulse threshold and faster transient recovery than the Schott fibers. Following a ^{60}Co Gamma-ray pulse of $3 \cdot 10^5$rad, the Corning system will be non-functional for 1.9min. This relatively long out time is primarily the result of the pulse dose used. To achieve an out time of 0.3s in the Corning system, the dose must be reduced to $3 \cdot 10^4$rad. The Corning low loss fiber is therefore not suitable for use in military avionic systems operating in a pulse nuclear radiation environment.

The transient attenuation induced in fiber optic bundles is higher (worse) at shorter wavelengths. The Sandia Report[55] shows that this is true for both SiO_2 and plastic fibers. For a 1.0M rad dose the peak transient absorption of Crofon fibers at 700nm is 63 times higher (worse) than the extrapolated Schott fiber at 900nm. This disadvantage for Crofon is partially offset by a faster transient recovery. The transient absorption of the Crofon decays to 10% of the peak value in 0.4s whereas the Schott fiber requires about 1.0s. Available data[55] indicate that the Schott fiber at 900nm has a more

desirable pulse-gamma transient characteristic than Crofon fiber at 700nm. Again, considering the anticipated difficulty of achieving a high-performance 700nm LED, it appears more likely that improved transient attenuation characteristics will result from a Schott type fiber operated at 900nm rather than a plastic fiber operated at 700nm.

3. Nuclear Pulse Response

All of the semiconductor components in the system of Figure 98 will respond directly to a high dose rate of ionizing radiation. In addition, ionizing radiation will cause the fiber optic bundle to luminesce in a broad spectrum with higher intensity at short wavelengths. The fiber optic luminescence will generate a photocurrent in the PIN photodiode. All of these direct pulse responses persist only for the duration of the pulse of ionizing radiation which will usually be less than 1μs. The nuclear pulse response will have the effect of injecting spurious bits into the data channel which will cause errors to be generated for the duration of the pulse. From Section IX.B* standard digital ICs are tolerant of gamma-ray dose rates of 10^7rad/s and radiation hardened ICs function at dose rates up to $3 \cdot 10^9$rad/s. Section IV.C* gives a gamma-ray dose rate threshold of 10^5rad/s for monolithic linear ICs. Properly designed hybrid linear circuits should tolerate dose rates up to 10^7rad/s. For a peak LED current of 100mA, a nuclear pulse light output equivalent to a 25mA bias will cause system errors. From Section VI.C* this corresponds to a gamma-ray dose rate of $1.75 \cdot 10^{10}$rad/s. Therefore, the SPX 1775 will function properly at any gamma-ray dose rate up to that level.

---

*In this Appendix.

For the Schott fiber system in Table XXIV, the optical signal power at the exit-end of the fiber optic bundle is 190μW. For a SPX 1777 responsivity of 0.5A/W this gives a PIN diode signal current of 95μA. A gamma-ray pulse response of 1/4 this value or 23.75μA will produce system errors. From Eq (258), the photodiode will give this current in response to a gamma-ray dose rate of 29k rad/s. For the Corning fiber system, the optical power at the end of the fiber optic bundle is 115μW and the error signal power is 28.75μW. In this case, the SPX 1777 will cause system errors when the gamma-ray dose rate is 17.5k rad/s.

The fiber optic luminescence output can be calculated from data presented in the Sandia Report[55] for the Schott and Corning systems. It is assumed for these calculations that a 100nm band pass optical filter centered at 900nm is used between the fiber optic bundle and the SPX 1777.

For the Schott fiber the luminescence constant at 900nm is 1.2×10^{-14}mW/cm-nm-rad-s^{-1} for 120 fibers with a core diameter of 4mil. Adjusting this luminescence constant to a 30m long 19 fiber bundle and correcting for 1.5dB of inherent self absorption and the 100nm filter gives a value of $4.0 \cdot 10^{-10}$mW/rad-s^{-1}. For a pulse power on the detector of 48μW the dose rate is

$$R = \frac{48 \cdot 10^{-3}\text{mW}}{4 \cdot 10^{-10}\text{mW/rad-s}^{-1}} \tag{276}$$

$$R = 1.2 \cdot 10^{8}\text{rad/s}$$

For the Corning fiber the luminescence constant at 900nm is 8×10^{-17}mW/cm-nm-rad-s^{-1} for a bundle of 64 fibers. Adjusting this value for a 30m long 19 fiber bundle and correcting for 0.45dB of inherent self absorption and the 100nm filter gives 6.5×10^{-12}mW/rad-s^{-1}. For a pulse power on the detector of 28.75μW the dose rate is

$$R = \frac{28.75 \times 10^{-3}\text{mW}}{6.5 \times 10^{-12}\text{mW/rad-s}^{-1}} \qquad (277)$$

$$R = 4.4 \times 10^{9}\text{rad/s}$$

The Schott fiber has a luminescence constant that is 150 times higher (worse) than the Corning fiber.

No definitive data is available for the luminescence of lead-silicate glasses. For a dose rate of 1.2×10^{8}rad/s it would require only 3μs for the Galileo system to accumulate a total dose of 355rads which would cause system failure due to permanent damage.

Comparing the nuclear pulse response error thresholds presented in the foregoing discussion shows that for the Schott and Corning systems the pulse response is dominated by the SPX 1777 PIN photodiode. The dose rates presented in Table XXIV are for the photodiode. For a 30m length, the Schott and Corning fibers have about the same degree of pulse hardening as the radiation hard digital ICs. From the Sandia Report[55], plastic fibers produce about 100 times more gamma-ray pulse luminescence than the Schott fiber and all fibers show pulse luminescence that peaks at short wavelength. Thus, there is a nuclear pulse hardening advantage in filtered operation of Schott or Corning fibers at 900nm as compared to plastic fibers at 700nm.

The impact of the nuclear pulse response on system performance is not serious provided the system is designed for this environment. All digital and linear ICs must be designed to avoid latch-up and self destruction as a result of the nuclear pulse. Regulated power supplies should be current limited to avoid component burn out for high dose-rate pulses. This is particularly true for the high-voltage bias supply on the PIN photodiode; a dose rate of 1.2×10^{9} rad/s will generate a current of 1.0A in the photodiode. A pulse current of this magnitude could be desctructive if the bias voltage remained at 100V.

Assuming the circuits are protected against burn-out, the major effect of a nuclear pulse is to cause system errors for the duration of the pulse plus an additional settling time for all of the circuits to regain normal operating levels. It should be possible to keep this electrical settling time as short as the 0.3s out time required for the transient attenuation recovery of the Schott fiber -- see Table XXIV. In a data bus, standard tests for nonstandard Manchester bits and parity checks will automatically reject all transmissions made during the pulse and recovery period. These rejected words will be requested again after recovery from the pulse.

C. CONCLUSIONS AND RECOMMENDATIONS

From Table XXIV the Schott fiber is shown to provide the best overall response in a nuclear radiation environment. Even so, the Schott fiber dominates the radiation performance of the system in every area except nuclear pulse response which is limited by the PIN photodiode.

For both plastic and SiO_2 fiber optic bundles, all degradation effects are more pronounced at short wavelength. Also, the Schott fiber operated at 900nm is superior to Crofon at 700nm on all major performance factors except speed of transient absorption recovery. For these reasons, the Schott type fiber optic bundles seem to offer the best probability of achieving radiation hard fibers. Research and devleopment on Schott type fibers at 900nm should receive priority over work on plastic fibers for use at shorter wavelengths. If significant reductions are made in the permanent neutron damage of fiber bundles, then effort will be required to neutron harden the PIN photodiode. If the permanent gamma-ray damage in fibers is reduced, then gamma-ray hardening of the LED will be required.

More extensive transient absorption measurements are needed on Schott type fibers. Other manufacturers' fiber optic products should be evaluated and measurements should be extended to higher doses and longer decay times. Doping studies should be performed to reduce the peak transient absorption in the Schott fibers and speed up the transient recovery. The exchange of deuterium for hydrogen in the hydroxyl concentration[70] in the Schott type fibers looks promising for reducing the inherent absorption at 940nm. If this idea is successful, the deuterated silica fibers could be used with a single heterojunction InGaAs LED at 930nm. An InGaAs edge emitter offers a factor of 10 improvement in both output power and speed compared to present GaAs edge emitters. The InGaAs unit should have lower thermal resistance than the comparable structure in AlGaAs.

The gamma-ray pulse response of the PIN photodiode is the dominating factor in the nuclear pulse response of the system. This nuclear pulse response can be reduced by decreasing the volume of the chip. A reduction factor of 25-30 can be achieved through proper chip design but a sophisticated package development effort will be required to minimize the loss of preirradiation system performance.

REFERENCES

1. J.R. Biard, "Optoelectronic Aspects of Avionic Systems", Final Technical Report AFAL-TR-73-164, Air Force Contract No. F33615-72-C-1565; June 1973, AD 910-760.

2. J.R. Biard and J.E. Shaunfield, "Optical Couplers", Interim Technical Report AFAL-TR-74-314, Air Force Contract No. F33615-74-C-1001; September 1974.

3. J.R. Biard and L.L. Stewart "Optoelectronic Data Bus", Final Technical Report AFAL-TR-73-271, Air Force Contract No. F33615-62-C-1911; October 1973, AD 914-009.

4. Glen E. Miller, Boeing Aerospace Company, Research and Engineering Division; Seattle, Washington; Private Communication.

5. C. Gifford, "Proposed Military Standard for Aircraft Internal Time Division Multiplex Data Bus", ASD/ENAIB, 23 July 1973.

6. J.D. Skilling, "Pulse and Frequency Response", The GR Experimenter, p.3, Nov.-Dec. 1968.

7. A.B. Carlson, *Communication Systems*, McGraw Hill, New York, p. 409; 1968.

8. R. Bracewell, *The Fourier Transform and Its Applications*, McGraw Hill, New York, Chapter 3; 1965.

9. M. Schwartz, W. R. Bennett, and S. Stein, *Communication Systems and Techniques*, McGraw Hill, New York, p. 66; 1966.

10. Dr. K. W. Heizer, Electrical Engineering Department, Southern Methodist University, Private Communication; March 1974.

11. A.F. Milton and L.W. Brown, "Nonreciprocal Access to Multi-terminal Optical Data Highways" Proceeding, 1973 IEEE/OSA Conference on Laser Engineering and Applications, Washington, D.C.; May 30-June 1, 1973, pp 24-25

12. W. Bart Bielawski, "A User's View of Optical Communications", IGC Conference; October 28-30, 1973.

13. H.F. Taylor, W.M. Caton and A.L. Lewis "Fiber Optics Data Bus System", DoD/Industry-Wide Integrated Optic and Fiber Optic Communications Conference, Naval Electronics Laboratory Center, San Diego, California; 15-17 May 1974.

14. G. Franklin and T. Hatley, "Don't Eyeball Noise", Electron Design, p. 184, Nov. 22, 1973.

15. Tove et-al, "Measurement of Drift Velocity of Electrons in Silicon by Exciting a Diode Structure with Short Superradiant Laser Pulses", IEEE Trans. Electron Devices, vol. ED-17, pp. 407-412, May 1970.

16. A. Papoulis, *The Fourier Integral and Its Applications*, McGraw Hill, New York, 1962.

17. R.D. Evans, *The Atomic Nucleus*, McGraw-Hill Book Company, 1955.

18. Richtyer, Kennard and Lauritsen, *Introduction to Modern Physics*, McGraw-Hill Book Company, 1955.

19. A.H. Compton and S.K. Allison, *X-Rays in Theory and Experiment*, D. Van Nostrand Company, 1935.

20. S. Glasstone, *The Effects of Nuclear Weapons*, US Government Printing Office, US AEC, 1962.

21. *DNA EMP Awareness Course Notes*, Second Edition DNA 2772T August, 1973.

22. L.W. Ricketts, *Fundamentals of Nuclear Hardening of Electronic Equipment*, John Wiley and Sons, New York, 1974.

23. H.L. Olesen, *Radiation Effects on Electronic Systems*, Plenum Press, New York, 1966.

24. D. Billington and J.H. Crawford, *Radiation Damage in Solids*, Princeton University Press, Princeton, N.J., 1961.

25. F.L. Vook, *Radiation Effects in Semiconductors*, Plenum Press, New York, 1968.

26. F. Larin, *Radiation Effects in Semiconductor Devices*, John Wiley & Sons, New York.

27. J.J. Loferski and P. Rappaport, "Radiation Damage in Ge and Si Detected by Carrier Lifetime Changes: Damage Changes:, Phys. Rev. 111 432 (1958).

28. A.D. Kantz, "The Average Neutron Energy of Reactor Spectra and Its Influence on Displacement Damage", Sandia Technical Memorandum 205-62 (53), August, 1962.

29. A.J. Dekker, *Solid State Physics*, Prentice-Hall Inc., Englewood Cliffs, N.J., 1957.

30. C. Kittel, *Introduction to Solid-State Physics*, John Wiley and Sons, Inc. 1956.

31. C. Peters, Fortsch, Chem. Forsch. 1, 613 (1950)

32. G. T. Dienes, "Introduction-Defects in Silicas", J. Phys. Chem. Solids 13, 277, (1960).

33. E. Lell, "Radiation Effects in Doped Fused Silica", *Physics and Chemistry of Glasses"* 3, 84, (1962).

34. S.M. Sze, *Physics of Semiconductor Devices,* Interscience, New York, pp. 663-665, 1969.

35. G. C. Messenger and E. L. Steele, "Statistical Modeling of Semiconductor Devices for the Tree Environment", IEEE Trans. on Nucl. Sci., NS-15, No. 6, pp. 133-139, December, 1968.

36. S.K. Manlief, "Neutron-Induced Damage in Silicon Rectifiers," IEEE Trans. On Nucl. Sci., NS-11, No. 5, pp. 47-54, November, 1964.

37. C.A. Goben et-al, "Neutron Fluence and Electric Field Strength Dependencies of the Rate of Volume Damage Introduction in Silicon P-N Junctions," IEEE Trans. on Nucl. Sci., NS-16, No. 6, pp. 43-52, December, 1969.

38. J.W. Easley, "Radiation Effects in Semiconductor Devices," Nucleonics, pp. 5i-56, July, 1962.

39. G.C. Huth in *Proceedings of 2nd Conference on Nuclear Radiation Effects on Semiconductor Devices, Materials and Circuits,* p. 49, Cowan Publishing Corp., New York, 1959.

40. A.S. Grove, *Physics and Technology of Semiconductor Devices,* John Wiley and Sons, Inc., 1967.

41. C. W. Gwyn et-al, "The Analysis of Radiation Effects in Semiconductor Junction Devices," IEEE Trans. on Nucl. Sci., NS-14, No. 6 pp. 153-169, December, 1967.

42. W.L. Brown, "Introduction to Semiconductor Particle Detectors," IRE Trans. on Nucl. Sci., NS-8, No. 1, pp. 2-7, January, 1961.

43. R.W. Kuckuck et-al, "Response Function and Sensitivity of Double-Diffused Silicon Detectors in High Dose Rate Fields," Lawrence Radiation Laboratory Report No. UCRL-14405.

44 A.A. Bergh, "Light-Emitting Diodes," Proc. IEEE, 60, pp.156-224 February, 1972.

45. Epstein, Share, Polimadei, and Herzog, "Gamma Irradiation and Annealing Effects in Nitrogen-Doped $GaAs_{1-x}P_x$ Green and Yellow Light-Emitting Diodes," IEEE Trans. on Nucl. Sci., NS-19, pp. 386-390, December, 1972.

46. Epstein, Share, Polimadei, "Effect of Neutron Irradiation on $GaAs_{1-x}P_x$ Electroluminescent Diodes," Appl. Phys. Lett., 23, pp. 472-474, October, 1973.

47. M. Petree, Appl Phys. Letters 3, 67 (1963).

48. C.E. Barnes, Phys. Rev. B1, 4755 (1970).

49. A.S. Eptstein, S. Share, R. A. Polimadei, and A. H. Herzog, IEEE Trans. Nucl. Sci. NS-19, 386 (1972).

50. C. E. Burns, J. Appl. Phys. 42, 1941 (1971).

51. R. A. Logan, H. G. White, and R. M. Mikulyak, Appl. Phys. Letters 5, 41 (1964).

52. Share, Epstein, and Polimadei, "Radiation Damage and Hardening Effects on Compensated GaAs Light-Emitting Diodes", IEEE Trans. on Nucl. Sci. NS-20, pp. 256-260, 1963.

53. Redfield, Wittke, and Pankove, PHys. Rev. B2, 1830 (1970).

54. G. H. Sigel and B. D. Evans, "Effects of Ionizing Radiation on Transmission of Optical Fibers," Appl. Phys. Lett. 24, 410 (1974).

55. Mattern, Watkins, Skoog, Brandon and Barsis, "The Effects of Radiation on the Absorption and Luminescence of Fiber Optic Waveguides and Materials," Sandia Report 74-8622, Sandia Laboratories, July, 1974. The results of this investigation are shown to be valid at low dose rates by L. M. Watkins, "Absorption Induced in Fiber Waveguides by Low Dose-Rate Electron and Gamma-ray Radiation," Sandia Report 75-8222; March 1975.

56. G.H. Sigel, Jr., NRL Memo Report 2704, Dec. 1973 (unpublished).

57. Am Am. Bishay, Ed., *Interaction of Radiation with Solids,* Plenum Press, New York (1967).

58. J.S. Van Wieringen and A. Kats, Philips Res. Rep. 12, 432 (1957).

59. G.H. Sigel et-al, "Radiation Effects in Fiber Optic Waveguides," NRL Report 2934, November, 1974.

60 E.W.J. Mitchell and E.G.S. Paige, "The Optical Effects of Radiation Induced Atomic Damage in Quartz," Phil, Mag. 1, 1085 (1956).

61 P.W. Levy, "Reactor and Gamma-Ray Induced Coloring of Corning Fused Silica," J. Phys. Chem. Solids, 13, 287 (1960).

62 C.N. Nelson and J.H. Crawford, "Optical Absorption in Irradiated Quartz and Fused Silica," J. Phys. Chem. Solids, 13, 296 (1960).

63. R.D. Maurer et-al, "Effect of Neutron- and Gamma-Radiation on Glass Optical Waveguides," Applied Optics, 12 No. 9, 2024 (1973).

64. Private Communication from E.H. Barsis, Sandia Laboratories, Livermore, California.

65. Kalus Becker, *Solid State Dosimetry* (CRC Press, Cleveland, Ohio), 1973.

66. J.A. Wall, "Transient Radiation Effects Tests of a Corning Radiation-Resistant Optical Fiber," AFCRL-TR-75-0012, January, 1975.

67. Private Communication from M.A. Archarekar, "Technical Objectives in Radiation Resistant F.O. Cable," Galileo Electro-Optics Corp. March, 1974.

68. E.J. Friebele, R.J. Ginther and G.H. Sigel, Jr., "Radiation Protection of Fiber Optic Materials: Effects of Oxidation and Reduction," Appl. Phys. Lett. 24, 412 (1974).

69. W.D. Compton and G.W. Arnold, Disc. Faraday Soc., 130 (1961).

70. J.E. Shelby and P.L. Mattern, presented at the fall meeting, Am. Ceram. Soc., Bedford Springs, Pa., Oct 9-11, 1974.

71. F. Larin, *Radiation Effects in Semiconductor Devices*, John Wiley and Sons, Inc., New York, 1968.

72. Olson, Alexander, and Antinone, "Radiation Response Study of New Radiation Hardened Low Power TTL Series", IEEE Trans. on Nuclear Sci., NS18. 243, December, 1971.

73. O. Tiainen and P. Jauho, "Radiation Resistance of Microelectronic Systems", IEEE Trans. on Nuclear Sci., NS17, 3, Aug., 1970.

74. J.R. Greenbaum, et al, "Radiation Models for Digital Integrated Circuits", IEEE Trans. on Nuclear Sci., NS19, 96, Dec., 1972.

75. C.U. Perkins and R.W. Marshall, "Radiation Effects on Monolithic Silicon Integrated Circuits," IEEE Trans. on Nucl. Sci., NS-13, No. 6, pp. 300-308, December, 1966.

76. A.A. Wittels and M.L. Eisenberg, "A Method for an Accurate Prediction of Degradation Characteristics and Quality Assurance of a 709 Amplifier", IEEE Trans. on Nuclear Sci., NS17, 173, December, 1970.

☆ U. S. GOVERNMENT PRINTING OFFICE: 1975 — 657-630/118